Upscaling of Thermodynamic Properties for Flow Simulation in Low Permeability Unconventional Reservoirs

Nicolas Sobecki

UPSCALING OF THERMODYNAMIC PROPERTIES FOR FLOW SIMULATION IN LOW PERMEABILITY UNCONVENTIONAL RESERVOIRS

A Dissertation Submitted to the Committee
on Graduate Studies of Sorbonne University
in Partial Fulfillment of the Requirements
for the Degree of Doctor of Philosophy

Nicolas SOBECKI

September 13, 2019

THÈSE DE DOCTORAT DE
SORBONNE UNIVERSITÉ

Géosciences, Ressources Naturelles et Environnement (ED 398)

Présentée par

Nicolas Sobecki

Pour obtenir le grade de
DOCTEUR de SORBONNE UNIVERSITÉ

Sujet de la thèse :

Mise à l'échelle des propriétés thermodynamiques pour la simulation des écoulements dans les réservoirs non-conventionnels de très faible perméabilité.

---

soutenue le 15 octobre 2019 à l'IFPEN, Rueil-Malmaison, France,

devant le jury composé de :

Dr. Didier-Yu Ding	IFPEN, FR	Promoteur et directeur de thèse
Dr. Carlos Nieto-Draghi	IFPEN, FR	Promoteur de thèse
Dr. Laurent Jeannin	Storengy-ENGIE, FR	Rapporteur
Dr. Flor Siperstein	University of Manchester, UK	Rapporteur
Dr. Benjamin Rotenberg	Sorbonne Université, FR	Examinateur
Dr. Yu-Shu Wu	Colorado School of Mines, USA	Examinateur

Abstract

Tight oil and shale gas reservoirs have a significant part of their pore volume occupied by micro (below 2nm) and mesopores (between 2 and 50nm). This kind of environment creates strong interaction forces in the confined fluid with pore walls as well as between its own molecules and then changes dramatically the fluid phase behavior and its thermodynamic properties. Pressure-Vapor-Temperature (PVT) modeling of such fluids becomes therefore a challenge in order to get accurate production forecast reservoir simulations. Furthermore along the flow from the matrix to the well through the fractures, the fluid will pass through a very heterogeneous pore size distribution (PSD) which will alter it differently according to the pore size and the spatial distribution. An important work has therefore to be done on developing upscaling methodology of the pore size distribution for large scale reservoir simulations. Firstly, molecular simulations are performed on pure components and mixtures in order to get reference thermodynamic properties at liquid/vapor equilibrium for different pore sizes. Then, the comparison with commonly used modified equation of state (EOS) in the literature highlighted the model of flash with capillary pressure and critical temperature and pressure shift as the best one to match reference molecular simulation results. Afterwards fine grid matrix/fracture simulations have been built and performed for different pore size distributions. The study has shown that the pore size distribution has an important impact on reservoir production and that this impact is highly dependent on the volume fraction of nanopores inside the matrix. Capillary pressure heterogeneity and pore radius dependent EOS cause gas flow slowdown or gas trapping inside the matrix and postponed gas flow apparition in the fractures during depletion which reduce the GOR (Gas-Oil Ratio) at the well. Coarse grid upscaling models have then been performed on the same synthetic case and compared to the reference fine grid results. The commonly used upscaling methodology of dual porosity model with average pore radius for the pore size distribution is unable to match the fine grid results. A new triple porosity model considering fracture, small pores and large pores with their own capillary pressure and EOS, together with MINC (Multiple Interacting Continua) approach, has shown very good match with the reference fine grid results. Finally a large scale stimulated reservoir volume with different pore size distribution inside the matrix has been built using the upscaling method developed here. The proposed triple porosity methodology is able to model the PVT of the confined fluid and its flow across a very heterogeneous pore size distribution up to the well through fractures in a large scale reservoir simulation.

Acknowledgment

First of all, I would like to express my greatest gratitude to my advisors, Dr. Didier-Yu Ding and Dr. Carlos Nieto-Draghi for their excellent guidance, patience and continuous support throughout my PhD study. It was a real privilege and a great pleasure to work with you, thank you very much. I also want to thank my committee members: Dr. Laurent Jeannin, Dr. Flor Siperstein, Dr. Benjamin Rotenberg and Dr. Yu-Shu Wu for their time and effort to review my dissertation and for providing me many valuable suggestions and comments.

I am very thankful to the GéoThermoHydroMécanique department of IFPEN for the financial support of this research. I would like to acknowledge all the engineers of the department for their support and helpful advice about my work. Among them, I want to give a special thanks to Dr. Benoit Noetinger for helping me to go twice to Colorado School of Mines in the USA as a visiting student. I am very grateful to Dr. Yu-Shu Wu for welcoming me there in his research center: the Energy Modeling Group (EMG). I also want to express my sincere thanks to my collaborator Dr. Shihao Wang with whom I had the pleasure of working in the EMG and who kindly gave me a tour of the campus and the city of Golden.

I want to express my gratitude to my colleagues and friends who made my stay in IFPEN very pleasant during these three years of PhD, Dr. Zady Ouraga, Dr. Omar Gassara, Razi Ben Ahmed, Dr. Anouk Beniest, Sebastien Szollozi, Vicky Aditya Hasan, Pierre Hacquard, Julien Gasser Dorado, Narges Dashtbesh, Dr. André Brüch and many others. I have learned a lot from you both personally and professionally. Special thanks are due to my sport and party buddies, Matthieu Mascle, Dr. Christopher Yeathes and Dr. Aurelien Cherubini with whom I had a lot of fun.

Last but not least, I would like to thank my family. My parents for their encouragements in my career choice and my beloved fiancée Marla Thomas who strongly supported me for the last three years.

Contents

List of Figures

List of Tables

Nomenclature

Variables

A	interface area
a	configuration of particles in a given statistical ensemble
d	distance between two cells
F	Molar flux exchange term
f	fugacity
g	gravity coefficient
H	slit pore width
J	J Leverett function
k	absolute permeability
k_B	Boltzmann constant
K_i	equilibrium constant of component i
k_{ij}	binary interaction coefficient between components i and j
k_r	relative permeability
L	liquid molar fraction
M	accumulation term
n	mole of the mixture
n_b	number of total grid blocks (or cells)
n_c	number of hydrocarbon components
N_{av}	Avogadro number

n_{comp}	total number of components
P	Parachor
p	pressure
P^{acc}	acceptation probability
P^{gen}	generation probability
p_b	bubble point pressure
P_c	critical pressure
p_c	capillary pressure
p_d	dew point pressure
q	internal sink/source term per unit of volume
R	gas constant
r	pore radius
r_K	effective radius
S	saturation
S_{wi}	residual water saturation
T	temperature
T_c	critical temperature
U	potential energy
V	vapor molar fraction
v	volume fraction
V^ϕ	Volume of phase ϕ
V_c	critical volume
V_m	molar volume
V_n	representative elementary volume of grid cell n
v_p	pore volume fraction
v_ϕ	Darcy velocity of phase ϕ

V_{block} matrix block volume

V_{cell} grid cell volume

X thermodynamic macroscopic property

x_i liquid molar fraction of component i

y_i vapor molar fraction of component i

Z compressibility factor

z_{ci} critical composition of component i

z_i molar fraction of component i

Z_{res} reservoir depth of the cell n

Greek Symbols

α pore structure parameter for the triple porosity calibration

δ distance from the carbon atom in AUA model

ϵ porosity

ϵ_{ij} depth of the interaction potential well between particles i and j

γ transmissivity

Λ thermal de Broglie length

λ mobility

μ chemical potential

μ_ϕ viscosity of phase ϕ

ω acentric factor

Φ fugacity coefficient

π transition matrix of the Markov chain

Ψ fluid potential

ρ molar density

ρ_s atomic density of the solid

ρ_{ens} distribution probability of a statistical ensemble

ρ_{mass}	mass density
σ	characteristic diameter of the molecule
σ_{ij}	distance between two particles i and j where attraction and repulsion are canceled
σ_{shape}	shape factor
σ_{vl}	interfacial tension
θ	contacting angle of the fluid

Subscripts

ϕ	fluid phase
b	bulk
F	fracture medium
f_1	facies 1
f_2	facies 2
f_3	facies 3
g	gas
i	component i of the mixture
L	large pore medium
l	liquid
M	matrix medium
o	oil
p	pore
S	small pore medium
v	vapor
w	water

Abbreviations

μVT	grand canonical ensemble
CDF	cumulative distribution function

CP	critical point
CPU	central processing unit
DP	dual porosity
EOS	equation of state
FIB	focused ion beam
$GCMC$	grand canonical Monte Carlo
$GEMC$	Gibbs ensemble Monte Carlo
GOR	gas oil ratio
IFT	interfacial tension
$MINC$	multiple interacting continua
MIP	mercury intrusion porosity
NPT	isotherm-isobar ensemble
NVT	canonical ensemble
PSD	pore size distribution
REV	representative elementary volume
SRV	stimulated reservoir volume
WI	well index

Chapter 1

Introduction

1.1 Context

Growth in the world economy requires more energy and demand is projected to increase by 30% in 2035 [21]. Even though the no fossil fuels (renewable and nuclear) will grow faster than fossil fuels, fossil fuels will still account for more than three-quarters of world energy consumption through 2040 and natural gas will represent the fastest-growing fossil fuel in the future (Figure 1.1).

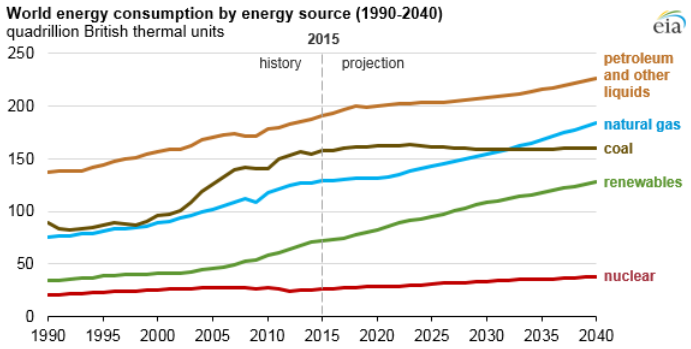

Figure 1.1: World energy consumption by energy source [132]

Among oil and gas production, unconventional resources such as shale gas and tight oil have received a great attention in the past decade and become the focus of the petroleum industry for the development of energy resources worldwide. Indeed according to U.S. Energy Information Administration [131] world tight oil production will more than double from 2015 to 2040 (Figure 1.2) and will represent almost 10% of the world oil production which is estimated to 113 million b/d in 2040 [132] or 109.1 million b/d in the new policies scenario [46]. Most of the projected increase will come from the United States, with much of the rest coming from countries such as Russia, Canada, and Argentina.

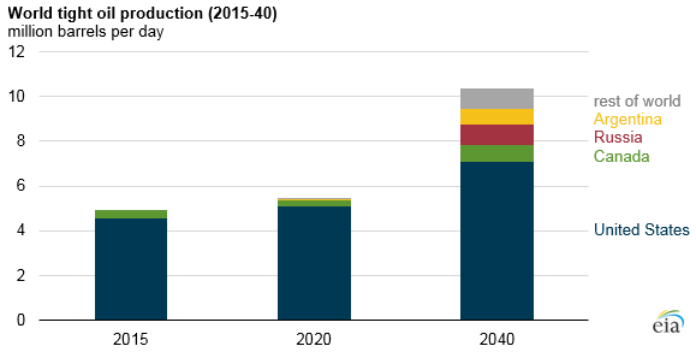

Figure 1.2: World tight oil production [131]

On the other hand shale resources become increasingly important to natural gas supply and shale production will account for around sixty percent of the increase in gas supplies to 2035 according to BP. It will represent 30% of the world natural gas production in 2040 [131]. Currently the US is the largest shale gas supplier in the world and they represent with Canada, China and Argentina, the four only countries which have commercial shale gas production now. Development of shale resources are expected in the future primarily in Mexico and Algeria.

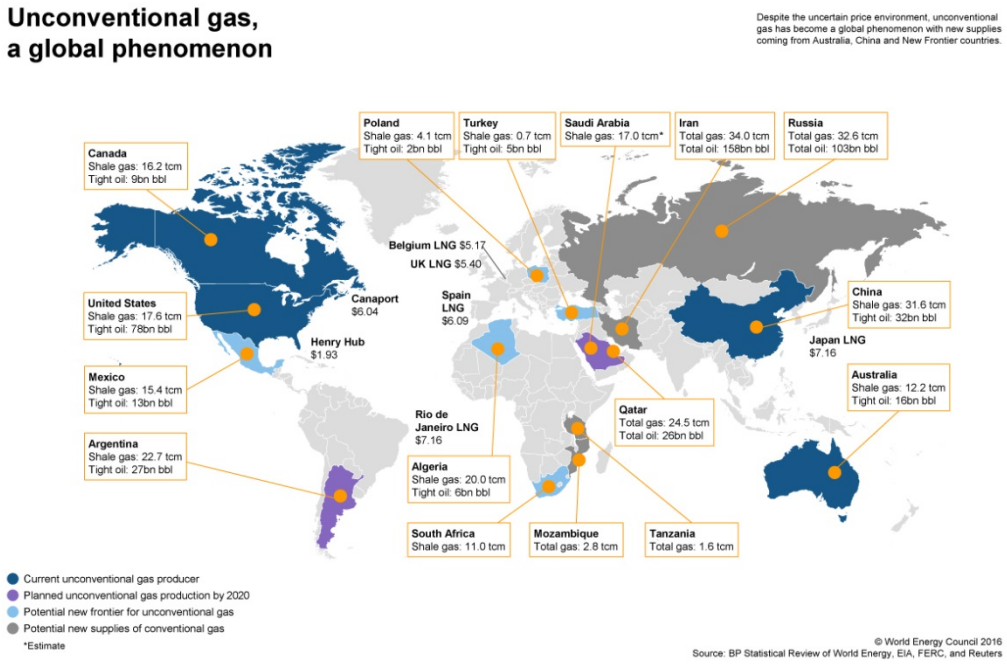

Figure 1.3: New supply landscape (technically recoverable landscape) [145](1tcm=35.3 trillion cubic feet)

The concept of "shale gas" is generally well understood. It corresponds to gas in the source

rock which has very low permeability. Regarding the term "tight oil", the definitions are not very clear. According to the IHS report [47]: "Shale gas is contained in low-permeability shale rock; tight sands gas is contained in low permeability sandstones and carbonates; and tight oil is contained in shales and low-permeability carbonates, and sandstones. Because all of these rocks have low permeability, they are informally referred to as being 'tight'." Being consistent with this definition, tight oil reservoir will then refer to all petroleum reservoir of very low permeability including shale plays and source rock with initial hydrocarbons fluid in liquid phase. Shale gas and tight oil resources are enormous worldwide and are mainly located in the US, Canada, China, Australia and Argentina (Figure 1.3), the shale gas technically recoverable reserves are estimated to 7576.6 trillion cubic feet and the tight oil reserves are estimated to 417.9 billion barrels [37]. For comparison, the world oil consumption in 2016 was 96.558 million barrel per day and the world natural gas consumption was 125.116 trillion cubic feet per annum [22]. Then the current resources of shale gas and tight oil represent around 60 years of world natural gas production and around 10 years of world oil production.

Unlike conventional reservoir, tight oil and shale gas reservoirs have extremely low permeability, in the order of a few hundred nano-darcies and are therefore very hard to produce without stimulation. The basic technical breakthrough, which made economical production of such reservoirs a reality was horizontal drilling of long boreholes of 2,000+ feet long and multi-stage (10-20) hydraulic fracturing in horizontal wells. On one hand long horizontal well drilling techniques allow to place the production well in contact with as much as possible of the reservoir matrix. On the other hand multi-stage hydraulic fracturing aims to stimulate intensively a large volume of the matrix and create a permeable reservoir. This intensive set of induced and propped hydraulic fractures provides the critical flow paths from the matrix to the horizontal well and enhances the well productivity.

The flow dynamics and the fluid behavior in shale gas and tight oil reservoirs are much more complex than those in conventional reservoirs. Indeed these unconventional reservoirs are characterized by highly nonlinear behavior of multiphase flow in extremely low-permeability rock, highly heterogeneous porous/fractured, and stress-sensitive rock. The flow is then coupled with many co-existing physical processes, such as adsorption/desorption phenomena [28, 110, 138], long-lasting transient nature of fracture-matrix interaction [150], geomechanics effects [153], Non-Darcy flow, Klinkenberg slippage effect, Knudsen diffusion [105, 157] and strong rock-fluid interaction within nano-pores or micro-fractures. The traditional conventional reservoir simulators may not be in general applicable for shale gas and tight oil reservoir simulation. That is why a lot of research has been done in order to get effective modeling tools for quantitative studies of these unconventional reservoir dynamics and performance, and for their optimal production schedules in the field.

This research will be focused on the last point listed above of shale gas/tight oil charac-

teristics: strong rock-fluid interaction within nano-pores or micro-fractures. This dissertation will study the thermodynamic behavior of hydrocarbons in such nano pores reservoirs and their modeling for large scale reservoir simulations.

1.2 Pore scale characterization of shale gas and tight oil reservoirs

1.2.1 Matrix composition

Tight oil and shale gas matrix can be mineralogically described using a ternary diagram with three dominant mineral components: carbonates, clay and silica. An example of this repartition is given by Chalmers et al. [24] on samples from several known shale reservoirs. Furthermore the matrix is associated with organic content known as kerogen. Using Focused Ion Beam Scanning Electron Microscopes (FIB/SEM) imaging technology, Ambrose et al. [8] performed micro-scale investigation of gas shale samples. They show that majority of gas pore volume is contained in the organic material. Chalmers et al. [24] also performed electron microscopy analyses images of shale samples using Field emission scanning electron microscope (FE-SEM). He shows that pore volumes are either present in clays or kerogen. An example of results is shown in Figure 1.4.

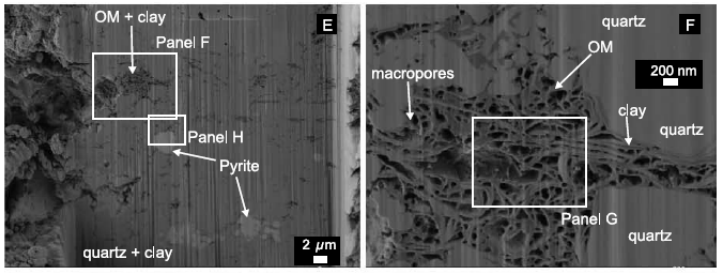

Figure 1.4: Field emission scanning electron microscope (FE-SEM) images of the Barnett sample Chalmers et al. [24].

Fluid molecules in shale media can be found in two different states: free molecules in the pores and adsorbed molecules on the pore surface. That is why Ambrose et al. [8] consider the adsorbed gas volume in its new methodology for shale gas in place calculation. Authors like Jin and Firoozabadi [54] also consider the dissolved molecules in the organic matter. In summary fluid is located in clays and kerogen where surface adsorption can be important.

1.2.2 Pore size distribution and petrophysical properties

In order to classify pores of a porous medium according to their size, the International Union of Pure and Applied Chemistry (IUPAC) has recommended the following classification:

- Micropores: pores with pore size below 2 nm
- Mesopores: pores with pore size between 2 nm and 50 nm
- Macropores: pores with pore size greater than 50 nm

The term pore size corresponds to the distance between two sides of a slited-shaped pore or the dimension of a pore throat. Several authors like Kuila and Prasad [61, 62] and Chalmers et al. [24] conducted experiments to investigate the pore system of gas shale reservoirs. They showed that shale matrix has an important fraction of micro to meso-pores and that the pores are mainly associated with clay minerals and organic matter. Usually pore-size analysis are made by mercury intrusion techniques for conventional reservoirs. However for unconventional shale reservoirs, instrumental limitations do not allow the mercury to access the full pore structure. Nitrogen gas-adsorption techniques can be used instead for micro and mesopores study but it fails to measure large pores (diameter higher than 200 nm). In the papers of Kuila and Prasad [61, 62] and Chalmers et al. [24], the method to measure pore size distribution were both mercury porosimetry and low-pressure gas adsorption. Chalmers et al. [24] conducted experiments on six samples obtained from drill cuttings, one each from the Barnett, Marcellus, Woodford, and Haynes-ville units and two from Doig formation. They used FIB milling coupled with high-magnification electron microscopy to image nanometer scaled porosity in gas shale reservoirs. These observations demonstrated that most of the macropores and mesopores are contained in aggregates of kerogen and clay. Furthermore it confirmed the interconnection between macropores with both coarse and fine mesopores. Kuila and Prasad [61] conducted experiments on clay and shale sample, the volume fraction of micropores in the studied samples ranges around 9% and can be as high as 19.23% in the ilite-Cambrian shale. In 2013, Kuila and Prasad [62] compare pore-size distribution of clay and shale samples. Modal size between the pore distribution ranges from 10-20 nm in shales and from 70-80 nm in pure clays (Figure 1.5).

Pommer [95] used scanning electron imaging on twenty samples from four wells in the eagle ford formation. Image processing methods aimed to determine pore size distribution. Other studies about pore size distribution in shale gas and tight oil reservoirs can be found in [29, 154, 104]. Wang and Reed [138] studied pore networks in gas shales and indexed porosity and permeability relationships of different shales plays. This shows the order of magnitude of porosity and permeability in such reservoir (Figure 1.6).

Since the size of hydrocarbon molecules is between 0.5 nm and 10 nm [83], a significant fraction of the fluid inside the matrix present solid-fluid interactions of the same order of magnitude as intermolecular interactions of fluid molecules. This fact strongly modifies the thermodynamic properties of confined fluids with respect to bulk phases.

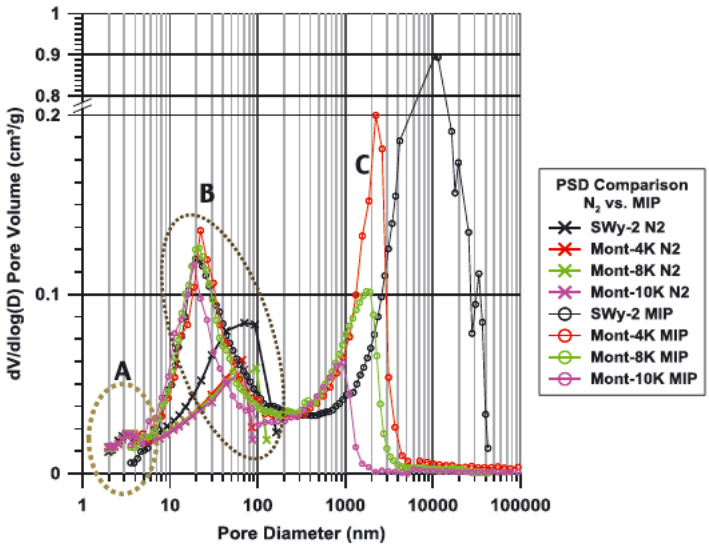

Figure 1.5: Comparison of N_2 gas adsorption and Mercury intrusion porosimetry (MIP) for pure clays. [62]

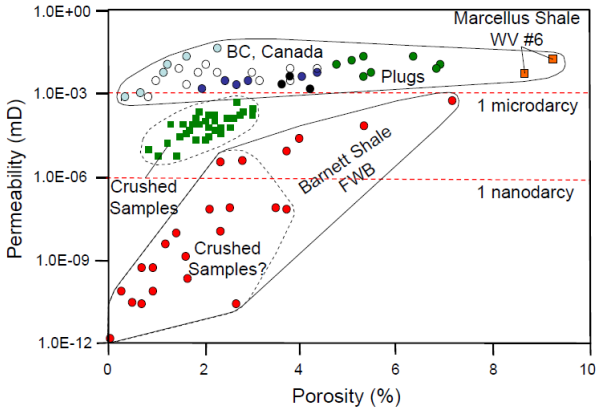

Figure 1.6: Porosity and permeability relationships of shale gas plays in north America measured using plugs and crushed samples. Data from the Marcellus Shale, West Virginia and from Canada using core plugs, and the Barnett Shale, Fort worth basin as red circles and black shale as green squares using crushed samples (Wang and Reed [138]).

1.3 Nano confinement effect

The most reliable methods to measure fluid properties are still the experimental techniques. However getting all fluid properties in confined media through experiments is very challenging because of many limitations. In the literature we can find coreflooding and nanofluidic experiments showing that the thermodynamic of the confined fluid differs from the bulk fluid. Data from field production like GOR (Gas-Oil ratio) for example also show anomalies which can be

explained by confinement.

1.3.1 Experiments

Al Ismail and Horne [3] conducted core-flooding experiments with gas condensate sample from Marcellus region. The core-flooding was conducted through Marcellus shale and conventional Berea sandstone. The results show that the variation of the gas composition along the direction of flow during depletion in the Marcellus shale was less than in the Berea sandstone core. Change in gas composition is due to combination of condensate dropout and relative permeability effect. Then phase behavior is affected by fluid-rock interaction in shale due to confinement. Wang et al. [139] conducted experiments on micro-channels connected to nano-channels with pure n-pentane. The system was gradually heated and vaporization occurs firstly in the micro-channel and after in the nano-channel. Nano confinement characterized by capillary pressure raises the boiling point temperature. Alfi et al. [5] conducted the same kind of experiments and shows that confinement has no effect on fluid behavior for capillary of 50 nm. They compared Hexane, heptane and octane bubble point from the nanofluidic experiments with Peng Robinson EOS solutions. The results were the same. Luo et al. [75] used differential scanning calorimetry to measure the bubble point of octane and decane confined in controlled pore glasses. They showed that bubble point is dramatically affected by pore diameter. Cho et al. [26] conducted experiments to directly measure bubble point of hydrocarbons in confined media. The bubble point pressure results of the hydrocarbon mixtures in the mesoporous materials were lower than those in the bulk. The mesoporous materials used were siliceous materials with an average pore size of about 4 nm.

1.3.2 Field observations

Several authors analyzed production GOR data from many wells from Eagle ford and Bakken shale play [125, 63, 84, 59]. They noticed anomalies in the GOR of different wells. During the production depending on the well, the GOR stays constant for a very long time with or without the short stepwise jump. Kumar, Hoffman et Prasad (2013) analyzed collectively GOR response for more than 500 horizontal wells of Reunion Bay, Sanish and Parshall fields from the North Dakota shale play. Because of extremely undersatured oil and no aquifer underlying the reservoir in the Bakken, the GOR is expected to follow the fluid expansion drive trend. However, in the Bakken, the GOR trends consistently deviate from the expected one. Kumar, Hoffman et Prasad (2013) identified four well GOR anomalies. An example of such anomaly is shown Figure 1.7. Even if the flowing well pressure P_{wf} is under the bubble point pressure measured in laboratory (estimated P_b), the GOR stays constant. The GOR represents the ratio between gas and oil flow-rate at surface conditions. For conventional reservoirs if the flowing well pressure (bottom hole pressure) is under the bubble point pressure of the fluid, it means that gas is released from oil inside the reservoir. Then, the volume of gas increases and the volume of oil decreases in the reservoir. That is why the GOR of the well increases at surface

conditions. This is not the case for the Eagle Ford well in Figure 1.7, which means that the thermodynamic or the flow of the fluid inside shale gas and tight oil reservoirs are different from conventional reservoirs.

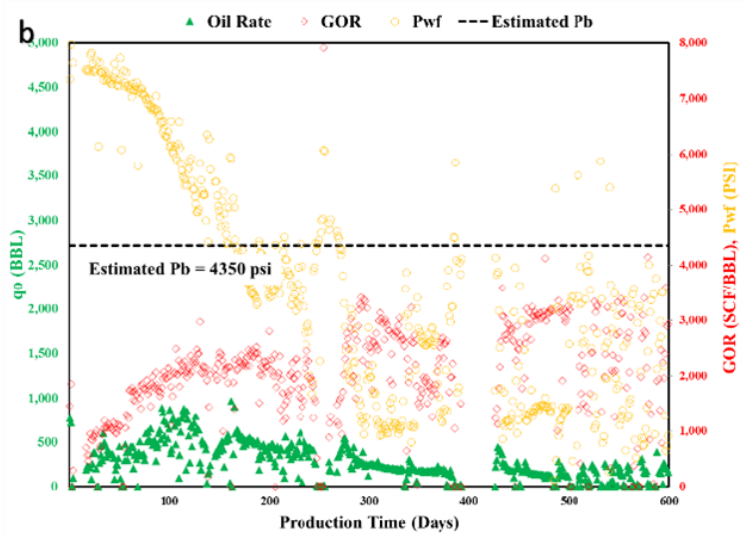

Figure 1.7: Production of a liquid rich shale oil Eagle Ford well Khoshghadam et al. [59]

1.4 Nano confinement thermodynamic model

1.4.1 Kelvin equation

The change of saturation point for confined fluid in nanotubes was seen in Wang et al. [139] in Section 1.3.1 and can be explained by Kelvin equation in a case of gas condensate system:

$$p^v = p^d exp(\frac{-2\sigma_{vl} V_m^l cos\theta}{rRT}) \tag{1.1}$$

with p_v: vapor saturation pressure of the confined fluid, p_d: dew-point pressure of the bulk fluid, r: radius of the capillary, R: universal gas constant, T: temperature, σ_{vl}: interfacial tension of the fluid, V_m^l: molar volume of the fluid, θ: contacting angle of the fluid.

As gas is not the wetting phase, $\theta < 90°$. Consequently, $exp(\frac{-2\sigma_{vl} V_m^l cos\theta}{rRT}) < 1$ and $p^v < p^d$. Therefore, capillary condensation occurs below the normal saturation pressure for a pure component. It is quite easy to understand. If we plunge a capillary in a container full of liquid, the liquid will go up into the capillary. The vapor/ liquid system is in equilibrium but the passage from vapor to liquid appears at lower pressure in the capillary due to gravity. The Kelvin radius r can be defined as the largest radius of pores where condensation occurs. In other words, all pores with a radius lower than the Kelvin radius will have gas condensate.

Shapiro and Stenby [111] generalized the Kelvin equation from the single component fluid to multi-component fluid. But Kelvin equation has some limitation for very small pores lower than 4 nm [81]. Furthermore this analytical solution only gives information for the bubble point pressure which is too limited for the whole fluid characterization in confined space.

1.4.2 Modified EOS

A lot of authors have worked on the modification of standard EOS or the development of new ones in order to model the thermodynamic of the confined fluid.

Flash with capillary pressure

The first main method method used to consider confinement in EOS is the inclusion of capillary in the flash calculation.Two phases are considered in equilibrium with two different pressures [6, 42, 45, 103, 107, 121, 124, 152, 155].

The capillary pressure is calculated with the Young-Laplace equation.

$$p_c = p^v - p^l = \frac{2\sigma_{vl} cos\theta}{r} \tag{1.2}$$

with p^v: vapor pressure, p^l: liquid pressure, σ_{vl}: interfacial tension θ: contact angle between the surface of the wetting phase and the wall of the tube r: capillary radius

The classic flash calculation considers the capillary pressure negligible because of large pores. Indeed Sigmund et al. [114] showed that measured dew-point or bubble-point pressures were found to be independent of the pressure of porous media for conventional reservoirs. In the case of shale reservoir, this assumption is no longer valid as shown in Section 1.3.1. By taking into account the capillary pressure, the coefficients of the cubic Peng-Robinson EOS are different for vapor and liquid. Furthermore, the equilibrium constant becomes function of capillary pressure too.

$$K_i = \frac{y_i}{x_i} = \frac{f_i^v/(\Phi_i^v p^v)}{f_i^l/(\Phi_i^l p^l)} = \frac{p^l \Phi_i^L}{p^v \Phi_i^v} = \left(\frac{p^l}{p_c + p^l}\right) \frac{\Phi_i^l}{\Phi_i^v} \tag{1.3}$$

with y_i: molar fraction of component i in vapor phase, x_i: molar fraction of component i in liquid phase, f_i^v: fugacity of component i in vapor phase, f_i^l: fugacity of component i in liquid phase, Φ_i^v: fugacity coefficient of component i in vapor phase, Φ_i^l: fugacity coefficient of component i in liquid phase,

The equilibrium constant must therefore be replaced in the flash algorithm as explained by Shapiro and Stenby [112]. The interfacial tension (IFT) is considered as a function of composition and molar density. The authors use different analytical Parachor models formulations like

the one proposed by Zuo and Stenby [159]:

$$\sigma_{vl} = (P_l\rho^l - P_v\rho^v)^\nu \tag{1.4}$$

$$P_l = \sum x_i P_i \tag{1.5}$$

$$P_v = \sum y_i P_i \tag{1.6}$$

$$P_i = (8.21307 + 1.97473\omega_i)T_{ci}^{1.03406}P_{ci}^{-0.82636} \tag{1.7}$$

with ν=3.6, σ_{vl}: interfacial tension (dynes/cm=mN/m), P_l: liquid parachor, P_v: vapor parachor, ρ^l: molar density of liquid phase (mole/cc), ρ^v: molar density of vapor phase (mole/cc), ω_i: acentric factor of component i, T_{ci}: critical temperature of component i (K), P_{ci}: critical pressure of component i (bar).

The flash algorithms used by the different authors are quite similar with few differences. Stimpson and Barrufet [122] add a second loop for the convergence of the capillary pressure. The criteria of convergence for the equilibrium constant and the capillary pressure can also be different from authors. Firincioglu et al. [42] add a contribution of the surface forces in the capillary pressure. The term added contains structural, electrostatic and adsorptive forces but they only include van der Waals forces for practicality. They compare the contribution from capillary and surface forces for confined oil. They show that surface forces remain small compared to capillary forces, however surface forces may become dominant at much smaller radius (about 1nm). Some authors improve this method by considering the thickness of the adsorbed layer in the Young-Laplace equation [35, 71]. More details about the flash algorithm will be given in Section 3.

Negative two phase flash is mainly used by authors, then no stability test is performed. However a phase envelope calculation is performed at the beginning in order to know whether or not the mixture fluid is monophasic or in two phases at the corresponding temperature and pressure conditions. This step will activate the flash calculation if the fluid is in two phases. Xiong et al. [152] propose a method to account for capillary pressure in bubble point calculation from the phase equilibrium condition. Sandoval et al. [107] have extended the work of Michelsen [78] to the calculation with capillary pressure. A system of $n_{comp} + 3$ equations has been solved using Newton's method, where n_{comp} is the number of components. All the authors show that capillary pressure causes suppression in bubble point pressure and that this suppression is a function of pore radius. The smaller the radius is, the more important the suppression is and capillary pressure has no impact for pore radius greater than 100 nm ([6]).This suppression of bubble point pressure will lead to reduction in oil density and viscosity during depletion [45].

Indeed, as the bubble point decreases the apparition of gas from oil is postponed during the depletion. Oil keeps its light components, that is why its density and viscosity are smaller. As shown in Figure 1.8, there is no shift at the critical point when using flash with capillary pressure method. At the critical point, there is only one phase known as supercritical fluid, then there is no capillary pressure. According to Teklu et al. [124], Nojabaei et al. [84], Jin et al. [52], Zhang et al. [155], lower dew-point is suppressed and upper dew-point is increased (Figure 1.8). Changes on the bubble point pressure are more important because difference between vapor and liquid density is higher at low temperature. Then the IFT and therefore the capillary pressure will be more important. Figure 1.8 shows that the shift of the bubble point becomes higher with a heavier oil. A lighter oil has a higher bubble point, then the pressure is higher when oil becomes gas than a heavier oil. As gas is compressible, the difference of density between oil and gas will be smaller at high pressure. Then the IFT will be smaller and therefore the capillary pressure. That explains why the shift is more important for heavier oil.

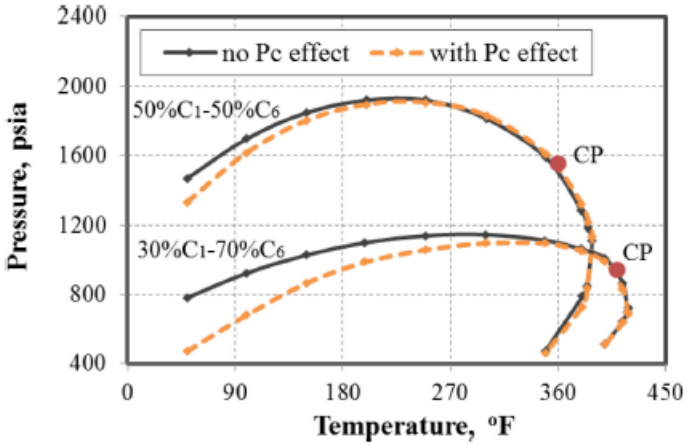

Figure 1.8: Phase envelopes for different C1/C6 mixtures in an oil wet system with r=20 nm Zhang et al. [155] using the capillary pressure method for the EOS.

Flash with shift of critical point

A second method to include confinement in flash calculation is to modify the critical properties such as, critical temperature T_c and critical pressure P_c. The flash algorithm is not modified, but the input data which are T_c and P_c of the components of the mixture are modified in function of the confinement. Viscosity is typically calculated from analytical solution like Lohrenz et al. [72] which is function of critical properties. Then the confined viscosities can be calculated. Several authors used this method [34, 6, 52, 106, 124, 35, 45]. Teklu et al. [124], Dong et al. [35], Haider and Aziz [45] use the correlation of Meyra et al. [77] (Equation 1.8) and Bird et al. [18] (Equation 1.9) to calculate the critical temperature and the critical pressure shift function of the pore radius. The shifts of the critical temperature and pressure are the same, they use

the same correlation.

$$\frac{T_{cb} - T_{cp}}{T_{cb}} = \frac{P_{cb} - P_{cp}}{P_{cb}} = 0.9409\frac{\sigma}{r_p} - 0.2415\left(\frac{\sigma}{r_p}\right)^2 \tag{1.8}$$

$$\sigma = 0.244\left(\frac{T_{cb}}{P_{cb}}\right)^{1/3} \tag{1.9}$$

with T_{cb}: bulk critical temperature (K), T_{cp}: confined critical temperature (K), P_{cb}: bulk critical pressure (atm), P_{cp}: confined critical pressure (atm), σ: characteristic diameter of the molecules (nm), r_p: pore radius (nm).

Figure 1.9 shows that with confinement the bubble point decreases, the upper dew-point decreases and the lower dew-point increases. These results are different from those of the flash with capillary pressure which show that upper dew-point increases and lower dew-point decreases. Condensate and oil viscosity decrease under confinement because of lower bubble point and dew point.

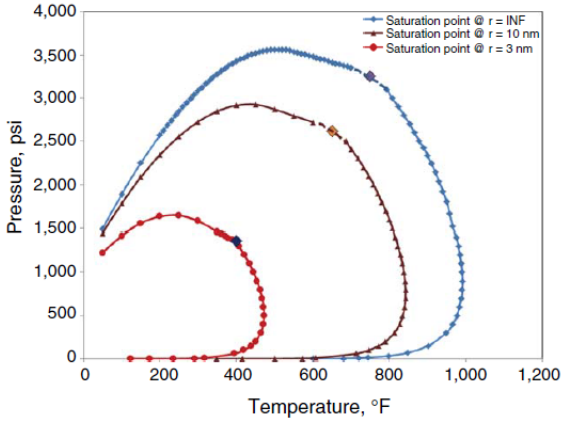

Figure 1.9: Phase envelope of Bakken oil in unconfined and confined pores. Teklu et al. [124] using the method of critical point shift for the EOS.

Others authors use molecular simulation results to build correlations. The results are for pure components and show difference between critical temperature and critical pressure shift. Devegowda et al. [34] use Singh et al. [116] molecular simulation results to calculate a correlation by plotting critical shift versus molecular weight for different radius. Alharthy et al. [6] also use the results of Singh et al. [116] but only for pore radius under 3 nm. Then a correlation for critical pressure and temperature shift was made for all size of pores. Jin et al. [52] use the results of Singh et al. [116], Singh and Singh [115] and Vishnyakov et al. [136] to build the correlations for critical temperature (Equation 1.10) and critical pressure (Equation 1.11). Sanaei et al. [106] have adjusted these correlations.

$$1 - \frac{T_{cp}}{T_{cb}} = 0.8493 \left(\frac{2r_p}{\sigma} \right)^{-1.241} + 0.015 \tag{1.10}$$

$$1 - \frac{P_{cp}}{P_{cb}} = 1.8 \left(\frac{2r_p}{\sigma} \right)^{-0.775} \tag{1.11}$$

It is interesting to notice that the two methods of capillary pressure consideration and shift of critical properties are also applied together [124, 36, 73, 158].

New EOS

Extensions of EOS have been proposed in the literature by including the pore/fluid interaction effect. Travalloni et al. [127] extended the van der Waals theory to confined fluids taking into account the interplay of molecule-molecule and molecule-wall interactions. In the same way Travalloni et al. [126], Islam and Sun [48] extended the Peng Robinson equation of state for the phase equilibrium of fluids in confined porous media. Barbosa et al. [11] reformulated the equation proposed by Travalloni et al. [126] with basis on molecular simulation. These extended EOS for fluids confined in porous media seem very difficult to implement for a mixture in a distribution of pores. Indeed the input parameters such as molecule-wall interaction parameters must be fitted for each components with experimental or molecular simulation results which are dependent of the radius of the adsorbent. Even they are more physically meaning, they are too complex to be used in the context of reservoir modeling. The different details of the EOS used in this work will be described in Chapter 3.

1.4.3 Molecular simulation

Molecular simulations are used to evaluate thermodynamic properties, starting from the knowledge of the intermolecular interactions. Unlike the bulk fluid which is described only by fluid-fluid intermolecular interactions, the confined fluid includes additional wall-fluid interactions. Molecular simulation appears to be the best way to approach the reality of the thermophysics of confined fluids. This approach will be described in detail in Chapter 3.

Ensemble based methods

Traditionally the study of confined fluid using Monte Carlo molecular simulation is performed by the Grand Canonical Monte Carlo ensemble (GCMC), which considers one box of simulation with constant chemical potential, volume and temperature (μVT). It was first introduced for confined fluid by Van Megen and Snook [133] for gas adsorption isotherm in slit like pores and has been widely used for confined pure components studies [10, 17, 85, 93, 96, 101, 33]. Pitakbunkate et al. [94] have applied GCMC to methane/ethane mixture phase behavior calculation. Jin et al. [50] have modified the GCMC ensemble to create the gauge-GCMC method

and studied pure systems, binary and ternary systems. The precise determination of the chemical potential corresponding to the condensation still remains a challenge and therefore impacts the precision of the liquid/vapor thermodynamic properties. Peterson and Gubbins [92] have proposed a method using integration of the grand free energy of pure compounds, Pitakbunkate et al. [93] have identified the phase change by plotting density versus fugacity and have observed the gap in density value. These methods may cause some errors in the location of the phase equilibrium also affecting the estimation of the critical point. The Gibbs Ensemble Monte Carlo (GEMC) developed by Panagiotopoulos [88] and improved by Panagiotopoulos et al. [86] does not have this problem as it considers one vapor box and one liquid box at equilibrium. It has been widely used for confined pure fluid equilibrium [43, 87, 102, 49] but very few studies have been done for mixtures [89, 68]. Other authors have used Grand Canonical Transition Matrix Monte Carlo (GCTMMC) [113] and Configurational-biais grand-canonical transition-matrix Monte Carlo simulations [116, 115] but only for confined pure component property calculations. However, to the best of our knowledge, analyses related to confined mixture properties and liquid and vapor pressures using GEMC ensemble are not available.

Impact on fluid

Whatever the ensemble used, all authors cited above agree on the fact that with confinement critical temperature and pressure of the fluid are shifted from their bulk value and vapor density increases while liquid density decreases. These observations are independent of pore shape and composition [115, 51] and pore size distribution [50].

Singh et al. [116] studied themophysical properties of confined alkanes: methane, butane, and octane. The intermolecular interactions were described with the modified Buckingham exponential intermolecular potential of Errington and Panagiotopoulos [38]. The pore is described as slit geometry of graphite or mica and the wall-fluid interaction is described by the 9-3 Steele potential. The evolution of critical pressure versus pore radius is different from the one of critical temperature. Liquid-vapor surface tension is suppressed under confinement and smaller than its bulk value. The thermodynamic properties are dependent on the nature of the surface: graphite or mica and the pore size. The phenomenon of adsorption can be observed near the wall with the local z-density. A layer of the fluid is adsorbed by the wall. This layer is not easy to define as fluctuation could occur in the space between walls. In another paper, Singh and Singh [115] studied the effect of pore shape and surface-fluid strength on the vapor-liquid equilibrium. Fluid-fluid interaction, attractive wall-fluid and hard wall-fluid interaction are represented by the simplified square-well and hard-wall potentials. The pore shapes analyzed are slit pore and cylindrical pore. This study pointed out that the critical property evolution with confinement is significantly affected by pore shape and surface field. In general, the authors observe that a stronger deviations with respect to bulk vapor-liquid equilibrium is observed whenever the fluid wall interactions are increased. Jin et al. [50] use gauge-GCMC (Bikai and Hadi [16]) to

generate phase diagram of methane for multiple cylindrical pores to understand the pore size distribution effect. This ensemble considers two boxes, one for the fluid system and the gauge box which serve as meters of chemical potential for the component loaded in the system box. Fluid-fluid interactions and fluid-wall interactions are modeled by a Lennard-Jones 12-6 potential. For a single pore and a multi pore system critical temperature and density are shifted with confinement. A greater shift effect is obtained if the pore system has more small pores and as expected the study shows that liquid will be first condensed in small pores.

Pitakbunkate et al. [93], Jin et al. [50], Jin and Nasrabadi [51], Pitakbunkate et al. [94] extended the molecular simulation methodology for mixture of two or three alkanes. Pitakbunkate et al. [93] used the Grand Canonical Monte Carlo simulations ensemble (GCMC) also called μVT ensemble and Lennard-Jones potential for the surface/fluid potential. They provided phase diagram for methane/ethane mixtures (Figure 1.10). The phase envelope of the confined fluid is shifted and closes with respect to phase envelope of bulk fluid. In a more recent work Pitakbunkate et al. [94] show that ethane is preferred over methane in the confined system and that most fluid molecules in the confined system tend to be adsorbed on the pore walls instead of remaining in the gas phase. Jin and Nasrabadi [51] analyzed different boundary conditions for pure fluids and ternary mixtures confinement using Gauge-GCMC. They used quartz, calcite and kerogen with slit and cylinder models. Cylinder pores provide a better confinement effect and calcite has the strongest adsorption effect. Jin [53] studied hysteresis effect on bubble point and dew point of pure nC8 and C1-nC6 mixture using GCMC simulations. The hysteresis between bubble and dew points increases with pore size and it decreases as pressure approaches critical pressure. Concerning the effect of confinement on fluid viscosity, Chen et al. [25] use a non-equilibrium molecular dynamics simulator for water molecules in a single-walled carbon-nanotube. They estimate effective shearing stress between the tube wall and the water molecules and show that it is reduced. Then they conclude that the apparent viscosity of the fluid is reduced.

Molecular simulation is a very effective way to obtain the properties of confined fluid for a certain level of confinement. It is the better way to understand and approach the reality of the thermo-physics in confined fluids. Critical temperature, pressure, and surface tension, and vapor and liquid densities can be determined with this method. However systematic molecular simulation is not possible for each fluid mixtures or pore geometry and surface properties of shale reservoirs. That is why the results can only be used as references for the calibration of a modified EOS.

1.4.4 Membrane effect and sieving

Instead of considering capillarity pressure or critical properties shift in the flash calculation, other authors like [4, 156, 44] have considered the membrane properties of Shale. As said in Section 1.2.2 volume fraction of micropores (< 2 nm) can be as high as 19.23% and the size of

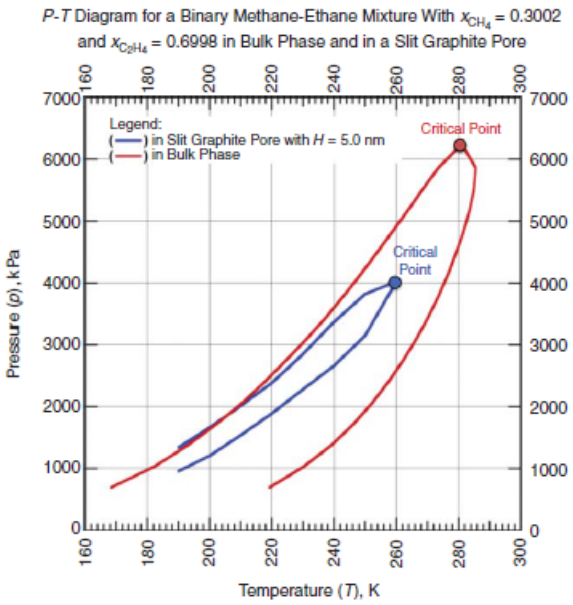

Figure 1.10: comparison of P-T diagrams for a binary methane/ethane mixture in bulk phase (experimental data) and in slit pore with 5 nm of separation Pitakbunkate et al. [93].

hydrocarbon molecules is between 0.5 nm and 10 nm Nelson (2009). It is therefore expected that some of hydrocarbon molecules will not penetrate in certain pores or through pore throats and others will. This phenomenon is known as steric hindrance. Then shale acts like a selective membrane or filter to hydrocarbons molecules and then the different pores will have different composition: this is the sieving effect. Geren et al. [44] introduced the concept of membrane efficiency: $\omega_f = 1 - \frac{f^l_{2y}}{f^l_{1y}}$, where f^l_{1y} and f^l_{2y} are the fugacities of the heavier component y in the liquid phase of "unfiltered" (1) and "filtered" (2) parts respectively (Figure 1.11). At equilibrium: $f^l_{1x} = f^l_{2x}$ for the lighter component x but due to the membrane effect, fugacities of the heavier component y are not considered equal $f^l_{1y} \neq f^l_{2y}$. Knowing pressure P_2, temperature T and molar fraction z_x, z_y in the system 2, flash calculation give f^l_{2x} and f^l_{2y}. For a given pressure difference between system 1 and 2: ΔP, composition of system 1 (z_x and z_y) is varied in order to get $f^l_{1x} = f^l_{2x}$. Then at equilibrium the two systems have different compositions. f^l_{1x} is calculated and membrane efficiency can be determined. Zhu et al. [156] extend this procedure with pressure depletion.

In his model, Alfi et al. [4] considered two sub-media of the matrix: small pores and large pores with two EOS to be solved simultaneously. The classic Peng Robinson EOS for large pore and the modified EOS from Travalloni et al. [126] to account for confinement effect in small pores. This equation needs two parameters (ϵ_p, δ_p) to be fitted. They are dependent on fluid molecules, pore radius and pore surface. ϵ_p accounts for the energy parameter of the interactions between a fluid molecule and a pore wall and δ_p is the range parameter of the attractive forces

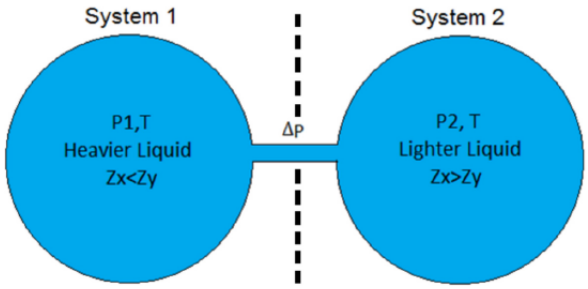

Figure 1.11: two pore system used to calculate membrane efficiency Geren et al. [44]

between molecules and pore. Contrary to Geren et al. [44] and Zhu et al. [156], Alfi et al. [4] consider the thermodynamic equilibrium as: $(f_{iL}^l = f_{iL}^v) = (f_{iS}^l = f_{iS}^v)$. Every components in large and small pores must have the same fugacity in both phases at equilibrium. The n_{comp}+1 equation system to solve is:

$$\begin{cases} ln(x_L^i \Phi_L^i p_L) = ln(x_S^i \Phi_S^i p_S) \\ \sum_{i=1}^{n_{comp}} x_S^i = 1 \end{cases} \tag{1.12}$$

with x_L^i: liquid molar fraction of component i in large pores, Φ_L^i: fugacity coefficient of component i in large pores, p_L: pressure in large pores, x_S^i: liquid molar fraction of component i in small pores, Φ_S^i: fugacity coefficient of component i in small pores, p_S: pressure in small pores, n_{comp}: number of components,

The nc+1 unknown are p_S and x_S^i, pressure and composition in large pores are given. The calculation details are not provided but seems to be very time consuming. For each time step in each cell, a first flash has to be done in Large pores to know the fugacity coefficient Φ_L^i. Then a second flash has to be done in small pores for a given pore radius by varying p_S and x_S^i to verify the system of equations. It seems that the authors consider that the pressures are the same in the two phases in the small pores. Furthermore the two parameters (ϵ_p, δ_p) must be fitted for all fluid molecules, pore radius and surface properties. The results of hydrocarbon distribution on small pores shows an apparent sieving effect due to size hindrance. Small pores have more light components and large pores have more heavier ones, their composition at equilibrium are completely different.

1.5 Large scale reservoir simulation

In order to perform large scale reservoir simulations some upscaling methodologies must be developed because of computational constraints. Large scale reservoir production is basically driven by the matrix/fracture exchange because shale gas and tight oil reservoirs are usually fractured and hydrocarbons are predominantly present in the matrix where fluid confinement

occurs. The accurate modeling of the transfer between matrix and fracture is therefore important to get correct large scale production forecast. Consequently, the upscaling of the matrix-fracture exchange process is studied in the scale of a matrix block size where the pore size distribution should be considered.

1.5.1 Matrix/fracture interaction modeling

Single porosity model

The single porosity model is the simplest methodology to model matrix/fracture interaction. It includes all fractures present in the reservoir by an explicitly discretization of the fractures using fine grid cells. Such approach was used by Cipolla et al. [28] in order to simulate a shale-gas reservoir where fractures were represented using very fine cells. This approach can be used to generate the reference solution, but cannot be applied to full field simulations because it requires a large number of grid cells and therefore a high computational CPU time.

Dual porosity model

The understanding and modeling of flow in fractured rocks has been studied since the 1960s [12, 144] and the dual porosity model has been widely used in the petroleum industry since then [56, 57]. This approach replaces the single porosity explicit discrete-fracture approach which is computationally intensive and requires specific details such as fracture and matrix spacial distribution and geometric properties. In this upscaling model the grid is separated into two sub grids: one for the fracture and one for the matrix (Figure 1.12c). Flow can occur between fracture cells but not between matrix cells which are considered as sources for fractures cells (dual-porosity single-permeability concept). The flow between matrix and fracture is modeled using a shape factor [20]. However, due to the ultra-low matrix permeability, the transient state of the flow between matrix and fracture is very long [150]. The quasi-steady state flow assumption of the dual porosity model is then unsuitable to model the matrix-fracture interaction. Dual-continuum models are therefore not suitable for flow modeling in shale formations.

MINC model

The flow in a fractured reservoir is composed of three different regimes. At the early time of depletion, the production comes from fractures. Then the matrix feeds the fractures until the inter-porosity transfer reach equilibrium. Finally flow in the matrix reaches the pseudo-steady state regime [109]. The dual porosity model is unable to handle the flow in the second flow regime which is the transient state. The idea is therefore to subdivided the matrix into several nested sub-blocks. The MINC (Multiple INteracting Continua) concept was developed by Pruess and Karasaki [99] and Pruess [97] to model heat and multiphase fluid flow in geothermal fractured porous media. It represents a generalization of the dual-continuum model. It allows

to describe gradients of pressures, temperatures, and concentrations inside the matrix by further subdividing individual blocks into one or multidimensional strings of nested meshes (Figure 1.12b). In order to understand the MINC concept, the flow in a cube can be approximated by one dimensional spherical flow [148].

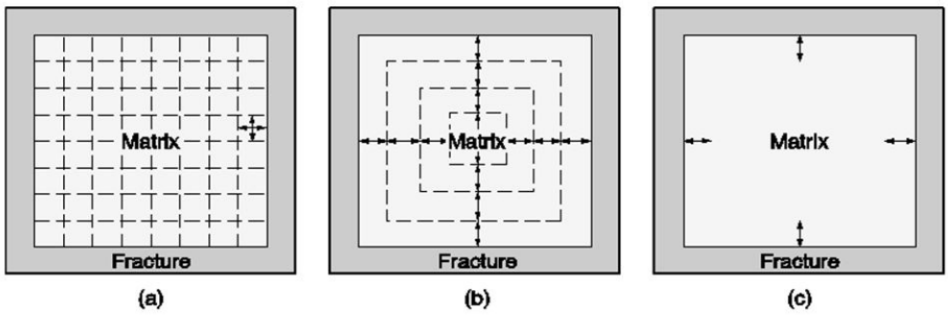

Figure 1.12: Different discretization concepts: (a) explicit discretization, (b) MINC discretization, (c) double-porosity discretization Wu and Pruess [149].

Let's consider a spherical matrix surrounded by a high permeability fracture with higher pressure initially. During the flow, the fluid moves along the radius from the origin of the matrix to the fracture. The different radius represent the fluid flow streamlines in the matrix. Therefore equipotential surfaces of pressure are concentric sphere proportional to all the radius from the origin. Then if sub matrix boundaries and the equipotential surface are overlapped, pressure at the center of any sub-blocks can represent the different flow equipotential in the matrix. Under this assumption, the equipotential lines (or surface) are squares (or cubic), this is almost the case. The MINC concept is then explained. The principle is to divide the matrix into a series of nested volume on the basis of distance from the nearest fracture. These volumes represent equipotential surfaces of the flow inside the matrix through the fracture.

Multi-porosity model

The triple porosity or multi porosity model is not new and has been proposed by several authors in the literature for describing flow through fractured rocks. Abdassah and Ershaghi [1] subdivided the matrix into two sub-domains with different porous medium properties. Bai et al. [9] used a triple porosity model with cracks, fissures and matrix. Liu et al. [70] considered a model with fractures, rock matrices and cavities. Wu et al. [147] subdivided the fracture into large fractures and small fractures. More recently these multi-porosity models have been applied to unconventional reservoirs. Wang et al. [137] proposed a multi-porosity, multi-physics model for gas flow in shale with five regions: hydraulic fractures, global natural micro-fractures, local micro-fractures, inorganic pores and organic pores. All sub-domains have their own properties and fluid flow regime models. For example, gas slippage effect is added in organic and inorganic

pores which have also different gas capacities for adsorption, and non-Darcy flow is used for fractures. Wang et al. [141] used a triple porosity model for shale gas production simulation. They considered three domains: natural and induced fractures, kerogen-hosted pores of approximately 25nm diameter and kerogen-hosted pores of approximately 1nm diameter. The gas flows from small pores through large pores to fractures. Knudsen diffusion is added in small pores and gas slippage effect is added in large pores.

1.5.2 Upscaling of the pore size distribution

For the simulation models discussed above, a nano confinement PVT model can be used, but the pore size distribution cannot be directly integrated. The pore size in shale gas and tight oil reservoir is not constant but is in fact very heterogeneous. The pore size distribution must therefore be taken into account in reservoir simulations and some upscaling methodologies must be developed because of computational constraints and time calculation. Some authors have included their modified thermodynamic flash (explained in Section 1.4.2) into a reservoir simulator in order to analyze the effect of confinement on reservoir production. Different upscaling methodologies of the pore size distribution are presented in the following sub-sections.

Average radius

Few authors have applied the pore size distribution in their model and most of them have considered an average pore radius inside a simulation cell (Firincioglu et al. [41], Sanaei et al. [106], Alharthy et al. [7], Haider and Aziz [45]). Alharthy et al. [7] used a double porosity model with three facies (unconfined pores, mid confined pores and confined pores) in the matrix subgrid corresponding to a given critical point shift, permeability and flow capillary pressure. Firincioglu et al. [41] used a black oil single porosity model with a random distribution of capillary pressure in the grid. The value of the bubble point in each cell is suppressed by the value of the capillary pressure inside the cell plus the excess suppression calculated from a correlation. Sanaei et al. [106] used a single porosity model with critical point shift method and ran reservoir simulations on a random pore size per cell according to a given distribution. Lopez Jimenez et al. [73] did the same work using both flash with capillary pressure and critical point shift. Haider and Aziz [45] ran numerical simulations for two different pore size distributions using a fixed pore radius per cell for flash computation with capillary pressure or critical point shifts, and concluded that oil production is increased when the percentage of cells of small pore radius is high. All the authors studied oil system and showed that oil production increases and gas production decreases compared to reservoir simulations using a bulk fluid without confinement. The bubble point is suppressed, then oil viscosity and density stay longer at a lower value. The gas breakthrough is postponed and then the GOR is lower for longer time.

Saturation dependent capillary pressure

Others authors considered the pore size distribution using the J Leverett functions or an effective radius r_K function of the saturation of the wetting fluid. Li et al. [67], Li and Mezzatesta [66] considered the effective radius as a function of saturation in the Laplace equation of the flash. From a pore size distribution, he defined the wetting fluid saturation as following:

$$S_l(r_K) = \frac{\sum_{r_i \leq r_K} \Delta V_i(r_i)}{\sum_{r_i} \Delta V_i(r_i)} \tag{1.13}$$

with S_l: wetting phase saturation, r_K: effective radius, r_i: radius of the pore size distribution, $\Delta V_i(r_i)$: pore volume corresponding to a pore size of r_i

This effective radius is built from a volumetric pore size distribution. They consider that the pore network is initially filled with oil and all pores are connected, the effective radius is then maximum. When gas appears firstly in larger pores during depletion, gas stays in larger pores and oil stays in smaller pores because of the oil wet characteristic of the rock. Then the effective radius represents the pore size limit between oil and gas phases. The pores with higher radius than the effective radius are filled with gas and the others with oil. They generated black oil properties according to this effective radius value but did not perform reservoir simulations. Nojabaei et al. [84] developed a method called "compositionally-extended Black Oil formulation". They use a flash algorithm with capillary pressure to generate Blackoil properties as a function of pressure for different pore sizes varying from 10 nm to infinitely large. These properties are gas and oil density, gas and oil viscosity, gas-oil ratio and volatile gas-oil ratio. A pore radius and initial pressure is assumed to perform a flash with a K value model based on blackoil properties. The K value model allows to solve the Rachford Rice equation without iteration on K. Then the gas and oil composition, IFT using a Parachor model and gas and oil saturation can be calculated. Oil and gas saturation and IFT allow to determine gas/oil capillary pressure thanks to the J function of air/mercury. Effective radius can be determined by the capillary pressure Young Laplace equation. The Loop is on the effective radius value, if it does not converge the operation is repeated. When the effective radius converge, the mass balance equation can be solved for the pressure. Wang et al. [143], Xiong et al. [152] used a single porosity model with flash with capillary pressure calculated by the J Leverett function at specific saturation.

$$J(S) = \frac{p_c(S)}{\sigma_{vl} cos\theta} \sqrt{\frac{k}{\epsilon}} \tag{1.14}$$

with S: wetting phase saturation, $P_c(S)$: capillary pressure at specific saturation, σ_{vl}: interfacial tension, θ: contact angle k: permeability ϵ: porosity

The Leverett J-function is a dimensionless function obtained experimentally and character-

istic of a rock type and therefore a pore size distribution. J is the same for different couple of fluids and rock properties, then it aims to adjust capillary pressure for wettability. Using the capillary pressure function of saturation and IFT, $p_c(S) = J(S)\sigma cos\theta\sqrt{\frac{\epsilon}{k}}$ allows to include the pore size distribution and to update the IFT by Parachor models during the flash. This methodology enables as well to create a link between the capillary pressure in the dynamic flow calculation and in the flash calculation.

These two methods are quite similar and seem not to be efficient. As the percentage in volume of micro and meso pores inside shale matrix is low, the effective radius value stays quite high (or low J Leverett function value) for a large range of wetting phase saturation during the flow simulation. Then the impact of confinement is very low and the fluid behaves like bulk. More details about the flash with saturation dependent capillary pressure algorithm are given in Section 3.2.3

Triple porosity model

Only Alfi et al. [4] considered the confined fluid behavior in his triple porosity model to account for filtration effect in shale reservoirs. He divided the porous media into three different sub-media: fracture, large pores and small pores. Peng-Robinson EOS is used for flash calculation in large pores and fractures, and a modified Peng-Robinson equation of state Travalloni et al. [126] is used for small pores with a specific radius. The two EOS must be solved simultaneously. All fugacities must be equal at equilibrium in both phases for the both sub media (large and small pores) for all components. Flow occurs between all the sub-media and thermodynamic equilibrium is verified between small and large pores. With this flash method, compositions at equilibrium are different for the two media. Small pores have more light components than large pores. Alfi et al. [4] explains this difference by the sieving effect. Then bubble point in small pores is higher than in larges pores because of the composition. Therefore during depletion, gas appears firstly in small pores. But the matrix of small pores has much smaller permeability than in large pores. So, the reservoir retains more of gas-rich fluid while allowing more oil to flow into the well. This behavior can be responsible for the anomalous gas oil ratios observed in liquid shales wells. That is why for a synthetic case simulation, the GOR production is lower with Alfi et al. [4] method than a base case without confinement. This method is interesting but seems to be very time consuming for PVT modeling and no clear details are given on the thermodynamic equilibrium calculation and how to model the flux between sub-grids. Besides, we are not sure if the thermodynamic equilibrium between small and large pores is predominant comparing to other effects such as capillarity during a dynamic flow simulation.

1.6 Research motivations and objectives

Tight oil and shale gas unconventional reservoirs are made up of a very heterogeneous pore size distribution ranging from several nanometers to micro-meters. The part of micro and mesopores can reach more than 20% of the distribution volume. Unlike the conventional reservoirs, a part of the fluid is then confined in micro and mesopores where the interaction between fluid molecules and between fluid and wall molecules are very important. The fluid thermodynamic behavior is therefore modified from the bulk one and becomes dependent on pore size. Along the flow from the matrix to the fractures, the fluid will then pass through pores with different PVT behavior and capillary pressures. The flow and production will inevitably be altered from a case without confinement and must therefore be modeled properly. Molecular simulations allow determining the thermodynamics of a few component mixtures in such pores but its coupling with a large scale reservoir simulator is impossible. Some works have therefore been done on the modification of the classic EOS used in reservoir simulators. Integrate the capillary pressure in the flash or shift the critical temperature and pressure of components have then become the ways to model and study the impact of confinement on field production. Different studies with a fixed pore radius and very few with a distribution of pores within the reservoir have shown that the confinement has a strong impact on the production. However, according to the best of our knowledge, no accurate upscaling methodology has been proposed in order to perform large scale reservoir simulations with confinement effect in a heterogeneous pore size distribution. A proper modeling of the coupling between fluid flow and thermodynamic equilibrium in an unconventional reservoir with distribution of pores is therefore critical for Oil&Gas companies in order to optimize their production.

The main challenges of modeling these phenomena at large scale are firstly to understand the thermodynamics of the confined fluid at the pore scale and to get reference results of confined fluid properties at equilibrium. Secondly, the aim is to build an EOS dependent on pore radius, which should be tested and validated with the reference data. And finally the challenge is to take into account the pore size distribution in the flow and thermodynamic reservoir simulation, which implies to develop upscaling methodologies.

This thesis work will be divided into four main parts, which are applied to different domains and scales. Nano-pore scale study of hydrocarbon molecules in thermodynamic equilibrium inside a slit pore will be performed using molecular simulation techniques in Chapter 2. Fluid modeling of the confined hydrocarbon thermodynamic behavior will be carried out using a radius dependent EOS and compared to reference molecular simulation results in Chapter 3. Then the modified EOS will be included into a reservoir simulator to perform fine scale matrix/fracture flow and thermodynamic modeling of hydrocarbons within a distribution of pores in Chapter 4. Finally in Chapter 5, a new triple-porosity model is proposed, and an associated upscaling methodology is presented in order to perform large scale reservoir simulations.

The objective of the first part is to simulate thermodynamic equilibrium of several pure components and mixtures in a slit pore for different pressure and temperature conditions and several pore sizes. The results of these simulations will aim to get reference properties at equilibrium such as phase density, phase molar fractions, critical pressure and temperature. In the second part, these reference data will be used to investigate the different pore radius dependent EOS proposed in the literature in order to highlight the best one. The modified EOS will be then included in a reservoir simulator and fine grid matrix/fracture simulation for different pore size distribution will be performed to get references for upscaling model development. The final objective is to develop a new triple-porosity model and a new upscaling procedure validated by the fine grid results. It aims to perform large scale reservoir simulation with pore size distribution and confinement model with low CPU time calculation and computer capacities.

Chapter 2

Molecular simulation

In molecular simulation, Monte Carlos method aims to generate in a given statistical ensemble a collection of configurations (spatial coordinates of molecules) representative of the system at equilibrium. In this collection, each configuration must satisfy the probability density of the given statistical ensemble. It is like a sampling of molecules positions at equilibrium for a specific statistical ensemble. Thermodynamic properties of the fluid can therefore be calculated as the average of the macroscopic properties over the number of configurations. As already said in the introduction (1.4.3), traditionally the study of confined fluid using Monte Carlo molecular simulation is performed by the Grand Canonical Monte Carlo ensemble (GCMC). As explained in 1.4.3, this method may lead to some errors because of its lack of precision and its inability to give confined pressure. Therefore, in this Chapter, we propose a new and robust method in the Gibbs Ensemble Monte Carlo (GEMC) ensemble aiming to get thermodynamic properties of mixtures and confined liquid and vapor pressures at equilibrium. Thermodynamic properties of pure fluids and mixture will be determined in confined spaces, emulating those in kerogen pores in shale reservoirs using GEMC ensemble. The pores will be modeled by slit pores with graphite walls with different sizes. These data obtained will represent references for the investigation of radius dependent EOS. This chapter is organized as follows: Section 2.1 gives theoretical background about numerical methods of statistical thermodynamic. Section 2.2 is devoted to the clarification of the different pressures considered in a porous medium with nano-pores. Section 2.3 is dedicated to the methodology and the workflow used to model the thermodynamic behavior of confined fluids. In Section 2.4 the main results devoted to pure fluids and mixtures are presented. The summary and discussions are drawn in Section 2.5.

2.1 Numerical methods of statistical thermodynamic

2.1.1 Principles of statistical thermodynamic

Statistical thermodynamic is a field of physics that studies the macroscopic properties of systems based on microscopic considerations. It allows understanding and forecast physical phenomena and macroscopic variables of a system from its constituent atoms and molecules. In brief statistical thermodynamic allows to make the link between classical thermodynamic at macroscopic scale and molecular physics at microscopic scale.

Let's consider a system of N atoms. Each atom is defined by its position vector r and its moment vector m. Then a configuration $a(r, m)$ of this system is a space of $6N$ dimensions. This space is called the phase space and a statistical ensemble corresponds to a sample of the configurations $a(r, m)$ in this phase space. The configuration space is a subset of the phase space corresponding to the position vectors r of dimension $3N$. In a statistical ensemble, the different configurations a are distributed according to a probability density $\rho_{ens}(a)$.

Now we define X as a macroscopic property of the system (pressure, volume, energy ...). At microscopic scale, X is dependent on the configuration a. This property also fluctuates with time because of collision between molecules (brownian move). Then $X(a(t))$ is a temporal function. The observed value of the macroscopic properties X_{obs} corresponds therefore to an average over time of a high number of different configurations of the system. We can write:

$$X_{obs} = \langle X \rangle_{time} = \lim_{t_{obs} \to \infty} \frac{1}{t_{obs}} \int_0^{t_{obs}} X(a(t))dt \tag{2.1}$$

For particles with sufficient mass and high temperature, Newton's laws can be solved numerically. This is the principle of the molecular dynamics. For systems with high numbers of particles, the fluctuation of X versus time can be very complex and it is very long to cover the phase space in its integrity. Gibbs therefore proposed an alternative method by replacing the temporal average by a statistical one. This is the principle of the molecular Monte Carlo method. The thermodynamic average (expectation of X) of a property in a given statistical ensemble is:

$$\langle X \rangle_{ens} = \sum_a X(a)\rho_{ens}(a) \tag{2.2}$$

The statistical thermodynamic is based on the ergodicity postulate which stipulates that temporal and statistical average are similar:

$$\langle X \rangle_{time} = \langle X \rangle_{ens} = X_{obs} \tag{2.3}$$

Therefore, for a given macroscopic property, the calculation using molecular dynamics method

or Monte Carlo method should give the same result accounting for uncertainties for a good sampling. In practice, molecular dynamics is suitable for the calculation of time-dependent properties like viscosity or diffusion coefficient. On the contrary Monte Carlo method is well adapted to phase equilibrium calculation. In this case, it is possible to simulate multi-phase systems without explicit interface.

2.1.2 Statistical ensembles

Three different statistical ensemble are used in this thesis and will be detailed in this section: the canonical ensemble (NVT), the isotherm-isobar ensemble (NPT) and the grand canonical ensemble (μVT). More details about the equations can be found in Ferrando [39] and Daan Frenkel and Berend Smit [32].

Canonical ensemble (NVT)

In the canonical ensemble also called NVT ensemble, the total number of particles N, the volume V and the temperature T are imposed to the system. It is like a closed container of fixed volume in a thermostat.

The partition function of the canonical ensemble is :

$$Q_{NVT} = \frac{V^N}{N!\Lambda^{3N}} \int_{s^N} exp(-\beta U(s^N)) ds^N \tag{2.4}$$

with $s^N = V^{-N} r^N$ the reduced coordinates. U the potential energy of the system. $\beta = \frac{1}{k_B T}$, where k_B is the Boltzmann constant and Λ is the thermal de Broglie wavelength.

In order to simulate the statistical ensemble for a given temperature, we can only consider the configuration space i.e., the position vector r^N. In the configuration space, the probability density of a configuration a is:

$$\rho_{NVT}(a) = \frac{exp(-\beta U(a))}{Z_{NVT}} \tag{2.5}$$

with Z_{NVT} the integral of configuration of the canonical ensemble.

$$Z_{NVT} = N!\Lambda^{3N} Q_{NVT} \tag{2.6}$$

Isotherm-isobar ensemble (NPT)

The isotherm-isobar ensemble also called NPT is a statistical ensemble where the total number of particles N, the pressure P and the temperature T are imposed to the system.

The partition function of the isotherm-isobar ensemble is:

$$Q_{NPT} = \frac{1}{N!\Lambda^{3N+3}} \int_V V^N exp(-\beta PV) dV \int_{s^N} exp(-\beta U(s^N)) ds^N \tag{2.7}$$

In the configuration space, the probability density of a configuration a is:

$$\rho_{NPT}(a) = \frac{1}{Q_{NPT}} \frac{exp(-\beta PV)V^N}{N!\Lambda^{3N+3}} exp(-\beta U(a)) \tag{2.8}$$

Grand canonical ensemble (μVT)

In the grand canonical ensemble, also called μVT, the temperature T, the volume V and the chemical potential μ are fixed. It is like a container of fixed volume in thermodynamic equilibrium with a reservoir of particles at fixed temperature. The μVT ensemble is a natural ensemble to use for adsorption studies. Indeed the gas in contact with the adsorbent can be considered as a reservoir that impose a temperature and a chemical potential on the adsorbed gas.

The partition function of the grand canonical ensemble is :

$$Q_{\mu VT} = \sum_{N=O}^{\infty} \frac{exp(\beta \mu N)V^N}{N!\Lambda^{3N}} \int_{s^N} exp(-\beta U(a)) ds^N \tag{2.9}$$

In the configuration space, the probability density of a configuration a is:

$$\rho_{\mu VT}(a) \propto \frac{exp(\beta \mu N)V^N}{N!\Lambda^{3N}} exp[-\beta U(a)] \tag{2.10}$$

2.1.3 Monte Carlo method

Metropolis Algorithm

In molecular simulation, the Monte Carlo method allows to generate a series of configurations in a given statistical ensemble. These configurations a are representative of the system at equilibrium. In this series, each configuration follows the probability density $\rho_{ens}(a)$ of the statistical ensemble considered. This series is also used to calculate the average of thermodynamic properties over the ensemble. The Equation 2.2 can be written as:

$$\langle X \rangle_{ens} = \frac{1}{\tau_{total}} \sum_{i=1}^{\tau_{total}} X(a_i) \tag{2.11}$$

with τ_{total} the number of configuration of the series. a_i a configuration i of the series.

As presented in Section 2.1.2, the probability density of the configurations are dependent of the partition function of the statistical ensemble considered. The multidimensional integral term of this function cannot be solved analytically or by standard numerical methods (Simpson's or trapezoidal rule for example). The Monte Carlo method is an innovative numerical method

which enables to calculate the average value of the thermodynamic property $\langle X \rangle_{ens}$ without estimate the partition function. It is a stochastic method using random numbers and based on the construction of a Markov chain. The system is transformed from a configuration to another one following a transition matrix π. This matrix is chosen in order to obtain the probability density ρ_{ens} of the statistical ensemble considered at each step. Each new configuration depends only on the previous configuration and not on the former ones. This enables to get a representative sampling of the phase space and avoid correlations from one configuration to the next one.

The condition for the Markov chain to converge to the probability density ρ_{ens} is the stationary condition:

$$\pi \rho_{ens} = \rho_{ens} \tag{2.12}$$

A sufficient condition for Equation 2.12 to be verified is the micro reversibility criterion between a configuration a and a new configuration b:

$$\rho_a \pi_{ab} = \rho_b \pi_{ba} \tag{2.13}$$

This criterion states that the probability to go from a configuration a to a configuration b is equal to the probability to go from a configuration b to a configuration a. In order to generate a Markov chain which verifies the equation 2.13, the Metropolis algorithm is used. The Metropolis algorithm is composed of two steps. The first step generates a configuration b from a configuration a. The second step states if this new configuration is accepted in the Markov chain. The transition matrix is expressed by:

$$\pi_{ab} = P^{gen}(a \to b).P^{acc}(a \to b) \tag{2.14}$$

where $P^{gen}(a \to b)$ is the probability to generate a configuration b from a. $P^{acc}(a \to b)$ is the probability to accept the new configuration b.

The micro-reversibility criterion is then written as:

$$\rho_a.P^{gen}(a \to b).P^{acc}(a \to b) = \rho_b.P^{gen}(b \to a).P^{acc}(b \to a) \tag{2.15}$$

The choise of Metropolis for the calculation of $P^{acc}(a \to b)$ is:

$$P^{acc}(a \to b) = min\left(1, \frac{\rho_b P^{gen}(b \to a)}{\rho_a P^{gen}(a \to b)}\right) \tag{2.16}$$

In order to increase the sampling of the configuration space, statistical bias can be used. They allow sampling preferentially a region of configuration space instead of another. In classical Monte Carlo simulations (without biais) the generation of a configuration is totally random. Then $P^{gen}(a \to b) = P^{gen}(b \to a)$ and Equation 2.16 is simplified by:

$$P^{acc}(a \to b) = min\left(1, \frac{\rho_b}{\rho_a}\right) \tag{2.17}$$

As the Metropolis algorithm uses the ratio $\frac{\rho_b}{\rho_a}$, the multidimensional integral term has not to be solved.

Two cases are possible in the Metropolis algorithm:

- if $\frac{\rho_b}{\rho_a} > 1$, then $P^{acc}(a \to b) = 1$ and the new configuration is added to the Markov chain.
- if $\frac{\rho_b}{\rho_a} < 1$, then a random number R between 0 and 1 is chosen in a continuous uniform distribution. The new configuration is accepted if $\frac{\rho_b}{\rho_a} > R$. Otherwise the previous configuration is duplicated or the movement is refused, which is the same for a practical point of view, but different for the estimation of the acceptance probability ratio at the end of the simulation.

Typical Monte Carlo moves

The generation of a configuration b from a configuration a of probability $P^{gen}(a \to b)$ is performed by a Monte Carlo move. Several typical moves will be detailed in this section for a single box of simulation. These different moves can be applied to the statistical ensembles presented in section 2.1.2. The different moves are presented bellow.

- translation move: this move consists to perform a simple translation of a molecule following a random direction.
- rotation move: it allows rotating the molecule around an axis through its center of mass and in random direction.
- volume change: the size of the simulation box is changed. A homothety is performed on the whole system keeping internal structure of the molecules.
- internal rotation or flip: this move is applied to flexible molecules. A randomly chosen force center of a molecule is rotated around the axis formed by its immediate neighbors.
- internal regrowth: this move is also applied to flexible molecules. An interaction site of a molecule is randomly chosen and translated to a new position.

Statistical bias can be used in order to 'artificially' increase the acceptance probability of several moves such as internal regrowth. This will not be developed in this thesis. More details about bias can be found in Ferrando [39], Daan Frenkel and Berend Smit [32]. Other specific moves are used for a given ensemble or for phase equilibrium calculations which imply two different boxes of simulation. This will be described in the next section.

2.1.4 Phase equilibrium calculation for a bulk fluid

Grand canonical ensemble

The Grand canonical Monte Carlo (GCMC) ensemble, also called μVT ensemble considers one simulation box with constant chemical potential (μ), constant volume (V) and constant temperature (T). This box is in thermodynamic equilibrium with a bulk reservoir of an infinite number of molecules.

A sequence of configurations are sampled using the Monte Carlo method with the Metropolis algorithm detailed in Section 2.1.3. In GCMC, simulations are usually initialized using a box initially empty and different trial moves are randomly proposed and accepted or not according to an acceptance probability. The acceptance probability can be calculated using Equation 2.17 with the μVT probability density (Equation 2.10). It gives the following expression:

$$P^{acc}(a \to b) = min(1, exp[-\beta(U(b) - U(a))]) \tag{2.18}$$

Standard moves in GCMC are translation, rotation and insertion/deletion of particles. Molecules containing internal degrees of freedom (such as n-pentane or n-decane) require specific moves able to sample different configurations. In this case we have used internal regrowth and flip. The insertion/deletion move is characteristic of the GCMC simulation. Particles are inserted or deleted inside the simulation box. An example of the acceptance probability calculation for this move using Equation 2.17 and Equation 2.10 is detailed below.

The creation of a particle is accepted with a probability:

$$P^{acc}(N \to N+1) = min(1, \frac{V}{\Lambda^3(N+1)} exp[\beta(\mu - U(N+1) + U(N))] \tag{2.19}$$

The removal of a particle is accepted with a probability:

$$P^{acc}(N \to N-1) = min(1, \frac{\Lambda^3 N}{V} exp[-\beta(\mu + U(N-1) - U(N))] \tag{2.20}$$

The new configuration respects the probability density of the statistical ensemble as well as the micro-reversibility (i.e., the possibility of starting in configuration a and returns to the same configuration a). At each Monte Carlo step (new configuration), the number of particles inside the box is calculated. When the stationary state is reached this number of particles at each step fluctuates around its average value and then the system is at equilibrium. μVT simulation is performed at volume and temperature constant for several chemical potential. Therefore the thermodynamic condition of the fluid can be described from ideal gas to compressed liquid if required. Different methods are used in order to find the equilibrium potential and then calculate the thermodynamic properties at liquid/vapor equilibrium. Peterson and Gubbins [92] have proposed a method using integration of the grand free energy of pure compounds.

Pitakbunkate et al. [93] have identified the phase change by plotting density versus fugacity and have observed the gap in density value. The values of the input fugacities can be approximated by bulk EOS calculation.

Gibbs ensemble

In molecular simulations, phase equilibrium calculation can be either simulated using a single box of simulation or as many boxes as there are phases. With a simulation box, the interface region gathers a high number of particles. The problem is that their properties are not representative of the homogeneous phases. The Gibbs ensemble Monte Carlo (GEMC) was therefore introduced by Panagiotopoulos et al. [86] without explicit interfaces with as many boxes as there are phases. Figure 2.1 is a schematic of the Gibbs ensemble for liquid and vapor phases.

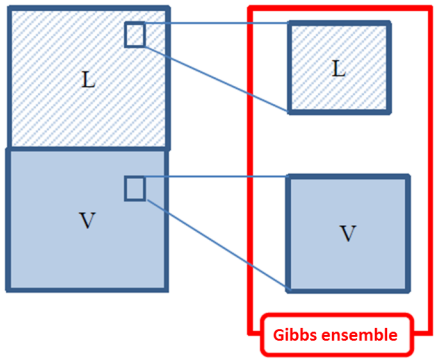

Figure 2.1: Schematic of the Gibbs ensemble

The Gibbs ensemble can be applied using the NVT ensemble or the NPT ensemble. Let's consider two simulation boxes A and B of respective volumes V_A and $V_B = V - V_A$ and respective number of particles N_A and $N_B = N - N_A$.

The partition function of the Gibbs NVT ensemble is expressed by the corresponding canonical ensemble of the two boxes.

$$Q_{Gibbs-NVT} = \sum_{V_A} \sum_{N_A} Q_{N_A V_A T} Q_{(N-N_A)(V-V_A)T} \tag{2.21}$$

The calculation gives the probability density of a configuration a in the Gibbs NVT ensemble:

$$\rho_{Gibbs-NVT}(a) \propto \frac{N!}{N_A! N_B!} V_A^{N_A} V_B^{N_B} exp(-\beta U(a)) \tag{2.22}$$

Let's consider an example of a mixture of two components 1 and 2. The number of particles in the box A is $N_A = N_A^1 + N_A^2$ and the number of particle in the box B is $N_B = N_B^1 + N_B^2$. The probability density of a configuration a in the Gibbs NPT ensemble is:

$$\rho_{Gibbs-NPT}(a) \propto \frac{(N_A^1+N_B^1)!}{N_A^1!N_B^1!}\frac{(N_A^2+N_B^2)!}{N_A^2!N_B^2!}V_A^{N_A}V_B^{N_B}exp(-\beta PV)exp(-\beta U(a)) \tag{2.23}$$

The Gibbs simulation considers two simulation boxes for vapor and liquid phase. For Gibbs NVT simulations, the total number of particles, the total volume of the two boxes and the temperature are constant. For Gibbs NPT simulations, the total number of particles, the pressure and the temperature are constant. As for the GCMC simulation, different trial moves are randomly proposed and accepted according to their acceptance probability. The moves are translation and rotation of a particles inside a box, transfer of a randomly selected particle from one box to the other and change of volume in such way that the total volume remains constant. As for GCMC simulations, longer chain molecules such as n-pentane and n-decane can have internal and rotation moves in addition. The two boxes are in thermodynamic and mechanical equilibrium, since pressure is equal for all coexisting phases.

After several Monte Carlo steps, the thermodynamic average of macroscopic properties can be calculated on stabilized configurations to give the thermodynamic properties of the fluid studied at liquid/vapor equilibrium.

Bubble point Monte Carlo pseudo ensemble (BPMC)

The Bubble point Monte Carlo (BPMC) pseudo-ensemble was first suggested by Ungerer et al. [129] and improved by Ferrando et al. [40] for bubble point thermodynamic properties calculation of a liquid mixture with a given composition. This pseudo ensemble can be either applied to the Gibbs NVT or the Gibbs NPT ensemble.

Ferrando et al. [40] used the BPMC pseudo ensemble in the Gibbs NVT ensemble. Two different simulation boxes for vapor and liquid phases are considered. Only the number of particles of the liquid phase is imposed, which allows setting the liquid composition and chemical potential. In addition the total volume and the temperature are imposed. The trial moves are the same as in the Gibbs NVT ensemble except for the particle transfer. The moves are translation and rotation of a particle inside a box, change of volume in such way that the total volume remains constant. Longer chain molecules such as n-pentane and n-decane have internal regrowth and rotation in addition. In order to guarantee the equality between liquid and vapor chemical potential of each component, insertion and deletion of particles are performed exclusively in the vapor phase.

The probability density of a configuration a in the configurations space is (Ferrando [39]):

$$\rho_{BPMC}(a) \propto \prod_i \left(\frac{(V^l)^{N_i^l}}{N_i^l!\Lambda_i^{3N_i^l}}\right)\left(\frac{(V^v)^{N_i^v}}{N_i^v!\Lambda_i^{3N_i^v}}\right) exp(-\beta U(a) + \sum_i \beta\mu_i^v N_i^v) \tag{2.24}$$

with N_i^l the number of components i in the liquid phase. N_i^v the number of components i in the vapor phase. V^l the volume of the liquid phase. V^v the volume of the vapor phase. μ_i the chemical potential of the component i.

The acceptance probability of the insertion and deletion moves inside the vapor box are equivalent to the acceptance probability of the transfer move between boxes in the standard Gibbs NVT ensemble. After the convergence of the simulation, saturated vapor composition and density are known and the bubble point can be calculated.

2.1.5 Phase equilibrium calculation for a confined fluid

In this section we will present the modifications that are performed in the grand canonical ensemble, Gibbs NVT ensemble and Gibbs NPT BPMC ensemble in order to calculate the thermodynamic properties of a confined fluid. Since the potential energy U of the different ensembles contains the total interaction forces between particles, confinement can be taken into account by adding fluid/solid interaction.

Grand canonical ensemble

In order to use the Grand canonical ensemble to model a confined fluid, no modification of the ensemble is needed. Only the fluid/solid interaction has to be taken into account. The Figure 2.2 represents a schematic of a GCMC simulation box for a fluid confined in the z direction emulating a slit pore of width H. The principle is the same as for bulk fluid, the simulation is performed for several values of the chemical potential. The values of the input fugacities can also be approximated by bulk EOS calculation. The equilibrium chemical potential is determined using Peterson and Gubbins [92] or Pitakbunkate et al. [93] method as explained in Section 2.1.4. Contrary to bulk system where periodic boundary conditions are applied in all directions for the bulk system, periodic boundary conditions are only applied in x and y directions of the space for the confined fluid.

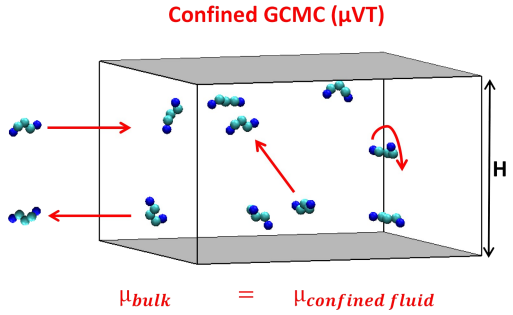

Figure 2.2: Schematic representation of a μVT simulation for the filling of a slit pore with n-pentane. μ corresponds to chemical potential and the arrows correspond to the different trial moves.

Gibbs NVT ensemble

The GEMC NVT ensemble for a confined fluid is very similar than for the bulk one presented in Section 2.1.4. In the case of confinement of a slit pore of width H, modification of the Gibbs NVT ensemble must only be done on the volume change trial move. This move must be allowed only in the directions orthogonal to the slit pore (i.e., x and y). A schematic representation of the confined Gibbs NVT simulation is given in Figure 2.3. As for GCMC for confined fluid, periodic boundary condition are only applied in x and y directions.

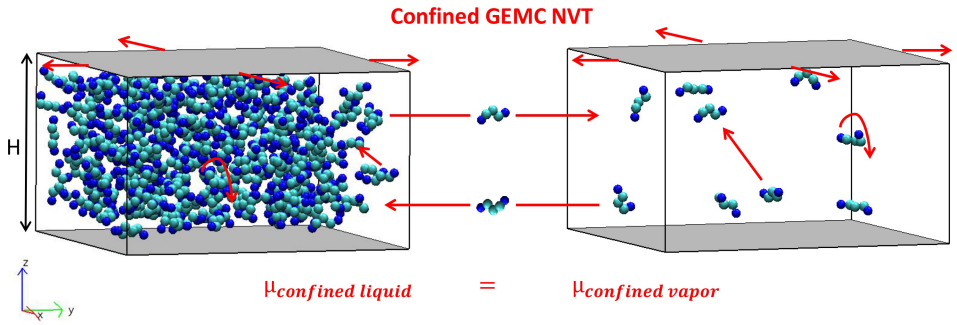

Figure 2.3: Schematic representation of the Gibbs NVT method for an example of n-pentane. The arrows correspond to the different trial moves (tranlsation, rotation, echange of particles, volume changes, in addition to internal rotation and regrowth which are not shown).

Bubble point Monte Carlo pseudo ensemble (BPMC)

In this thesis, we have adapted the BPMC pseudo ensemble presented in Section 2.1.4 in the Gibbs NPT ensemble for confined fluid mixture. Instead of considering one liquid box and one vapor box, we consider one box for the bulk saturated liquid fluid and one box for the confined fluid (Figure 2.4). These two boxes are in thermodynamic equilibrium. The pressure in the non-confined box is constant as is the system's temperature. The BPMC pseudo ensemble is characterized by a Monte Carlo move consisting of keeping constant the number of particles of the bulk saturated liquid mixture and inserting and deleting particles in the confined fluid box. In addition, the volume of the bulk box changes whereas the volume of the confined fluid box remains constant. Translation and rotation of particles inside the boxes and regrowth and flip for flexible molecules are performed according to the acceptance probability. Periodic boundary conditions are applied in all directions for the bulk box and in x and y directions for the box of the confined fluid.

2.1.6 Force field

For bulk fluids, only fluid-fluid interaction are taken into account. The fluid-fluid interaction is modeled by the Lennard-Jones 12-6 potential (equation 2.25):

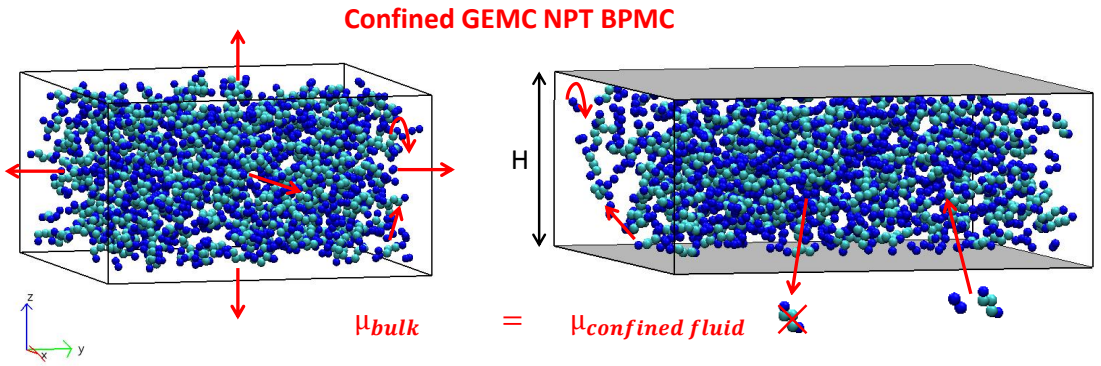

Figure 2.4: Schematic representation of the GEMC NPT BPMC method for an example of ethane/*n*-pentane mixture. μ corresponds to chemical potential and the arrows correspond to the different trial moves.

$$U_{ij}{}^{LJ}(r_{ij}) = 4\epsilon_{ij}\left(\left(\frac{\sigma_{ij}}{r_{ij}}\right)^{12} - \left(\frac{\sigma_{ij}}{r_{ij}}\right)^{6}\right) \tag{2.25}$$

where r_{ij} is the distance between two particles i and j, ϵ_{ij} is the Lennard-Jones well depth and σ_{ij} is the van der Waals radius.

For a confined fluid, the main forces taken into account in the system are the interaction potentials between particles. There are three interaction types: fluid-fluid interaction, solid-fluid interaction and solid-solid interaction. The Steele potential [43, 120] is used to model solid-fluid interactions. This potential considers only the first layer of the graphite pore wall; the remaining layers are considered as continuum solid [113], and solid-solid interaction is fully neglected. The Steele 9-3 potential is written as (equation 2.26):

$$u_{sf}(z) = \frac{2}{3}\pi\rho_s\epsilon_{sf}\sigma_{sf}{}^{3}\left(\frac{2}{15}\left(\frac{\sigma_{sf}}{z}\right)^{9} - \left(\frac{\sigma_{sf}}{z}\right)^{3}\right) \tag{2.26}$$

where z corresponds to the distance between solid and fluid particles, ρ_s is the atomic density of the solid, σ_{sf} represents the distance between two atoms of the fluid and the surface where attractive and repulsive forces are canceled, ϵ_{sf} is an energy and represents the depth of the potential well of fluid-solid interactions at the minimum of the function. The values of these parameters can be found in Porcheron et al. [96] and are provided in Table 2.1. Lorentz-Berthelot combining rules are used for solid/liquid and liquid/liquid interactions (equation 2.27):

$$\begin{cases} \sigma_{ij} = \frac{\sigma_{ii}+\sigma_{jj}}{2} \\ \epsilon_{ij} = \sqrt{\epsilon_{ii}\epsilon_{jj}} \end{cases} \tag{2.27}$$

As already said, periodic boundary conditions are applied in all directions for the bulk system and in x and y directions for the confined fluid. In order to increase the calculation performance,

the Lennard-Jones interactions are only calculated in a sphere of radius r_c (cut-off radius), which is generally the half-length of the simulation box. Standard long-range correction for the energy and the pressure are applied for bulk fluid calculations only. Long-range correction is not used for the slit pore as there are no periodic boundary conditions in the slit width direction. All studied molecules are described using the AUA4 (Anisotropic United Atoms model) optimized parameters [19, 128]. The CH_2 and CH_3 molecules are represented by a single center of force located near the geometric center of the atoms of each molecule. The AUA model consists of a displacement of the Lennard Jones centers of force toward the hydrogen atoms. The magnitude of the shift between the carbon center and the interaction site is the adjustable parameter δ. All bond lengths are kept fixed. For long-chain n-alkanes, intramolecular interactions are considered by means of additional energy terms including bending and torsion. In addition, LJ interactions are applied between atoms of the same molecule separated by four bonds. Atoms separated by two bonds interact via a harmonic bending potential (equation 2.28):

$$\frac{U_{bend}}{k_B} = \frac{1}{2} k_{bend} (cos\theta - cos\theta_0)^2 \tag{2.28}$$

where k_B is the Boltzmann constant, k_{bend} is the bending constant, and θ and θ_0 are the bending angle and the equilibrium bending angle, respectively. Atoms separated by three bonds interact by a torsional potential of the following form (equation 2.29):

$$\frac{U_{tors}}{k_B} = \sum_{n=0}^{8} a_n (cos\phi)^n \tag{2.29}$$

where ϕ is the torsional angle and a_n are constants.

2.1.7 Calculation of the system thermodynamic properties

When the stationary state is reached in the simulations, the number of particles inside the simulation box at each step fluctuates around its average value and then the system is at equilibrium. The average of a macroscopic propriety X is then calculated using equation 2.30.

$$< X >= \frac{1}{n} \sum_{i=1}^{n} X(r_i^n) \tag{2.30}$$

where n is the number of configurations and r_i^n the positions of the particles in configuration i (or sampling i).

The density of component i at equilibrium is calculated using equation 2.31.

$$\rho_i = \frac{< N_i > M_i}{V N_{av}} \tag{2.31}$$

with N_i the number of particles i, M_i the molar mass of the particle i, V the volume of the simulation box and N_{av}, the avogadro number.

For mixtures, phase densities and molar fractions are calculated using equations 2.32 to 2.35.

$$\rho_l = \frac{\sum_i < N_i^l > M_i}{V N_{av}} \tag{2.32}$$

$$\rho_v = \frac{\sum_i < N_i^v > M_i}{V N_{av}} \tag{2.33}$$

$$x_i = \frac{< N_i^l >}{\sum_i < N_i^l >} \tag{2.34}$$

$$y_i = \frac{< N_i^v >}{\sum_i < N_i^v >} \tag{2.35}$$

where l subscription refers to liquid phase and v refers to vapor phase.

The pressure is estimated using the virial equation (equations 2.36)

$$\begin{aligned} < p >= \frac{<N> k_B T}{V} + \frac{1}{3V} \sum_i \sum_{j>i} \vec{r_{ij}}.\vec{f_{ij}} = \\ \frac{<N> k_B T}{V} + \frac{1}{3V} \sum_i \sum_{j>i} ((r_{ij} f_{ij})_{xx} + (r_{ij} f_{ij})_{yy} + (r_{ij} f_{ij})_{zz}) \end{aligned} \tag{2.36}$$

$$\vec{f_{ij}} = -\vec{\nabla}(U(\vec{r_{ij}})) \tag{2.37}$$

where N is the average number of particles inside the simulation box, k_B is the boltzmann constant, T is the temperature and $\vec{f_{ij}}$ is the intermolecular force (equation 2.37) with $\vec{r_{ij}}$ the distance between particle i and j and U the interaction potential. In this calculation calculation, for confined fluids, we have included the solid-fluid contribution in z direction of the Steele potential. This fact makes the different elements of the virial (xx, yy and zz) anisotropic, contrary to it is observed in bulk phases when all elements are equal in average. This explains why we have two different pressures inside the liquid and the vapor phases. For the calculation of the critical pressure, we have used the value of the vapor phase.

The critical parameters are estimated with the least square fit of the following scaling law (equation 2.38) [135].

$$\rho_l - \rho_v = B(1 - \frac{T}{T_c})^{\beta} \tag{2.38}$$

where β=0.325 and B is the constant to fit. The critical temperature estimated is then used to calculate the critical density from the least square fit of the following equation (equation 2.39) [134].

$$\frac{\rho_l - \rho_v}{2} = \rho_c + A(1 - \frac{T}{T_c}) \tag{2.39}$$

where ρ_c is the critical density and A is the constant to fit.

Finally the critical pressure is obtained from the Antoine equation (equation 2.40), which is derived from the Clausius Clapeyron equation, which results from the fitting of the vapor pressure values obtained at each temperature.

$$ln(P_c) = C + \frac{D}{T_c} \tag{2.40}$$

where C and D are constants to adjust. C and D correspond respectively to the intercept and the slope of $\ln(P_v)$ versus 1/RT, where P_v is the vapor pressure.

In the case of a binary mixture, an initial estimate of the critical pressure P_c is found, assuming the following scaling law (equation 2.41) with α=0.325:

$$\rho_l - \rho_v = \gamma(P - P_c)^\alpha \tag{2.41}$$

The procedure is identical to T_c determination for a pure compound. The estimate of critical pressure is used to perform the regression of λ and μ, assuming the second following scaling law (equation 2.42) for binary mixtures with alpha=0.325:

$$y_i - x_i = \lambda_1(P_c - P) + \mu(P_c - P)^\alpha \tag{2.42}$$

where x_i and y_i are the liquid and the vapor molar fraction of the component i of the binary mixture. The critical pressure P_c corresponds to the minimum dimensionless error on equation 2.41 and equation 2.42.

The regression of critical composition z_{ci} is on the basis of equation 2.39 in the same way as ρ_c for a pure compound.

$$\frac{y_i + x_i}{2} = z_{ci} + \lambda_2(P_c - P) \tag{2.43}$$

The coexistence densities and compositions can be calculated according to equation 2.44 to 2.47.

$$x_i = z_{ci} + (\lambda_2 - \frac{\lambda_1}{2})(P_c - P) - \frac{\mu}{2}(P_c - P)^\alpha \tag{2.44}$$

$$y_i = z_{ci} + (\lambda_2 + \frac{\lambda_1}{2})(P_c - P) + \frac{\mu}{2}(P_c - P)^\alpha \tag{2.45}$$

$$\rho_l = \rho_c + \gamma(P - P_c) + \frac{\lambda}{2}(P_c - P)^\alpha \tag{2.46}$$

$$\rho_v = \rho_c + \gamma(P - P_c) - \frac{\lambda}{2}(P_c - P)^\alpha \tag{2.47}$$

2.2 Considerations of the reference pressure in confinement

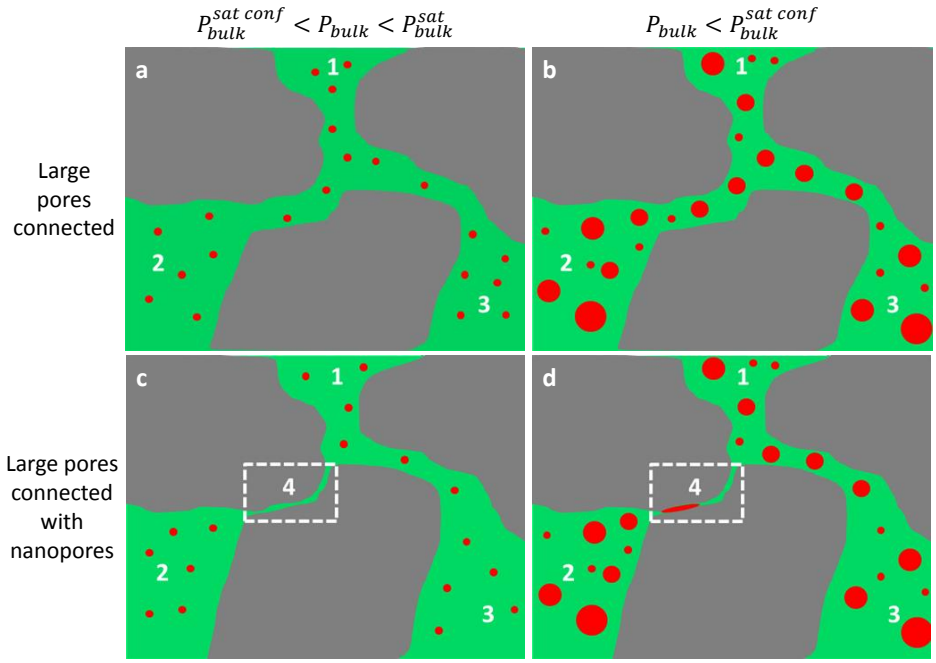

Figure 2.5: Schematic of large pore and nanopore network in tight oil reservoirs; oil is represented in green and gas is represented in red. a) Large pore connected with pressure between saturation pressure of a single bulk fluid (${P_{bulk}}^{sat}$) and saturation pressure of bulk fluid connected to confined fluid where first bubble appears in confined fluid (${P_{bulk}}^{sat\ conf}$). Gas appears in every 3 pores. b) Large pore connected with pressure below saturation pressure ${P_{bulk}}^{sat\ conf}$, volume of gas is increasing homogeneously in the 3 pores. c) Large pore (1, 2, 3) connected with nanopore 4 with pressure between ${P_{bulk}}^{sat}$ and ${P_{bulk}}^{sat}$. Gas appears in large pores but not in nanopore. d) Large pore (1, 2, 3) connected with nanopore 4 with pressure below ${P_{bulk}}^{satconf}$. Gas volume in large pores is increasing and gas begins to appear in nanopore.

Saturated bulk pressure and saturated confined pressure are often compared in the literature in studies using EOS modification by critical point shift [6, 45, 124, 35, 34, 52, 106] or capillary pressure method [6, 42, 45, 103, 107, 121, 124, 152, 155]. Comparison between classic EOS and

modified EOS for confined fluid modeling showed that the bubble point pressure decreases with confinement. Pitakbunkate et al. [93, 94] built phase diagram of methane-ethane mixture in nanopores and compared it to a bulk fluid. According to the phase diagrams, the bubble point pressure decreases with confinement. All the authors cited above only used a unique pressure as reference to describe the system without giving further details. However the pressure definition for a confined system in a pore network is not trivial and need some explanations. It is important to clarify the definition of the link between pore network topology and the different pressures that can be observed in confinement. To compare the bulk fluid to the confined fluid, we compare in reality two systems: a bulk fluid and a bulk fluid in thermodynamic equilibrium with a confined fluid. The two systems have a bulk pressure but the thermodynamic properties of the fluid at equilibrium are not the same: the first one has no interactions with the graphite slit pore when the second does. In the case of a bulk fluid in thermodynamic equilibrium with a confined fluid, three pressures are observed for a given equilibrium state: the bulk pressure of the fluid and the pressures of the vapor and liquid phases of the confined fluid. Figure 2.5 illustrates a schematic representation of two different pore networks in tight oil reservoirs. The first system considered is constituted by three large pores completely connected (1, 2, 3) in Figure 2.5.a and b; the liquid and vapor pressures are the same in each pore as the saturation pressure, therefore during the depletion gas phase appears at the same time in each pores during depletion. The second system considered is constituted by three large pores (1, 2, 3) and one nanopore (4) in Figure 2.5.c and b. In this system, for bulk pressure between the bulk fluid saturation pressure and the confined fluid saturation pressure (Figure 2.5.c), gas phase appears only in large pores and not in the nanopores. In contrast, for bulk pressure under the confined fluid saturation pressure, gas also appears in the nanopores and three different pressures are present in the system (Figure 2.5.d): the bulk pressure and the liquid phase and the vapor phase of confined fluid pressures are all different. In conclusion, in order to compare a bulk fluid to a confined fluid two different systems are considered: a bulk fluid and a bulk fluid pressure in thermodynamic equilibrium with a confined fluid. The bulk pressure is considered as reference. As GCMC simulation only considers one pressure, therefore Pitakbunkate et al. [93, 94] naturally choose to use the pressure corresponding to the chemical potential of the GEMC simulation.

2.3 Methodology for confined fluid thermodynamic properties calculation

From now on, GCMC ensemble is used for the calculation of thermodynamic properties of mixtures at equilibrium in confined space by molecular simulation. However the precise determination of the chemical potential of each component of the mixture at liquid/vapor thermodynamic equilibrium remains a challenge and leads to a lack of precision in the results. Furthermore no ensemble is now able to calculate confined liquid and vapor pressure at thermodynamic equilibrium of pure components or mixtures. We therefore propose in this thesis a new methodology

in the GEMC ensemble allowing the calculation of precise thermodynamic properties of mixtures in confined space at equilibrium and confined liquid and vapor pressures. In this section we explain the the workflow used to model confined fluid thermodynamic behavior and how to get its properties such as density, phase composition and pressures. We give the details of the different systems studied, the statistical ensemble used, the molecular simulation parameters and the data post-processing. The Gibbs code from IFPEN and the Laboratoire de Chimie Physique (LCP) at University Paris-Sud has been used for all the molecular simulations cited in this paper [130]. No modification of the Gibbs code has been done during this thesis, the focus of the work was to develop a new methodology and workflow in order to model confined fluid thermodynamic behavior and how to get its properties.

2.3.1 Case studies

The case study is hydrocarbon fluid confined in a nanometric pore, such as kerogen pores present in tight oil and shale gas reservoirs. We propose to model the reservoir pores with slits pores with graphite walls. Two infinite parallel slices are in the orthogonal directions to the slit pore (i.e. x and y) and the slit pore has a width of length H in the z direction. In order to first validate the intermolecular potential models with experimental or analytical results, all simulations were first performed for bulk fluids. The chosen pure components are methane, ethane, n-pentane and n-decane and the chosen mixtures are methane/ethane and ethane/n-pentane. Two different workflows are used for pure components and mixtures. These workflows are presented in the schematics Figure 2.6 and they are detailed in Section 2.3 and 2.4.

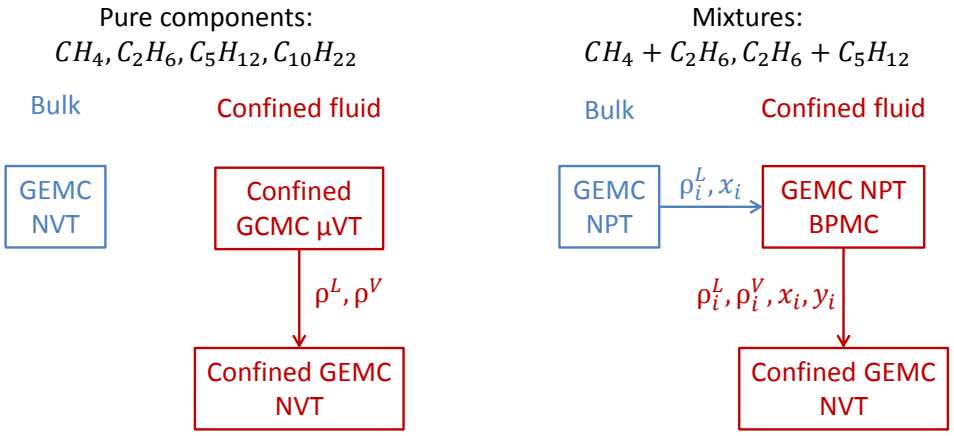

Figure 2.6: Schematic of the simulation workflow used in this study for the simulation of the liquid-vapor equilibrium of pure compounds and mixtures in confinement.

2.3.2 Pure components workflow

As mentioned earlier, confined fluid studies using Monte Carlo molecular simulation are usually performed by the Grand Canonical Monte Carlo ensemble (GCMC) [10, 17, 85, 93, 96, 101, 94, 50]. However this method has several drawbacks. Firstly, the identification of phase change chemical potential remains challenging and complex [92]. Secondly, the pressure of vapor and liquid inside the pore at thermodynamic equilibrium cannot be obtained easily. The pressure inside a simulation box is estimated by the virial Equation (Equation 2.36) which corresponds to the average of the diagonal terms of the pressure tensor. In addition to the lack of precision for the determination of the value of the equilibrium chemical potential, the particle insertion leads to strong fluctuations in the virial Equation during the Monte Carlo simulations. The results will therefore not be exploitable. That is why we propose to use the Gibbs Ensemble Monte Carlo (GEMC) presented in Section 2.1.5 to study such fluids. It is important to mention that solid-fluid interactions are modeled by an analytical intermolecular potential which is function of z (see details in 2.1.6). This means that solids are considered as a continuum media, therefore, it is possible to modify the volume of the pores in x and y directions without any problems. GEMC NVT simulation allows us to get accurate readings of the liquid/vapor equilibria properties but it needs good initial estimation of densities of each phase to converge. The confined GCMC μVT simulations (Section 2.1.5) will therefore be used to get initial vapor and liquid densities for pure components. These densities will then be used to calculate the number of particles in each phase in order to initialize the vapor and liquid boxes of the GEMC NVT simulation for pure components. All these simulations have been performed for several isotherms and pore widths.

2.3.3 Mixtures workflow

As for pure components, the application of GEMC NVT simulation for mixtures needs a good initial estimation of densities with the additional molar fraction of each component in each phase to converge. Because of the importance of convergence issues and the complex use of GCMC ensemble for mixtures, a more appropriate ensemble called GEMC NPT BPMC presented in Section 2.1.5 have been used in this study in order to initialize the Monte Carlo simulations for mixtures.

The bulk liquid box is initialized thanks to a classic GEMC NPT simulation for a bulk fluid and the confined fluid box is initially empty of molecules. As represented in Figure 2.7 for an ethane/n-pentane mixture, the number of particles of the different components in the confined box will fluctuate between the liquid and the gas phase during the simulation. Average values of the number of particles in each phase can be obtained by plotting histograms of the number of particles for each component which can be fitted to a sum of two Gaussian curves (Equation 2.48). α_i^1, α_i^2, β_i^1 and β_i^2 are the constants to fit for one component i and N_i, N_i^v and N_i^l correspond to the number of particles of component i, the average number of particles

in the vapor and the liquid phase for a component i at equilibrium respectively. These number of particles in each phase can be used as an initialization for a confined GEMC NVT simulation for accurate results on thermodynamic properties of the confined fluid and vapor and liquid pressures determination.

$$f(N_i) = \alpha_i^1 e^{-\frac{(N_i - N_i^v)^2}{2\alpha_i^{2\,2}}} + \beta_i^1 e^{-\frac{(N_i - N_i^l)^2}{2\beta_i^{2\,2}}} \tag{2.48}$$

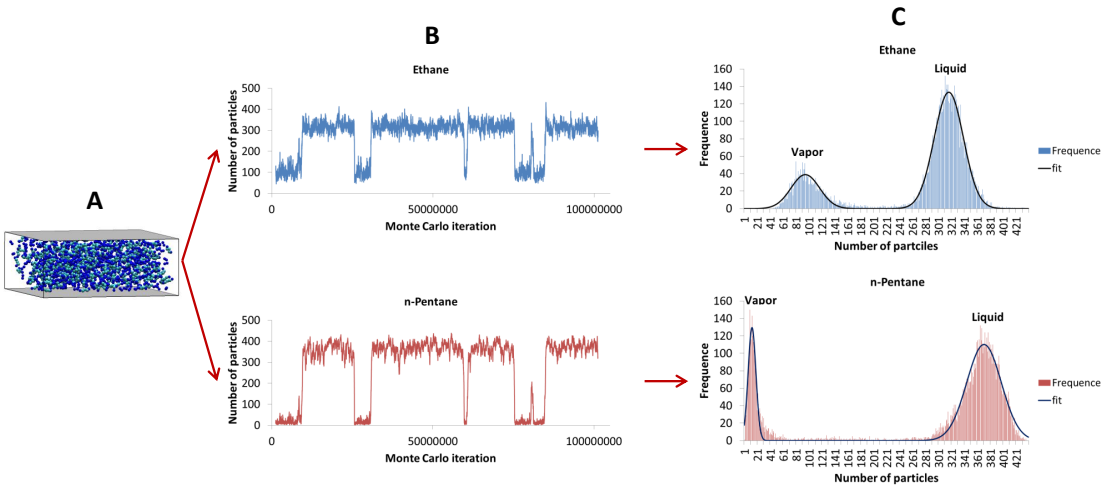

Figure 2.7: GEMC NPT BPMC post processing, example of ethane/n-pentane. A) Confined fluid box with constant volume. B) fluctuation of the number of particles of C_2H_6 and C_5H_{12} inside the confined slit pore. C) Histogram of the number of particles of each species showing the bimodal probability of particles in the vapor and liquid phase.

2.3.4 Simulation parameters

The non-flexible and flexible molecule parameters describing the force field are given in [96, 19, 128] and are summarized in Tables 2.1 and 2.2. The simulation box parameters are summarized in Table 2.3 where L_x, L_y, L_z corresponds to the box lengths in the x, y, z directions respectively. The initial values of L_x and L_y lengths were adapted in function of the critical point proximity for all simulations ensembles. The different move probabilities and Monte Carlo steps used for non-flexible and flexible molecules are summarized in Tables A.1, A.2, and A.3 of Appendix A.1. The simulation data post-processing are given in Section 2.1.7.

In conclusion of this section, two workflows have been presented for equilibrium thermodynamic properties calculation of confined fluid. The first one for confined pure components and the second one for mixtures. The summary of these workflows are given in Figure 2.6. Concerning the pure components, GEMC NVT simulations have been performed for the bulk fluid and confined GCMC μVT has been used as an initialization for the confined GEMC NVT

Table 2.1: Fluid-fluid and solid-fluid parameters.

Atom	ϵ (K)	σ (nm)	δ (nm)	ρ_s $(10^{-5}nm^{-3})$	M $(10^{-3}kg/mol)$
CH_4	149.92	0.37372			16.043
AUA CH_2	86.291	0.34612	0.038405		14.03
AUA CH_3	120.15	0.36072	0.021584		15.03
Steele	47.0651	0.38663		3.3	

Table 2.2: Intramolecular force field parameters with δ the distance from the carbon atom.

Bond length C-C	$r_0(nm)$ 0.1535	
Bend CH_2 $CH_3-CH_2-CH_2$ $CH_3-CH_2-CH_2$	$\theta(^\circ)$ 120.15	$k_{bend}(K)$ 3.6072
Torsion $CH_3-CH_2-CH_2-CH_2$ $CH_2-CH_2-CH_2-CH_2$	$a_i(K)$ $a_0 = 1001.35$ $a_1 = 2129.52$ $a_2 = -303.06$ $a_3 = -3612.27$ $a_4 = 2226.71$	 $a_5 = 1965.93$ $a_6 = -4489.34$ $a_7 = -1736.22$ $a_8 = 2817.37$

Table 2.3: Simulation box parameters.

Simulation	box length (nm)						Monte Carlo steps
GCMC μVT	L_x		L_y		L_z		
	3		3		pore width		5x10^7
GEMC NVT	Liquid box			Vapor box			
	L_x	L_y	L_z	L_x	L_y	L_z	
	5	5	pore width	9	9	pore width	Appendix A
NPT BPMC	bulk liquid box			confined fluid box			
	L_x	L_y	L_z	L_x	L_y	L_z	
	6	6	pore width	7	7	pore width	Appendix A

simluations. Pure components simulations will be performed for several isotherms and pore widths. Concerning the mixtures, GEMC NPT simulations will be done for the bulk fluid. The resulting liquid properties will be used to initialize the bulk liquid box of the GEMC NPT BPMC simulations, finally confined liquid and vapor properties will be used for the confined GEMC NVT simulations. These simulations will be performed for different isotherms and for a pore width of 3 nm. The workflow presented will be applied to several pure components and mixtures in the next section.

2.4 Results

This section will present the results of the molecular simulation workflows described in 2.3.2 and 2.3.3 with simulation parameters and data post-processing detailed in Appendix A.1 and Section 2.1.7 respectively. The pure components studied are $CH_4, C_2H_6, C_5H_{12}, C_{10}H_{22}$ and the mixtures are $CH_4 - C_2H_6$ and $C_2H_6 - C_5H_{12}$.

2.4.1 Pure fluids

We start the results section by showing the effect of confinement on phase density of pure fluid. Figure 2.8 shows the density phase diagram of $CH_4, C_2H_6, C_5H_{12}, C_{10}H_{22}$ at bulk condition and with pore confinement. Bulk simulations well match the reference data. As a general trend we can observe that confined fluid vapor density increases and the confined fluid liquid density decreases with confinement for all the studied molecules. Fluid/pore interaction attracts particles near the pore wall and creates an adsorption layer. Consequently the vapor density, which is the average density inside the entire pore, will be larger than the bulk density because of this adsorption layer. Pore walls participate in particle cohesion: close to the walls, the molecules are highly structured imposing a translation order from the surface wall to the pore.

Confined liquid is less dense than liquid bulk. Walls impose order through strong layering, slightly increasing the inter-particle distance in z direction, which is larger than the one observed in disorder bulk phases. Consequently confined liquid density is less than the bulk one [60]. Another consequence of this behavior is the reduction of the critical temperature with respect to the bulk. The critical temperature is indeed estimated with the least square fit of the scaling law function of liquid and vapor densities (Equation 2.38).

The pressure is estimated by the virial equation (Equation 2.36), which takes into account the diagonal elements of the pressure tensor. The anisotropic effect induced by the presence of the walls are therefore take into consideration in our simulations. The critical pressure is calculated using confined vapor pressure and Equation 2.40. The evolution of critical temperature versus pore length differs from the evolution of critical pressure (see Figure 2.9 and Appendix A.2, Figure A.1). The curve is different for each component and naturally tends towards bulk value at high pore length. It is worth remembering that pressure calculation in confined pores does not include long-range correction of pressure and energy as it is usually done for bulk calculations. That is why critical pressure for large pores slightly differs from the bulk value.

The comparison with data from the literature (Figure 2.9) shows that results for critical temperature are close to those from Singh and Singh [115], Pitakbunkate et al. [93]. Several correlations are used in the literature to describe the evolution of critical temperature and pressure with confinement [77, 52]. Concerning the critical temperature, the correlation from Jin et al. [52] is well adapted and matches the observed results. Our results for the critical pressure

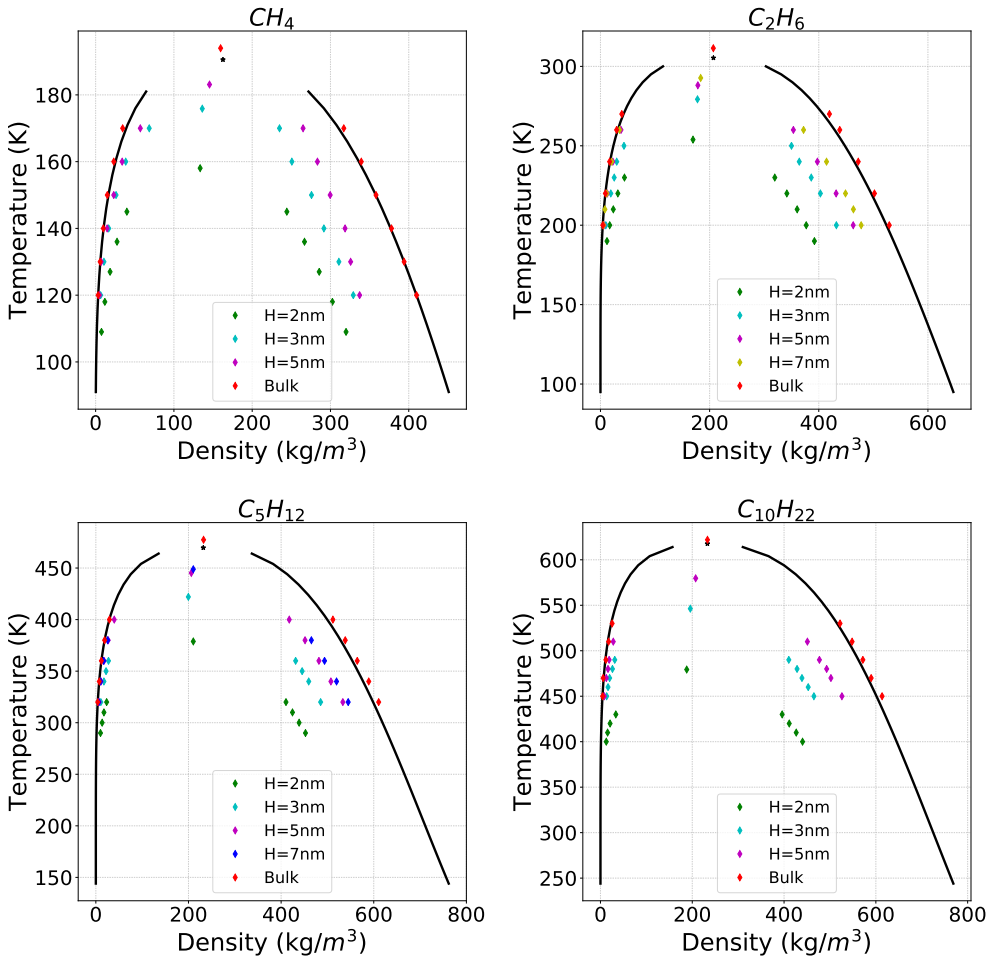

Figure 2.8: Results of the liquid vapor NVT simulations for CH_4, C_2H_6, C_5H_{12} and $C_{10}H_{22}$ for different pore widths. The black curves are reference bulk values from the National Institute of Standards and Technology database website [64].

are not as close to the literature data [115, 93] as those from critical temperature because the methods used by the previous authors to compute the pressure are different. Pitakbunkate et al. [93] performed GCMC simulations and used the pressure of the bulk fluid in equilibrium with the confined fluid and monitored the end of density discontinuity versus pressure, which is very challenging. Singh and Singh [115] ran simulations in the Grand Canonical Transition Matrix Monte Carlo (GCTMMC) ensemble to get saturation pressure for different temperatures. Then the critical pressure was obtained by fitting Equation 2.40. That is probably one of the reasons the difference between our results and those from the literature. Concerning the correlation for those critical pressure, the analytical solution from Meyra et al. [77] shows a better match with molecular simulation results than the one of Jin et al. [52], which leads to negative values of $\frac{P_{c_{conf}}}{P_{c_{bulk}}}$ when applied to longer alkane chains inside small pores.

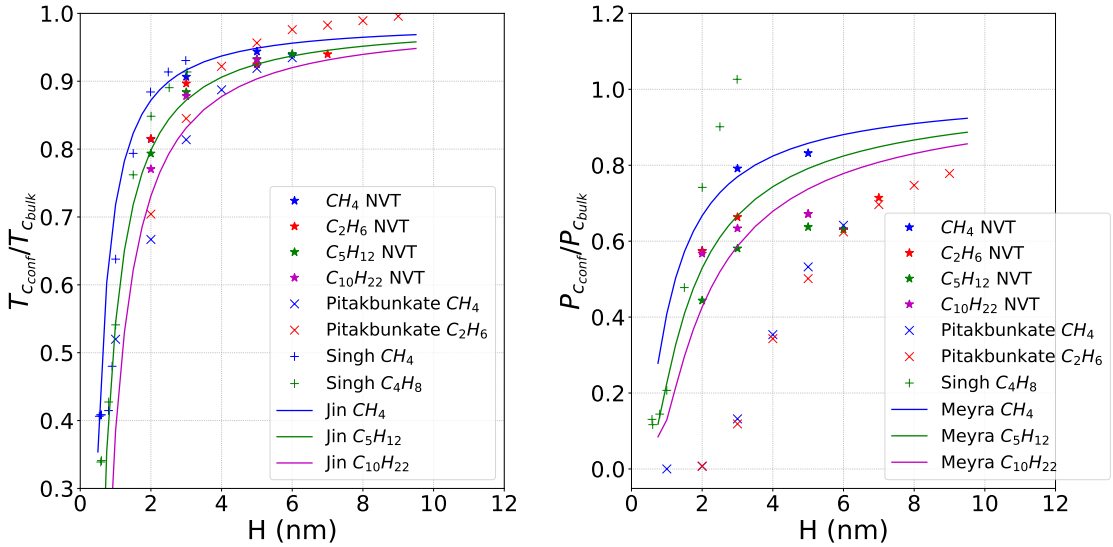

Figure 2.9: Comparison of critical temperature (left) and pressure (right) versus pore length (H) evolution with literature. The stars correspond to the NVT results for the studied pure components. The 'x' symbols correspond to the results of Pitakbunkate et al. [93]. The '+' symbols correspond to the results of Singh and Singh [115]. Finally the line correspond to the correlations of Jin et al. [52] for critical temperature and Meyra et al. [77] for critical pressure.

Unlike the bulk fluid where vapor and liquid pressure are equal at equilibrium, confined fluids have different values of vapor and liquid pressures. The pressure can no longer be considered as a reference for thermodynamic equilibrium but chemical potential or fugacity must be used instead. Comparing bulk saturation pressure with confined vapor and liquid pressure in a P-T phase diagram, for example, is of no practical interest, as the bulk and the confined fluids are not at the same thermodynamic equilibrium state. An alternative of using chemical potential as reference is the use of the bulk pressure of both systems: bulk fluid and bulk fluid in thermodynamic equilibrium with a confined fluid (see Section 2.2). An example of the difference in pressure between the vapor and liquid phase for different pore confinement for the n-pentane is shown in Figure 2.10. The pressures are calculated using the Virial in the two boxes of the NVT simulation. The vapor pressure is positive for all pore widths and increases with confinement at a constant temperature as can be seen in Figure 2.10. As the gas molecules become closer due to the smaller slit pore length constraints, the interaction between molecules is enhanced and the Virial pressure increases. The liquid pressure increases also with confinement, but its value goes from negative to positive. The slit pore is by assumption infinitely rigid, therefore the two graphite sheets cannot deform themselves under the action of capillary pressure or van der Waals solid-fluid-solid interactions as in reality [108]. For bigger pores (5 nm and 6 nm) the liquid tends as to densify itself but this is prevented by the pore constraints. That is why the virial pressure is negative. For smaller pores, the molecules are much more closer, so repulsions could occur and the sum of the total forces gives a positive virial pressure. The mechanical con-

straint of the slit length and the Steele potential between wall and fluid causes inhomogeneity of pressure inside the fluid. Disjoining pressure occurs in the perpendicular direction of the slit surface in function of the length of the adsorbed layer [60, 13].

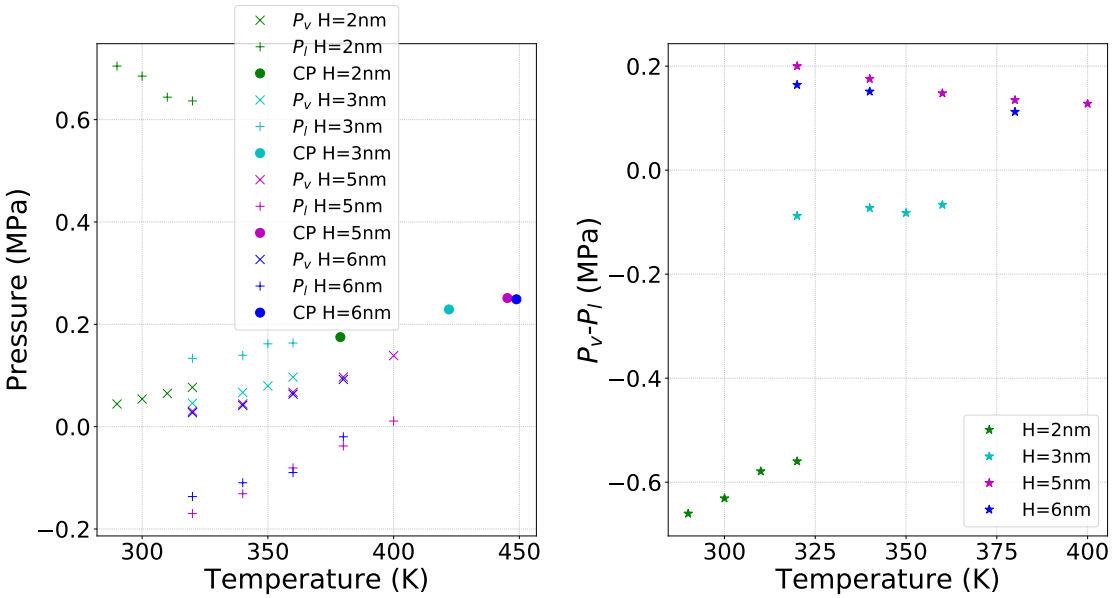

Figure 2.10: Pressures (left) and capillary pressures (right) of C_5H_{12}. The 'x' symbols corresponds to confined vapor pressure NVT results. The '+' symbols correspond to confined liquid pressure NVT results and the circles correspond to critical point 'CP'. The star symbols on the right plot correspond to the difference between confined vapor and liquid pressure.

We have also analyzed the behavior of the capillary pressure as can be seen in Figure 2.10. For the biggest pores (5 nm and 6 nm) the capillary pressure is positive and decreases with temperature until reaching the critical point where the capillary pressure must be zero. The positivity of the capillary pressure shows the wettability of the surface to the liquid phase, which is common in conventional reservoirs between oil and gas. Positive capillary pressure is when having wet fluid-surface and negative is when having dry ones. The values of the capillary pressure for the 5 nm slit pore are higher than the ones obtained for the 6 nm slit pore, which is consistent with the Laplace equation. However the behavior is totally different for the smaller pores (2 nm and 3 nm) where the capillary pressure is negative and increases with temperature towards zero at the critical point. It is important to mention that at such small scales the Laplace-Young equation is no longer applicable [13, 27].

The confined NVT simulation has allowed us to precisely calculate thermodynamic properties of several pure components. The calculation of critical temperature and pressure evolution for several pore sizes has provided reference data to validate the more convenient correlations proposed in the literature. Furthermore confined vapor and liquid pressure has been calculated for one pure components which is a total novelty.

2.4.2 Mixtures

Liquid/vapor thermodynamic equilibrium calculations are performed for two mixtures: methane/ethane and ethane/n-pentane using the workflow described in Figure 2.6 in Section 2.3.1. A pore length of 3 nm is used for both mixtures.

Methane-Ethane

The mixtures workflow of Figure 2.6 has been performed for the mixture $CH_4 - C_2H_6$ at five isotherms: 200 K, 220 K, 230 K, 240 K, 260 K. Post-processing explained in Section 2.1.7 allowed us to obtain the different equilibrium thermodynamic properties of confined fluids. In order to understand why a confined NVT simulation is needed after a GEMC NPT BPMC simulation, an example of results obtained for a specific isotherm for these two simulations is shown in Figure 2.11.

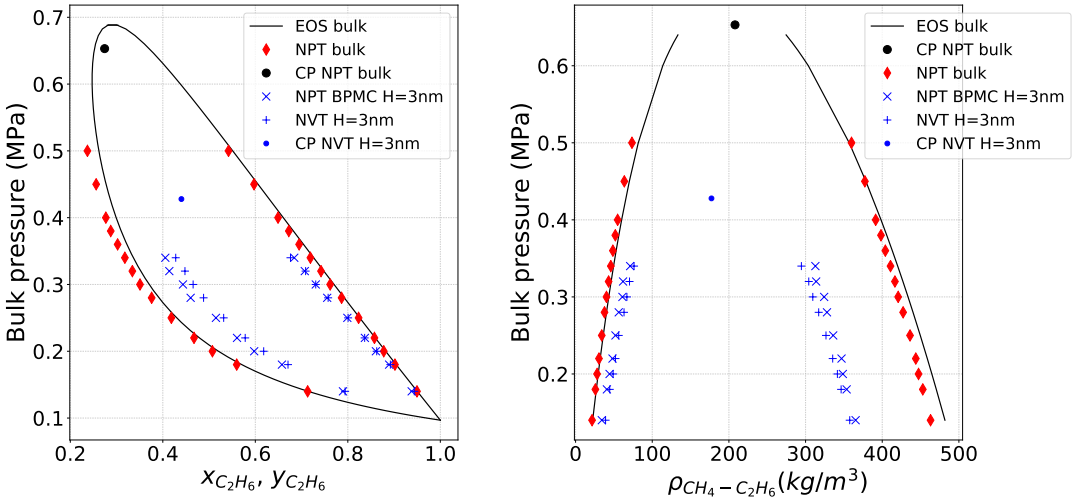

Figure 2.11: Pressure molar fraction (left) and pressure density diagrams (right) for methane/ethane at 240 K. The black line corresponds to EOS Peng Robinson results. The red diamonds correspond to bulk NPT results with the critical point (CP) in black circle. The blue symbols 'x' correspond to NPT BPMC results for H=3 nm. The blue symbols '+' correspond to NVT results for H=3 nm with the critical point in blue circle.

The GEMC NPT BPMC and confined NVT results are quite similar until they get close to the critical point where we observe strong fluctuations of the number of particles in the GEMC NPT BPMC simulations. Indeed, close to the critical point, the two modes of the number of particle histogram are very difficult to detect (see Figure 2.7C). Furthermore the statistical uncertainty of the GEMC NPT BPMC results (around 10 molecules) is much higher than the NVT results (around one molecule) at high temperatures close to the critical point. After the analysis of our simulation results, we conclude that GEMC NpT BPMC has the drawback that you can't obtain the confined liquid and vapor pressures. After this information, we have

adopted then the strategy described in Figure 2.6, where the GEMC NPT BPMC results are used to initialize the confined Gibbs NVT simulations to get better results. We should mention, however, that this method is quite fast and can be used as a first scan to estimate the phase diagram of a fluid in confinement for temperatures inferior to 0.7 times the critical one. Finally, we should mention that the GEMC NpT BPMC is the only one able to guarantee a direct connection of the confined fluid with the thermodynamic conditions of the fluid in the bulk (see Section 2.3), which is also required for the initialization of the Gibbs NVT simulations.

As observed for pure components, the vapor density increases and the liquid density decreases with confinement for all isotherms (see Figure 2.12).

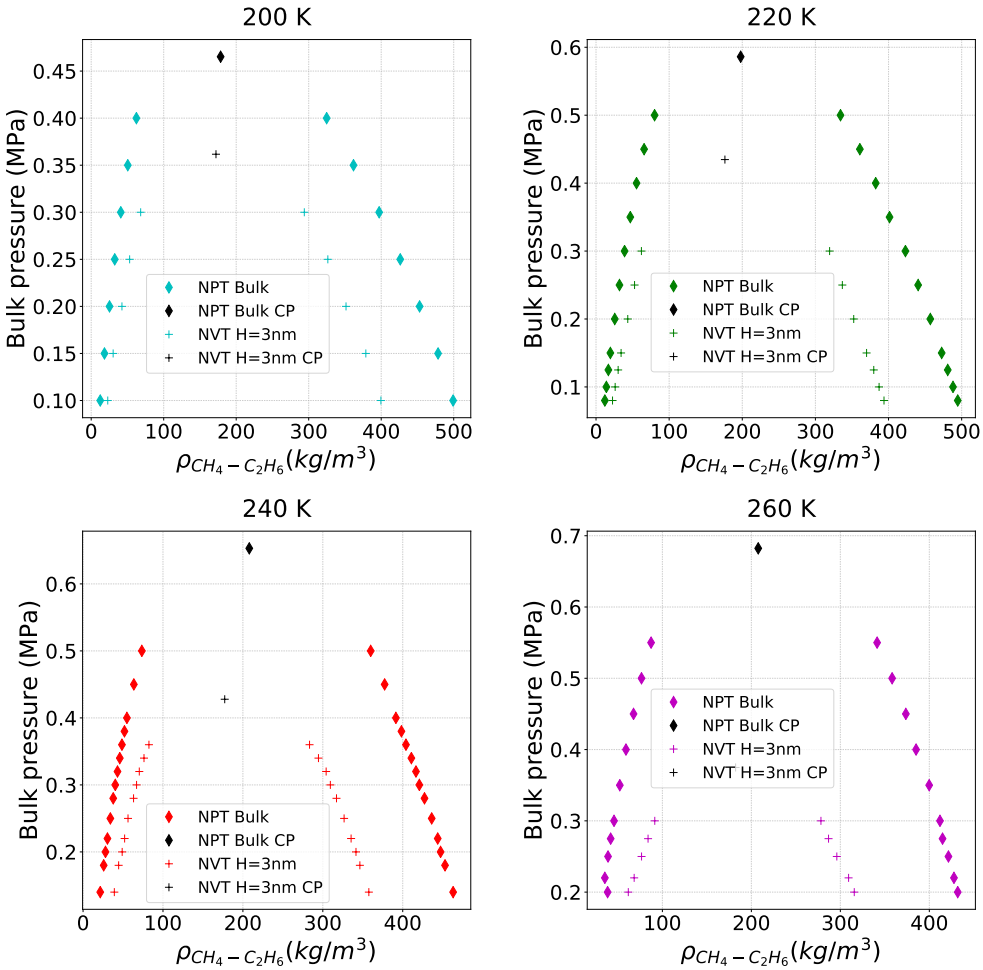

Figure 2.12: Comparison of pressure-density diagram of methane/ethane for a bulk (diamond) and a confined fluid ('+') for different isotherms. CP refers to critical point.

The critical pressure decreases with a value below the bulk value for all isotherms (see Figure 2.13). Using the pressure-molar fraction diagrams for different isotherms obtained in

Appendix A.2 Figure A.2, a pressure-temperature diagram can be built for a specific concentration of methane/ethane. Indeed, one value of ethane molar fraction corresponds to one value of dew-point pressure and bubble-point pressure for each isotherm. An example of this diagram for a mixture of 34.9% methane and 65.1% ethane is shown in Figure 2.14. It is observed that the phase envelope of the confined fluid has shifted and closed itself from its bulk value. The critical temperature and pressure have shifted from the bulk value to a lower value and the bubble-point pressure decreases as the dew-point pressure increases. This observation is valid regardless of the proportion of methane and ethane in the mixture.

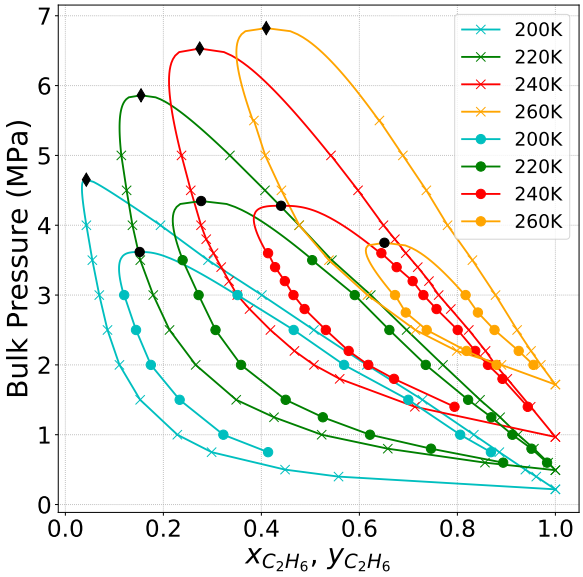

Figure 2.13: Comparison of pressure-molar fraction diagram of methane/ethane for a bulk and confined fluid for different isotherms. The 'x' symbol corresponds to bulk NPT results, the critical points of each isotherm are in black diamonds. The circles correspond to confined NVT results for H=3 nm, the critical points of each isotherm are in black circles. The lines near the critical point are obtained from the correlations 2.44 and 2.45. The remaining lines are obtained from linear interpolation between 'x' symbol or circles.

In the pressure-molar fraction diagrams for the confined fluid (see Figure 2.13), the bulk pressure corresponds to the pressure in the pores 1, 2 and 3 in the schematic Figure 2.5, when the first gas bubble appears in the nanopore 4. The molar fraction of ethane presented in the pressure-molar fraction diagram (see Figure 2.13) corresponds to the molar fraction of ethane in the fluid inside the nanopore 4.

Unlike the bulk fluid, the spacial distribution of ethane and methane molecules inside the silt pore is not homogeneous due to the solid-fluid interactions. An example of the density profile in z direction for methane/ethane mixture at 220 K and 2 MPa is shown in Figure 2.15. The initial composition is made of 39.5% methane molar fraction and 60.5% ethane molar fraction, which gives at equilibrium for 220 K and 20 MPa the liquid molar fractions $x_{CH_4} = 0.265$,

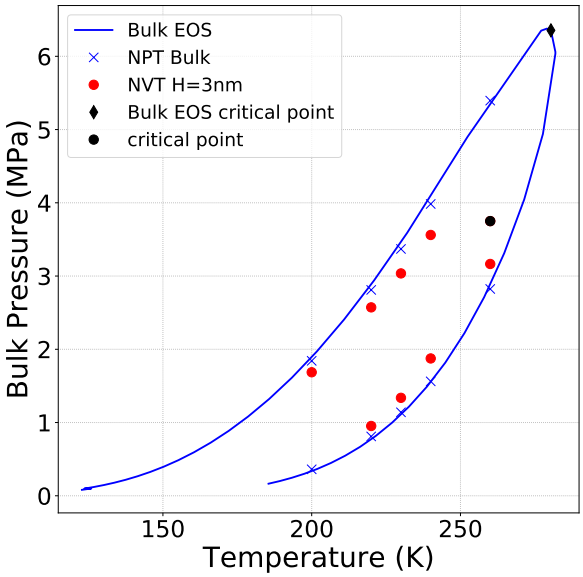

Figure 2.14: Example of a pressure-temperature diagram for a mixture of 34.9% methane and 65.1% ethane. The blue line corresponds to EOS Peng Robinson results with the critical point in black diamond. The 'x' symbols correspond to bulk NPT results and the red circles correspond to confined NVT results for H=3 nm with the critical point in black.

$x_{C_2H_6} = 0.735$ and the vapor molar fractions $y_{CH_4} = 0.642$, $y_{C_2H_6} = 0.358$. The density profile corresponds to the number of particles of methane and ethane per nm^3 in each slices of 0.003 nm width along z direction for the slit pore of 3 nm width. The simulation parameters and post-processing details are given in Appendix A.1. For both vapor and liquid the density of molecules is higher close to the wall than at the center of the pore. The selectivity of the confined system towards methane or ethane in comparison with the bulk one can be calculated with Equation 2.49.

$$S_{C_2H_6/CH_4} = \frac{x_{confined,C_2H_6}/x_{confined,CH_4}}{x_{bulk,C_2H_6}/x_{bulk,CH_4}} \tag{2.49}$$

This selectivity is calculated in the adsorbed layers of the vapor and the liquid phase. As expected we obtain a symmetric profile where particles accumulate close to the wall surface. The adsorbed layer is defined as the first minima or the last value before the plateau of the density profile. The layer length is 0.6 nm and 0.5 nm for the vapor and liquid phase respectively. Our results give a selectivity of $S_{C_2H_6/CH_4}$=1.17 for the vapor phase and $S_{C_2H_6/CH_4}$=0.81 for the liquid phase. It means that compared to bulk, ethane is preferentially adsorbed in the vapor phase, whereas methane is preferentially adsorbed in the liquid phase of the confined system.

The confined NVT simulation initialized by the NPT BPMC ensemble has allowed us to calculate thermodynamic properties of confined methane/ethane mixture and build a phase dia-

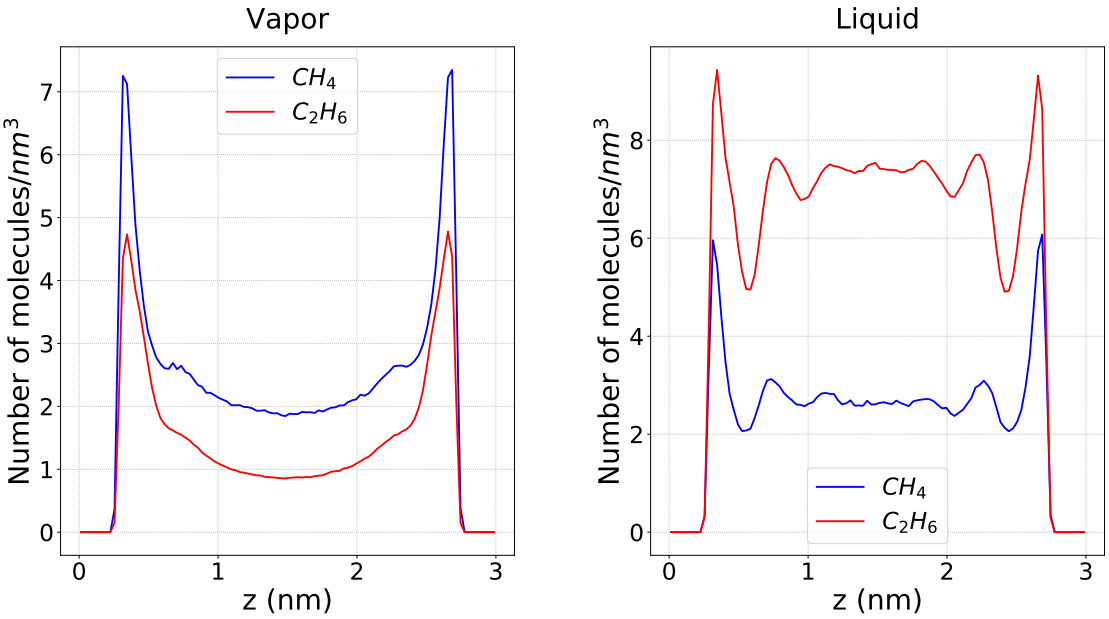

Figure 2.15: Local z density profile of methane/ethane in a 3 nm slit pore at 220 K and 2 MPa for vapor (left) and liquid (right) for an initial composition of 39.5% methane molar fraction and 60.5% ethane molar fraction.

gram with the bulk pressure as reference for the thermodynamic equilibrium. In order to validate the method, the same workflow will be applied to another mixture and confined pressures will be calculated.

Ethane/*n*-Pentane

We applied the same approach as in Section 2.4.2 to simulate the behavior of the mixture $C_2H_6 - C_5H_{12}$ for five isotherms: 320 K, 330 K, 340 K, 350 K, 360 K and 370 K. The results of the pressure versus density of the mixture are shown Figure 2.16. The details of the simulation parameters and data post treatment are provided in Appendix A.1 and Section 2.1.7 and as explained previously in Section 2.4.2, all the results presented come from the Gibbs ensemble NVT simulations.

Similar to the previous case, the vapor density increases and the liquid density decreases with confinement for all isotherms with respect to the non-confined bulk phase (see Figure 2.16). The critical pressure decreases with a value below the bulk value for all isotherms (see Figure 2.17). The pressure-molar fraction diagrams for different isotherms shown in Figure 2.17 allow the construction of a pressure-temperature diagram for a specific ethane/*n*-pentane concentration (59.7% ethane and 40.3% *n*-pentane) as can be seen in Figure 2.18. Regardless of the proportion of ethane and *n*-pentane in the mixture, the phase envelope of the confined fluid is shifted inwards and closes itself from its bulk value. The critical temperature and pressure are shifted from the

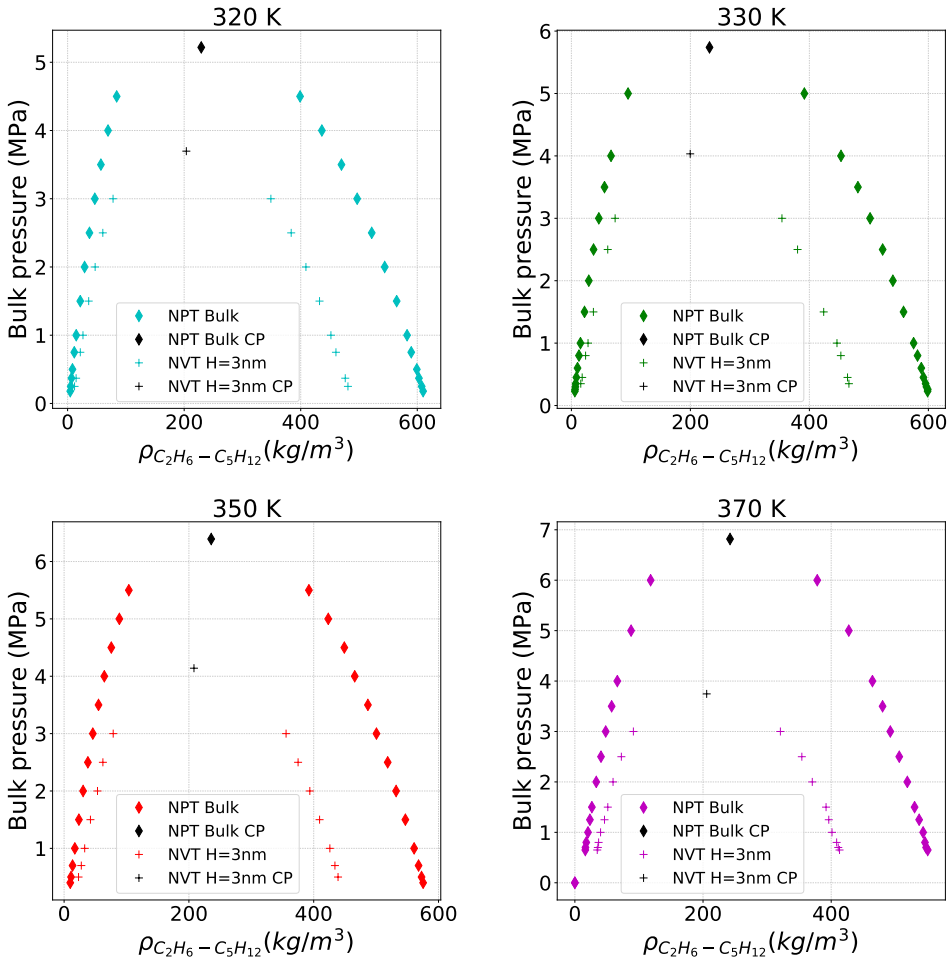

Figure 2.16: Comparison of pressure-density diagram of ethane/n-pentane for a bulk (diamond) and a confined fluid ('+') for different isotherms. CP refers to critical point.

bulk value to a lower value and the bubble-point pressure decreases as the dew-point pressure increases.

An example of the density profile in the z direction for the ethane/n-pentane mixture at 340 K and 2 MPa is shown in Figure 2.19. The initial composition is made up of 50.4% ethane molar fraction and 49.6% n-pentane molar fraction, which gives at equilibrium the liquid molar fractions $x_{C_2H_6} = 0.351$, $x_{C_5H_{12}} = 0.649$ and the vapor molar fractions $y_{C_2H_6} = 0.758$, $y_{C_5H_{12}} = 0.242$. The vapor and liquid molar fraction values are coherent with Figure 2.19 where there is more methane in the vapor phase and more ethane in the liquid phase. Details of parameters and post-processing are given in Appendix A.1. Here again, the densities of molecules in the vapor and liquid phases are higher close to the walls due to fluid/wall interactions. In this case, the selectivity of the adsorbed layers of the confined system towards ethane and n-pentane compared to bulk can be calculated using Equation 2.50. The adsorbed layer length is 0.7 nm

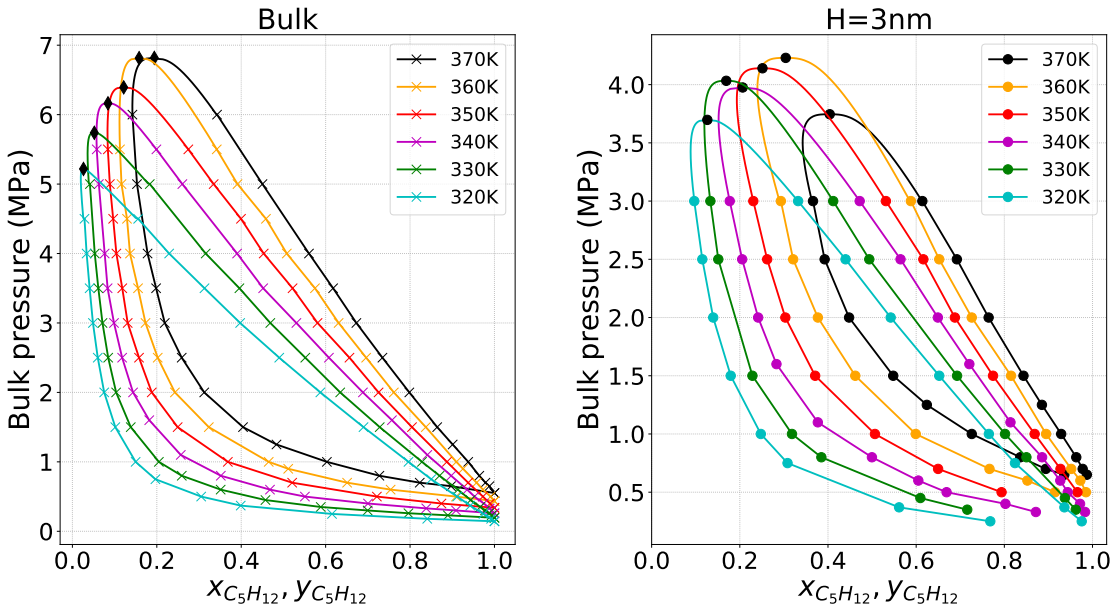

Figure 2.17: Pressure-molar fraction diagram of ethane/n-pentane for different isotherms for a bulk (left) and a confined fluid (right). The 'x' symbols correspond to bulk NPT results; the critical points of each isotherm are in black diamonds. The circles correspond to confined NVT results for H=3 nm; the critical points of each isotherm are in black circles.

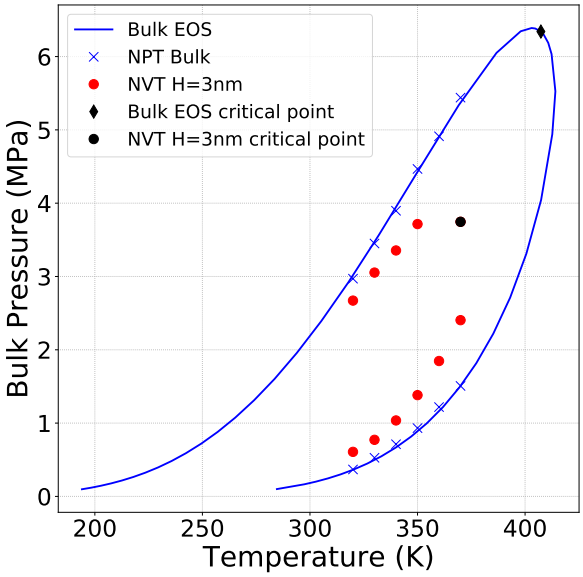

Figure 2.18: Example of a Pressure-Temperature diagram for a mixture of 59.7% of ethane and 40.3% of n-pentane. The blue line correspond to EOS Peng Robinson results with the critical point in black diamond. The 'x' symbols correspond to bulk NPT results and the red circles correspond to confined NVT results for H=3nm with the critical point in black.

and 0.6 nm for the vapor phase and the liquid phase respectively. The results give a selectivity of $S_{C_5H_{12}/C_2H_6}$= 1.16 for the vapor phase and $S_{C_5H_{12}/C_2H_6}$= 0.7 for the liquid phase. It means that compared to bulk, n-pentane is preferentially adsorbed in the vapor phase of the confined system, whereas ethane is preferentially adsorbed in the liquid phase.

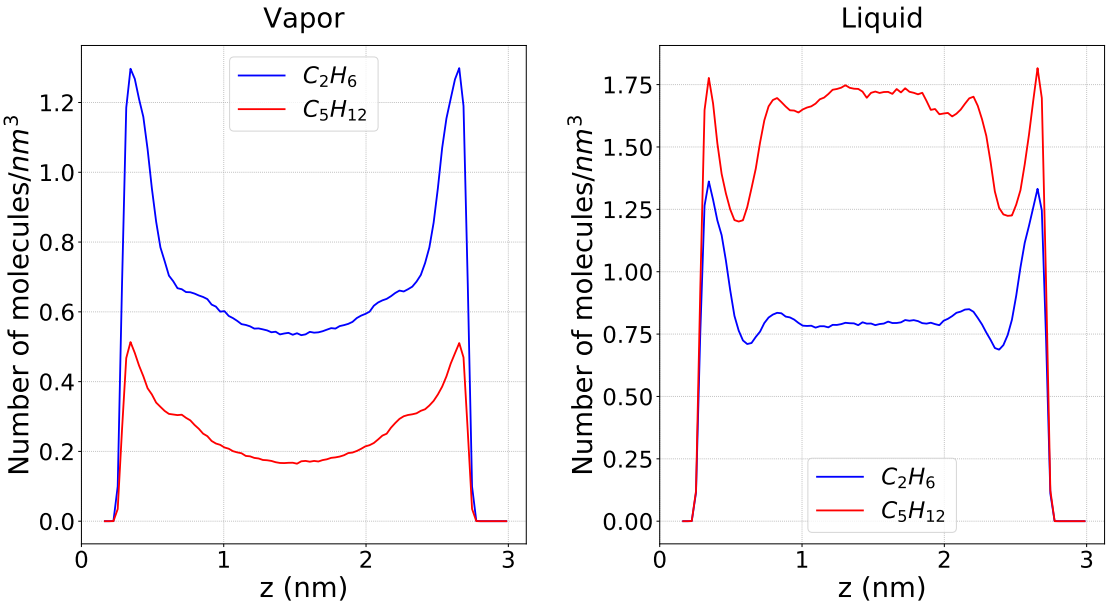

Figure 2.19: Local z density profile of ethane/n-pentane in a 3 nm slit pore at 340 K and 2 MPa for vapor (left) and liquid (right) for an initial composition of 50.4% ethane molar fraction and 49.6% n-pentane molar fraction.

$$S_{C_5H_{12}/C_2H_6} = \frac{x_{confined,C_5H_{12}}/x_{confined,C_2H_6}}{x_{bulk,C_5H_{12}}/x_{bulk,C_2H_6}} \tag{2.50}$$

A pressure-molar fraction diagram of ethane/n-pentane mixture at 320K for bulk and confined fluid is given in Figure 2.20. The green curve corresponds to the saturation pressure of the bulk fluid (${P_{bulk}}^{sat}$) versus n-pentane molar fraction, the blue curves give the pressures of a bulk fluid connected to a confined fluid when the first bubble appears in the confined fluid (${P_{bulk}}^{sat\ conf}$) and the red and the orange curves give respectively the vapor (${P_{conf}}^{v}$) and liquid pressure (${P_{conf}}^{l}$) of the confined fluid connected to a bulk fluid as explained in Figure 2.5. All these pressures are different but only ${P_{bulk}}^{sat\ conf}$, ${P_{conf}}^{v}$ and ${P_{conf}}^{l}$ are at the same thermodynamic equilibrium state, i.e. the same chemical potential (dash line in Figure 2.20). In order to compare bulk fluid and confined fluid (see Section 2.2), bulk pressure can be used as the reference in both systems: a single bulk fluid and a bulk fluid, thermodynamically connected to a confined fluid. Then the comparison between ${P_{bulk}}^{sat}$ and ${P_{bulk}}^{sat\ conf}$ enables to say that the bubble point is decreased with confinement. This conclusion cannot be applied to a system at the same thermodynamic equilibrium because confined liquid and vapor pressures are higher than the bulk pressure (Figure 2.20).

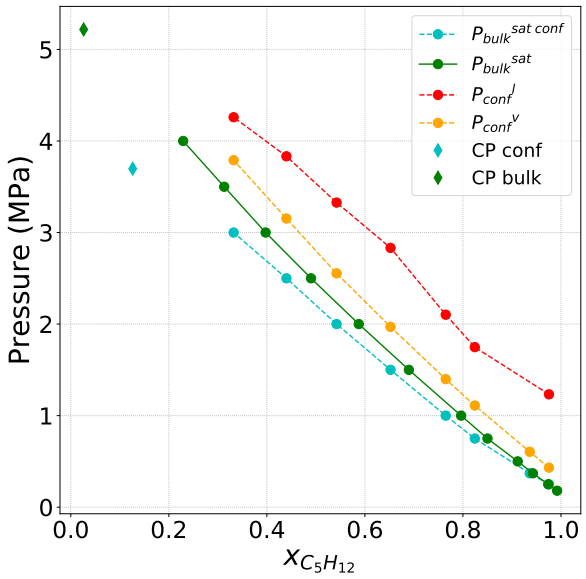

Figure 2.20: Pressures of ethane/n-pentane at 320 K and H=3 nm. $P_{bulk}{}^{sat\ conf}$ correspond to the bulk pressure of a bulk fluid in thermodynamic equilibrium with a confined fluid. Its critical point is 'CP conf'. $P_{conf}{}^{v}$ and $P_{conf}{}^{l}$ are vapor and liquid pressures of a confined fluid in thermodynamic equilibrium with a bulk fluid. $P_{bulk}{}^{sat}$ is the bulk pressure of a single bulk fluid with critical point 'CP bulk'.

The application of the workflow using GEMC NPT BPMC ensemble as an initialization of the confined NVT simulation has been applied to two mixtures and showing very good results. A Phase diagram of confined methane/ethane and ethane/n-pentane has been built with bulk pressure as reference. Furthermore confined vapor and liquid pressures for ethane/n-pentane have been calculated and compared to bulk pressure which is a total novelty.

2.5 Summary and discussions

The thermodynamic equilibrium properties of several pure components and mixtures in slit graphite pores have been calculated and analyzed. Furthermore, a detailed explanation and a calculation of the different pressures considered in a porous medium with nano-pores have been performed. The pure components studied were methane, ethane, n-pentane and n-decane. The mixtures studied were methane/ethane and ethane/n-pentane.

In this work, the confined GEMC NVT simulation has been used instead of the more traditional GCMC simulation because of its limitations. The GCMC simulation could lead indeed

to some errors in the liquid/vapor equilibrium properties because of the challenge in identification of chemical potential phase change. Furthermore the GCMC simulation is not able to give accurate values of confined liquid and vapor pressure. As the GEMC NVT simulation considers two confined boxes for each phase, the accuracy of the results is considerably improved. Since the GEMC NVT needs a good initialization in order to converge, two different workflows for pure components and mixtures have therefore been proposed to overcome this problem. The confined GCMC μVT simulation is used getting approximate initial vapor and liquid densities of pure components for confined GEMC NVT simulation. A new ensemble: the Gibbs ensemble constant temperature and pressure Monte Carlo with bubble-point movement (GEMC NPT BPMC) has been used for the initialization of the confined GEMC NVT simulation for mixtures. The mixture workflow is divided into three steps. The first step uses the standard Gibbs ensemble Monte Carlo at constant pressure and temperature (GEMC NPT). If no experimental data is available, it establishes the bulk saturated liquid equilibrium used in the bulk liquid box of the GEMC NPT BPMC simulation. In addition, this method can serve as a validation of the quality of the force field to reproduce the phase bahavior of the studied system. In the GEMC NPT BPMC simulation, two boxes are in thermodynamic equilibrium, the bulk box and the confined box. This simulation allows to get approximate values of densities and molar fraction of each components in each phase. These values are finally used to initialize the confined GEMC NVT simulation. Besides giving the thermodynamic properties of a confined fluid at equilibrium, this workflow allows us to make the link between the bulk fluid pressure and the confined vapor and liquid pressures of a confined fluid. Even if the workflow contains several steps, it can be ealsily implemented by scripts that automatically concatenate the successive simulations. Overall, the final process is less time consuming than a random or heuristic search of initial conditions for the GEMC NVT simulations.

For all pure components considered in this study, the vapor density increases and the liquid density decreases with confinement compared to the bulk. The critical temperature and pressure are reduced as the pore width decreases and they approach to the bulk values at large pore sizes. However the evolution of critical temperature and pressure versus pore size follow different trends and should be treated with different correlations. Unlike the bulk fluid, where vapor and liquid pressure are equal at equilibrium, confined fluids have different vapor and liquid pressures. The change of sign of capillary pressure as the pore size decreases attests to a more complex behavior where the standard Laplace equation is no longer valid and disjoining pressure may occur [13, 27]. For the two mixtures studied regardless of the composition, the observations for density are the same as for pure components. The vapor density increases and the liquid density decreases with confinement compared to the bulk. The pressure versus molar fraction diagrams allowed us to build an example of a pressure versus temperature diagram for a specific composition. The phase envelope of the confined fluid is shifted inwards and closes with respect to phase envelope of bulk fluid. The critical temperature and pressure are shifted from the bulk value to a lower value. Finally the bubble-point pressure decreases as the dew-point

pressure increases. The selectivity of the confined system compared to bulk for the mixtures methane/ethane and ethane/n-pentane in a given thermodynamic conditions has been studied. The observations are that the heavier component is preferentially adsorbed in the vapor phase, whereas the lighter component is preferentially adsorbed in the liquid phase. That is to say that compared to bulk fluid, the composition at liquid/vapor equilibrium of the confined fluid has heavier components in the vapor phase and lighter components in the liquid phase than the bulk fluid composition. Finally the different pressures of ethane/n-pentane in a 3nm pore size have been calculated and compared to bulk. As mentioned in Section 2.2 two systems were in reality compared: a single bulk fluid and a bulk fluid in thermodynamic equilibrium with a confined fluid. Only one pressure is present in the first system: the bulk pressure of single bulk fluid. Three different pressures are present in the second system: the bulk pressure of a bulk fluid in thermodynamic equilibrium with a confined fluid, the confined vapor pressure and the confined liquid pressure. The calculation and comparison of the different pressures observed in the confined systems is one of the main contribution of the present work and it is, to the best of our knowledge, a novelty in this field.

All these results for pure components and mixtures provide relevant information concerning the understanding of the phase behavior in confined systems such as shale gas and tight oil reservoirs. This behavior is completely different compared to the bulk fluid. Furthermore, all these data may be used as reference values for the development of radius dependent EOS calibration.

Chapter 3

Thermodynamic modeling

This Chapter aims to firstly give detailed explanations of the thermodynamic behavior modeling obtained with EOS of fluid with and without confinement. Several equations and phase equilibrium algorithms will be precisely described. After this methodology overview, the results of the different proposed algorithms will be compared with reference results of the molecular simulation obtained in Chapter 2 for two mixture examples confined in a 3 nm slit pore. Finally the best method to model the confined fluid thermodynamic behavior will be highlighted according to the match with reference molecular simulation results.

3.1 Vapor-liquid equilibrium calculation without confinement

A flash calculation is the determination of the equilibrium between the vapor and the liquid phase for a given fluid at a certain temperature and pressure using an equation of state (EOS). Firstly the theory of EOS for pure components and mixtures will be presented. Then, the equilibrium calculation will be explained with its algorithm [2, 79].

3.1.1 EOS theory

An EOS is an analytical expression relating the pressure p, to the temperature T, and the molar volume V_m. Numerous EOS have been developed and improved. The best known and the simplest EOS is the ideal gas equation. The general form of the EOS is expressed in the following equation:

$$p = p_{repulsion} - p_{attraction} \tag{3.1}$$

where p is the pressure. The expression of the two pressures $p_{repulsion}$ and $p_{attraction}$ depends on the EOS.

Cubic equations of state, such as Peng and Robinson [91] EOS are routinely used in the Oil&Gas industry for compositional reservoir simulations. This EOS will therefore be presented firstly for pure components and after for mixtures. The Peng-Robinson EOS for pure components is:

$$p = \frac{RT}{V_m - b} - \frac{a\alpha(T)}{V_m(V_m + b) + b(V_m - b)} \tag{3.2}$$

The parameters used in Equation 3.2 for pure components are detailed in the Table below:

Table 3.1: Peng-Robinson EOS parameters for pure components

$p_{repulsion}$	$p_{attraction}$	a	b	Ω_a	Ω_b
$\frac{RT}{V_m - b}$	$\frac{a\alpha(T)}{V_m(V_m+b)+b(V_m-b)}$	$\Omega_a \frac{R^2 T_c^2}{P_c}$	$\Omega_b \frac{RT_c}{P_c}$	0.45724	0.0778

where:

$$\begin{cases} \alpha(T) & = (1 + m(1 - \sqrt{T_r}))^2 \\ T_r & = \frac{T}{T_c} \end{cases} \tag{3.3}$$

and

$$\begin{aligned} m &= 0.3796 + 1.54226\omega - 0.2699\omega^2, \ if \ \omega \leq 0.49 \\ m &= 0.379642 + 1.48503\omega - 0.1644\omega^2 + 0.016667\omega^3, \ if \ \omega > 0.49 \end{aligned} \tag{3.4}$$

with P_c: critical pressure, T_c: critical temperature, ω: acentric factor, R: ideal gas constant, V_m: the molar volume.

The Peng-Robinson EOS (Equation 3.2) can be expressed in a more practical form in term of the compressibility factor: $Z = \frac{pV_m}{RT}$.

$$Z^3 + (B-1)Z^2 + (A - 3B^2 - 2B)Z - (AB - B^2 - B^3) = 0 \tag{3.5}$$

The expression of the coefficient A and B are given in Table 3.2

The cubic EOS (Equation 3.5) can be solved analytically using the Cardan procedure for example (Appendix B). Like all cubic EOS, the resolution yields to one real root in the one-phase region and three real roots in the two-phase region. In the two phase region, the Gibbs free energy criteria allows to pick the two correct physical roots. The right root is selected on

Table 3.2: Cubic Peng-Robinson EOS parameters for pure components

A	B
$\frac{(a\alpha)p}{R^2T^2}$	$\frac{bp}{RT}$

the basis of whichever minimizes the Gibbs energy the most. The largest root corresponds to the compressibility factor of the gas phase and the smallest positive root to that of the liquid.

The above Peng-Robinson EOS is valid for pure components. To express these equations for mixtures some nomenclatures must be defined. The mole fraction of a component i in a mixture of mole n is given by:

$$z_i = \frac{n_i}{n} = x_i L + y_i V \tag{3.6}$$

with z_i: mole fraction of component i in the mixture, n: mole of the mixture, n_i: mole of component i in the mixture, x_i: molar fraction of the component i in the liquid phase, y_i: molar fraction of the component i in the vapor phase, L: molar fraction of the liquid phase, V: molar fraction of the vapor phase.

The expression of x_i, y_i, L and V are given Table 3.3.

Table 3.3: molar fraction equations

x_i	y_i	L	V
$\frac{n_{il}}{n_l}$	$\frac{n_{iv}}{n_v}$	$\frac{n_l}{n}$	$\frac{n_v}{n}$

with n_l: mole of liquid in the mixture, n_v: mole of vapor in the mixture, n_{il}: mole of the component i in the liquid phase of the mixture, n_{iv}: mole of the component i in the vapor phase of the mixture.

By definition of the total mole fraction in a mixture:

$$\begin{cases} \sum_i x_i = 1 \\ \sum_i y_i = 1 \\ \sum_i z_i = 1 \\ L + V = 1 \end{cases} \tag{3.7}$$

Cubic Peng-Robinson EOS formulation for mixtures is expressed for liquid and vapor phase by:

$$Z^3 + (B_m - 1)Z^2 + (A_m - 3B_m^2 - 2B_m)Z - (A_m B_m - B_m^2 - B_m^3) = 0 \tag{3.8}$$

with the coefficients expressed using the Van der Waals mixing rules detailed in the following Table 3.4. The coefficient A_m and B_m are different for liquid and vapor. Then two cubic Peng-Robinson EOS must be solved.

Table 3.4: Cubic formulation of EOS for mixture

A_m	B_m		$(a\alpha)_m$	b_m
$\frac{(a\alpha)_m p}{R^2T^2}$	$\frac{b_m p}{RT}$	Liquid	$\sum_i \sum_j x_i x_j \sqrt{a_i a_j \alpha_i \alpha_j}(1 - k_{ij})$	$\sum_i x_i b_i$
		Vapor	$\sum_i \sum_j y_i y_j \sqrt{a_i a_j \alpha_i \alpha_j}(1 - k_{ij})$	$\sum_i y_i b_i$

k_{ij} is an empirically determined correction factor which is called the binary interaction coefficient. These coefficients are used to model the intermolar interactions through empirical adjustment of the $(a\alpha)_m$. a_i, α_i and b_i have the same form as pure components (Table 3.1) but are function of critical properties T_{ci} and P_{ci} and acentric factor ω_i of each component i of the mixtures as detailed in Table 3.5 and Equation 3.9.

Table 3.5: Peng-Robinson EOS parameters for mixture

a_i	b_i	α_i	T_{ri}
$\Omega_a \frac{R^2 T_{ci}^2}{P_{ci}}$	$\Omega_b \frac{RT_{ci}}{P_{ci}}$	$(1 + m_i(1 - \sqrt{T}_{ri}))^2$	$\frac{T}{T_{ci}}$

$$\begin{aligned} m_i &= 0.3796 + 1.54226\omega_i - 0.2699\omega_i^2, \ if \ \omega_i \leq 0.49 \\ m_i &= 0.379642 + 1.48503\omega_i - 0.1644\omega_i^2 + 0.016667\omega_i^3, \ if \ \omega_i > 0.49 \end{aligned} \tag{3.9}$$

Peng-Robinson EOS can be improved by introducing a volume correction parameter c_i. This parameter does not change the vapor/liquid equilibrium calculation. It modifies the liquid and gas volumes. The volume translation method uses the following expressions:

$$V_{corr}^l = V_m^l - \sum_i x_i c_i \tag{3.10}$$

$$V_{corr}^v = V_m^v - \sum_i y_i c_i \tag{3.11}$$

with $V_m^l = \frac{Z^l RT}{p}$: uncorrected liquid molar volume, $V_m^v = \frac{Z^v RT}{p}$: uncorrected vapor molar

volume, V^l_{corr}: corrected liquid molar volume, V^v_{corr}: corrected vapor molar volume, c_i can be calculated by the correlation of Péneloux et al. [90] for example:

$$c_i = (0.0115831168 + 0.411844152\omega_i)\frac{T_{ci}}{P_{ci}} \tag{3.12}$$

3.1.2 Phase equilibrium calculation: standard TP flash

A PT flash is a calculation whose aim is to determine how a feed stream having a molar composition z_i splits into two phases, i.e. a liquid phase and a vapor phase at defined pressure (p) and temperature (T). The main goal in this calculation is the determination of the outstreams composition, in other words the liquid and vapor compositions. Considering a flash drum, where it is known the system pressure (p), temperature (T) and the feed composition (z_i), it is feasible to solve the flash calculations using a combination of correlations given by the mass balance and the liquid-vapor equilibrium correlations.

In a multicomponent mixture, the component fugacity in each phase is introduced to develop a criterion for thermodynamic equilibrium. Fugacity can be interpreted physically as a potential for transfer of a component between phases. For example if a component i has a lower fugacity in the liquid than in the vapor phase, the transfer of the component i will occur from the vapor to the liquid phase. Therefore, the condition of the thermodynamic equilibrium can be expressed by:

$$f^v_i = f^l_i,\ 1 \leq i \leq n_{comp} \tag{3.13}$$

with f^l_i: fugacity of the component i in the liquid phase, f^v_i: fugacity of the component i in the vapor phase, n_{comp}: number of components in the system

The fugacity coefficient of component i in a mixture is defined for liquid (Equation 3.14) and vapor (Equation 3.15) as:

$$\Phi^l_i = \frac{f^l_i}{x_i p^l} \tag{3.14}$$

$$\Phi^v_i = \frac{f^v_i}{y_i p^v} \tag{3.15}$$

At equilibrium ($f^v_i = f^l_i$), the ratio, $K_i = \frac{y_i}{x_i}$, can be redefined in terms of fugacity coefficient (Equation 3.16) because capillary pressure is considered negligible for large pores ($p^v = p^l$) [114].

$$K_i = \frac{y_i}{x_i} = \frac{f^v_i/(\Phi^v_i p^v)}{f^l_i/(\Phi^l_i p^l)} = \frac{\Phi^l_i}{\Phi^v_i} \tag{3.16}$$

The fugacity coefficients are calculated from the following expressions:

$$ln(\Phi_i^l) = \frac{b_i(Z^l-1)}{b_m} - ln(Z^l - B_m) - \frac{A_m}{2\sqrt{2}B_m}\left(\frac{2\Psi_i}{(a\alpha)_m} - \frac{b_i}{b_m}\right) ln\left(\frac{Z^l + (1+\sqrt{2})B_m}{Z^l - (1-\sqrt{2})B_m}\right) \quad (3.17)$$

$$ln(\Phi_i^v) = \frac{b_i(Z^v-1)}{b_m} - ln(Z^v - B_m) - \frac{A_m}{2\sqrt{2}B_m}\left(\frac{2\Psi_i}{(a\alpha)_m} - \frac{b_i}{b_m}\right) ln\left(\frac{Z^v + (1+\sqrt{2})B_m}{Z^v - (1-\sqrt{2})B_m}\right) \quad (3.18)$$

$$\Psi_i = \sum_j x_j \sqrt{a_i a_j \alpha_i \alpha_j (1-k_{ij})} \quad (3.19)$$

The variables Z^l and Z^v comes from the Peng-Robinson EOS resolution.

The equilibrium ratio of the component i is defined as: $K_i = \frac{y_i}{x_i}$. By definition, we have: $x_i = \frac{z_i}{L+VK_i}$ and $y_i = \frac{z_i K_i}{L+VK_i}$. Since $\sum_i y_i - \sum_i x_i = 0$, then replacing L by $1-V$, we get the Rachford-Rice equation:

$$\sum_i \frac{(K_i - 1)z_i}{1 + V(K_i - 1)} = 0 \quad (3.20)$$

This equation allows to calculate V knowing K_i and then x_i and y_i.

All these equations are used for the liquid-vapor equilibrium calculation in the algorithm presented in Section 3.1.4. This algorithm is also called a flash calculation.

3.1.3 Saturation point calculation

In order to save CPU time calculation, the equilibrium flash calculation is only done if the fluid has two phases. Then dew-point pressure and bubble point pressure at a given temperature are determined in order to know if the flash calculation is needed.

For a given temperature, the dew-point pressure p_d is the pressure at which an infinitesimal amount of liquid first appears. It is described mathematically by: $y_i = z_i$, and V=1, then $\sum_i \frac{z_i}{K_i} = 1$ and $\sum_i \frac{z_i}{K_i} = \sum_i \frac{z_i}{\Phi_i^l/\Phi_i^v} = \sum_i \frac{z_i f_i^v}{\Phi_i^l z_i p_d} = 1$, which gives:

$$p_d - \sum_i \frac{f_i^v}{\Phi_i^l} = 0 \quad (3.21)$$

This equation can be solved by the Newton-Raphson method [2].

For a given temperature, the bubble-point pressure p_b is the pressure at which the first bubble of gas is formed. It is described mathematically by: $x_i = z_i$ and $L = 1$, then $\sum_i z_i K_i = 1$ and

$$p_b - \sum_i \frac{f_i^l}{\Phi_i^v} = 0 \tag{3.22}$$

This equation can also be solved by the Newton-Raphson method [2]. For information, Michelsen [78] proposed another method where a system of $n_{comp} + 2$ equations has to be solved, with n_{comp} being the number of components. But this method is not used in this thesis.

3.1.4 Algorithm of the standard flash in a reservoir simulation

A flash calculation is an algorithm combining the liquid-vapor equilibrium equations using EOS with the component mass balance equations. It allows to calculate the ratio K_i at liquid-vapor equilibrium and then determine the liquid-vapor properties of the fluid at thermodynamic equilibrium. The initial condition of the thermodynamic flash are the pressure p, the temperature T and the mixture composition of the feed defined by z_i. This information comes from the reservoir simulation. In addition, the properties of the i^{th} components of the fluid must be defined. These properties are: acentric factor ω_i, critical pressure P_{ci}, critical temperature T_{ci}, binary interaction coefficient k_{ij} and molar mass M_i. In a compositional reservoir simulation, the flash is performed in each cells at each time step. As the flash calculation is very time consuming, the saturation point calculation is firstly performed to know if the fluid is monophasic or biphasic at the initial conditions. In a case of two phase condition, the flash calculation is performed. As the flash method used is a two-phase negative flash [31], no Gibbs energy phase stability test is needed before the liquid/vapor equilibrium calculation. Figure 3.1 illustrates the flash algorithm which aims to determine the equilibrium ratio of a mixture.

- Step 1: the initialization step assumes a first value of K_i for each components i. This starting value comes from the Wilson's equation:

$$K_i^A = \frac{P_{ci}}{p} exp\left(5.37(1+\omega_i)\left(1 - \frac{T_{ci}}{T}\right)\right) \tag{3.23}$$

- Step 2: The Rachford Rice equation (3.20) is solved to determine the vapor molar fraction V. This equation is solved by a combination of the Newton Raphson and binary search method. If the solution does not convergence after 20 Newton-Raphson iterations, the binary search method is applied. The procedure adopted is the negative flash developed by Curtis H.Whitson and Michael L.Michelsen [31]. Then unphysical values of molar fraction (V or L higher than 1 or lower than 0) are considered as they still give physical values for x_i and y_i. The solution V is between $V_{min} = \frac{1}{1-max(K_i)}$ and $V_{max} = \frac{1}{1-min(K_i)}$ which represent the limits of the binary search method. The solution V gives $L = 1 - V$, $x_i = \frac{z_i}{L+VK_i}$ and $y_i = \frac{z_i K_i}{L+VK_i}$.

- Step 3: The cubic EOS (Equation 3.8) is solved for vapor and liquid pressure to give Z^l and Z^v. Then the fugacity coefficients Φ_i^l and Φ_i^v are determined using the equations of

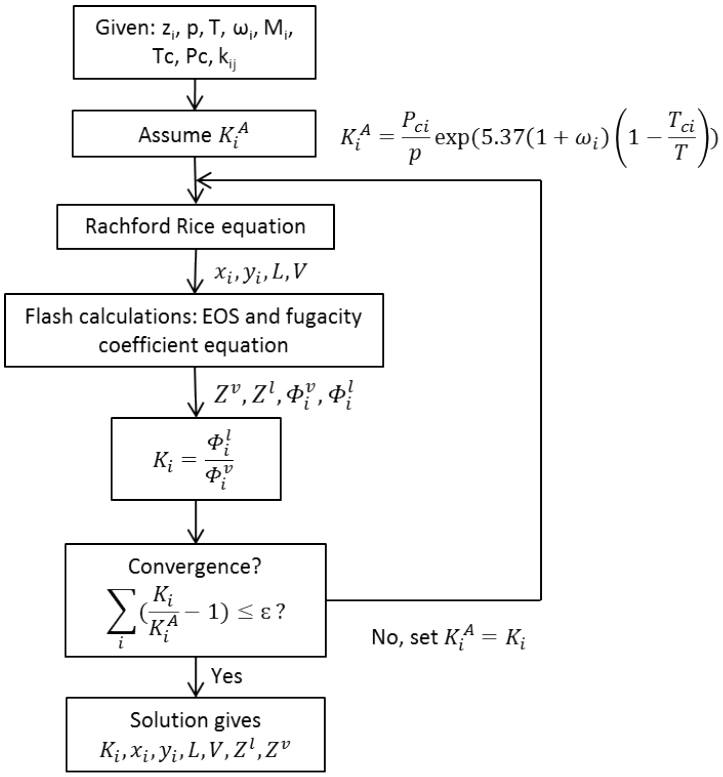

Figure 3.1: Classic multi-components flash calculation algorithm [2]

fugacity coefficient (Equations 3.18 and 3.19).

- Step 4: The new equilibrium ratio is calculated $K_i = \frac{\Phi_i^l}{\Phi_i^v}$.
- Step 5: If the condition $\sum_i \left(\frac{K_i}{K_i^A} - 1\right) \leq \epsilon$ is satisfied, then the convergence has been reached. If not, step 2 through 5 are repeated with the new K_i value. The value of K_i is calculated by assuming its formulation at equilibrium (Equation 3.16) when the fugacities of each component in each phase are equal. Then if this value converges, it corresponds to the equilibrium value.

The flash calculation gives the equilibrium ratio of each components: K_i, the molar fraction of each components in each phases: x_i and y_i, the molar fraction of each phase: L and V and the compressibility factor of liquid and vapor phase: Z^l and Z^v. These parameters allow to calculate densities and saturations of oil and gas for the flow calculation in the reservoir simulator.

$$\begin{cases} \rho_g = \frac{p}{Z^v RT} \\ \rho_o = \frac{p}{Z^l RT} \end{cases} \tag{3.24}$$

$$\begin{cases} \rho_{mass\_g} = \sum_i y_i M_i \rho_g \\ \rho_{mass\_o} = \sum_i x_i M_i \rho_o \end{cases} \tag{3.25}$$

$$\begin{cases} S_g = \frac{V^v}{V^v+V^l} = \frac{(Vn)/\rho_g}{(Vn)/\rho_g+(Ln)/\rho_o} = \frac{V}{V+\frac{\rho_g}{\rho_o}L} \\ S_o = \frac{L}{L+\frac{\rho_o}{\rho_g}V} \end{cases} \tag{3.26}$$

with ρ_g: the molar density of vapor (mol/m^3), ρ_o: the molar density of liquid (mol/m^3), ρ_{mass_g}: the mass density of vapor (g/m^3), ρ_{mass_o}: the mass density of liquid (g/m^3), S_g: the gas saturation, S_o: the oil saturation, V^v: volume of vapor, V^l: volume of liquid. We consider that there are no mole exchange between hydrocarbon components and water. Then, in presence of water, the equations 3.26 are multiplied by $(1 - S_w)$, with S_w the water saturation.

3.2 Vapor-liquid equilibrium calculation with confinement

Different methods to model the thermodynamic behavior of confined fluid using EOS have been developed in the literature as explained in the introduction Section 1.4.2. In the following subsections, the approaches utilized in this work, i.e. flash with capillary pressure, flash with critical point shift and flash with saturation dependent capillary pressure are presented in details. The different equations and the steps of the algorithms will be clearly described.

3.2.1 Flash with capillary pressure

Phase equilibrium calculation

As explained in the introduction Section 1.4.2, a lot of authors have included capillary pressure in the flash calculation in order to model the thermodynamic behavior of a confined fluid [6, 42, 45, 103, 107, 121, 124, 152, 155]. Based on the different approaches used by the authors, a flash algorithm is proposed in this section with some improvement according to the convergence issues. The different steps and equations will be detailed.

In a confined fluid, liquid and vapor pressure are no longer considered equal. Their difference is represented by the capillary pressure, which is modeled by the Young-Laplace equation (Equation 1.2). The same cubic Peng-Robinson EOS (equation 3.8) is used to model the confined fluid but with different coefficients A_m and B_m for liquid and vapor (Table 3.6).

The proposed flash algorithm is illustrated in figure 3.2. The initial condition are the same as for the flash without confinement. In addition, we need to set a pore radius r, a contact angle θ and the reference pressure. In this work the contact angle θ is considered to be zero for all the simulations, and the reference pressure is considered to be the pressure of the liquid as mass conservation equation resolution in compositional reservoir simulators is generally performed for oil. The different steps are detailed below.

Table 3.6: Cubic formulation of EOS for mixture

	A_m	B_m	$(a\alpha)_m$	b_m
Liquid	$\frac{(a\alpha)_m p^l}{R^2T^2}$	$\frac{b_m p^l}{RT}$	$\sum_i \sum_j x_i x_j \sqrt{a_i a_j \alpha_i \alpha_j}(1-k_{ij})$	$\sum_i x_i b_i$
Vapor	$\frac{(a\alpha)_m p^v}{R^2T^2}$	$\frac{b_m p^v}{RT}$	$\sum_i \sum_j y_i y_j \sqrt{a_i a_j \alpha_i \alpha_j}(1-k_{ij})$	$\sum_i y_i b_i$

- Step 1: The initial value of K_i is computed by the Wilson's equation (3.23) for each components i and capillary pressure is considered to be zero initially.
- Step 2: The Rachford-Rice equation (3.20) is solved to get molar fraction of each components in each phases as for standard flash.
- Step3: The cubic Peng-Robinson EOS (Equation 3.8) is solved for liquid and vapor phases to get Z^l and Z^v. Then the fugacity coefficients Φ_i^l and Φ_i^v are determined using the equations of fugacity coefficient (Equations 3.17 and 3.18).
- Step 4: The interfacial tension is calculated by the parachor model of Zuo and Stenby [159] (Equation 1.4). Then capillary pressure p_c is calculated by the Young-Laplace equation (Equation 1.2).
- Step 5: The new equilibrium ratio K_i is calculated as a function of capillary pressure (Equation 1.3)
- Step 6: The convergence of fugacity and capillary pressure is checked. If the convergence is achieved, then the solution has been reached. If not, steps 2 to 5 are repeated with the new K_i value. The update of the capillary pressure in the loop follows an under-relaxation scheme in order to avoid convergence issues, especially during reservoir simulations. Indeed the Rachford-Rice equation (3.20) has a physical solution only if one of the K_i is higher than one [31]. Considering the formulation of the update of K_i (Equation 1.3), the value of the capillary pressure cannot be too high in an iteration step for the flash calculation. In our algorithm, the capillary pressure is increased gradually by a factor of $\frac{1}{\alpha}$ in the iterations. The value of α generally used is 10.

saturation point calculation

The saturation point calculation allows to know whether or not the mixture fluid is monophasic or biphasic for a given pressure and temperature condition. Therefore this step will activate the flash calculation step if the fluid is biphasic. This calculation is different from the one presented in Section 3.1.3 because of capillary pressure. From the phase equilibrium condition, there are the following relations: $\sum_i y_i = \sum_i \frac{f_i^v}{\Phi_i^v p^v} = \sum_i \frac{f_i^l}{\Phi_i^v p^v} = 1$, then $\sum_i \frac{f_i^l}{\Phi_i^v} = \sum_i \frac{\Phi_i^l x_i p^l}{\Phi_i^v} = p^v = p^l + p_c$ Finally, we obtain the following iterative relation for the bubble point calculation where $z_i = x_i$ is considered:

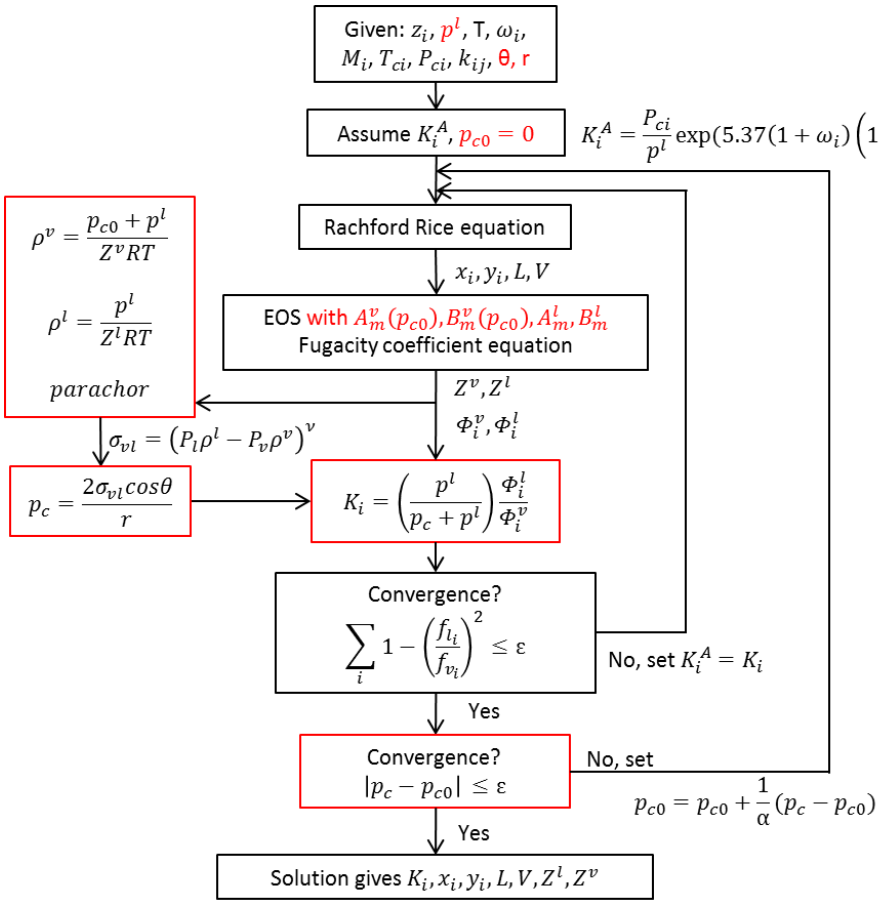

Figure 3.2: Algorithm of flash with capillary pressure

$$p^l_{iter+1} = p^l_{iter} \sum_i \frac{\Phi_i^l z_i}{\Phi_i^v} - p_c(x_i, y_i) \tag{3.27}$$

The same method can be used to determine the dew-point:

$$p^g_{iter+1} = p^g_{iter} \sum_i \frac{\Phi_i^v z_i}{\Phi_i^l} - p_c(x_i, y_i) \tag{3.28}$$

where the index *iter* is the iterative step to solve the equation. Another method is proposed by Sandoval et al. [107] who have adapted the work of Michelsen [78] taking into account the capillary pressure.

3.2.2 Flash with shift of critical point

As explained in introduction Section 1.4.2, the flash with shift of critical point is the second main method used in the literature [34, 6, 52, 106, 124, 35, 45]. This method does not need a

modification of the standard flash explained in Section 3.1.4. Only the input parameters such as critical temperature T_{ci} and critical pressure P_{ci} have to be modified for each components i and a given pore size. The challenge is to get accurate correlations of the evolution of critical properties versus pore size. Thanks to the molecular simulation study (Section 2.4.1), two correlations, one for critical temperature and one for critical pressure have been validated using molecular simulation results as reference (Figure 2.9). The correlation of Jin et al. [52] (Equation 1.10) is used for critical temperature and the one from Meyra et al. [77] (Equation 1.8) is used for critical pressure evolution versus pore size. These correlations have been validated for pure components. In order to know if the pure component correlations are extensible for mixture, i.e. they can model the critical point of the mixtures numerically by the mean of the EOS, a comparison with molecular simulation results for methane/ethane and ethane/n-pentane mixture obtained in Section 2 is performed.

The critical pressures and temperatures for the different mixtures of methane/ethane for a bulk fluid and a confined fluid are shown in Figure 3.3. Regardless of the mixture, the confined fluid (represented in red) always has a smaller value of the critical pressure and critical temperature than the bulk fluid (represented in blue). The results from molecular simulation (represented by crosses) have been compared to critical-point calculations described by Peng-Robinson EOS using the PVTFlow^{TM} software (IFPEN-Beicip-KAPPA partnership [55]). Pure component critical pressure and temperature of methane and ethane for a 3 nm slit width calculated from Meyra et al. [77] and Jin et al. [52] correlations respectively have been used to model numerically, by EOS, the critical point of the confined fluid. A critical point is identified whenever a point of the phase envelope has an equilibrium constant equal to unity. The bulk values of critical pressure and temperature between GEMC NPT simulation (blue crosses) and EOS calculation (blue line) are quite close as can be seen in Figure 3.3. Concerning the confined fluid, the numerical results obtained from EOS (red line) show the same trend as the results obtained by molecular simulation (red crosses).

Critical temperature and pressure calculated by molecular simulation and EOS based methodology have also been compared for the ethane/n-pentane mixture Figure 3.4. The critical pressure and temperature of ethane and n-pentane confined in a 3 nm slit pore obtained from Meyra et al. [77] and Jin et al. [52] correlations respectively, have been used as an input for the PVTFlow^{TM} software. It aims to model numerically the mixture critical point of the confined fluid. The bulk values of critical temperature and pressure obtained from GEMC NPT results and EOS calculation are very close (blue crosses and line respectively). Concerning the results for the confined fluid, we observe a better agreement of both approaches for the critical temperature than the critical pressure.

For a given pore size, the critical temperature and pressure values of pure components have been used to model numerically the critical point of methane/ethane and ethane/n-pentane

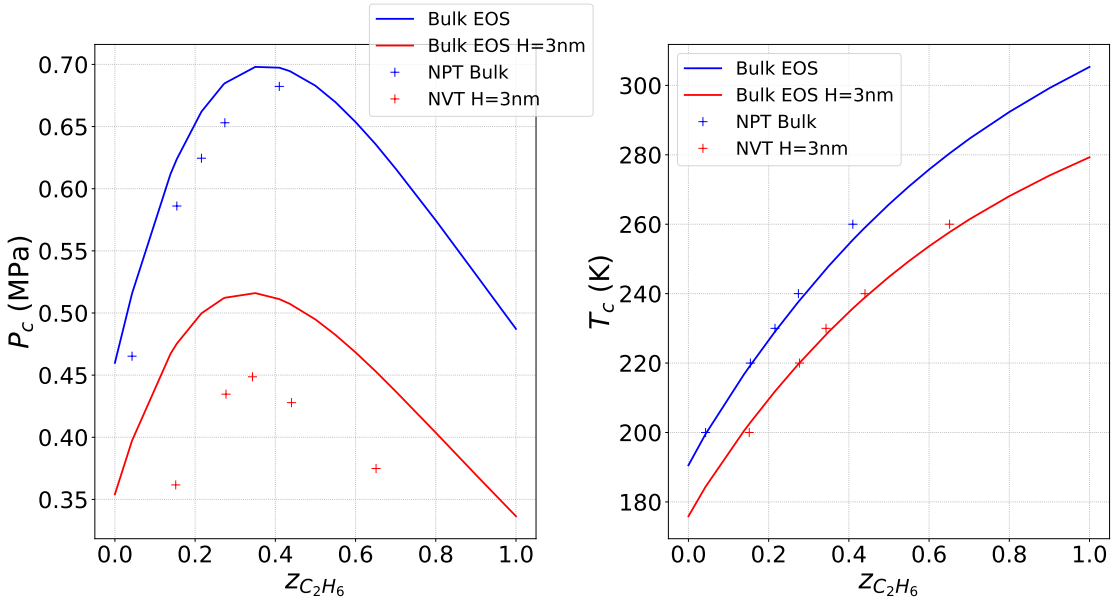

Figure 3.3: Evolution of critical pressure (left) and temperature (right) of methane/ethane mixture versus ethane molar fraction for bulk and confined fluid. The blue line corresponds to numerical results obtained from Peng-Robinson EOS for the bulk fluid. The red line corresponds to numerical results obtained from Peng-Robinson EOS with critical temperature and pressure shift from Jin et al. [52] and Meyra et al. [77] correlations respectively. The blue '+' symbols correspond to critical point NPT results for bulk and the red ones correspond to critical point NVT results for confined fluid in H=3 nm pore length.

mixtures by the mean of a EOS. These calculated results have been compared to the reference critical point of mixtures obtained through the use of molecular simulations. The numerical model using EOS results is consistent with the molecular simulation results for mixtures. Therefore the method used by several authors [6, 45, 124, 35, 34, 52, 106] to model the confined fluid by adding shift of critical pressure and temperature of pure components in the flash calculation is reliable concerning the critical point calculation. The pure component correlations of Jin et al. [52] for critical temperature and Meyra et al. [77] for critical pressure shift calculation can also be used to model the critical point of mixtures numerically by the mean of the EOS.

The two methods of flash with capillary pressure and shift with critical point can also be used together. In that case the correlations are used to calculate critical pressure and temperature for a specific pore size, then these input values are used in the flash with capillary pressure detailed in Section 3.2.1.

3.2.3 Flash with saturation dependent capillary pressure

The two previous flash described in Section 3.2.1 and 3.2.2 aim to model the thermodynamic properties of a confined fluid for a given pore size. Some authors have proposed methodologies

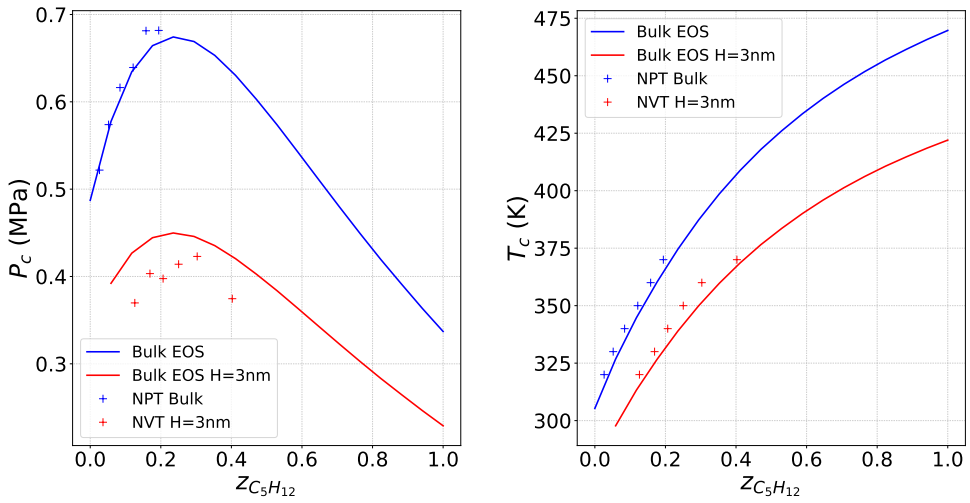

Figure 3.4: Evolution of critical pressure (left) and temperature (right) of ethane/n-pentane mixture versus n-pentane molar fraction for bulk and confined fluid. The blue line corresponds to numerical results obtained from Peng-Robinson EOS for the bulk fluid. The red line corresponds to numerical results obtained from Peng-Robinson EOS with critical temperature and pressure shift from Jin et al. [52] and Meyra et al. [77] correlations respectively. The blue symbols '+' correspond to critical point NPT results for bulk and the red ones correspond to critical point NVT results for confined fluid in H=3 nm pore length.

to account for the pore size distribution instead of a specific pore size in the flash calculation [67, 66, 84, 143, 152] (Section 1.5.2). The idea is to consider the capillary pressure function of the wetting saturation using an effective radius for example. The pore size distribution is taken into account in the effective radius function $r_K(S_o)$.

The effective pore radius versus oil saturation is built from a volumetric pore-size distribution. A pore radius size distribution is not always volumetric but a volumetric distribution can be found through a transformation. For example, if capillary tubes are considered, a tube of radius r has a volume $\pi r^2 L$ with L the length of the tubes. Therefore the radius squared distribution allows to obtain the volumetric pore size distribution. In order to move from a probability density function of r to a probability density function of r^2, a transformation is required. Let R be the random variable of the pore radius with $f_r(x)$ as the density function. The probability function of the random variable $U = R^2$ is calculated by:

$$P(U \leq u) = P(R^2 \leq u) = P(R \leq \sqrt{u}) = \int_0^{\sqrt{u}} f_r(x)dx = \int_0^u \frac{f_r(\sqrt{y})}{2\sqrt{y}}dy \tag{3.29}$$

So, the density function of the squared radius is given by:

$$f_{r^2}(u) = \frac{f_r(\sqrt{u})}{2\sqrt{u}} \tag{3.30}$$

Then the oil saturation function of the effective radius $S_o(r_K)$ is the normalized cumulative distribution function (CDF) of f_{r^2}. If initial water saturation is taken into account, the general equation is:

$$S_o(r_K) = (1 - S_{wi}) \frac{CDF_{f_{r^2}}(r_K)}{CDF_{f_{r^2}}(r_{K\_max})} \tag{3.31}$$

If spherical pores are considered, the distribution of the random variable $U = R^3$ should be computed. An example of effective radius is shown Figure 3.5 for a pore size distribution modeled by a lognormal distribution of mean 3 and standard deviation of 1 for pore sizes between 0 and 100 nm.

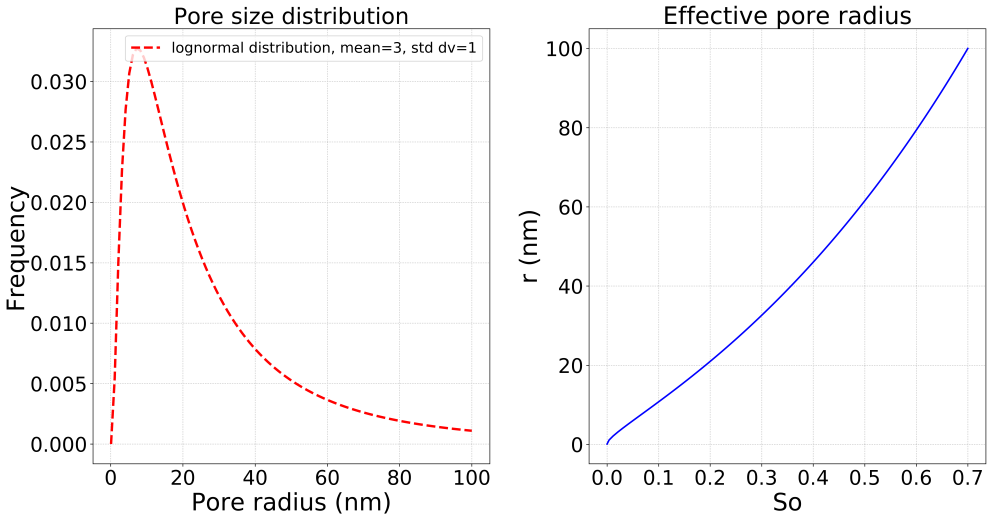

Figure 3.5: Example of effective radius for a PSD modeled by a lognormal distribution of mean 3 and standard deviation of 1 for pore sizes between 0 and 100 nm.

The flash algorithm described in Figure 3.6 is based on Li et al. [67] work. The inputs are the same as the flash with capillary pressure (Section 3.2.1) except that the radius is replaced by the effective radius for a given oil saturation. The oil saturation input comes from the reservoir simulation results at a given time step and cell. The capillary pressure is initially considered equal to zero and not calculated by the Young-Laplace equation. The different steps of the algorithm are very similar to the flash with capillary pressure (3.2.1) except that the capillary pressure loop is replaced by the effective radius loop. The oil saturation calculated by the flash after fugacity convergence is used to calculate the effective radius thanks to the input function of effective radius versus oil saturation. The effective radius is compared to its value at the previous steps and this process is repeated until the convergence of the effective radius value.

This flash method aims to provide the thermodynamic properties of a confined fluid for

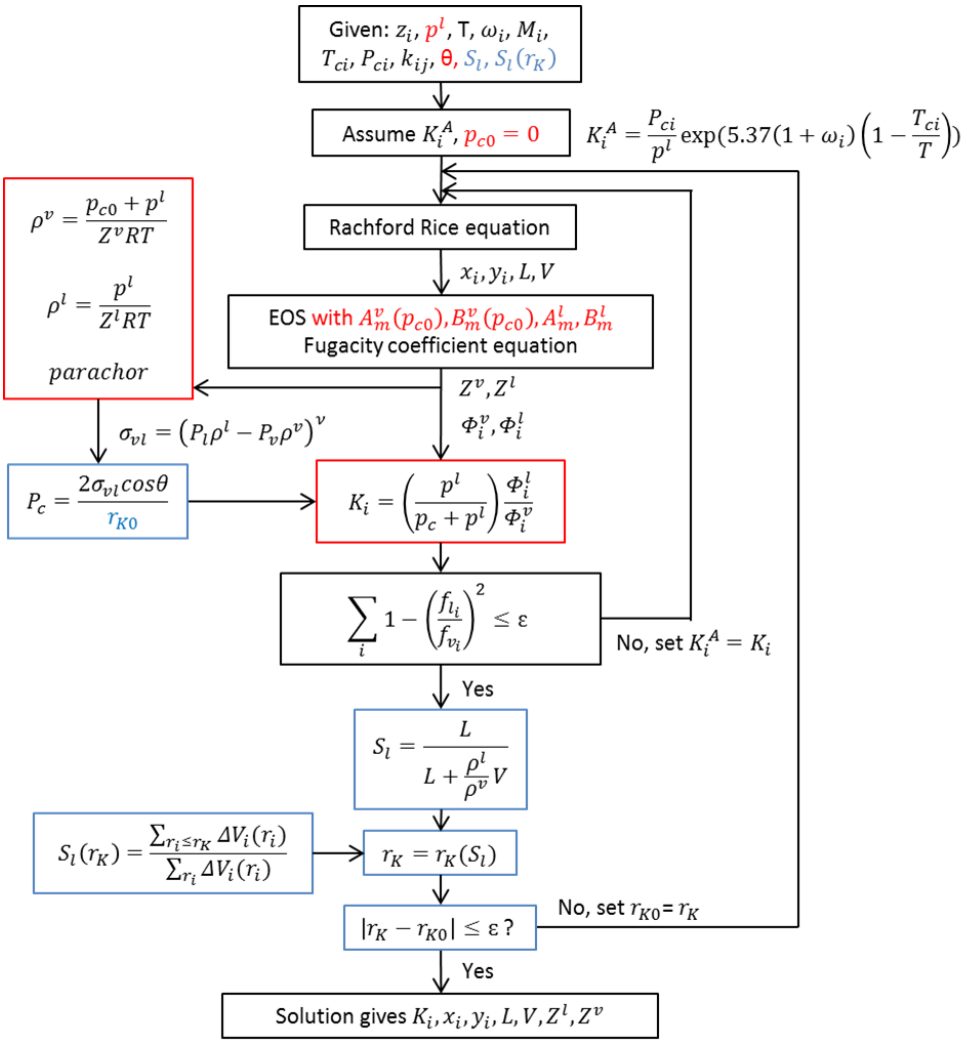

Figure 3.6: Algorithm of flash with saturation dependent capillary pressure

a given pore size distribution. The molecular simulations are considered as reference here to evaluate the different flash methodologies used in the literature. The molecular simulations were performed for a given pore size, then only the flash with capillary pressure and the flash with critical point shift will be evaluated thanks to the molecular simulation results in the following part.

3.3 Comparison with molecular simulation results

The thermodynamic properties at liquid/vapor equilibrium of confined hydrocarbon mixtures obtained using molecular simulation (chapter 2) are considered as reference data for the evaluation of the different EOS modification presented in Section 3.2.1 and 3.2.2. The effect of

confinement on fluid properties, already analyzed in Chapter 2 can be observed in Figure 3.7 and 3.8. The bulk results are represented in black crosses and the confined fluid results are represented in red circles. The vapor density increases and the liquid density decreases with confinement (Figure 3.7 and 3.8 right). The critical pressure decreases with a value bellow the bulk value and the bubble point decreases whereas the dew point increases with confinement (Figure 3.7 and 3.8 left). The three main methods used in the literature such as flash with capillary pressure, flash with shift of critical point and flash with both methods used together have been compared with molecular simulation results for methane/ethane in a 3 nm slit pore at 240K (Figure 3.7) and for ethane/n-pentane in a 3 nm slit pore at 370K (Figure 3.8).

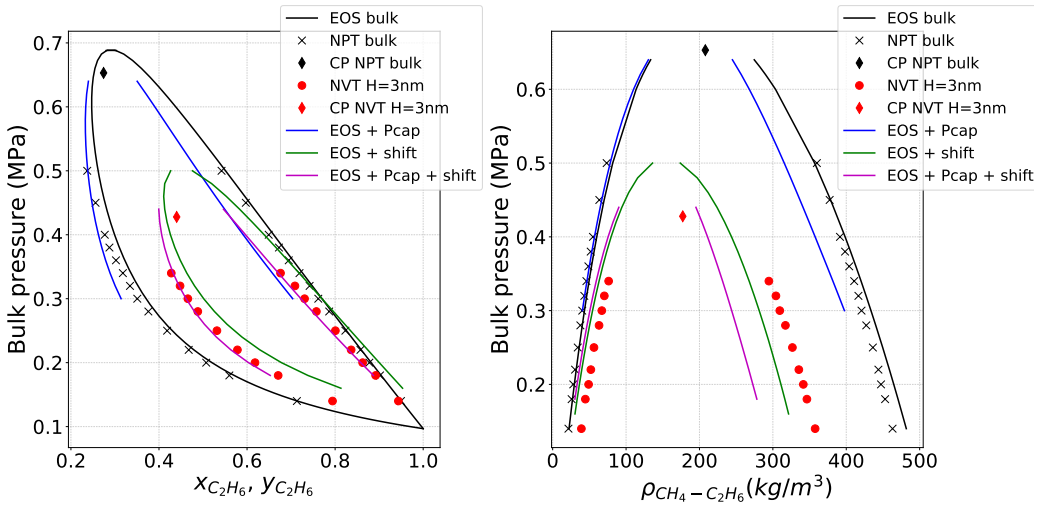

Figure 3.7: Comparison of EOS modifications with molecular simulation results for methane/ethane mixture at 240K in a 3nm slit pore. EOS + Pcap corresponds to a flash with capillary pressure with a 3nm pore length. EOS + shift corresponds to a flash with shift of critical pressure and temperature following the Meyra et al. [77] and Jin et al. [52] correlation respectively with a 3nm pore length. EOS + Pcap + shift corresponds to both methods used at the same time.

The Peng-Robinson EOS (black curves) match very well the molecular simulation results for a bulk fluid. The objective here is to find a good modified EOS which has the best possible match with confined molecular results. For the flash simulations with capillary pressure, gas pressure is used as reference in the algorithm (Figure 3.2) instead of oil because the mixtures are mainly composed of light components. In comparison with the results for a bulk fluid (black curves), the results using the flash with capillary pressure method (blue curves) show a lower bubble point and dew point. The phase envelope is like rotating around the bulk critical point. The critical point is constant with confinement because the fluid is monophasic in that state and then capillary pressure is equal to zero. Vapor density is almost the same than the bulk fluid and liquid density decreases compared to the bulk fluid. The flash with critical point shift

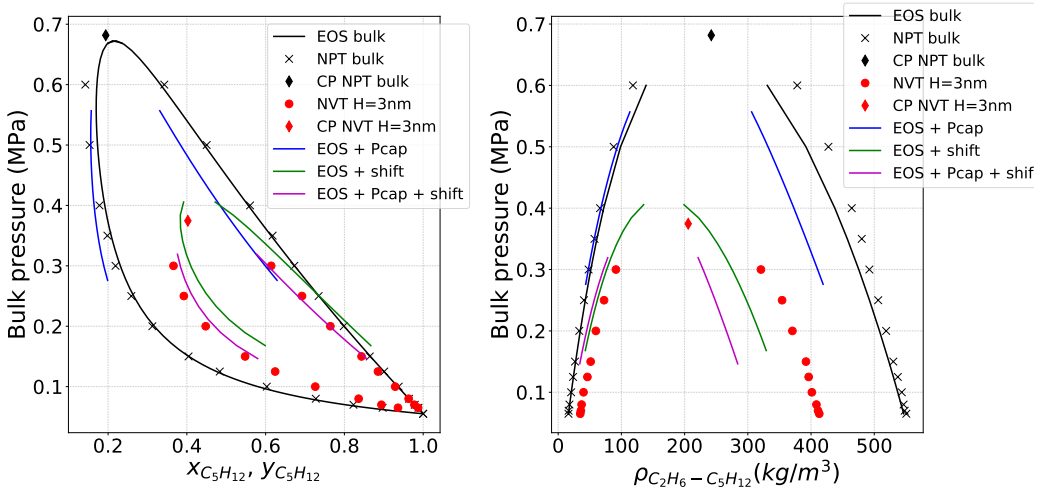

Figure 3.8: Comparison of EOS modifications with molecular simulation results for ethane/n-pentane mixture at 370K in a 3nm slit pore. EOS + Pcap corresponds to a flash with capillary pressure with a 3nm pore length. EOS + shift corresponds to a flash with shift of critical pressure and temperature following the Meyra et al. [77] and Jin et al. [52] correlation respectively with a 3nm pore length. EOS + Pcap + shift corresponds to both methods used at the same time.

(green curves) uses two different correlations for critical temperature and pressure as explained in Section 3.2.2. The bubble point decreases or increases compared to the bulk fluid according to the mixture composition and the dew point increases. The vapor density increases and the liquid density decreases compared to the bulk fluid. Overall the flash with shift of critical point gives better results than the flash with capillary pressure for these two examples. But the method of flash with capillary pressure and shift of critical properties (purple curve) is the most suitable method for matching the reference molecular simulation data of methane/ethane and ethane/n-pentnae in 3 nm slit pore (red circles). For the two mixtures studied, the match is very good for the phase envelope but some improvement must be done for the density. A volume correction such as Péneloux et al. [90] which is independent of the flash calculation can be used. However, this modification is out of the scope of the present thesis.

3.4 Summary and discussions

This section provided a detailed explanation and understanding of the thermodynamical modeling of fluid using EOS with and without confinement. The Peng-Robinson EOS for pure components and mixtures and the classic two phase flash algorithm have been detailed. Different thermodynamical models for confined fluid have been presented either for a fixed pore radius or a pore size distribution using an effective pore radius.

The flash with capillary pressure needs a modification of the standard flash in order to take into account the capillary pressure modeled by the Young-Laplace equation with a Parachor model for the interfacial tension. Two loops are necessary in the flash, a loop for the fugacity convergence and a loop for the capillary pressure convergence. Therefore the time of calculation is increased. Furthermore an under-relaxation scheme for the capillary pressure is included in the capillary pressure loop. Instead of using the new capillary pressure calculated, an average with the last iteration value is used. This method enables to treat convergence issues that can occur in the Rachford Rice equation resolution. At least one of the equilibrium ratio of the different component must be above one in order to have a solution. If the capillary pressure is too high, this problem can occur because of the formulation of the update of the equilibrium ratio. In summary this method is necessary to improve convergence issue especially in a compositional reservoir simulation. The flash with critical point shift does not need a modification of the standard flash without confinement. Only the input values such as critical temperature and critical pressure must be given as a function of the pore radius. The correlation of Meyra et al. [77] for pure component critical temperature and the correlation of Jin et al. [52] for pure component critical pressure have been validated with the reference molecular simulation results (chapter 2). They are therefore used to model the evolution of the pure component critical properties versus pore size. Moreover, they are able to get accurate critical point of confined fluid. Indeed mixture critical point obtained numerically by the mean of EOS are similar to the reference confined critical point from molecular simulation. The two methods of flash with capillary pressure and shift of critical points can be used together using a flash with capillary pressure and input values of critical pressure and temperature obtained by the correlations cited above. The flash with saturation dependent capillary pressure take into account the pore size distribution instead of a given pore size radius. The algorithm is similar to the flash with capillary pressure with one loop for the fugacity convergence and one loop for the effective radius convergence.

In order to evaluate the different thermodynamic behavior models for a confined fluid proposed in the literature, a comparison with reference values from the molecular simulation has been done. Two mixtures have been used: methane/ethane and ethane/n-pentane in a 3 nm slit pore. For the two examples at given temperature, the best match is obtained with a flash with both capillary pressure and critical point shift. The match is not perfect but this is until now the best method to model confined fluid PVT behavior. Some improvement must be done on the density which is independent on the flash, and one possible solution is to use volume corrections. To the best of our knowledge, this is the first time that the different flash methods for a confined fluid have been compared and analyzed with reference results from molecular simulation.

Chapter 4

Matrix/fracture interaction with pore size distribution

The flash with capillary pressure presented in Section 3.2.1 has been included in a reservoir simulator. The program is developed based on an existing compositional simulator MSFLOW_COM [151, 146]. In this Chapter, the mathematical model of the compositional simulator will be presented in Section 4.1 with its numerical resolution for a single porosity model in Section 4.2. Then some simulations for different matrix block geometries with different pore size distribution will be performed in Section 4.3. The results will be finally analyzed and discussed in Section 4.4.

4.1 Mathematical model

The single porosity compositional model is based on the mole conservation equation of every hydrocarbon component i and water.

$$\begin{cases} \frac{\partial M^i}{\partial t} = F^i + q^i \\ \frac{\partial M^w}{\partial t} = F^w + q^w \end{cases} \tag{4.1}$$

where i represents the hydrocarbon components (total number n_c) and w the water component.

The mass balance equation is evaluated by moles. The accumulation term M^i describes the variation of mole per unit of volume and time. It is equal to the mole flux exchange term F^i plus the internal sink/source term per unit of volume q^i for each component. We consider that there is no mass transfer between hydrocarbon (oil and gas) phases and water phase.

The accumulation term of the hydrocarbon components i and water is expressed by:

$$\begin{cases} M^i = \epsilon(\rho_o S_o x_i + \rho_g S_g y_i) \\ M^w = \epsilon \rho_w S_w \end{cases} \tag{4.2}$$

with ϵ: the reservoir porosity, ρ_o and ρ_g: the oil and gas molar densities, S_o and S_g: the oil and gas saturations, x_i and y_i: the oil and gas molar fraction of each components. ρ_w: water molar density, S_o: oil saturation.

The mole flux from molecular diffusion is considered negligible. Therefore the mole flux for each hydrocarbon components i and water is calculated from Darcy flow by the following equation:

$$\begin{cases} F^i = -\nabla \,.\, (\rho_o x_i \vec{v_o} + \rho_g y_i \vec{v_g}) \\ F^w = -\nabla \,.\, (\rho_w \vec{v_w}) \end{cases} \tag{4.3}$$

$\vec{v_\phi}$ is the Darcy velocity of each phase ϕ=o, g, w: oil, gas and water:

$$\vec{v_\phi} = \frac{k k_{r\phi}}{\mu_\phi} \nabla (p_\phi - \rho_\phi g Z_{res}) \tag{4.4}$$

with k: reservoir absolute permeability, $k_{r\phi}$: relative permeability of phase ϕ, μ_ϕ: viscosity of phase ϕ, p_ϕ: pressure of phase ϕ, g: gravity coefficient, Z_{res}: reservoir depth.

The water relative permeability in water-oil system $k_{rw}(S_w)$ and the gas relative permeability in gas-oil system $k_{rg}(S_g)$ are input parameters as a function of water saturation or gas saturation respectively. The input functions come from laboratory experiments or from correlations like Brooks and A. T. Corey [23]. The three phase relative permeabilities are then got by the Stone II model [123]. The model considers that the three phase water relative permeability is equal to the one in the two phase water-oil system $k_{rw}(S_w)$, the three phase gas relative permeability is equal to the one in the two phase gas-oil system $k_{rg}(S_g)$ and finally the three phase oil relative permeability is calculated using a correlation function of water and gas saturation $k_{ro}(S_w, S_g)$. The liquid and gas viscosities are calculated using the correlation from Lohrenz et al. [72]. This correlation is a function of the components properties (T_{ci} and p_{ci}), components molar fractions (x_i and y_i) and liquid and vapor densities. The viscosity of water is considered constant or implemented by a table.

In order to solve the equation system of mass conservation equations of each components, some additional relations are needed to close the system. These closure equations are saturation constraint (Equation 4.5), composition constraints (Equation 3.7, 3.20 and EOS) and capillary pressure functions.

$$S_o + S_w + S_g = 1 \tag{4.5}$$

$$\begin{cases} p_w = p_o - p_{cow}(S_w) \\ p_g = p_o + p_{cog}(S_g) \end{cases} \tag{4.6}$$

The water-oil capillary pressure $p_{cow}(S_w)$ and gas-oil capillary pressure p_{cog} are obtained from laboratories experiments or correlations. As oil pressure p_o is considered as reference, these funtions allow to calculate water and gas pressures p_w and p_g respectively. The oil-gas capillary pressure function used for the flow calculation is not necessarily the same as the one used in the flash calculation. For example in the flash presented in Section 3.2.1 the capillary pressure is calculated by the Young-Laplace equation (1.2). Typically the capillary pressure for the flow calculation and for the flash should be the same but more details will be given in Section 5.1.4 showing the consequences of considering a saturation dependent capillary pressure in the flash calculation.

4.2 Numerical methods

In this section, the governing equations of the flow of each fluid component presented in the previous Section 4.1 are discretized and solved using numerical methods. The design of the simulation program is also presented.

4.2.1 Equations discretization

The space discretization of the equation is performed using a finite-volume based method developed by Narasimhan and Witherspoon [82] and applied by Pruess [98]. The Figure 4.1 represents the space discretization and the geometry data used in the finite volume method. The left Figure represents an arbitrary representative elementary volume (REV) V_n or grid cell with its flux F_{nm} applied at each surface A_{nm}. The right figure described the geometry of two neighboring grid blocks of volume V_n and V_m separated by a distance of d_n and d_m from their interface of area A_{nm}.

The volumetric integration of the governing composition equations (4.1) over the REV V_n gives:

$$\iiint_{V_n} \frac{\partial \epsilon(\rho_o S_o x_i + \rho_g S_g y_i) dV}{\partial t} = \iiint_{V_n} -\nabla \,.\, (\rho_o x_i \vec{v_o} + \rho_g y_i \vec{v_g}) dV + \iiint_{V_n} q_i dV \tag{4.7}$$

The application of the divergence theorem converts the volume integral of the flux term into a surface integral:

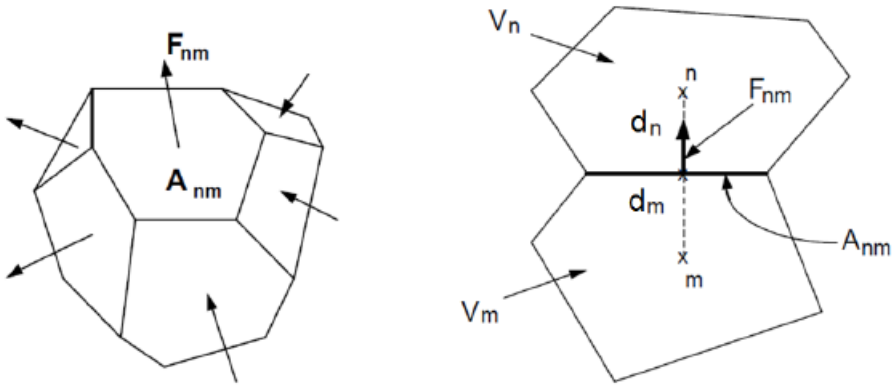

Figure 4.1: Space discretization and geometry data in the finite volume method, Pruess [98]

$$\iiint_{V_n} \frac{\partial \epsilon(\rho_o S_o x_i + \rho_g S_g y_i) dV}{\partial t} = \oiint_{\Gamma_n} -(\rho_o x_i \vec{v_o} + \rho_g y_i \vec{v_g}) \vec{n} d\Gamma + \iiint_{V_n} q_i dV \tag{4.8}$$

with Γ_n: the surface areas of the cells and $\vec{n}$: the unit vector normal to the surface where is applied the flux.

The Equation 4.8 can then be discretized in Equation 4.9. Volume integrals are replaced by volume average and surface integral is evaluated with discrete sum over surface average segments.

$$\frac{d[V_n \epsilon(\rho_o S_o x_i + \rho_g S_g y_i)]}{dt} = \sum_{m \in \eta_n} (\rho_o x_i \vec{v}_{o\_nm} + \rho_g y_i \vec{v}_{g\_nm}) \vec{n} A_{nm} + q_i V_n \tag{4.9}$$

with $\vec{v}_{o\_nm}$: oil flow from grid cell n to m, $\vec{v}_{g\_nm}$: gas flow from grid cell n to m, η_n: all neighboring cells directly connecting grid cell n and A_{nm}: the surface areas between them.

The time is discretized fully implicitly to assure stability and the Darcy equation (4.4) is applied for velocity. The above equation is then discretized in time and space with a two-point flux approximation scheme in the following equation:

$$\begin{aligned} &\frac{[V\epsilon(\rho_o S_o x_i + \rho_g S_g y_i)]_n^{t+1} - [V\epsilon(\rho_o S_o x_i + \rho_g S_g y_i)]_n^t}{\Delta t} = \\ &\sum_{m \in \eta_n} [(\rho_o x_i \lambda_o)_{nm+\frac{1}{2}}^{t+1} \gamma_{nm} (\Psi_{om}^{t+1} - \Psi_{on}^{t+1}) + (\rho_g y_i \lambda_g)_{nm+\frac{1}{2}}^{t+1} \gamma_{nm} (\Psi_{gm}^{t+1} - \Psi_{gn}^{t+1})] \\ &+ (V q_i)_n^{t+1} \end{aligned} \tag{4.10}$$

with $\lambda_\phi = \frac{k_{r\phi}}{\mu_\phi}$: the mobility of phase ϕ. The index $nm + \frac{1}{2}$ corresponds to the interface between

n and m and an upstream scheme is used for the mobility term. The index t + 1 is the current time step and t is the previous time step.

The transmissivity is given by:

$$\gamma_{nm} = \frac{A_{nm} k_{nm+\frac{1}{2}}}{d_n + d_m} \tag{4.11}$$

The flow potential including pressure and gravity term of phase ϕ for cell n is defined as:

$$\Psi_{\phi n}^{t+1} = p_{\phi n}^{t+1} - \rho_{\phi n+\frac{1}{2}}^{t+1} g Z_{resn} \tag{4.12}$$

with Z_res the reservoir depth.

The water component discretized equation is given as below:

$$\frac{(V\epsilon\rho_w S_w)_n^{t+1} - (V\epsilon\rho_w S_w)_n^t}{\Delta t} = \sum_{m\in\eta_n} (\rho_w \lambda_w)_{nm+\frac{1}{2}}^{t+1} \gamma_{nm} (\Psi_{om}^{t+1} - \Psi_{on}^{t+1}) + (V q_w)_n^{t+1} \tag{4.13}$$

For a grid block n of pressure $p_{\phi n}$ connected to a well with production pressure p_{well}, its sink/source term for hydrocarbon and water components can be evaluated by the following equations:

$$(q_i)_n^{t+1} = (\rho_o x_i \lambda_o)_n^{t+1} WI(p_{on}^{t+1} - p_{well}^{t+1}) + (\rho_g y_i \lambda_g)_n^{t+1} WI(p_{gn}^{t+1} - p_{well}^{t+1}) \tag{4.14}$$

$$(q_w)_n^{t+1} = (\rho_w \lambda_w)_n^{t+1} WI(p_{wn}^{t+1} - p_{well}^{t+1}) \tag{4.15}$$

where WI is the well index, mainly relating with the permeability and geometry of the grid block n, and the well skin factor.

The Equations 4.10 and 4.13 represent the final fully implicitly discretized equations of the compositional flow. They must be linearized in order to be solved numerically.

4.2.2 Numerical solution

The discretized Equation 4.10 and 4.13 for hydrocarbon component i and water w can be rewritten in term of residual forms $R_{i,n}^{t+1}$ and $R_{w,n}^{t+1}$ as bellow. The liquid and vapor molar fraction of each component are expressed in function of molar fraction z_i as $x_i = \frac{z_i}{L+VK_i}$ and $y_i = \frac{z_i K_i}{L+VK_i}$.

$$R_{i,n}^{t+1} = \frac{V\epsilon}{L+VK_i}\frac{(\rho_o S_o z_i + \rho_g S_g K_i z_i)_n^{t+1} - (\rho_o S_o z_i + \rho_g S_g K_i z_i)_n^t}{\Delta t} - \sum_{m\in\eta_n} \frac{\gamma_{nm}}{L+VK_i}[(\rho_o z_i \lambda_o)_{nm+\frac{1}{2}}^{t+1}(\Psi_{om}^{t+1} - \Psi_{on}^{t+1}) + (\rho_g K_i z_i \lambda_g)_{nm+\frac{1}{2}}^{t+1}(\Psi_{gm}^{t+1} - \Psi_{gn}^{t+1})] - (Vq_i)_n^{t+1} \quad (4.16)$$

$$R_{w,n}^{t+1} = \frac{(V\epsilon\rho_w S_w)_n^{t+1} - (V\epsilon\rho_w S_w)_n^t}{\Delta t} - \sum_{m\in\eta_n} (\rho_w\lambda_w)_{nm+\frac{1}{2}}^{t+1}\gamma_{nm}(\Psi_{om}^{t+1} - \Psi_{on}^{t+1}) - (Vq_w)_n^{t+1} \quad (4.17)$$

The residual Equations 4.16 and 4.17 are n_c+1 independent coupled non-linear equations for each grid cells of volume V_n. They represent the equation system to solve for the compositional flow.

According to the Gibbs phase rule, the number of degrees of freedom in a compositional system is $n_{comp}+2-n_\phi$, with n_{comp} the total number of components (hydrocarbon and water) and n_ϕ the number of phases. However the phase saturation constraint (Equation 4.5) adds $n_\phi - 1$ degrees of freedom. Furthermore if the system studied is isothermal, then the degree of freedom of temperature is removed. The minimum number of primary variables needed to be solved is therefore $n_{comp}+2-n_\phi+n_\phi-1-1 = n_{comp} = n_c+1$. The same number of independent equations are required to solve them. The primary variables chosen in this program are the water saturation, the oil pressure and overall molar fraction of the first n_c-1 components.

$$\vec{x}_n = \begin{bmatrix} S_w \\ p_o \\ z_1 \\ \vdots \\ z_{n_c-1} \end{bmatrix}^n \quad (4.18)$$

where $\vec{x}_n$ is the primary variable vector for grid block V_n.

The n_c+1 independent equations to solve the primary variables are Equations 4.16 and 4.17. The secondary variables are all the other fluid parameters considered in the system of equations. They can be determined from the primary variables. The flash calculation detailed in Section 3.1.4 and Section 3.2.1 needs primary variables such as overall molar fraction and oil pressure as input. Then overall liquid and vapor molar fraction L and V, liquid and vapor molar fraction of each components x_i and y_i and liquid and vapor molar densities ρ_o and ρ_g are calculated by the flash. Afterwards, oil and gas viscosities can be calculated thanks to the Lohrenz et al. [72] correlation and oil and gas saturation can be calculated thanks to the primary variable S_w and

Equations 3.26. Finally relative permeabilities and capillary pressures can be calculated using their saturation dependent functions. A summary of the different equations and variables used is given 4.1.

Table 4.1: Summary of variables and equations used

Equations	Primary variables	Secondary variables
$R_{i,n}^{t+1}$ (4.16)	p_o, z_1, ..., z_{n_c-1}	L, V, K_i, ρ_o, ρ_g, μ_o, μ_g, S_o, S_g, $k_{r\phi}$, p_{cow}, p_{cog}
$R_{w,n}^{t+1}$ (4.17)	S_w	

Lets define the system of non-linear equations 4.21 to solve at time step t+1 total number of grid blocks n_b. The unknown vector of the system equation $\vec{X}^{t+1}$ gathers the primary variables of all the grid blocks at time step t+1. The system of equation is composed of the equations 4.16 and 4.17 for every grid blocks.

$$\vec{X}^{t+1} = \begin{bmatrix} \vec{x}_1^{t+1} \\ \vdots \\ \vec{x}_{n_b}^{t+1} \end{bmatrix}_{n_b(n_c+1)} \tag{4.19}$$

$$\vec{R}_n^{t+1}(\vec{x_n}^{t+1}) = \begin{bmatrix} R_{1,n}^{t+1} \\ \vdots \\ R_{n_c,n}^{t+1} \\ R_{w,n}^{t+1} \end{bmatrix}_{n_c+1} \tag{4.20}$$

$$\vec{R}^{t+1}(\vec{X}^{t+1}) = \begin{bmatrix} \vec{R}_1^{t+1} \\ \vdots \\ \vec{R}_{n_b}^{t+1} \end{bmatrix}_{n_b(n_c+1)} = \vec{0} \tag{4.21}$$

This system of equations can be solved by the Newton-Raphson method. The Newton-Raphson scheme to solve the equation system 4.21 gives the equation below:

$$\mathbf{J}_{R^{t+1}}(\vec{X}_p^{t+1})(\vec{X}_{p+1}^{t+1} - \vec{X}_p^{t+1}) = -\vec{R}^{t+1}(\vec{X}_p^{t+1}) \tag{4.22}$$

where p is the Newton iteration of current time step t+1 and $\mathbf{J}_{R^{t+1}}$ is the Jacobian matrix defined bellow:

$$\mathbf{J}_{R^{t+1}}(\vec{X}_p^{t+1}) = \begin{bmatrix} \frac{\partial \tilde{R}_1^{t+1}(\vec{X}_p^{t+1})}{\partial \tilde{X}_{1,p}} & \cdots & \frac{\partial \tilde{R}_1^{t+1}(\vec{X}_p^{t+1})}{\partial \tilde{X}_{n_b(n_c+1),p}} \\ \vdots & \ddots & \vdots \\ \frac{\partial \tilde{R}_{n_b(n_c+1)}^{t+1}(\vec{X}_p^{t+1})}{\partial \tilde{X}_{1,p}} & \cdots & \frac{\partial \tilde{R}_{n_b(n_c+1)}^{t+1}(\vec{X}_p^{t+1})}{\partial \tilde{X}_{n_b(n_c+1),p}} \end{bmatrix}_{n_b(n_c+1)\times n_b(n_c+1)} \tag{4.23}$$

where $\tilde{R}_i^{t+1}$ is the coordinate i of the vector $\vec{R}^{t+1}$ and $\tilde{X}_i^{t+1}$ is the coordinate i of the vector $\vec{X}^{t+1}$.

The derivatives coefficients of the Jacobian matrix of coordinates (i,j) can be obtained with numerical differentiation method. A small incremental value $\Delta\tilde{X}_j$ is used to calculate the derivatives numerically. The secondary variables must be re-calculated with new primary variables $\vec{X}_p^{t+1} + \Delta\tilde{X}_j$ in the $\tilde{R}_i^{t+1}(\vec{X}_p^{t+1} + \Delta\tilde{X}_j)$ term. The derivatives can be obtained with sufficient accuracy with $\Delta\tilde{X}_j$ set as 10^{-6} to 10^{-8} of current value of $\tilde{X}_j$.

$$\frac{\partial\tilde{R}_i^{t+1}(\vec{X}_p^{t+1})}{\partial\tilde{X}_j} = \frac{\tilde{R}_i^{t+1}(\vec{X}_p^{t+1} + \Delta\tilde{X}_j) - \tilde{R}_i^{t+1}(\vec{X}_p^{t+1})}{\Delta\tilde{X}_j} \tag{4.24}$$

In summary the Newton iterative method allows to solve the unknown $\delta\vec{X}_p^{t+1} = \vec{X}_{p+1}^{t+1} - \vec{X}_p^{t+1}$ with the following equation.

$$\mathbf{J}_{R^{t+1}}(\vec{X}_p^{t+1})\delta\vec{X}_p^{t+1} = -\vec{R}^{t+1}(\vec{X}_p^{t+1}) \tag{4.25}$$

The Equation 4.25 represents the global linear system to solve using a solver to get $\delta\vec{X}_{p+1}^{t+1}$ at each newton iteration p and then the solution $\vec{X}^{t+1}$ at the time step t+1 after Newton convergence. The convergence criteria of the Newton iteration corresponds to the maximum of the residuals at iteration step p over the $n_b(n_c + 1)$ equations i:

$$max_i \left|\tilde{R}_i^{t+1}(\vec{X}_p^{t+1})\right| \leq \epsilon \tag{4.26}$$

4.2.3 Program implementation

The flow chart of the simulation run is presented Figure 4.2. The initial values of the primary variables come from the input values given by the user. Then initial secondary variables are calculated thanks to the flash calculation and the time loop starts. Each time steps generally require a lot of Newton iterations to converge. The Jacobian construction for each grid blocks needs to perform flash calculation in order to get the new secondary variables associated to the new primary variables used for the numerical differentiation (Equation 4.24). The linear system of equations coming from the Newton iteration scheme (Equation 4.22) is solved using a numerical solver. More details about the linear solver used can be founded in Wang [140]. Then the primary and secondary variables are updated for the next Newton iteration. This process is repeated until the Newton loop converges. Afterwards the Newton loop is performed for a new time step until reaching the total simulation time.

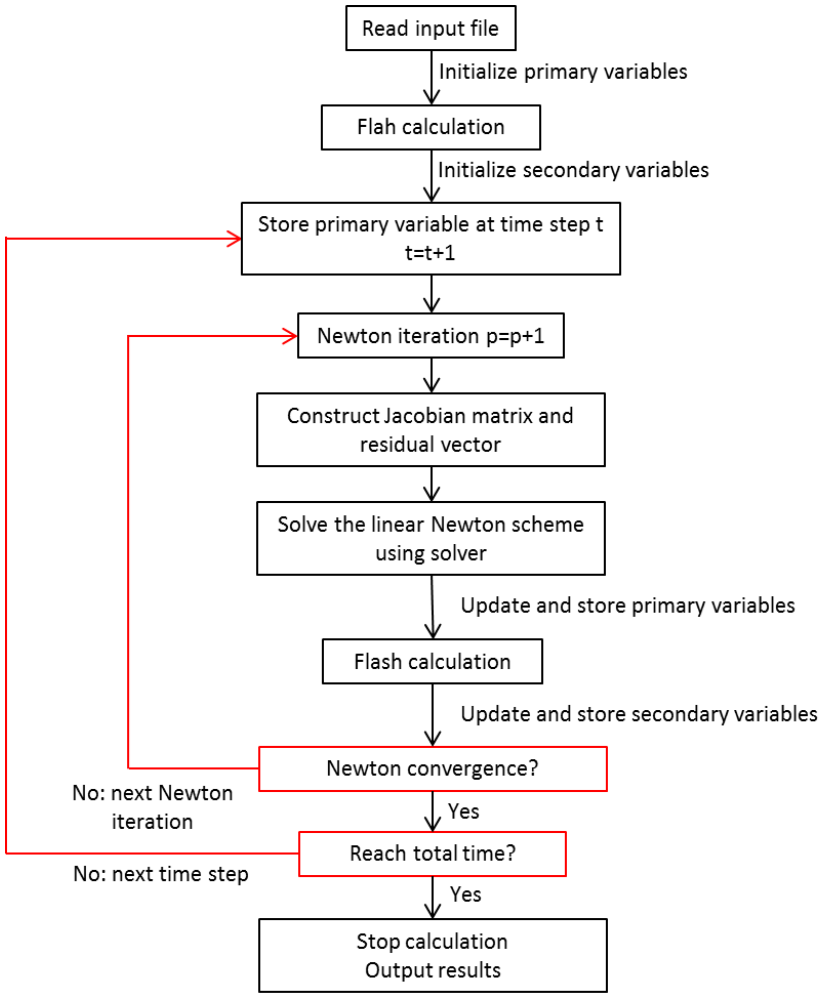

Figure 4.2: Simulator Algorithm

4.3 Numerical study of matrix/fracture flow

As shale gas and tight oil reservoirs are usually fractured, and the nanopore physics impact only the fluid flows inside the matrix medium and between the matrix and fracture transfer, we will study the matrix-fracture exchange process in the scale of a matrix block size. The pore size distribution (PSD) should be considered in this matrix-fracture interaction where the fracture are explicitly discretized.

4.3.1 Simulation setup

In order to study the impact of the PSD on reservoir production, a synthetic reservoir case representing the matrix/fracture interaction has been built with different PSD. The synthetic case is a two dimensional single porosity model representing the matrix/fracture exchange. A tight matrix rock of 20m length, 20m width and 0.2m thickness (in yellow Figure 4.3) is surrounded by a fracture of 0.001m width (in purple Figure 4.3). Pressure in the fracture is maintained at a constant value of 100 bar and only oil and water are present at the initial condition. The initial pressure is 200 bar in the matrix block and depletion is simulated to model flow from the matrix towards the fracture. Bakken oil [84, 152] is used for the simulations and the different compositional parameters are given in Table 4.2 and Table 4.3. For information, bubble point of the bulk fluid at the reservoir temperature of 373.15 K is 176.7 bar. All the simulation parameters are summarized in Table 4.4. In order to get reliable results, the grid is very fine with grid cells of 0.2x0.2x0.2m. The permeability of the matrix has been chosen to be 100 nD in accordance with works from Wang and Reed [138].

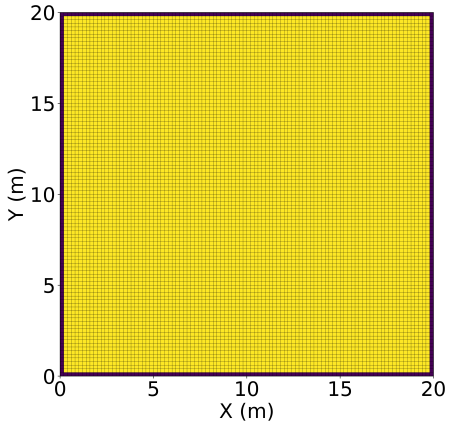

Figure 4.3: Simulation geometry

The matrix PSD is divided into three facies corresponding to different ranges of pore size and porosities (Table 4.5). Facies 1 corresponds to the small pores with pore radius ranging from 2 to 10nm, Facies 2 corresponds to pores from 10 to 100nm and Facies 3 corresponds to pore radius above 100 nm, where confinement has no effect on the fluid phase behavior which is therefore

Table 4.2: Compositional data for Bakken oil

Component	z_i	p_c (MPa)	T_c (K)	M_i (kg/kgmol)	ω_i	V_c (m3/kgmol)
C1	0.36736	4.599	190.56	16.04	0.0115	0.0986
C2	0.14885	4.872	305.32	30.07	0.0995	0.1455
C3	0.09334	4.248	369.83	44.10	0.1523	0.2000
C4	0.05751	3.796	425.12	58.12	0.2002	0.2550
C5-C6	0.06406	3.181	486.38	78.30	0.2684	0.3365
C7-C12	0.15854	2.505	585.14	120.56	0.4291	0.5500
C13-C21	0.0733	1.721	740.05	220.72	0.7203	0.9483
C22-C80	0.03707	1.311	1024.72	443.52	1.0159	2.2474

Table 4.3: Binary interaction parameters for Bakken oil

	C1	C2	C3	C4	C5-C6	C7-C12	C13-C21	C22-C80
C1	0	0.005	0.0035	0.0035	0.0037	0.0033	0.0033	0.0033
C2	0.005	0	0.0031	0.0031	0.0031	0.0026	0.0026	0.0026
C3	0.0035	0.0031	0	0	0	0	0	0
C4	0.0035	0.0031	0	0	0	0	0	0
C5-C6	0.0037	0.0031	0	0	0	0	0	0
C7-C12	0.0033	0.0026	0	0	0	0	0	0
C13-C21	0.0033	0.0026	0	0	0	0	0	0
C22-C80	0.0033	0.0026	0	0	0	0	0	0

Table 4.4: Simulation parameters

	Matrix	Fracture
Number of cells	100x100x1	4x101x1
dx/dy/dz (m)	0.2/0.2/0.2	0.001/0.2/0.2 or 0.2/0.001/0.2
k(D)	10^{-7}	10
porosity	facies dependent	1
Initial pressure (bar)	200	
Initial temperature (K)	373.15	
Initial water saturation Swi	0.3	
Fracture pressure (bar)	100	

considered as a bulk fluid. The PSD in Facies 1 and 2 is generated by a lognormal distribution with a mean of 3 and a standard deviation of 1 (Figure 4.4). Five PSD are considered in the matrix, which correspond to different fractions of the three facies (Table 4.6). The Table 4.6 gives the geometric volume fraction v_{fi} of each Facies i and the pore volume fraction $v_{pfi} = \frac{v_{fi}\epsilon_{fi}}{\sum_i v_{fi}\epsilon_{fi}}$ of each Facies i. The distribution D2 corresponds to the PSD of a typical shale reservoir studied by Kuila and Prasad [62] and interpreted by Alharthy et al. [6]. Five realizations d1, d2, d3,

d4, d5 for each of the five PSD: D1, D2, D3, D4 and D5 are generated. So, in total, twenty five realizations are obtained. An example of one of the five realizations d1 for distribution D2 is showed Figure 4.5. The left part of the Figure corresponds to one of the five realizations of the spacial distribution of the three facies: 1, 2, 3 for D2. The Facies 0 corresponds to the fracture. The right part of the figure corresponds to the pore size values in these three facies. A pore radius of 100 nm corresponds to a bulk fluid without confinement effect. Realization examples of the fives realizations 'd' for the PSD D1 and realization examples of the fives PSD 'D' are given in Appendix C.1.1 and C.1.2 respectively. It is assumed that the three facies have the same relative permeability but different capillary pressures (Figure 4.6). Capillary pressure is assigned according to the pore size, the Facies 3 which corresponds to bulk fluid has zero capillary pressure unlike Facies 1 and 2 (Figure 4.6).

Table 4.5: Pore size distribution properties

Facies	Pore size (nm)	porosity
1	2-10	ϵ_{f1}=0.02
2	10-100	ϵ_{f2}=0.05
3	$>$ 100	ϵ_{f3}=0.1

Table 4.6: Grid volume and pore volume per facies for the different distributions 'D'

Distribution	Geometric volume fraction (%)			Pore volume fraction (%)		
	Facies 1 (v_{f1})	Facies 2 (v_{f2})	Facies 3 (v_{f3})	Facies 1 (v_{pf1})	Facies 2 (v_{pf2})	Facies 3 (v_{pf3})
D1	10	20	70	2.5	12	85.5
D2	19	22	59	5	15	80
D3	20	40	40	6	31	63
D4	25	45	30	9	39	52
D5	35	50	15	15	53	32

The two commonly used methods of flash with capillary pressure (Section 3.2.1) and flash with critical properties shift (Section 3.2.2) have been chosen for the PVT modeling of the fluid in Facies 1 and 2. The fluid in Facies 3 is considered to have no confinement effect, then the flash is not modified.

4.3.2 Fine grid results

Before showing production results for different pore size distributions detailed in the previous section, results of recovery factor and GOR for homogeneous pore size inside the matrix are presented in Figure 4.7 for the same simulation setup. This is currently the commonly used method in the literature for considering PSD (Section 1.5.2). The simulation for the bulk fluid has no capillary pressure and no modification of the flash. The simulations for homogeneous pore size

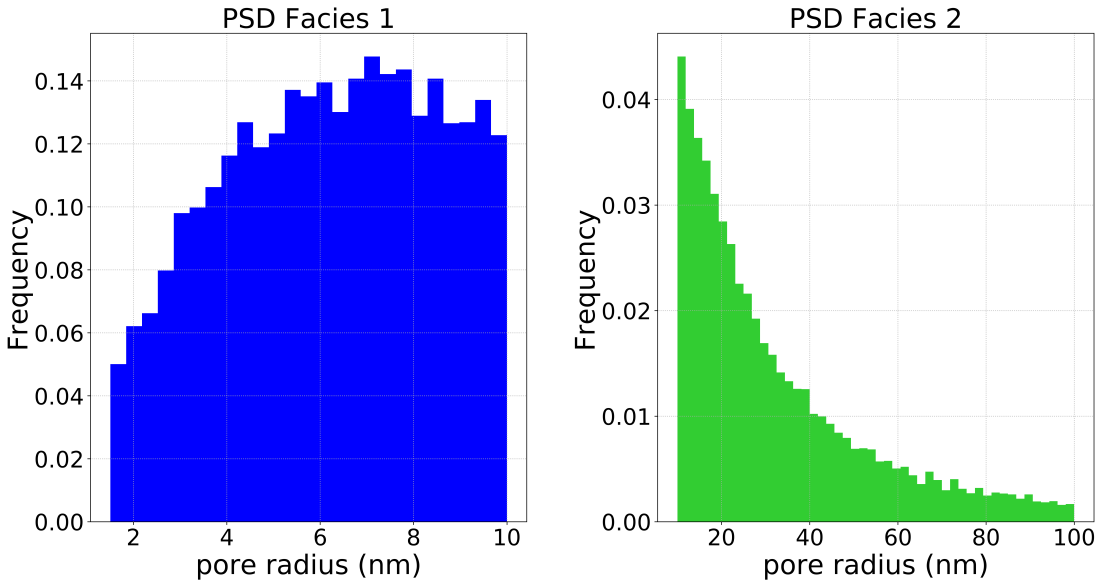

Figure 4.4: Histogram of an example of a PSD sample for Facies 1 and 2 using the log-normal law distribution with a mean of 3 nm and a standart deviation of 1 nm.

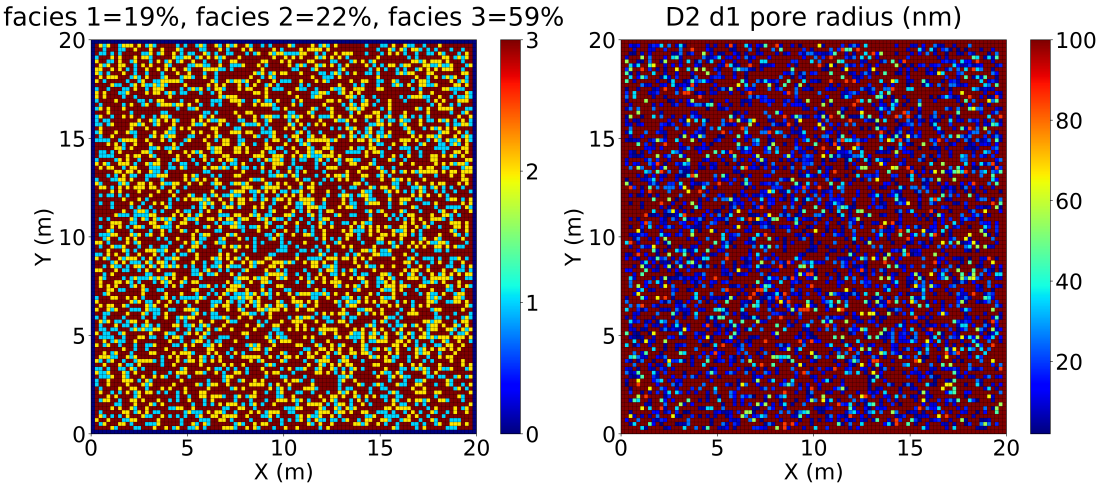

Figure 4.5: Example of facies and pore size distribution

inside the matrix have no capillary pressure for fluid flow and a modified flash with capillary pressure (Section 3.2.1) in the matrix. The confinement reduces the gas-oil ratio (GOR) and keeps it constant for a longer time, which is consistent with observations on the field and in the literature (Sections 1.3.2 and 1.5.2). As gas apparition is postponed during depletion because of the reduction of bubble point, confinement decreases the gas accumulation. It also causes the oil to keep low density and viscosity because of light components always in the liquid phase. Then confinement helps to produce more oil but gas apparition also allows to keep the reservoir

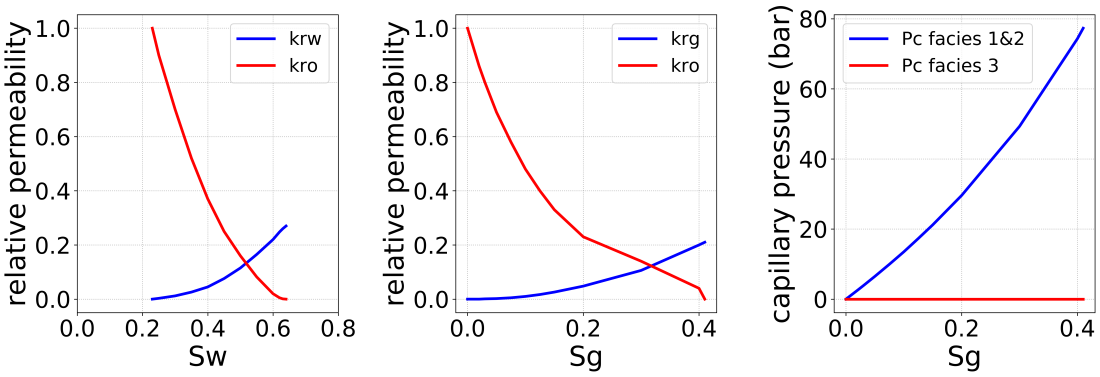

Figure 4.6: Relative permeability and capillary pressure curves

pressure high. That is why 3nm and 5nm confinement cases produce less oil than the bulk case.

Considering a single average radius inside the matrix for a PSD in the scale of a matrix block has been used by many authors in the literature (Section 1.5.2). But this approach is not accurate as heterogeneity of capillary pressure and pore size dependent PVT behavior is not taken into account. That is why in this thesis, the PSD is explicitly described with one pore radius in each cells at very fine scale. As explained in the previous section, five simulations corresponding to different realizations have been performed for each distribution D. Figure C.11 in Appendix C.1.3 is an example of the production results for the five realizations of D1. Although spacial heterogeneity of PSD, capillary pressure and PVT behavior are different due to extremely small pore sizes, the results are quite similar for each of the five realizations 'd'. This is because the pore size realization is not spatially correlated and this kind of distributions can be homogenized in the considered volume, which is a representative element volume. An example of simulation case with important difference of production results for different realizations 'd' is given in Appendix C.2. In order to compare the different distributions 'D', the production data of the five realizations of each 'D' is represented by their average value P50. We first present the results with flash with capillary pressure used for PVT modeling for Facies 1 and 2.

The gas and oil recovery factors and the gas-oil ratio (GOR) of the different distributions D are compared to the same case simulations using a bulk fluid in Figure 4.8. The bulk fluid is represented with zero capillary pressure in the entire matrix and no modification of the flash. As the porosities are different for each distributions D, the simulation production results for a bulk fluid are also different. For all cases, the oil production increases, the gas production and the GOR decreases with fluid confinement in comparison with the bulk fluid results. Two different effects are present and can explain this observation: the capillary pressure heterogeneity and the pore size dependent PVT modeling of the fluid. The capillary pressure heterogeneity slows down or even stop the gas flow from Facies 3 to fractures. As capillary pressure is higher in

Facies 1 and 2, a large volume of gas stays stuck in Facies 3 where capillary pressure is zero. The density of oil will then become lighter and the matrix pressure will be maintained for a longer time. Therefore gas production decreases and oil production increases, then the GOR does not increase. On the other hand the modification of the flash with capillary pressure decreases the bubble point of the oil. Gas apparition is then postponed during depletion and oil stays lighter for a longer time, which leads to the same conclusion for production observations. These two effects of capillary pressure heterogeneity blocking gas volume in large pores and modified PVT behavior effect postponing gas apparition can be seen in Figure 4.9.

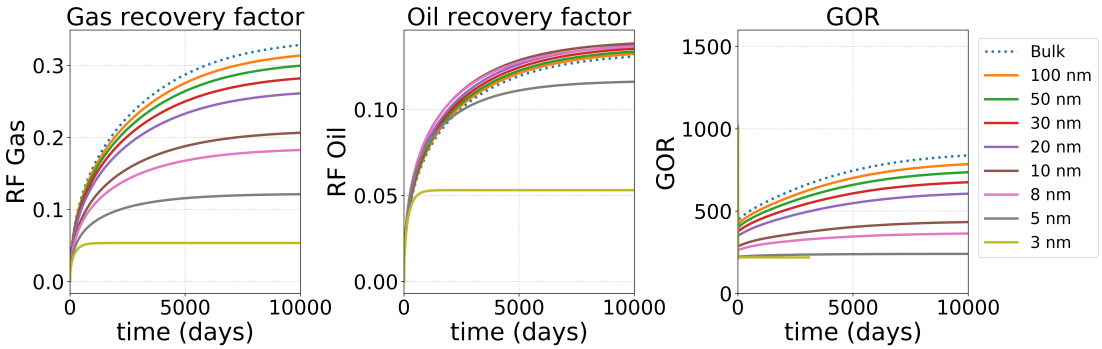

Figure 4.7: Production results for homogeneous pore size

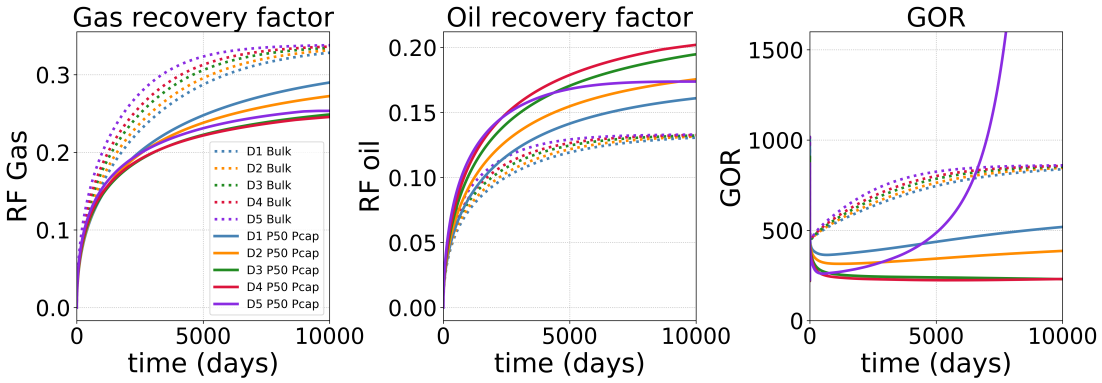

Figure 4.8: Comparison of production results for the different distributions for bulk and confined fluid with a flash with capillary pressure.

Lets focus now on the comparison of the P50 value of reservoir production for the different distributions D (Figure 4.8). When the volume fraction of nanopores of Facies 1 and 2 increases (i.e. from D1 to D5), the production of oil increases until D4 and then decreases. Furthermore the gas production and the GOR decreases until D3 or D4 (they have almost the same P50) and then increases. The capillary pressure heterogeneity has a strong impact on production for low percentage of nanopores in the matrix because large volume of Facies 3 might be surrounded by Facies 1 and 2 where the capillary pressure is very high. Then important volume of gas stays

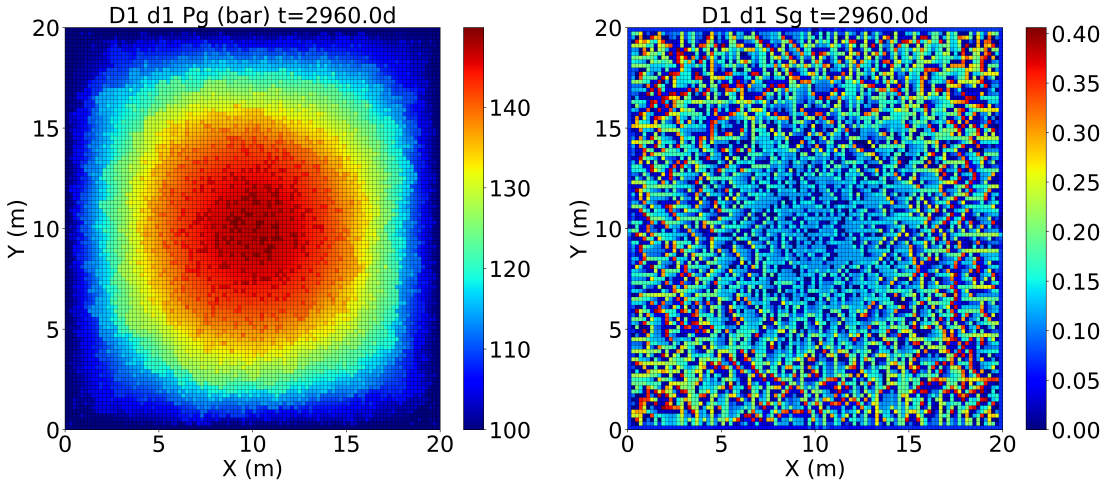

Figure 4.9: Example of gas pressure field (left) and gas saturation field (right) for distribution D1 d1 at 2960 days.

stuck in Facies 3. When the percentage of nanopores becomes important (D4, D5), the volume of Facies 3 surrounded by Facies 1 and 2 is very small and no gas entrapment occurs. However the volume of cells with lower bubble point due to modified PVT modeling becomes significant to impact the production. For the studied cases it seems that the impact on production of capillary pressure heterogeneity is more important than confined fluid PVT behavior. This could explain the trend inversion of the curves from D4 to D5.

The impact of pore size dependent PVT modeling can be analyzed by comparing reservoir simulation models with capillary pressure heterogeneity with and without confined fluid PVT model. A simulation without confined fluid PVT model corresponds to a classic flash for a bulk fluid. Figure 4.10 shows the difference between these two models for d1, one of the five realizations. The two different models are quite similar from D1 to D3 which mean that modified PVT modeling has no strong impact on production for such distributions. However for D4 and especially D5 with higher volume fraction of nanopores in the matrix, the difference between the two models is significant. This means that pore radius dependent EOS has an important impact on production for these distributions with high volume fraction of nanopores.

The production results for the five different distributions 'D' are now presented with flash with critical pressure and temperature (see details in Section 3.2.2) used for the PVT modeling of Facies 1 and 2 (Figure C.12 in Appendix C.1.3). The conclusions are similar to the case with a flash with capillary pressure. Compared to the flash with bulk fluid, the oil production increases, the gas production and the GOR decreases with fluid confinement. However it is important to note that changing critical pressure and temperature alters the fluid which provides a different initial mass, transport and volumetric properties in the single phase compared to

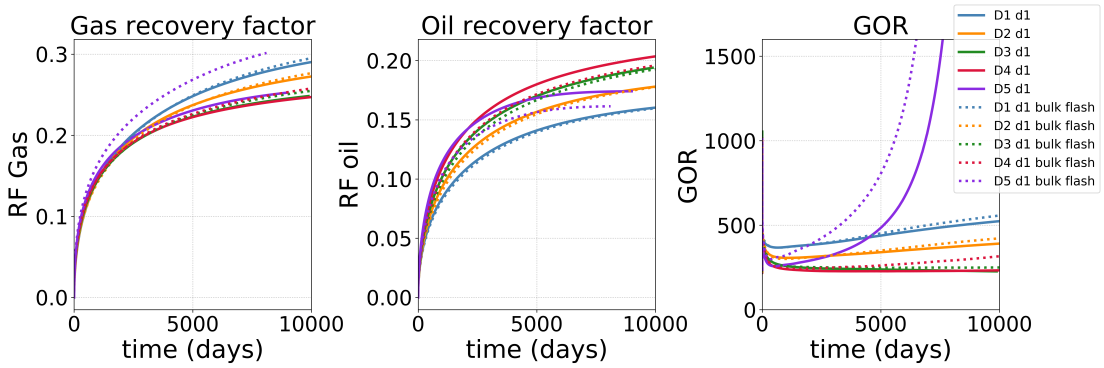

Figure 4.10: Impact of modified EOS on production

bulk. Comparing results for a bulk fluid and different distributions 'D' might then not be very proper. That is why we plot and compare the recovery factors. Concerning the evolution of production against the increase nano-pores volume fraction (from D1 to D5), the observations are also the same. The production of oil increases until D4 and then decreases, the production of gas and the GOR decreases until D3 and then increases. The explanations used for the case of flash with capillary pressure are applicable to the case of flash with critical point shift.

The comparison of the production results for the two flash methodologies (flash with capillary pressure and flash with critical point shift) is shown Figure 4.11. The results for D1, D2 and D3 are very similar. Indeed the small pores have a low volume fraction inside the matrix, so the impact of modified PVT modeling is negligible compare to capillary pressure heterogeneity. However for D4 and D5 with a higher proportion of nanopores, the difference is quite significant because the two modified PVT models are different.

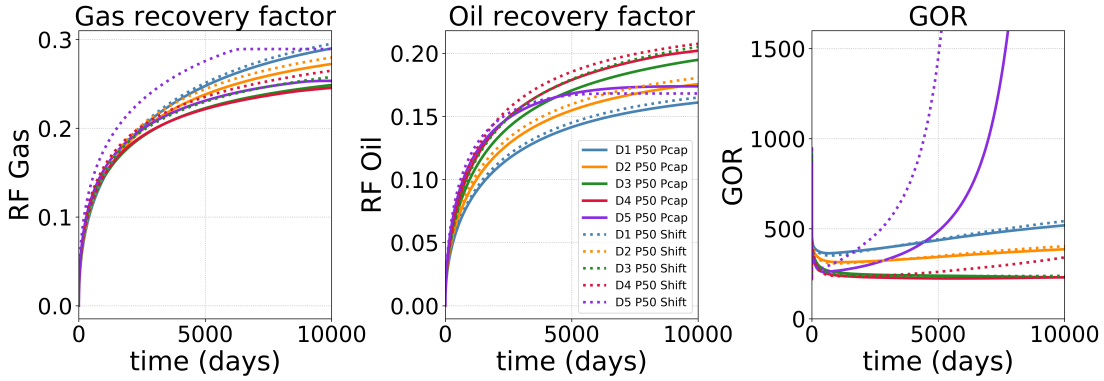

Figure 4.11: Comparison of production results for different distributions 'D' between flash with capillary pressure (Pcap) and flash with critical point shift (Shift).

The same simulations for the five distributions 'D' have been performed for two different

matrix/fracture geometries with the matrix block size of 10x10 m and 40x10 m (Figure 4.12 and Figure 4.13). The two geometries are also made up of a tight matrix (in yellow Figures 4.12 and 4.13) surrounded by a fracture (in purple Figures 4.12 and 4.13). Their dimensions and their number of cells are summarized Table 4.7. All the simulation setups are the same as detailed in Section 4.3.1. The simulation results of the two geometries are presented in Appendix C.3 Figure C.18 for block size of 10x10 m and in Appendix C.4 Figure C.19 for block size of 40x10 m. The flash with capillary pressure methodology is used. The trend of the production curves for the different distributions are similar to the initial geometry with the matrix block size of 20x20 m, but with a different time scale.

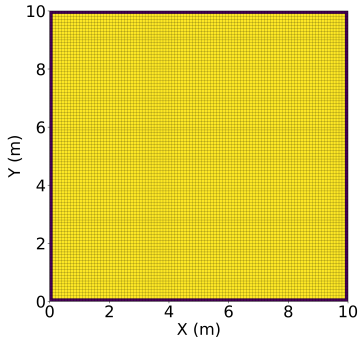

Figure 4.12: Simulation with the matrix block size of 10x10 m: geometry 2

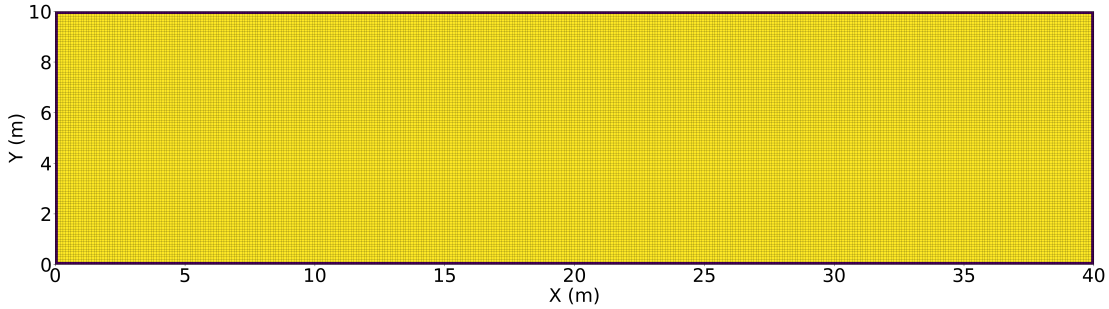

Figure 4.13: Simulation with the matrix block size of 40x10 m: geometry 3

Table 4.7: Geometry parameters

	Geometry 2		Geometry 3	
	Matrix	Fracture	Matrix	Fracture
Number of cells	100x100x1	404	400x100x1	1004
dx/dy/dz (m)	0.1/0.1/0.1	0.001/0.1/0.1 or 0.1/0.001/0.1	0.1/0.1/0.1	0.001/0.1/0.1 or 0.1/0.001/0.1

4.4 Summary and discussion

The modified flash with capillary pressure developed in Section 3.2.1 has been included in a compositional reservoir simulator. The mass conservation equations of each components are discretized in space using a finite-volume based method. The discretization in time is performed using a full implicit scheme. The primary variables are oil pressure, water saturation and molar fraction of the $n_c - 1$ first components. They are independent on the variables used inside the flash calculation. This therefore enables to modify the flash easily. The discretized equations are solved numerically using Newton-Raphson method and linear solver.

The matrix/fracture exchange is the main driver of tight oil and shale gas reservoir production. These reservoirs are indeed usually highly fractured and the majority of hydrocarbons are located in the matrix where confinement occurs. Therefore the matrix/fracture interaction is studied in the scale of a matrix block size. Unlike considering homogeneous pore size radius inside a matrix block studied by many authors in the literature, different PSD are considered at very fine scale in this thesis. This enables to take into account the heterogeneity of capillary pressure and pore size dependent PVT behavior. Five PSD (D1 to D5) are considered with different volume fractions of nanopores.

For all the PSD studied, the impact of pore confinement on reservoir production increases the oil production and decreases the gas production and the GOR compared with the bulk fluid. It is manifested by two effects: capillary pressure heterogeneity and pore size dependent PVT modeling. The impact of capillary pressure heterogeneity on reservoir production is significant for slightly low percentage of nano-pores (D1 to D3). Large volume of gas might be trapped in very large pores with zero capillary pressure surrounded by tiny pores with high capillary pressure. The impact of pore size dependent PVT modeling becomes significant for higher volume fraction of nano-pores (D4 and D5). The volume of oil with lower bubble point becomes then significant to impact the production. The observations are similar for a flash with capillary pressure, a flash with critical point shift and different geometries.

All the results shown in this section comes from reservoir simulations using a very fine grid and can therefore be considered as reliable results. Nonetheless, large scale reservoir simulations need upscaling methodologies because of computational limits. In the following chapter, the fine grid results above will be used as references to compare different coarse grid simulation methodologies.

Chapter 5

Upscaling for large scale reservoir simulation

The matrix/fracture exchange modeling is crucial for accurate tight oil and shale gas reservoir production forecasting. In order to perform large scale reservoir simulations, upscaling methodologies must be developed because of computational constraints and very detailed characterization of matrix and fracture spacial distribution and geometries. The upscaling of the matrix/fracture interaction is more complex than that in conventional reservoirs because of low matrix permeability and very heterogeneous PSD with pore radius dependent PVT. Some methodologies are proposed in the literature. The previous study of matrix/fracture interaction at very fine scale in Chapter 4 gives reference results to investigate upscaling methodologies. The first section of this chapter therefore presents and investigates the different upscaling methodologies proposed in the literature. Then a new triple porosity model is proposed and its mathematical model is detailed in Section 5.2. The upscaling methodology of the triple porosity and its validation by the reference results is presented in Section 5.3. Finally the developed triple porosity model is applied to a large scale simulation case of a fractured well in a stimulated reservoir volume (SRV) in Section 5.4.

5.1 Dual media model

The methodologies proposed in the literature in order to upscale the matrix/fracture exchange and the pore size distribution are presented in the introduction Section 1.5. These methodologies are based on a dual media model. In this Section, we will first present the dual-porosity and MINC concept and theory. Then, we will investigate the dual-porosity model and the MINC method to evaluate which one is suitable for low permeability reservoir simulations with bulk fluid. If one method does not adapt to simulate low permeability reservoirs, it will not be used further for the upscaling study for the PSD. Finally the methodologies proposed in the literature

to upscale the PSD will be investigated for the cases presented in Section 4.3.1.

5.1.1 Dual-porosity model

The dual-porosity model was originally developed by Barenblatt et al. [12] and Warren and Root [144]. This concept has already been introduced in introduction Section 1.5.1. It represents a fractured reservoir with two media: matrix and fracture. The schematic Figure 5.1 gives details about the flow connections and the considered systems. In a grid, any matrix cell is associated to a fracture cell located at the same grid location. Matrix and fracture grids are identical and superposed. In a given cell, there are N identical matrix block and each one behaves as a block located at the center of the cell.

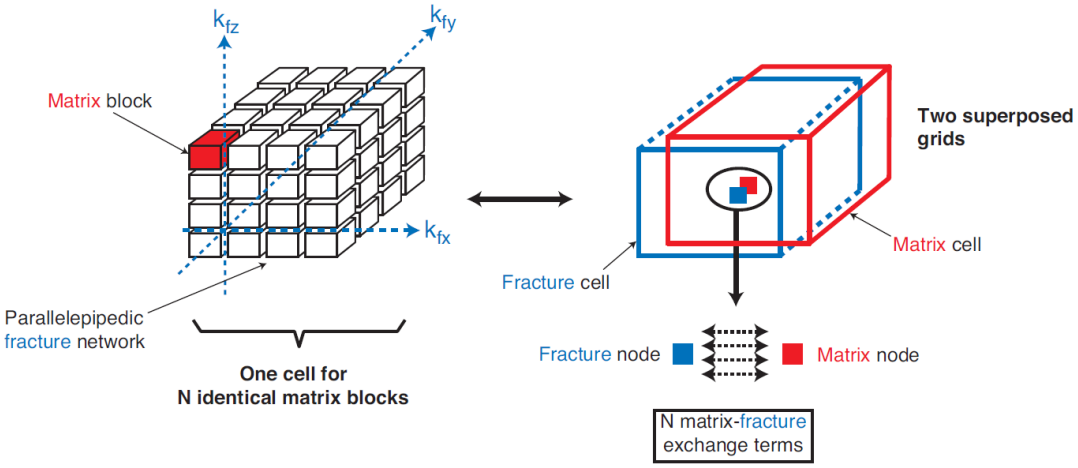

Figure 5.1: Schematic of the dual-porosity method [65].

The mole conservation equation applied to matrix (M) and fracture (F) media is presented in the following equations in term of mole per unit of volume for every components i.

$$\begin{cases} \frac{\partial M_M^i}{\partial t} = F_M^i - F_{MF}^i \\ \frac{\partial M_F^i}{\partial t} = F_F^i + q_F^i + F_{MF}^i \end{cases} \tag{5.1}$$

where q_F^i is the internal sink/source term per unit of volume for the components i in the fracture. The sink/source term is negligible in matrix as the majority of fluid is produced through fractures. F_M^i is the flux exchange between matrix blocks. F_F^i is the flux exchange between fracture cells. F_{MF}^i is the flux between matrix and fracture for the component i. In a dual-porosity single permeability model, the mole transfer between cells of the same media is only possible for the fracture media. Then the term F_M^i is equal to zero. The model which considers mole transfer between matrix cells F_M^i is called a dual porosity dual permeability model. In this thesis, only the dual porosity single permeability model is used.

The accumulation term of the hydrocarbon components i and water for each media $\xi = M, F$ is expressed by:

$$\begin{cases} M_\xi^i = \epsilon_\xi(\rho_o S_o x_i + \rho_g S_g y_i) \\ M_\xi^w = \epsilon_\xi \rho_w S_w \end{cases} \tag{5.2}$$

All the parameters have already been defined in Section 4.2.1. The index o is used for oil and g for gas.

The mole flux for each hydrocarbon components i and water for each media $\xi = M, F$ is calculated from Darcy flow by the following equation:

$$\begin{cases} F_\xi^i = -\nabla \,.\, (\rho_o x_i \vec{v_o} + \rho_g y_i \vec{v_g}) \\ F_\xi^w = -\nabla \,.\, (\rho_w \vec{v_w}) \end{cases} \tag{5.3}$$

The flux between matrix blocks and the fracture is computed numerically. The space discretization using a finite-volume method described in Section 4.2 is applied to Equation 5.3 for matrix and fracture media. The transfer flux between a matrix block and the surrounding fractures is expressed as the sum of the fluxes through each faces j of the matrix block assuming a steady-state matrix-fracture transfer.

For a three dimensions matrix block, the flux between a matrix block (M) of size L_x, L_y, L_z and the surrounding fracture (F) for a component i is, by considering only the capillary force:

$$\begin{cases} f_{MF}^i = -(\sum_{j=1}^6)\gamma_{MF}^j[(\rho_o x_i \lambda_o)^M(\Psi_o^F - \Psi_o^M) + (\rho_g y_i \lambda_g)^M(\Psi_g^F - \Psi_g^M)] \\ f_{MF}^w = -(\sum_{j=1}^6)\gamma_{MF}^j(\rho_w \lambda_w)^M(\Psi_w^F - \Psi_w^M) \end{cases} \tag{5.4}$$

with γ_{MF}^j the transmissivity from the matrix block to the fracture face j. λ_ϕ is the mobility of phase ϕ already defined in Section 4.2.1. Ψ_ϕ^ξ is the flow potential of phase ϕ of the medium $\xi = M, F$. This parameter is also defined in Section 4.2.1. γ_{MF}^j corresponds to the transmissivity between matrix and fracture.

This discretization can also be written as:

$$\begin{cases} f_{MF}^i = -V_{block}\sigma_{shape}[(\rho_o x_i \lambda_o)^M(\Psi_o^F - \Psi_o^M) + (\rho_g y_i \lambda_g)^M(\Psi_g^F - \Psi_g^M)] \\ f_{MF}^w = -V_{block}\sigma_{shape}(\rho_w \lambda_w)^M(\Psi_w^F - \Psi_w^M) \end{cases} \tag{5.5}$$

with $\sigma_{shape} = \frac{\sum_{j=1}^6 \gamma_{MF}^j}{V_{block}}$ called the shape factor. $V_{block} = L_x L_y L_z$ is the matrix block volume.

A cell gathers several identical matrix blocks, the matrix/fracture transfer between a matrix cell and the corresponding fracture cell must therefore take into account all the matrix blocks.

The ratio between the cell volume and the matrix block volume gives the number of matrix blocks in a cell. The flux between matrix and fractures cells F^i_{MF} is therefore:

$$F^i_{MF} = \frac{V_{cell}}{V_{block}} f^i_{MF} \tag{5.6}$$

Warren and Root [144] proposed a formulation of the shape factor σ. It is a constant matrix-fracture-exchange factor that only depends on the geometry and characteristic size of the matrix blocks assuming a steady-state matrix-fracture transfer. Many different values for the shape factor have been proposed in the literature. The Table 5.1 summarized the shape factor most used in the literature. The values in the Table corresponds to $\sigma_{shape}a^2$, for a cubic block of lateral dimension a ($L_x = L_y = L_z = a$), exchanging fluids for 1D, 2D or 3D flow transfer cases.

Table 5.1: Comparison of Shape factors $\sigma_{shape}a^2$ reported in the literature [20]

Case	Warren and Root [144]	Kazemi et al. [58]	Coats [30]	Lim and Aziz [69]	Quintard and Whitaker [100]
1D	12	4	8	π^2 (9.87)	12
2D	32	8	16	$2\pi^2$ (19.7)	28.4
3D	60	12	24	$2\pi^2$ (29.6)	49.6

5.1.2 MINC method

The MINC model stands for 'Multiple INteracting Continua' and has been developed by Pruess and Karasaki [99] and Pruess [97]. This concept has already been explained in the introduction Section 1.5.1. The MINC model is an extension of the dual porosity model as it divides the matrix block into a series of nested volume on the basis of the distance from the nearest fracture. It allows to take into account the transient state of the flow between matrix and fracture which can be very long for low permeability reservoirs [150]. MINC method treats the problem entirely by numerical methods in a fully transient way. It consists in a fully transient representation of the inter-porosity flow. In general, the MINC model provides a better numerical approximation for transient fracture-matrix interactions than the dual-porosity model. The schematic Figure 5.2 gives details about the MINC discretization in two dimensions. $d_{j,j+1}$ corresponds to the distance between each MINC volume j and $j+1$. L_{xj} and L_{yj} correspond to the size of each MINC volumes j. The size of the matrix block is $L_{x1} \times L_{y1}$

The mole conservation equation applied to a MINC volume j of the matrix block (M) is presented in the following equations in term of mole per unit of volume for every components i.

$$\frac{\partial M^i_{M,j}}{\partial t} = F^i_{M,j} \tag{5.7}$$

The accumulation terms for a MINC volume j: $M^i_{M,j}$ is expressed as the equation 5.2. The

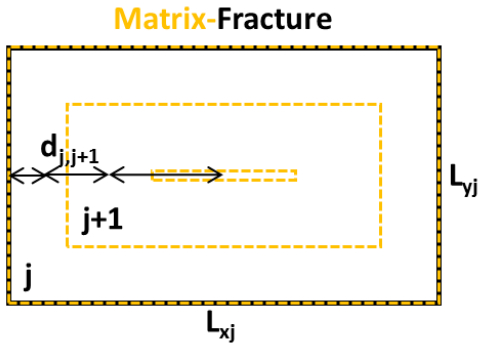

Figure 5.2: Schematic of the MINC method in two dimensions.

flux between two MINC volumes j and $j+1$ of a matrix block is calculated in the following equation for the two dimension case.

$$\begin{cases} f^i_{M,j,j+1} = -\gamma_{j,j+1}[(\rho_o x_i \lambda_o)^{j+1}(\Psi_o^{M,j} - \Psi_o^{M,j+1}) + (\rho_g y_i \lambda_g)^{j+1}(\Psi_g^{M,j} - \Psi_g^{M,j+1})] \\ f^w_{M,j,j+1} = -\gamma_{j,j+1}(\rho_w \lambda_w)^{j+1}(\Psi_w^{M,j} - \Psi_w^{M,j+1}) \end{cases} \tag{5.8}$$

$$\gamma_{j,j+1} = \frac{k^{j,j+1} A_{j,j+1}}{d_{j,j+1}} \tag{5.9}$$

with $A_{j,j+1} = 2(L_{xj} + L_{yj})(dz)$ is the area surrounding a MINC volume j. $\gamma_{j,j+1}$ corresponds to the transmissivity between two consecutive MINC volumes j and $j+1$. $k^{j,j+1}$ corresponds to the matrix permeability between the MINC volumes j and j+1 which is a weighted harmonic average of these two volumes. dz is the length of the grid in the z direction.

The flux between each MINC volume j inside a matrix cell is defined in the following equation for the two dimension case. The number of matrix blocks inside a cell is equal to $\frac{V_{cell}}{V_{block}}$ with $V_{block} = L_{x1}L_{y1}(dz)$

$$F^i_{M,j} = \frac{V_{cell}}{V_{block}}(f^i_{M,j-1,j} + f^i_{M,j,j+1}) \tag{5.10}$$

$F^i_{M,0} = \frac{V_{cell}}{V_{block}} f^i_{M,0,1}$ corresponds to the flux between fracture ($j = 0$) and the nearest MINC volume from the fracture ($j = 1$).

In the following, the dual porosity model and the MINC method are compared to the reference fine grid simulations in ultra low permeability reservoirs.

5.1.3 Simulation in homogeneous medium

The matrix-fracture transfer modeling using dual-porosity model and MINC method is first investigated for an homogeneous case with bulk fluid, ie without pore size dependent PVT model. These methods are illustrated Figure 5.3 for the case of the matrix block size of 20x20m presented in Section 4.3.1. The production results for a bulk fluid of these two models are compared to the fine grid reference results in Figure 5.4. The dual porosity model (D2 2P) is unable to match the fine grid results (Bulk fine). On the contrary the method with ten matrix MINC discretizations (2P MINC 10) matches very well the bulk fine grid results. As the permeability of the matrix is very low, the fracture-matrix interaction shows a long-lasting transient flow [150]. The quasi-steady state flow assumption of the dual porosity model is therefore unsuitable to model the matrix-fracture interaction. The more rigorous MINC concept is adapted as a generalization of the dual-continuum model. It describes pressure gradient between fractures and matrix by further subdividing individual blocks.

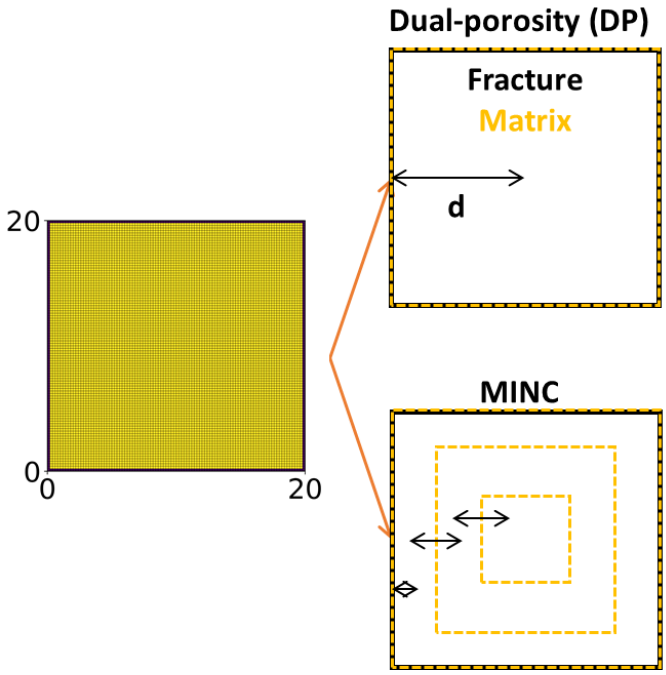

Figure 5.3: Dual porosity model with and without MINC matrix discretization.

Different shape factor for the dual-porosity simulation have also been tried, and none of them can match the reference solution. The dual porosity model with MINC discretization allows to match the fine grid results of matrix/fracture transfer for a bulk fluid. This model will then be used to investigate the upscaling methodologies of the PSD for a fluid with pore radius dependent PVT.

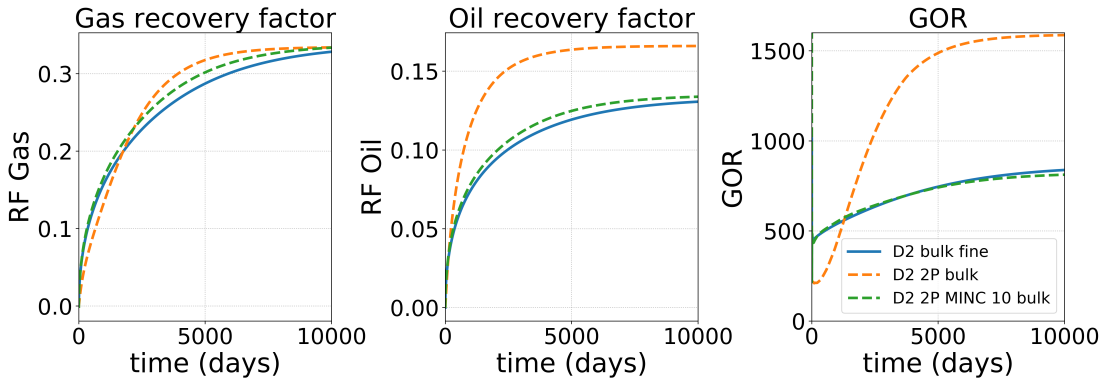

Figure 5.4: Production results for a bulk fluid corresponding to distribution D2 using single porosity fine grid model (fine) and standard dual porosity model (2P) and MINC (2P MINC) matrix discretization.

5.1.4 Simulation in heterogeneous medium

In the literature two main methods are used for the upscaling of the PSD: the first one considers an average pore radius to account for the PSD and the second one considers a saturation dependent capillary pressure in the flash calculation (Section 1.5.2). Here, we use these methods to the distribution D2 for the case with matrix block size of 20x20m (Section 4.3.1). The flash used for the upscaling methodologies is either a flash with capillary pressure and average radius or a flash with an effective radius function of oil saturation (Figure 3.5 Section 3.2.2). The production results for a confined fluid in the distribution D2 are given in Figure 5.5 for the reference fine grid simulation (D2 P50), for different average radius (D2 DP MINC 10) and the effective radius (D2 DP MINC 10 r_eff).

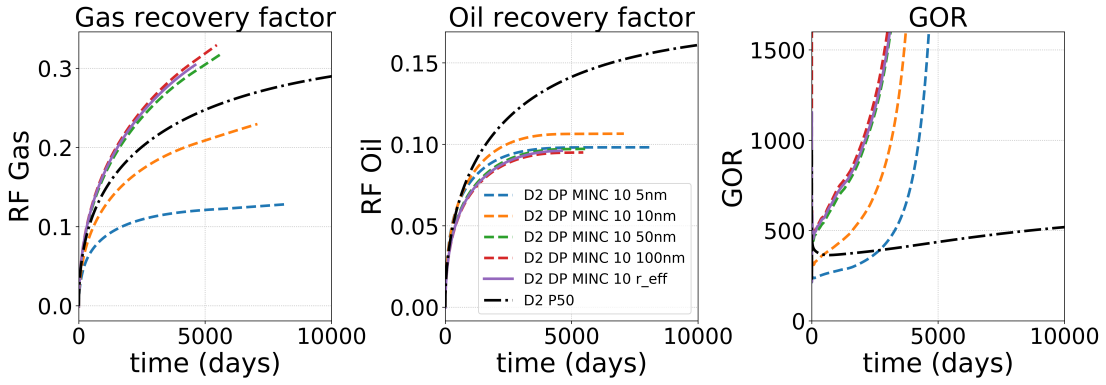

Figure 5.5: Production results for distribution D2 using single porosity fine grid model (D2 P50), dual porosity model with MINC matrix discretization (D2 DP MINC 10) and effective radius (D2 DP MINC 10 r_eff).

No average pore radius from 5 nm to 100 nm is able to match the fine grid results. For

GOR production the average radius should be between 5 nm and 10 nm. This range of values is impossible to match the reference results for gas and oil production. Therefore upscaling the PSD using an average pore radius seems not to be adapted. The effective radius method gives results very similar to the case of a pore radius of 100 nm. We have seen in Section 4.3.2 that the confinement effect is negligible for a flash with capillary pressure and pore radius above 100 nm. The results are similar to a flash without confinement modeling a bulk fluid. As the gas saturation in the matrix is low during depletion, the effective radius value is high and a large volume fraction of small pores is neglected. The effective radius method is therefore not adapted to upscale the PSD. None of the upscaling methodologies proposed in the literature are able to match the fine grid production results of a matrix/fracture transfer with a PSD and pore radius dependent PVT. A new triple porosity upscaling methodology is therefore developed in this thesis.

5.2 A new triple porosity model

Multi-porosity models such as triple porosity model have been used in the literature for different applications (Sections 1.5.1 and 1.5.2). There are a lot of studies in hydrology aiming to model the matrix/fracture exchange. Matrix and fractures media are subdivided into several media in order to improve the model accuracy because of the presence of cavities [70] or fractures of different scales [147]. These models have also been used for unconventional reservoir in order to account for the different gas flow regime in function of their Knudsen number and therefore the pore size in the matrix [137, 141]. Only Alfi et al. [4] used a triple porosity model to take into account the confined fluid behavior function of pore size and what he called the sieving effect. That method is interesting but seems to have several drawbacks as explained in Section 1.5.2. First, considering the thermodynamic equilibrium between large pores and small pores predominant to other effect such as capillarity may be not adapted. Furthermore the long transient state of flow between matrix and fracture is not taken into account. Finally no details are given for the mathematical model and the flux calculation between media. In this thesis, a new triple porosity model which aims to upscale the matrix/fracture exchange for unconventional reservoirs with very heterogeneous PSD and pore radius dependent PVT is presented.

5.2.1 Concept

The idea is to conceptualize the matrix/fracture transfer with a PSD into three media: fractures, small pores and large pores. The source of the flow is considered to be mainly in large pores because they gather the largest volume of hydrocarbons. Then in the flow from large pores to fractures, the fluid flows across small pores which surround large pores to finally be produced through the fractures. In other words, the model considers that flow occurs from large pores to fractures through small pores as illustrated in Figure 5.6. The direct flow between large pores and fractures is neglected. Peng-Robinson EOS is used in large pores and fractures, and

the modified Peng-Robinson with capillary pressure is used in small pores (Section 4.3.2). The capillary pressure used for flow calculation is equal to zero in large pores and it is function of saturation in small pores. The fluid which is predominantly present in large pores must go through small pores to join the fractures. As the gas-oil capillary pressure of small pore is higher than large pores, the gas flow up to the fracture is slowed down. Furthermore as the PVT model of the small pore is pore size dependent, then the gas apparition is postponed during depletion. Therefore the two effects of capillary pressure heterogeneity and the confined fluid PVT behavior detailed in Section 4.3.2 are taken into account in the triple porosity model. The three subdomains have their own porosity and permeability respecting the fine grid properties.

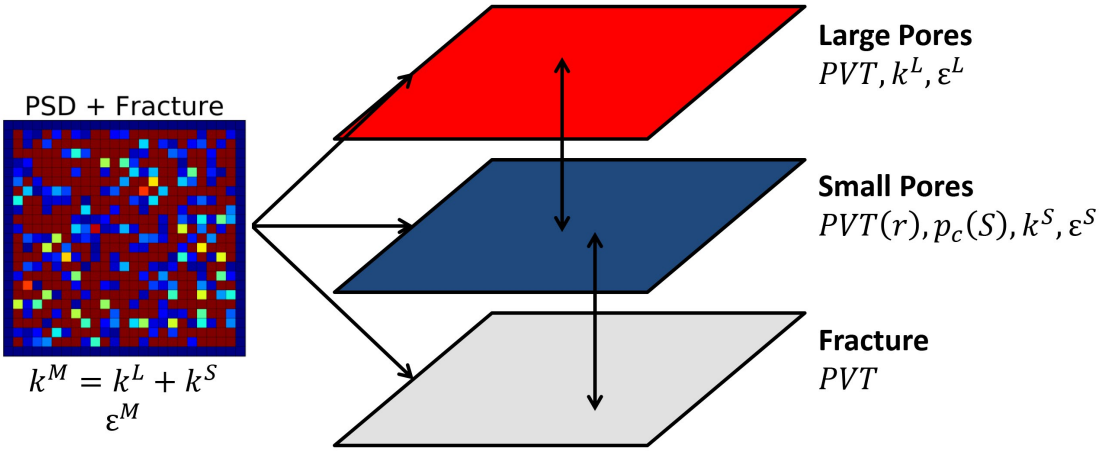

Figure 5.6: Schematic of triple porosity model for one matrix/fracture block

5.2.2 Mathematical model

Contrary to the dual-media model presented in Section 5.1, the flow is calculated in three media: large pores, small pores and fracture considering mole transfer between them. The mole conservation equation of every components i for each media: large pores (L), small pores (S) and fractures (F) is expressed by the following equations in moles per unit of volume.

$$\begin{cases} \frac{\partial M_L^i}{\partial t} = F_L^i - F_{LS}^i \\ \frac{\partial M_S^i}{\partial t} = F_S^i + F_{LS}^i - F_{SF}^i \\ \frac{\partial M_F^i}{\partial t} = F_F^i + q_F^i + F_{SF}^i \end{cases} \tag{5.11}$$

where M_L^i, M_S^i, M_F^i are the accumulation terms of the component i in the media L, S and F respectively. F_L^i, F_S^i, F_F^i are the mole flux exchange of component i in each media. F_{LS}^i is the mole flux between large pores to small pores and F_{SF}^i is the mole flux between small pores to fractures. q_F^i is the internal sink/source term per unit of volume for component i in the fracture. We have similar model for the water component.

The sink/source terms in large pores and small pores are neglected as we consider that the majority of the production/injection occurs in fractures. The large pore medium gives a mole flux F^i_{LS} to the small pore medium. The small pore medium receives mole flux from large pores F^i_{LS} and gives mole flux to fracture F^i_{SF}. Finally the fracture medium received mole flux from small pores F^i_{SF}. The flow model we consider between media explains the additional mole flux terms in the Equation 5.11.

The accumulation term of the hydrocarbon component i for each medium $\xi = L, S, F$ is expressed by:

$$\begin{cases} M^i_\xi = \epsilon_\xi(\rho_o S_o x_i + \rho_g S_g y_i)_\xi \\ M^w_\xi = \epsilon_\xi(\rho_w S_w)_\xi \end{cases} \tag{5.12}$$

As in single porosity model, the mole flux for each hydrocarbon component i and water for each medium $\xi = L, S, F$ is calculated from Darcy flow by the following equation:

$$\begin{cases} F^i_\xi = -\nabla \,.\, (\rho_o x_i \vec{v_o} + \rho_g y_i \vec{v_g})_\xi \\ F^w_\xi = -\nabla \,.\, (\rho_w \vec{v_w})_\xi \end{cases} \tag{5.13}$$

The mole flux terms between media F^i_{LS} and F^i_{SF} are not easy to express analytically. They can be expressed in a discrete form. A finite-volume based method is used for the space discretization of the system of Equation 5.11. The same method detailed in Section 4.2.1 for the single porosity model has been used. The mole flux terms per unit of volume F^i_{LS} and F^i_{SF} can therefore be expressed in their spacial discretization form. Their expression will be detailed in the next section.

5.2.3 Discretization of the model

The main concept and mathematical model of the triple porosity approach have been given in the previous section. The details of the model and the flux term calculation are now presented. The large pore and small pore media are subdivided into several nested meshes using the MINC methodology as illustrated Figure 5.7 left for two different reasons. Firtly, the discretization of the matrix allows to take into account the long transient state of the flow between matrix and fracture because of the very low matrix permeability. Secondly, in order to well reflect the flow at fine scale, the triple porosity model also considers internal flow between large and small pores. In the flow from large pore to the fracture, the fluid can flow directly to small pores or continue to flow in another large pore media before finally flow to small pores. In the model, an exchange term is given between the large and small pores for each MINC volume j. The flow between small pores and fractures is only possible for the out-most small pore MINC volume. This flux is similar to the standard MINC model.

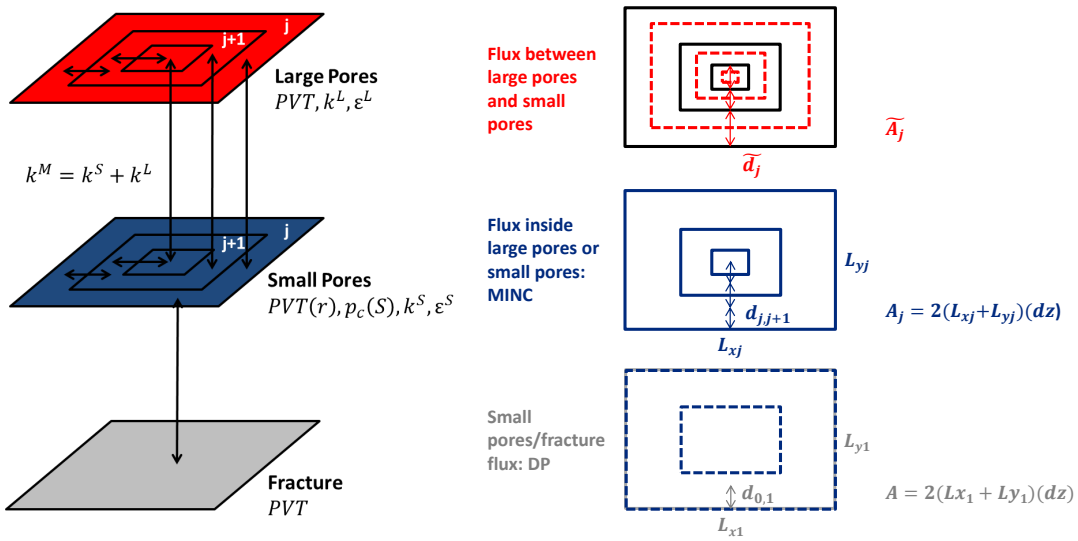

Figure 5.7: Schematic of triple porosity model discretization for one matrix/fracture block

On each MINC volume j, the system of Equations 5.11 can be written in a discretized form in both large and small pore for each component i.

$$\begin{cases} \frac{\partial M^i_{L,j}}{\partial t} = F^i_{L,j} - F^i_{LS,j} \\ \frac{\partial M^i_{S,j}}{\partial t} = F^i_{S,j} + F^i_{LS,j} - F^i_{SF} \end{cases} \tag{5.14}$$

The flux terms are calculated using their spacial discretization form. Let's take an example of a two dimension rectangular matrix block of dimension $L_{x1} \times L_{y1}$ with isotropic permeability as illustrated Figure 5.7. The flux between two MINC volumes j and j+1 of a matrix block inside the large pores and small pores medium $\xi = L, S$ for the components i is:

$$\begin{cases} f^i_{\xi,j,j+1} = -\gamma^\xi_{j,j+1}[(\rho_o x_i \lambda_o)^{j+1}_\xi (\Psi^{\xi,j}_o - \Psi^{\xi,j+1}_o) + (\rho_g y_i \lambda_g)^{j+1}_\xi (\Psi^{\xi,j}_g - \Psi^{\xi,j+1}_g)] \\ f^w_{\xi,j,j+1} = -\gamma^\xi_{j,j+1}(\rho_w \lambda_w)^{j+1}_\xi (\Psi^{\xi,j}_w - \Psi^{\xi,j+1}_w) \end{cases} \tag{5.15}$$

$$\gamma^\xi_{j,j+1} = \frac{A_{j,j+1} k^\xi}{d_{j,j+1}} \tag{5.16}$$

with $A_{j,j+1} = 2(L_{xj} + L_{yj})(dz)$ is the area surrounding a MINC volume j. $\gamma^\xi_{j,j+1}$ the transmissivity between two MINC volumes j and $j+1$ of the medium $\xi = S, L$, ie large pores or small pores. $d_{j,j+1}$ is the distance between two MINC volume j and $j+1$. These parameters are illustrated Figure 5.7 right. k^ξ is the permeability of the medium $\xi = S, L$ which is constant for a medium. λ_ϕ is the mobility of phase ϕ already defined in Section 4.2.1. $\Psi^{\xi,j}_\phi$ is the flow potential of phase ϕ for the MINC volume j of the medium $\xi = S, L$. This parameter is also

defined in Section 4.2.1. The terms $(\rho_o x_i \lambda_o)_\xi^{j+1}$, $(\rho_g y_i \lambda_g)_\xi^{j+1}$ and $(\rho_w \lambda_w)_\xi^{j+1}$ are computed with an upstream scheme according to the potential values in large and small pores ($\xi = S, L$).

The flux $F_{\xi,j}^i$ on each MINC volume j of medium $\xi = S, L$ for the component i is defined in the following equation for the two dimensions case. It is similar to the one presented in Section 5.1.2 describing the MINC method. The number of matrix blocks inside a cell is equal to $\frac{V_{cell}}{V_{block}}$ with $V_{block} = L_{x1} L_{y1}(dz)$.

$$F_{\xi,j}^i = \frac{V_{cell}}{V_{block}} (f_{\xi,j-1,j}^i + f_{\xi,j,j+1}^i) \tag{5.17}$$

The flux calculation between large pores and small pore media is a total novelty in this model. It is assumed that the transfer is proportional to an intrinsic parameter α, representing the average pore structure between large and small pores. Moreover, it is proportional to the average surface area perpendicular to the flow direction and inversely proportional to the average traveled distance along the flow direction in the MINC volume. On a MINC volume j the flux is computed by:

$$\begin{cases} F_{LS,j}^i = -\frac{V_{cell}}{V_{block}} \gamma_j^{LS} [(\rho_o x_i \lambda_o)_{\xi,j} (\Psi_o^{S,j} - \Psi_o^{L,j}) + (\rho_g y_i \lambda_g)_{\xi,j} (\Psi_g^{S,j} - \Psi_g^{L,j})] \\ F_{LS,j}^w = -\frac{V_{cell}}{V_{block}} \gamma_j^{LS} (\rho_w \lambda_w)_{\xi,j} (\Psi_p^{S,j} - \Psi_p^{L,j}) \end{cases} \tag{5.18}$$

$$\gamma_j^{LS} = \alpha \frac{\tilde{A}_j k^M}{\tilde{d}_j} \tag{5.19}$$

with γ_j^{LS} the transmissivity between the two media large pores and small pores for a MINC volume j. k^M is the permeability in the matrix. $\tilde{A}_j = \frac{2(L_{xj}+L_{yj})+2(L_{xj+1}+L_{yj+1})}{2}(dz)$. $\tilde{d}_j$ is the width of MINC volume j. These parameters are illustrated Figure 5.7 right. The average pore structure parameter α depends on PSD and is to be determined. $\xi = S$ or L according to the potential values in large and small pores (upstream scheme).

The flux between the small pore medium nearest MINC volume from the fracture and the fracture medium for components i is approximated by:

$$\begin{cases} F_{SF}^i = -\frac{V_{cell}}{V_{block}} \gamma^{SF} [(\rho_o x_i \lambda_o)_{\xi,1} (\Psi_o^F - \Psi_o^{S,1}) + (\rho_g y_i \lambda_g)_{\xi,1} (\Psi_g^F - \Psi_g^{S,1})] \\ F_{SF}^w = -\frac{V_{cell}}{V_{block}} \gamma^{SF} (\rho_w \lambda_w)_{\xi,1} (\Psi_p^F - \Psi_p^{S,1}) \end{cases} \tag{5.20}$$

$$\gamma^{SF} = \frac{A_{0,1} k^{SF}}{d_{0,1}} \tag{5.21}$$

with γ^{SF} the transmissivity between the outermost MINC volume in the small pore medium and the fracture medium. $A_{0,1} = 2(L_{x1} + L_{y1})(dz)$. The index j=0 corresponds to the fracture and the index $j = 1$ corresponds to the nearest MINC volume from the fracture. These parameters are illustrated Figure 5.7 right. k^{SF} is the average permeability between the nearest MINC volume of small pores from the fracture and the fracture medium. $\xi = S$ or F according to the potentials (upstream scheme).

It is important to only consider the small pore/fracture flow through the nearest MINC subdivision from the fracture. At fine scale only a small volume fraction of the matrix is in contact with the fracture. A small volume fraction of large pores or small pores must therefore be in contact with the fracture. The contact between large pores and fracture is not considered in this model. Indeed considering the flow from large pores to fracture through small pores enables to model the stall phenomenon observed at fine scale because of high capillary pressure in small pores. Therefore only a small volume fraction of small pores is considered in contact with the fracture. This small fraction is modeled by the outermost MINC volume of small pore medium.

The triple porosity model presented in this section has several unknown parameters to be determined. These parameters are the pore structure parameter α which involves in the transmissivity between the large pore and small pore media, the average pore radius value used for the flash in the small pore medium, the permeabilities and the porosities of small pore or large pore medium. They can be matched using the fine grid results as references. The strategy developed in this thesis is to use the fine grid results to calibrate the triple porosity model.

5.3 Upscaling

5.3.1 Methodology

The triple-porosity coarse grid simulation is performed on the same matrix block as the fine grid simulation presented in Section 4.3.1. An initial pressure is given at the matrix media, and a constant fixed pressure is imposed at the fractures. The matrix-fracture exchange rates are considered as the matching data. We will change various coarse grid triple-porosity parameters to calibrate the transfer rates from the fine grid simulations.

The fine grid model of matrix/fracture transfer with a block size of 20x20m presented in Section 4.3.1 is used as reference here for the calibration of the triple porosity model. The number of MINC discretization volumes used is the same than the one used for the upscaling of the matrix/fracture interaction for a bulk fluid in a dual porosity with MINC discretization in Section 5.1.3. The number of MINC volumes used in the triple porosity model is then ten. The large pore medium corresponds to the volume fraction of the matrix without confinement effect on the fluid. On the contrary the small pore medium includes a flash with capillary pressure

to take into account the confinement effect on the fluid inside nanopores. Therefore the large pore medium corresponds to the Facies 3 of the fine grid model and the small pores medium corresponds to the Facies 1 and 2 of the fine grid model. The properties of the three Facies are summarized in Table 4.5 in Section 4.3.1. Each distribution 'D' have different volume fraction of the three Facies (Table 4.6). The volume of large pore and small pore media must therefore be adapted for each distributions. The system of Equations 5.22 bellow gives the large pore and small pore volumes and porosities as a function of the matrix properties. The porous volume of the matrix and the volume fraction of each Facies are conserved.

$$\begin{cases} \epsilon^M V^M = \epsilon^L V^L + \epsilon^S V^S \\ \epsilon^M = \epsilon_1 v_{f1} + \epsilon_2 v_{f2} + \epsilon_3 v_{f3} \\ \epsilon^S = \frac{\epsilon_1 v_{f1} + \epsilon_2 v_{f2}}{v_{f1} + v_{f2}} \\ \epsilon^L = \epsilon_3 \\ V^L = v_{f3} V^M \\ V^S = (v_{f1} + v_{f2}) V^M \end{cases} \tag{5.22}$$

where $\epsilon^M, \epsilon^L, \epsilon^S$ are the porosities of the matrix, large pore and small pore medium respectively. V^M, V^L, V^S are the volumes of the matrix, large pore and small pore medium respectively. v_{f1}, v_{f2}, v_{f3} are the volume fractions of the Facies 1, 2, 3 respectively. Their values for each distribution 'D' are given in Table 4.6 in Section 4.3.1.

To reduce the number of calibration parameters, we assume that the flow between large pores and small pores is parallel. That means that the permeability of the matrix is equal to the sum of the permeabilities of small pores and large pores.

$$k^M = k^L + k^S \tag{5.23}$$

Here, the large pore permeability k^L reflects the connection between large pores, which are in reality separated by small pores. It is also possible that there are not direct connection between them. Other assumptions can also be used, for example, the weighted harmonic average: $\frac{V^M}{k^M} = \frac{V^L}{k^L} + \frac{V^S}{k^S}$, but this relation is not tested in this thesis.

Several calibration parameters are considered in the triple porosity model in order to match the fine grid production results. The main parameters are firstly the pore radius r used in the flash with capillary pressure (Section 3.2.1) performed in the small pore medium. Secondly, the pore structure parameter α in the flux between large pore and small pore media (Equation 5.19). Moreover, the permeability of the large pore medium k^L which gives the permeability in small pores medium k^S thanks to Equation 5.23. The small pore medium gathers Facies 1 and 2 which includes pores from 2 to 100 nm. The effect of confinement is very low for pore radius higher than 50 nm (see Figure 4.7 in Section 4.3.2), so a volume fraction of fluid in the small

pore medium may behave almost like a fluid in large pore medium without confinement effect. Therefore the volume fraction of large pores medium v_{f3} is also considered as a calibration parameter v_L. In order to respect the pore volume conservation of matrix, the porosity of the large pores medium is calculated by:

$$\epsilon^L = \frac{\epsilon^M - (1 - v_L)\epsilon^S}{v_L} \tag{5.24}$$

with $\epsilon^S = \frac{\epsilon_1 v_{f1} + \epsilon_2 v_{f2}}{v_{f1} + v_{f2}}$. So the porous volume of the matrix block is unchanged, because $\epsilon^L V^L + \epsilon^S V^S = \epsilon^L v_L V^M + \epsilon^S (1 - v_L) V^M$. We replace ϵ^L by Equation 5.24 and we find $\epsilon^L V^L + \epsilon^S V^S = \epsilon^M V^M$.

In conclusion there are four calibration parameters. Firstly, the average pore radius used in the small pore medium flash r. Secondly, the pore structure parameter α used in the transmissibility between large pore and small pore media. Afterwards, the large pore permeability k^L, which reflects the connection between different large pores. Finally, the large pore volume fraction v_L which is linked to the large pore porosity ϵ^L by the system of Equations 5.24. The different parameters are summarized Table 5.2.

Table 5.2: Calibration parameters of the triple porosity model

Calibration parameter	meaning
r	pore radius used in the flash with capillary pressure performed in the small pore medium
α	pore structure parameter used in the transmissibility between large pore and small pore media (Equation 5.19)
k^L	permeability of the large pore medium which is linked to k^S (Equation 5.23)
v_L	large pore volume fraction in the matrix which is linked to ϵ^L (Equation 5.24)

5.3.2 Numerical examples

A calibration of the triple porosity model using the four calibrations parameters as variables has been performed for each of the five distributions 'D'. The values of the calibration parameters which allow to get a good match with the fine grid production results are summarized Table 5.3 for every distributions 'D'. A certain logic is observed in the evolution of calibration parameters versus the increasing volume fraction of nano-pores from D1 to D5. The pore radius decreases from D1 to D3 because the radius is representative of the volume fraction of nano-pores in the

matrix. The large pore medium permeability decreases from D1 to D5 because at fine scale the volume of large pores surrounded by small pores decreases. Therefore in the triple porosity model the fluid can flow directly from large pores to small pores without internal flow inside large pore medium. The average pore structure parameter α depends on the PSD and the contact area between large and small pores. The large pore volume fraction is not used as a fitting parameter from D1 to D3, it is equal to the volume fraction of Facies 3 v_{f3}. The large pore volume fraction is increased for D4 and D5 in order to take into account the volume fraction of small pores with relatively large radius whose fluid behaves like bulk. The evolution of the different calibration parameters is not monotonic from D1 to D5 because the large pore volume fraction of D4 and D5 is modified.

Table 5.3: Calibration parameters

PSD	r (nm)	k^L (nD)	α	$v_L(\%)$	ϵ^L
D1	60	60	0.06	70	0.1
D2	6	60	0.08	59	0.1
D3	5	30	0.21	40	0.1
D4	7	0	0.14	40	0.0848
D5	10	0	0.08	40	0.061

The comparison between the calibrated triple porosity model and the fine grid production results for the distribution D1 is given Figure 5.8. It corresponds to the simulation case with a matrix block size of 20x20m. The results for the others distributions D2, D3, D4, D5 are given Figure D.1 to D.4 in appendix D.1. For all the distributions, the match between the triple porosity (3P MINC 10) and the fine grid (P50) production results is very satisfactory.

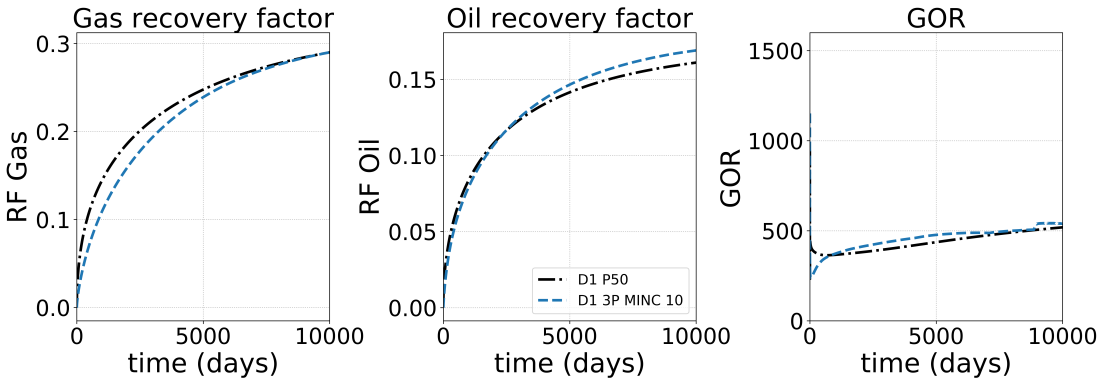

Figure 5.8: Calibration of D1 for block size 20x20m

We believe that the four calibration parameters: r, α, k^L and v_L for the triple porosity model depend mainly on the PSD. They do not depend a lot on the matrix block size and form.

In the following, the same calibration parameters summarized in Table 5.3 have been used for different simulation cases with different matrix/fracture configurations with matrix block sizes of 10x10m and 10x40m. These simulations cases have been presented in Section 4.3.2 and fine grid simulations have been performed. The comparison of triple porosity and fine grid production results for matrix block size of 10x10m which distribution D1 is given Figure 5.9. The results for the other distributions D2, D3, D4, D5 are given in the appendix D.2 Figure D.5 to D.8.

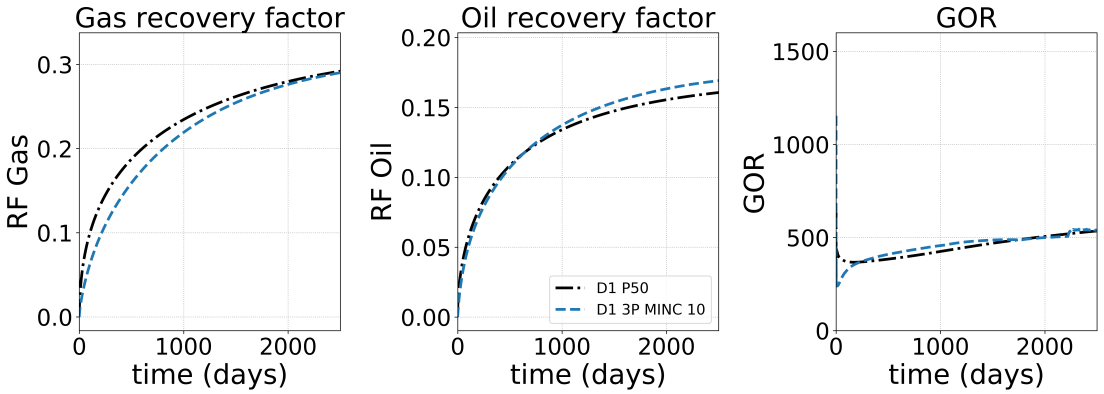

Figure 5.9: Calibration of D1 for block size 10x10m

The comparison of triple porosity and fine grid production results for matrix block size of 10x40m and for distribution D1 is given Figure 5.10. The results for the other distributions D2, D3, D4, D5 are given in the appendix D.3 Figure D.9 to D.12.

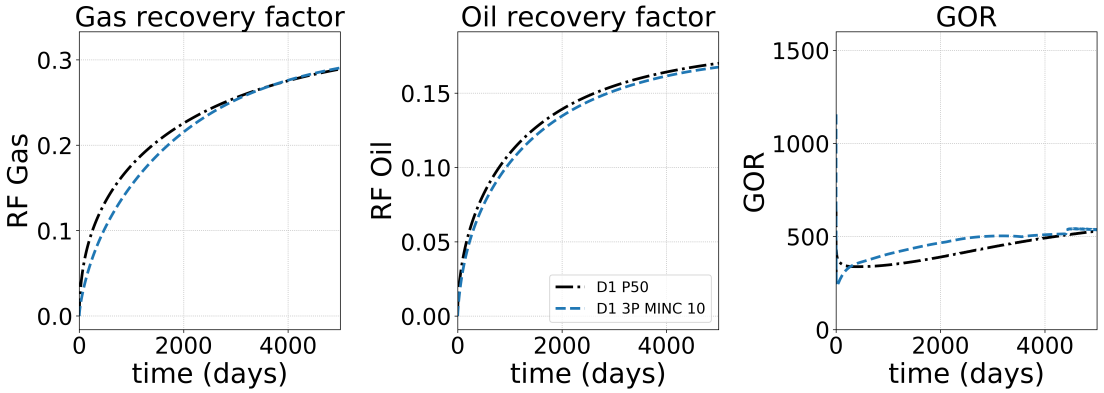

Figure 5.10: Calibration of D1 for block size 10x40m

The match between the triple porosity model and the fine grid production results are very good for all the distributions and for the different block sizes and matrix/fracture configurations. Given a PSD, only one calibration of the triple porosity model for a given matrix/fracture

configuration is necessary to upscale all other matrix/fracture configurations. The triple porosity model developed in this thesis is therefore efficient and robust. An upscaled model of the matrix/fracture interaction has been fitted for each of the five distributions 'D'. This model does not depend on the matrix/fracture configuration or the matrix block size. A large scale reservoir simulation case can therefore be built with this triple porosity approach.

5.4 Simulation of a fractured well in a stimulated reservoir volume (SRV)

In the literature, the reservoir simulation for an ultra low permeability reservoir at SRV scale is generally made with a single and a dual porosity model with a discrete pore size distribution of one value per cell or an average pore radius [41, 106, 7, 45, 73]. We propose here to apply the triple porosity model presented above to a large scale reservoir simulation of a horizontal producing well in a SRV.

5.4.1 Reservoir model

The large scale reservoir simulation model is represented in Figure 5.11. The flow between cells of the same medium is only possible for the fracture medium as illustrated by the arrows in Figure 5.11. F_F^i should therefore not be zero in Equation 5.11. The flux between a given cell of the fracture medium with its neighboring cells is calculated using Equation 5.13. The matrix is considered heterogeneous with different PSD inside. Then a spacial distribution of the different distributions 'D' has been built. The different calibrated triple porosity model for a given distribution 'D' presented in the previous section for one fracture cell are therefore linked together through the fracture medium according to their spacial coordinates. The different upscaled parameters of the triple porosity models for each distributions 'D' are the same as the one used in previous section in Table 5.3.

A SRV simulation case has been built according to Figure 5.12 with one horizontal well in the center. The 2D grid is 2000m length and 1300m width and the cell dimensions in the x, y and z directions are 100x100x10m. The matrix block size used for the matrix-fracture transfer modeling is 20x20m. Therefore, there are 5 matrix blocks per cell. The fracture permeability in the well cells is fixed to 100D and the remaining SRV have an equivalent fracture permeability of 0.01D and 0.001D as illustrated in Figure 5.12 left. A random realization of the different distributions D1, D2, D3, D4, D5 has been performed in the matrix as illustrated Figure 5.12 right. The distribution corresponds to a volume fraction of 15% of D1, 40% of D2, 10% of D3, 15% of D4 and 20% of D5. The simulation setup is the same as the one detailed in Section 4.3.1. Bakken oil is used for the simulation, the initial pressure in the SRV is 200 bar and the production pressure of the well is fixed to 100 bar. The production from the SRV through the

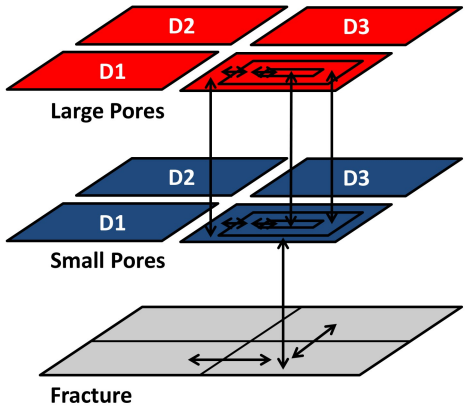

Figure 5.11: Schematic of MINC triple porosity model for SRV simulation

horizontal well is simulated during 10 000 days.

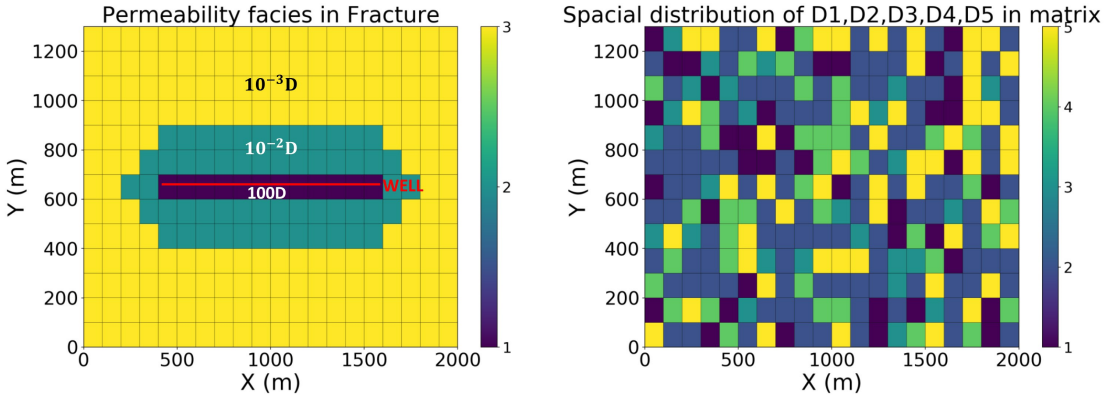

Figure 5.12: SRV fracture grid and spacial distribution of D1, D2, D3, D4, and D5 in matrix

5.4.2 SRV production results

Figure 5.13 represents the production results for bulk fluid in a dual porosity MINC method ("Bulk 2P MINC 10") and for confined fluid. The confined fluid production is modeled by the dual porosity MINC method ("D distribution 2P MINC 10") and the triple porosity model ("D distribution 3P MINC 10"). The "Bulk 2P MINC 10" model corresponds to a dual porosity model with 10 MINC volumes and zero capillary pressure. The classic Peng Robinson EOS is used and different porosities are assigned in each cell according to the PSD. The "D distribution 2P MINC 10" model corresponds to a dual porosity model with 10 MINC volumes, capillary pressure and pore radius dependant EOS in the matrix. Similarly, different porosities are assigned in each cell (or PSD). The pore radius assigned to each cell corresponds to the one used in the calibrated triple porosity model for the PSD considered. The confined "D distribution 3P

MINC 10" model corresponds to the triple porosity model presented in section 5.3 with different upscaled parameters for each cell (or PSD) summarized in Table 5.3. The dual-porosity MINC simulation is usually used in the literature to study tight oil and shale gas reservoirs production with nanopore modified PVT behavior. The differences between the triple-porosity MINC simulation and the dual-porosity MINC simulation are very large (Figure 5.13). As observed at matrix/fracture interaction scale, the production results of the "D2 3P MINC 10" model shows higher oil production and lower gas production and GOR than the "Bulk 2P MINC 10" results. This trend observed at fine scale (Section 4.3.2) and in field observation (Section 1.3.2) is not represented by the "D distribution 2P MINC 10" model mostly used in the literature. We therefore believe that the triple porosity approach gives more reliable results, and the dual porosity model is not very accurate to handle the pore size distribution issue.

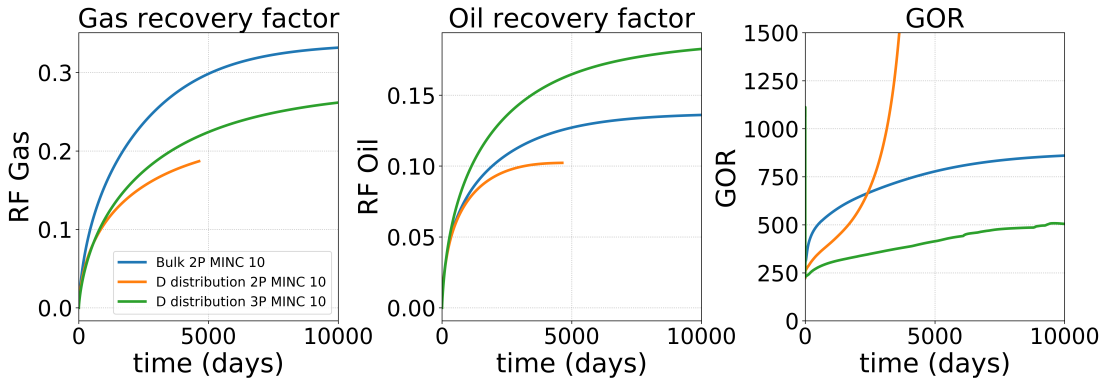

Figure 5.13: Production results of the SRV with spacial distribution of D1, D2, D3, D4 and D5

Pressures and saturation fields have been plotted in Figure 5.14, 5.15 and 5.16 for a specific time (980 days) in each sub domains of the triple porosity model: fracture (F), small pores (SP) and large pores (LP). The gas saturation is higher in the large pore medium than in the small pore medium. This is due to the bubble point decrease in the small pore medium because of the pore dependent PVT behavior. The gas pressure is higher than the oil pressure only in the small pores medium. Indeed, capillary pressure is equal to zero in large pore, which is not the case in small pores. This difference of capillary pressure participates to slow down the gas flow from large pore medium to fracture through small pore medium where capillary pressure is high. This example shows that the effect of pore size dependent PVT behavior and capillary pressure heterogeneity observed at fine scale (Section 4.3.2) are taken into account in the triple porosity model.

5.5 Summary and discussions

The upscaling of the matrix/fracture interaction for unconventionnal reservoirs, which needs to take into account a very heterogeneous PSD and pore radius dependent PVT behavior, is

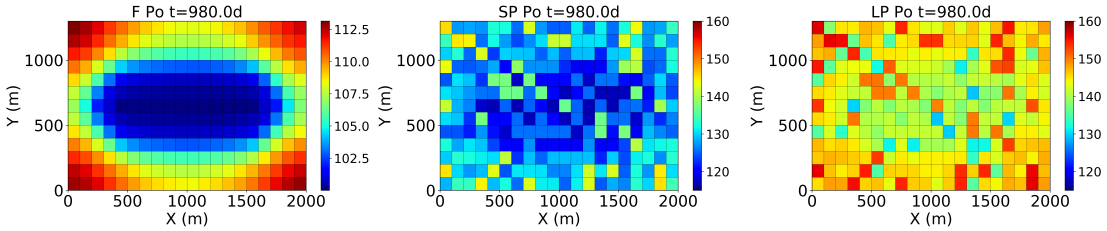

Figure 5.14: Oil pressure field in fracture (F), small pore (SP) and large pore (LP) of the triple porosity model at 980 days

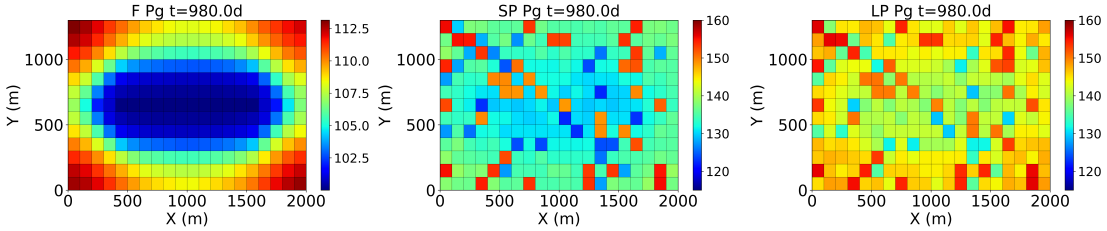

Figure 5.15: Gas pressure field in fracture (F), small pore (SP) and large pore (LP) of the triple porosity model at 980 days

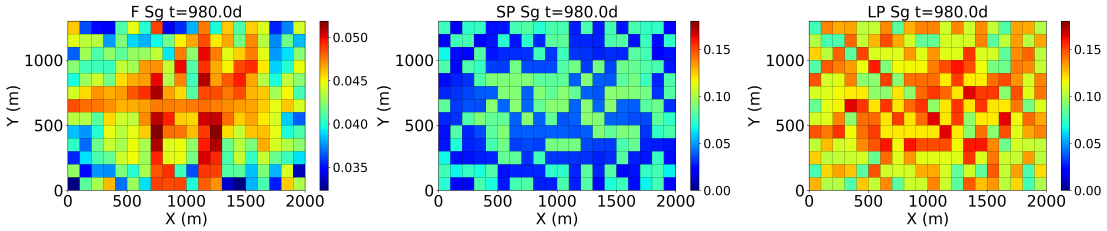

Figure 5.16: Gas saturation field in fracture (F), small pore (SP) and large pore (LP) of the triple porosity model at 980 days

crucial for accurate large scale production results. Some upscaling methodologies are proposed in the literature either for matrix/fracture exchange or PSD upscaling. Comparing the coarse grid results with reference fine grid simulations presented in Section 4 has allowed to conclude about the relevance of the upscaling models. The simulation of the flow between matrix and fracture for a bulk fluid needs a dual porosity with a MINC discretization of the matrix in order to take into account the long transient state of the flow because of low matrix permeability. The methodologies proposed for the upscaling of the PSD such as the commonly-used dual porosity MINC model with an average pore radius (whatever the pore radius size) or effective pore radius are unable to match the fine grid results. A new triple porosity model has therefore been presented in this chapter.

The new triple porosity model has been built with three domains: fracture, small pores and

large pores. The flow goes from the large pores to the fracture through the small pores. Fracture and large pore domain have a classic Peng Robinson EOS with zero capillary pressure for the flow calculation. The small pore domain has a modified Peng Robinson EOS with capillary pressure and a saturation dependent capillary pressure for the flow calculation. The two effects of capillary pressure heterogeneity and pore radius dependent EOS are therefore taken into account in the upscaled model. A MINC discretization is performed in the matrix medium with a fraction of small pores and large pores corresponding to a given PSD, and the flow transfer is considered both inside them and between them. This discretization enables to firstly take into account the long transient state of the flow between matrix and fracture. Secondly, it enables to consider internal flow inside large pore and small pore media before flowing to the next medium. A calibration of the triple porosity model for several PSD fine grid results has been done using four fitting parameters: the pore radius used in the small pore medium flash r, the pore structure parameter α of the flux between large pores and small pores, the large pore permeability k^L, and the large pore porosity ϵ^L which is linked to the large pore volume fraction v_L. The same fitting parameters have been used for different matrix/fracture configuration and matrix block sizes. The match between fine grid and triple porosity model production results is very good for all the studied cases. The new triple porosity model built is therefore robust and efficient. It enables to simulate large scale reservoir production.

A large scale SRV model has been built by taking into account the pore size distribution and its spatial variation over the simulation cells. The different calibrated triple porosity model for a given PSD have been linked together through the fracture medium according to their spacial coordinates. The SRV has been simulated with different coarse grid models. The triple porosity approach has shown quite different results, compared to the commonly-used dual porosity models with an equivalent nanopore radius. We believe that the triple porosity approach is more suitable for the handling of complex physics in nanoporous reservoirs, and gives more reliable results. An increase of oil production and a decrease in gas production and GOR is observed compare to the bulk, which is not the case for a dual porosity model.

Chapter 6

Conclusion and discussion

In this Chapter, we summarize and conclude this work. Furthermore some suggestions of future work are presented.

6.1 Summary and conclusion

Unconventional low permeability reservoirs are characterized by a very heterogeneous pore size distribution (PSD) and an important volume fraction of nanopores. These particularities modifies the PVT behavior of the fluid which becomes pore size dependent. Then, along the flow from the matrix to the fracture, the fluid flows through pores with different thermodynamic behavior and capillary pressures. The flow and the reservoir production are therefore inevitably altered from a conventional case without fluid confinement. This thesis has therefore proposed a methodology in order to model accurately the flow and the thermodynamic behavior of the fluid in unconventional low permeability reservoir. This modeling is crucial in Oil&Gas industry for proper reservoir production forecast and optimization. The thesis work was focused on four main parts detailed below.

- The Monte Carlo molecular simulation has allowed to study and get reference results of the thermodynamic properties and behavior of a confined fluid at liquid/vapor equilibrium. A new methodology and workflow in the Gibbs ensemble has been established for pure components and mixtures confined in a slit pore. The confined GEMC NVT simulation has been used instead of the more traditional GCMC simulation because of its limitations. Even though the GEMC NVT simulation is more precise and allows confined pressure calculation, it needs good initialization to converge. Therefore, the use of confined GCMC μVT simulation in nanopores has been used to get approximate initial vapor and liquid densities of pure components and the pseudo-ensemble GEMC NPT BPMC has been adapted for confined fluid for the initialization of the confined GEMC NVT simulation for mixtures. The liquid/vapor equilibrium thermodynamic properties of the confined fluid

are completely different from the bulk one. Phase envelopes of different mixtures have been built and show that the bubble-point pressure decreases as the dew-point pressure increases with confinement and the critical point is shifted from its bulk value. A work of analysis has been done in order to clarify the consideration of the reference pressure in confinement. When we compare a bulk fluid to a confined fluid, two systems are in reality compared. A single bulk fluid and a bulk fluid in thermodynamic equilibrium with a confined fluid. Only one pressure is present in the first system and three different pressures are present in the second system: the bulk pressure and the confined liquid and vapor pressures. In these systems, the bulk pressure can then be used as reference. The calculation and comparison of the different pressures observed in the confined systems are to the best of our knowledge, a novelty in this field. All the results for pure components and mixtures provide relevant information concerning the understanding of the phase behavior in confined systems and can be used as reference values for the development of pore radius dependent EOS.

- Thanks to the reference results from molecular simulation, we have highlighted the best pore size dependent thermodynamic flash proposed in the literature. The different methods proposed in the literature have been investigated and improved. A flash with capillary pressure has been implemented and the algorithm has been improved using an under relaxation scheme for capillary pressure in order to avoid divergence issues. The correlation of Meyra et al. [77] for pure component critical temperature and the correlation of Jin et al. [52] for pure component critical pressure have been validated with the reference molecular simulation results. Moreover, a comparison between mixture molecular simulation results and mixture critical point calculation by means of EOS has proven that the correlations are extensible to mixtures. These correlations are therefore chosen for the flash with critical temperature and pressure shift. The flash with capillary pressure, the flash with critical point shift and both methods used together have been applied to two different confined mixtures at given temperature, pressure and pore size and the results have been compared to reference molecular simulation results. The best match is obtained with a flash with both capillary pressure and critical point shift. To the best of our knowledge, this is the first time that the different flash methods for a confined fluid have been compared and analyzed with reference results from molecular simulation.

- The modified pore size dependent EOS has been included into a reservoir simulator. It allows to study the impact of confinement on the matrix/fracture exchange which is the main driver of tight oil and shale gas reservoir production. Reservoir simulations have been performed for different PSD at the matrix block scale with very fine grids. Besides studying the impact of confinement on production, this enables to get reference production results for the development of upscaling methodologies for large scale reservoir simulations. For all the PSD studied, the impact of pore confinement on reservoir production increases the oil production and decreases the gas production and the GOR compared with the

bulk fluid. It is manifested by two effects: capillary pressure heterogeneity and pore size dependent PVT modeling. The impact of capillary pressure heterogeneity on reservoir production is significant for slightly low percentage of nano-pores. Large volume of gas might be trapped in very large pores with zero capillary pressure surrounded by tiny pores with high capillary pressure. The impact of pore size dependent PVT modeling becomes significant for higher volume fraction of nano-pores. The volume of oil with lower bubble point becomes then significant to impact the production.

- Large scale unconventional low permeability reservoir simulation needs upscaling methodologies because of computational constraints. Upscaling methodologies proposed in the literature either for matrix/fracture exchange or PSD upscaling have been investigated using fine grid production results at the matrix block scale as reference. We have shown that the commonly-used dual porosity MINC model with an average pore radius (whatever the pore radius size) or effective pore radius are unable to match the fine grid results. A new triple porosity model has therefore been developed in this thesis. Our model considers three domains: fracture, small pores and large pores with their own PVT model and petrophysic properties. A pore size dependent PVT model is used in the small pore medium and classic bulk PVT model is used in large pores and fracture media. A MINC discretization is performed in the matrix medium. This discretization enables to firstly take into account the long transient state of the flow between matrix and fracture. Secondly, it enables to consider internal flow inside large pores and small pores media before flowing to the next medium. A calibration of the triple porosity model for several PSD fine grid results have been done using four fitting parameters. The same fitting parameters have been used for different matrix/fracture configuration and matrix block sizes. The match between fine grid and triple porosity model production results is very good for all the studied cases. The new triple porosity model built is therefore robust and efficient. As an application case, a large scale SRV model with heterogeneous PSD has been built using our triple porosity model. The triple porosity approach has shown quite better results, compared to the commonly-used dual porosity models with an equivalent nanopore radius. We believe that the triple porosity approach is more suitable for the handling of complex physics in nanoporous reservoirs, and gives more reliable results.

The methodology developed in this thesis to model unconventional low permeability reservoir production is summarized in Figure 6.1. This is a multi-scale approach where the thermodynamic and the flow of the confined fluid has been modeled and studied from nano-pore scale to matrix/fracture scale and finally reservoir scale. From given PSD measured in laboratories for different facies of a reservoir, different fine scale reservoir simulations can be performed for these PSD at matrix block scale. This fine grid simulation includes the modified pore size dependent EOS. These fine grid results are used to calibrate the triple porosity for the different PSD. Then a large scale SRV can be built using the triple porosity model calibrated for the different PSD corresponding to the reservoir facies. Finally we can get accurate production results of the SRV

considering fluid confinement. This methodology has been the subject of a patent [117]. One paper has been published based on the methodology and results presented in Chapter 2 [118] and a conference paper has been published relating to the triple porosity model [119]. I am the second author of the paper [142] proposing a technique to speed up the time consuming flash calculation using deep learning. Finally, a paper concerning the results presented in Chapter 4 and the new triple porosity model developed in Chapter 4 is in process of writing.

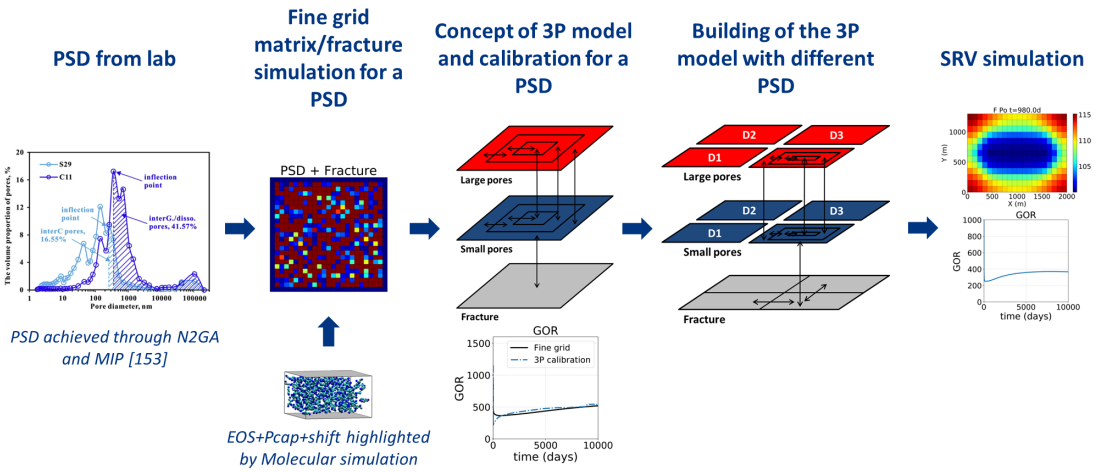

Figure 6.1: Schematic of the methodology developed in this thesis to model accurately unconventional reservoir including strong PSD heterogeneity and pore size dependent PVT behavior of the fluid.

6.2 Suggestions for future work

- Monte Carlo molecular simulation has been performed on four pure components: methane, ethane, n-pentane and n-decane and two mixtures: methane/ethane and ethane/n-pentane. The liquid-vapor equilibrium calculations have been done for different pore sizes and temperature for pure components and for 3 nm pore size and different compositions, pressure and temperature for mixture. In order to test the methodology developed using the confined GEMC NVT simulation, it would be interesting to perform simulations for other pure components, mixtures and pore sizes. Furthermore it would give more reference results for modified or new EOS development. The density functional theory (DFT) and fundamental-measure theory (FMT) may represent an interesting alternative to the Monte Carlo molecular simulation in order to study thermodynamic behavior of confined fluid [14, 15, 80, 76]. The equilibrium density distribution is calculated through the minimization of the grand potential which implies to solve the Euler-Lagrange equation. It is a theoretical method with a faster calculation time than molecular simulation. However, some challenges are still present like the flexible molecule model or the confined phase

adsorption length definition.

- In this thesis, different flash methods used in the literature to model confined fluid PVT behavior have been implemented and compared to reference molecular simulations. The best match is obtained for the flash including capillary pressure and the shift of the critical point. The match is not perfect and can be improved by calibration of given parameters of the modified EOS. For example, volume correction parameters, the contacting angle of the fluid and the interaction parameters can be used as optimization parameters. Methods considering the modification of existing EOS like Peng-Robinson are mainly used because it is easier to implement into a reservoir simulator. New EOS incorporating fluid confinement have been developed in the literature [126, 11, 74]. An interesting work could be to implement one of these new EOS and compare their results with reference ones from molecular simulations for a given confined fluid properties.

- The fine grid matrix/fracture exchange simulation for different PSD is very time consuming because of the capillary pressure loop in the flash and the presence of divergence issues. Some work can be done on the algorithm to speed up the convergence time and its robustness. An interesting work has been done by Wang et al. [142] to speed up the time consuming flash calculation using deep learning. A data-based proxy flash calculator has been developed using an initial guess obtained from the deep neural network with an accuracy above 95%. With the implementation of the proxy calculator, the number of iterations of the flash calculation has been effectively reduced by 50%. Three dimensional fine grid simulations should be done to investigate the contribution of the gravity effects for the confined fluid in the matrix-fracture transfer. Correlation length for the pore size distribution needs also to be considered in the geostatistical realizations and in the interaction of the matrix-fracture flow.

- The new triple porosity model developed in this thesis has been calibrated and validated using fine grid reservoir simulation results at the matrix block size. In order to test the robustness of the model, calibration and validations should be made on a discrete fracture network instead of on rectangular matrix blocks. Furthermore, several hypothesis have been made on fine grid reference simulations such as the same relative permeability curve on all the facies. Additional test and improvements should then be made using different relative permeabilities per facies for example. Finally the triple porosity model should be applied to a three dimension reservoir model. The actual triple porosity model considers the flux between grid cells only by the fracture medium. There is not direct fluid flow between two matrix grid cells. A new triple porosity model might be necessary to take into account direct matrix flow.

Appendix A

Molecular simulation Appendices

A.1 Simulation parameters

The different move probabilities and Monte Carlo steps used for non-flexible and flexible molecules are summarized in Table A.1 for GCMC μVT simulations, in Table A.2 for GEMC NVT simulations and in Table A.3 for GEMC NPT BPMC simulations.

Table A.1: Simulation parameters for GCMC simulations.

	Move	Probability
Non flexible molecules	Translation	0.25
	Rotation	0.25
	Insertion/deletion	0.5
Flexible molecules	Translation	0.1
	Rotation	0.1
	Internal regrowth	0.1
	Internal rotation	0.1
	Insertion/deletion	0.6

Local z density of the confined fluid has been built by averaging the number of particles per slice. 100 000 000 Monte Carlo iterations have been performed on a equilibrated GEMC NVT simulation with an output of the particles coordinated every 5000 steps, then there are in the end 20 000 configurations which have been averaged per slice. The space between the two walls has been divided into 100 slices. As the slit width is 3 nm, each slice represents 0.003 nm. The liquid and the vapor boxes used are of lengths 5x5x3 nm for the $CH_4 - C_2H_6$ mixture. The liquid box length are 9x9x3 nm and the vapor boxes are 7x7x3 nm for the $C_2H_6 - C_5H_{12}$ mixture.

Table A.2: Simulation parameters for GEMC NVT simulations.

Type of molecules	Period	Monte Carlo steps	Moves	Probability
Non flexible molecules	1	10^6	Translation	0.3
			Rotation	0.3
			Volume change	0.4
	2	10^8	Translation	0.2
			Rotation	0.2
			Volume change	0.05
			Particle transfer	0.55
Flexible molecules	1	10^6	Translation	0.25
			Rotation	0.25
			Internal regrowth	0.25
			Internal rotation	0.25
	2	10^8	Translation	0.175
			Rotation	0.175
			Internal regrowth	0.15
			Internal rotation	0.145
			Volume change	0.005
			Particle transfer	0.35

A.2 Results

The different results for pure components and mixtures are given in figure A.1 and figure A.2.

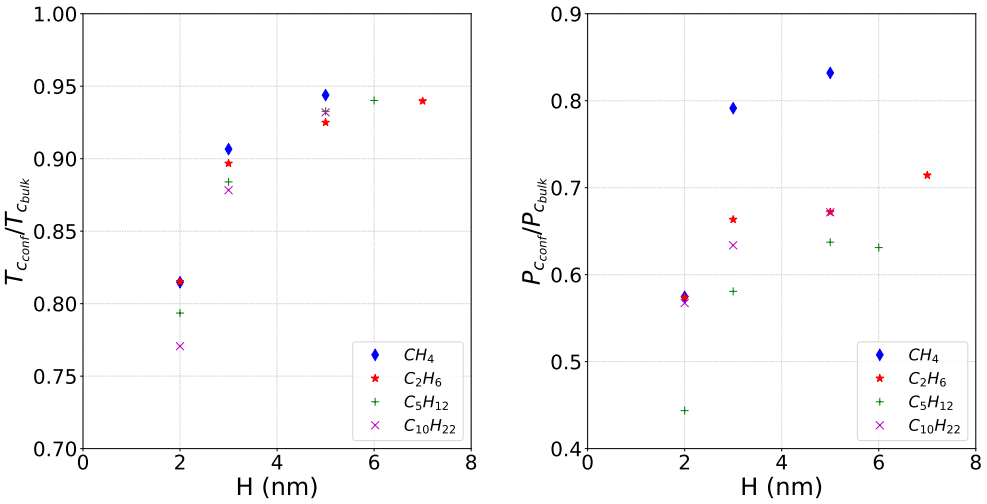

Figure A.1: Evolution of critical temperature (left) and pressure (right) versus pore diameter (H) for CH_4, C_2H_6, C_5H_{12} and $C_{10}H_{22}$.

Table A.3: Simulation parameters for GEMC NPT BPMC simulations.

Type of molecules	Period	Monte Carlo steps	Moves	Probability
Non flexible molecules	1	10^6	Translation	0.3
			Rotation	0.3
			Volume change	0.4
	2	10^8	Translation	0.2
			Rotation	0.2
			Volume change	0.05
			BPMC	0.55
Flexible molecules	1	10^6	Translation	0.1
			Rotation	0.1
			Volume change	0.6
			Internal regrowth	0.1
			Internal rotation	0.1
	2	10^8	Translation	0.1
			Rotation	0.1
			Internal regrowth	0.1
			Internal rotation	0.1
			Volume change	0.05
			BPMC	0.55

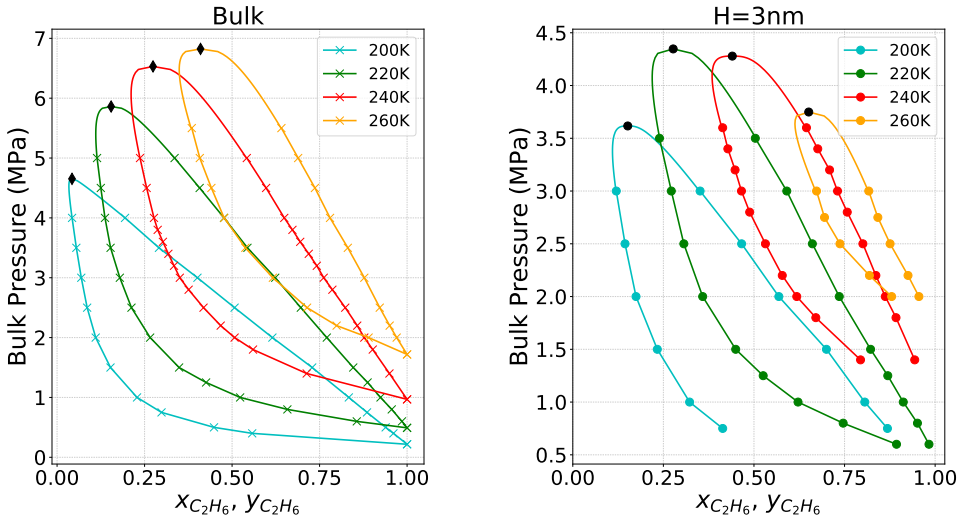

Figure A.2: Pressure-molar fraction diagram of methane/ethane for different isotherms for a bulk (left) and a confined fluid (right). The 'x' symbols correspond to bulk NPT results, the critical points of each isotherm are in black diamonds. The circles correspond to confined NVT results for H=3 nm, the critical points of each isotherm are in black circles.

Appendix B

Thermodynamic modeling Appendices

B.1 Solving the cubic polynomial equation

The Cardan procedure enables to compute analytically the roots of the third order polynomial:

$$Z^3 + a_1 Z^2 + a_2 Z + a_3 = 0 \tag{B.1}$$

taking

$$Q = \frac{3a_2 - a_1^2}{9} \tag{B.2}$$

$$R = \frac{a_2 a_1}{6} - \frac{a_3}{2} - \frac{2a_1^3}{27} \tag{B.3}$$

the discriminant is given by:

$$D = Q^2 + R^2 \tag{B.4}$$

- If $D > 0$, there is only one real root:

$$Z = \sqrt{3}R + \sqrt{D} + \sqrt{3}R - \sqrt{D} - \frac{a_1}{3} \tag{B.5}$$

- If $D = 0$, there are three real roots, with two equals:

$$\begin{cases} Z_1 = 2\sqrt{3}R - \frac{a_1}{3} \\ Z_2 = Z_3 = -\sqrt{3}R - \frac{a_1}{3} \end{cases} \tag{B.6}$$

- Else if $D < 0$ there are three real roots:

$$\begin{cases} Z_1 = 2\sqrt{-Q}cos\left(\frac{\theta}{3}\right) - \frac{a_1}{3} \\ Z_2 = 2\sqrt{-Q}cos\left(\frac{\theta}{3} + \frac{2\pi}{3}\right) - \frac{a_1}{3} \\ Z_3 = 2\sqrt{-Q}cos\left(\frac{\theta}{3} + \frac{4\pi}{3}\right) - \frac{a_1}{3} \\ \theta = arccos\left(\frac{R}{\sqrt{-Q^3}}\right) \end{cases} \tag{B.7}$$

Appendix C

Matrix/fracture interaction with PSD Appendices

C.1 Block size 20x20m

C.1.1 Five realizations of D1

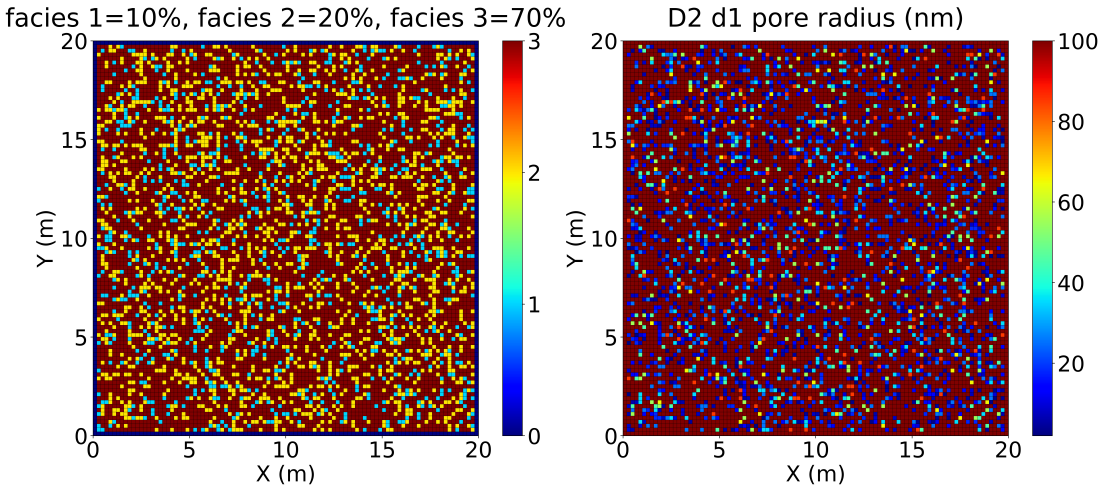

Figure C.1: Facies and pore radius field inside the matrix for distribution D1 d1 (block size of 20x20m).

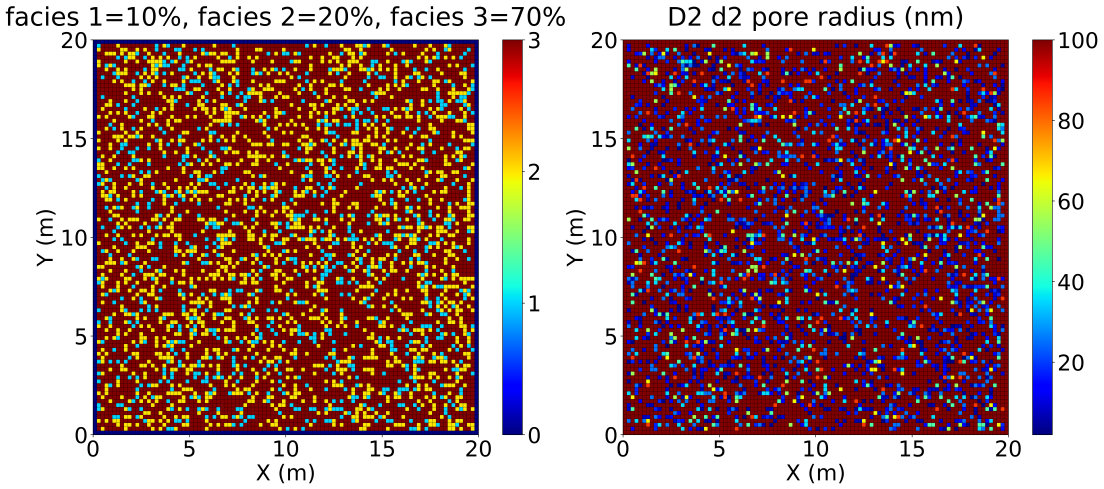

Figure C.2: Facies and pore radius field inside the matrix for distribution D1 d2 (block size of 20x20m).

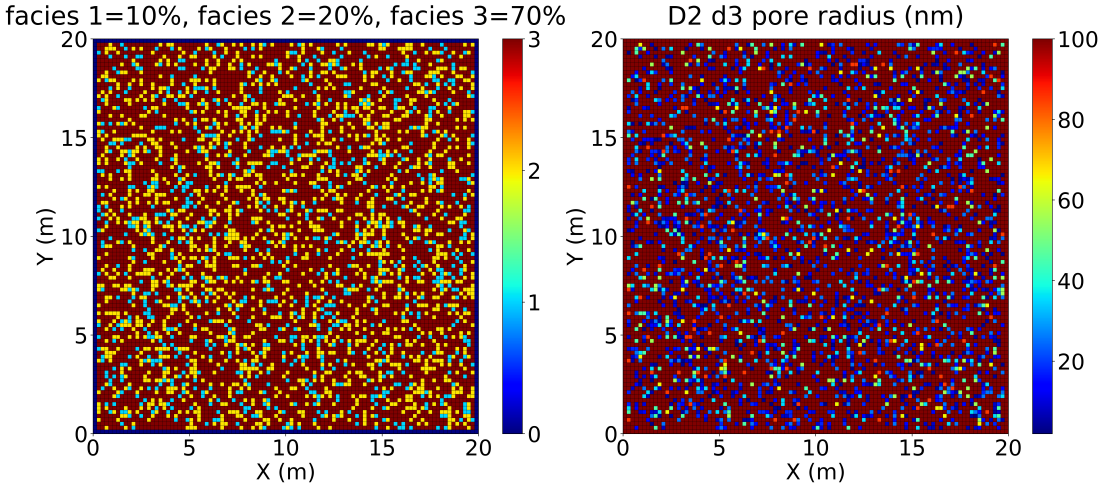

Figure C.3: Facies and pore radius field inside the matrix for distribution D1 d3 (block size of 20x20m).

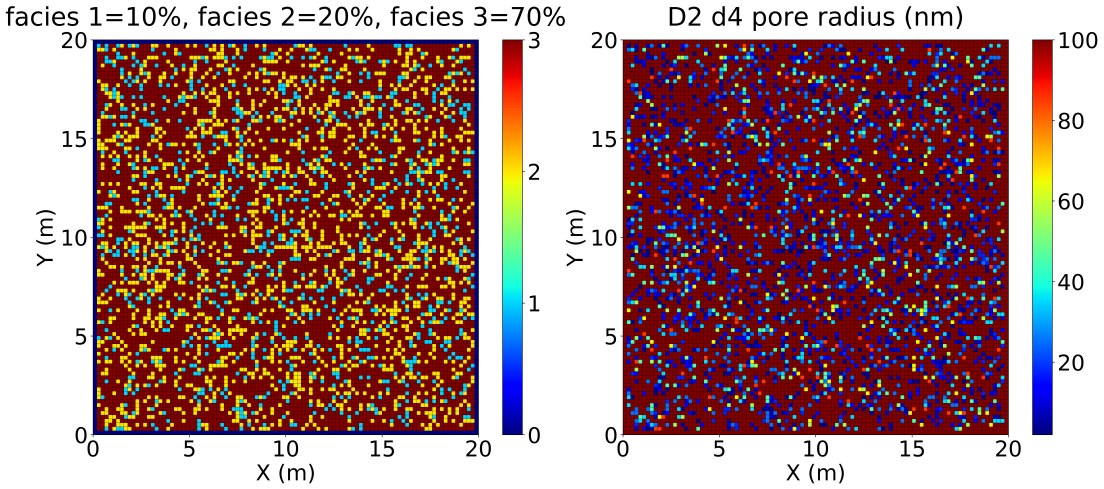

Figure C.4: Facies and pore radius field inside the matrix for distribution D1 d4 (block size of 20x20m).

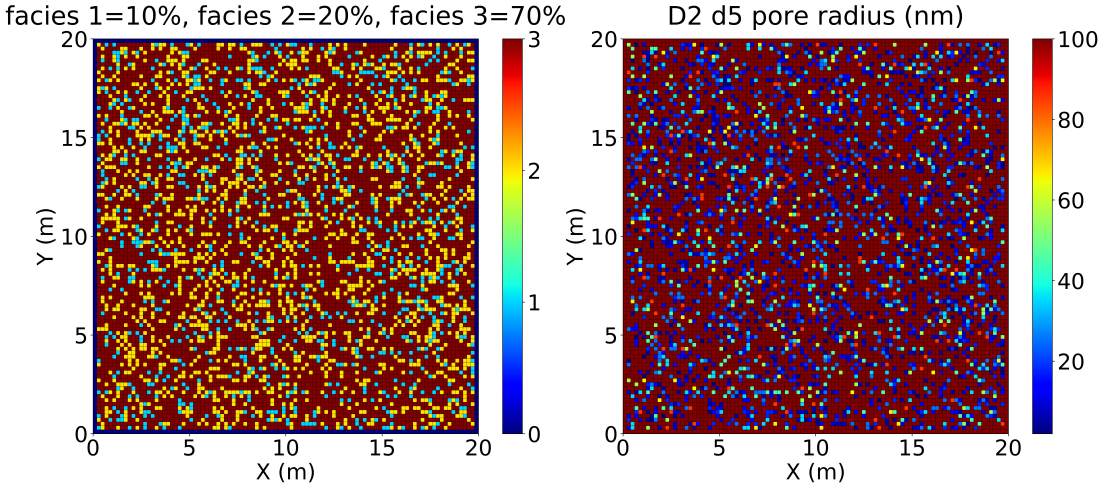

Figure C.5: Facies and pore radius field inside the matrix for distribution D1 d5 (block size of 20x20m).

C.1.2 Distributions D

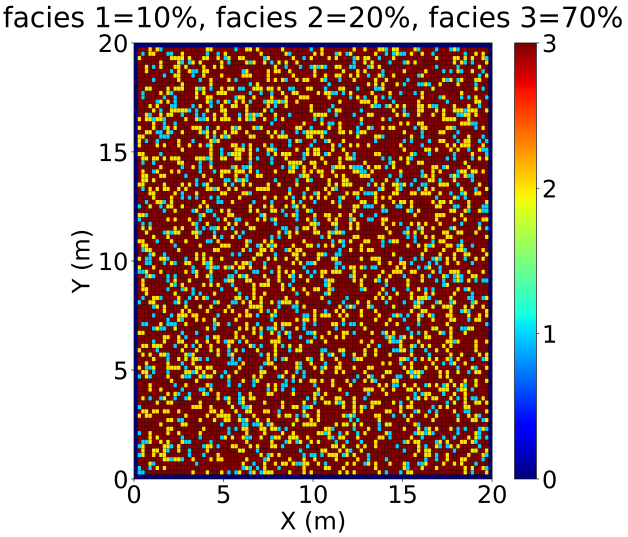

Figure C.6: Facies field inside the matrix for distribution D1 d1 (block size of 20x20m).

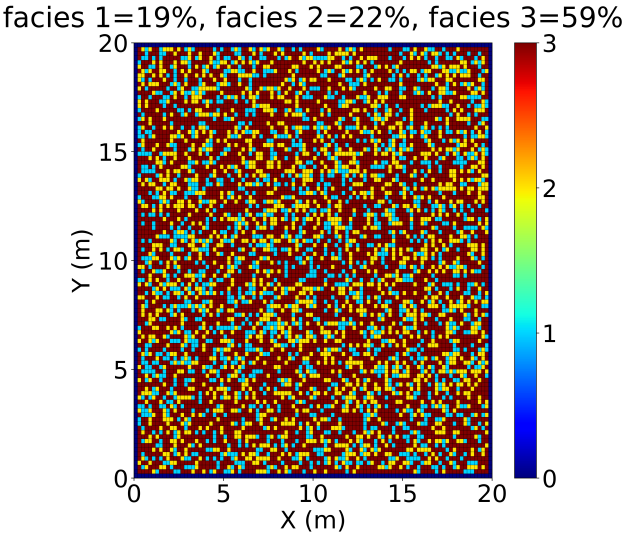

Figure C.7: Facies field inside the matrix for distribution D2 d1 (block size of 20x20m).

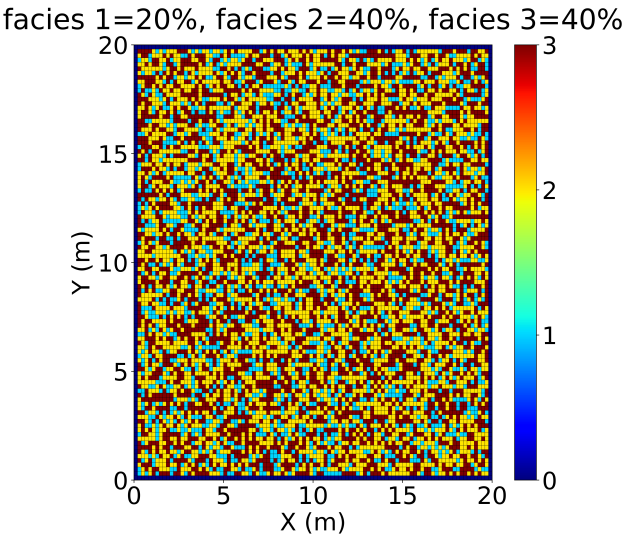

Figure C.8: Facies field inside the matrix for distribution D3 d1 (block size of 20x20m).

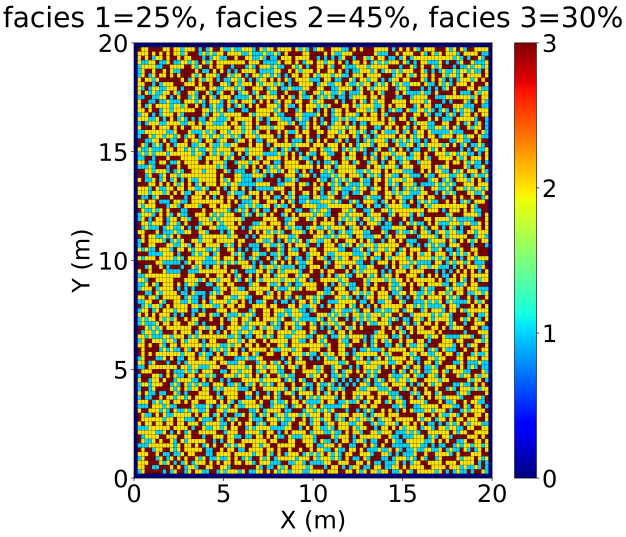

Figure C.9: Facies field inside the matrix for distribution D4 d1 (block size of 20x20m).

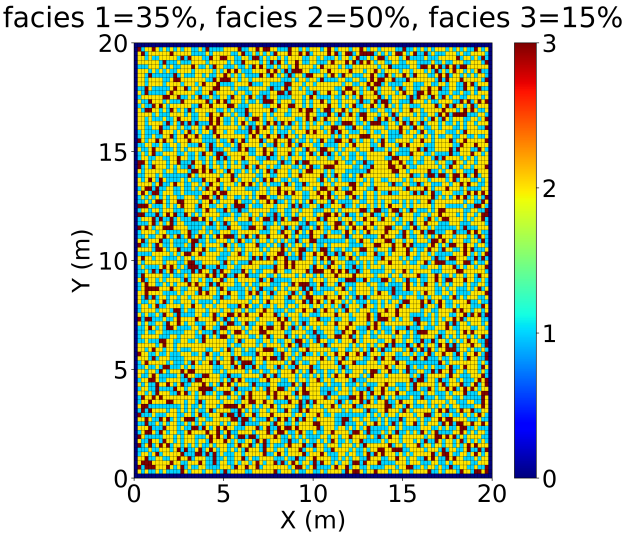

Figure C.10: Facies field inside the matrix for distribution D5 d1 (block size of 20x20m).

C.1.3 Simulation results

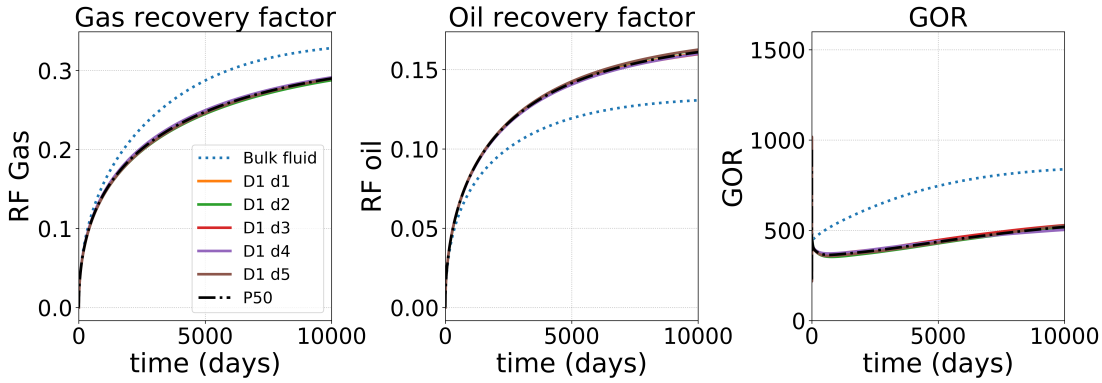

Figure C.11: Production results for the five samples of distribution D1 compared to bulk (block size of 20x20m).

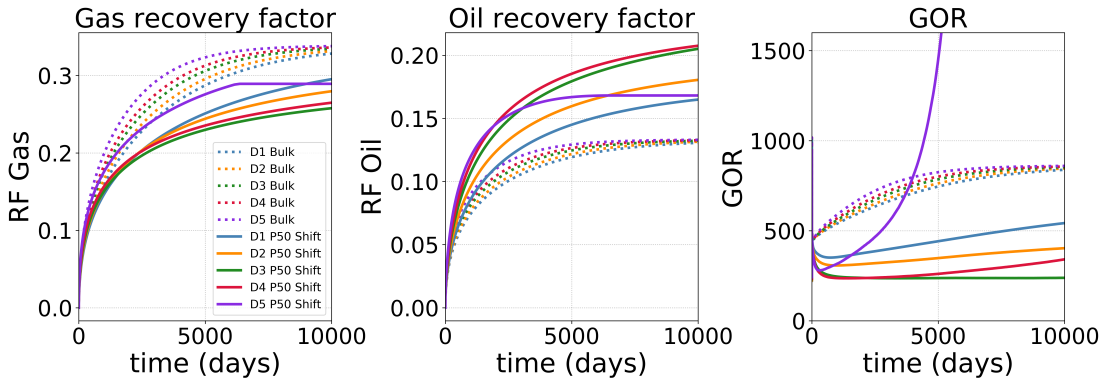

Figure C.12: Comparison of production results for the different distributions for bulk and confined fluid with a flash with critical point shift (block size of 20x20m).

C.2 1D matrix block with size 5x0.5m

The simulation cases with a 1D matrix block are presented Figure C.13. The considered domain of the matrix block size is 5x0.5m. The simulation setup is the same than the one presented in Section 4.3.1.

C.2.1 Examples of realizations of D1

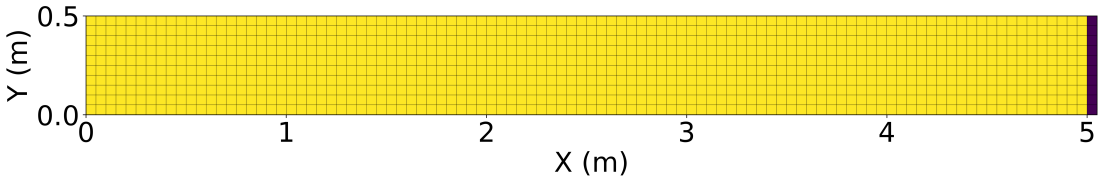

Figure C.13: Geometry with a block size of 5x0.5m. The matrix is in yellow and the fracture is in purple.

Table C.1: Geometry parameters with a block size of 5x0.5m

	Matrix	Fracture
Number of cells	100x10x1	1x10x1
dx/dy/dz (m)	0.05/0.05/0.05	0.05/0.05/0.05

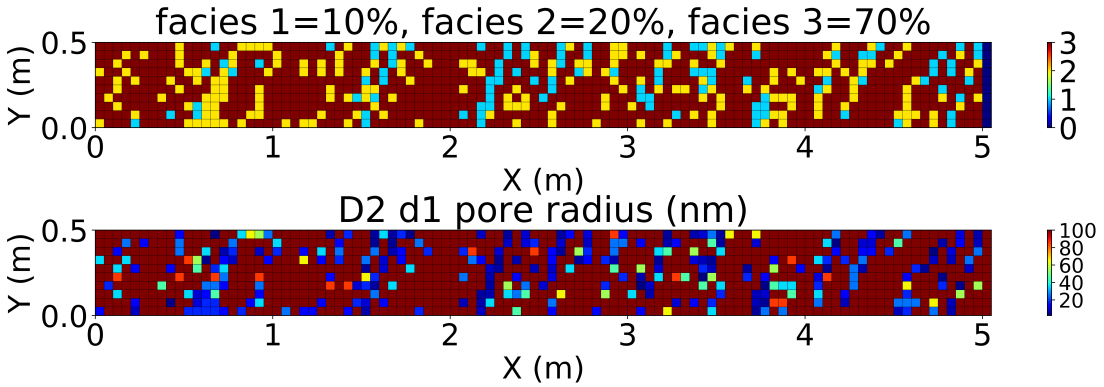

Figure C.14: Facies and pore radius field inside the matrix for distribution D1 d1 (1D matrix block with considered domain 5x0.5m)

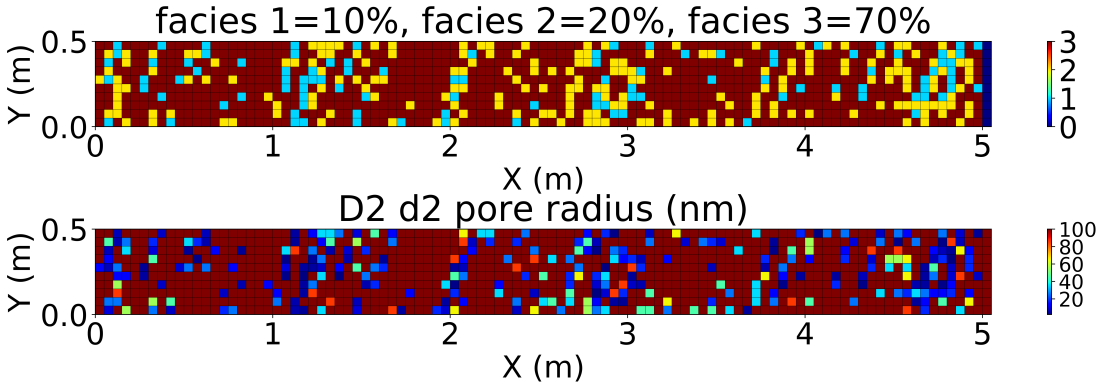

Figure C.15: Facies and pore radius field inside the matrix for distribution D1 d2 (1D matrix block with considered domain 5x0.5m)

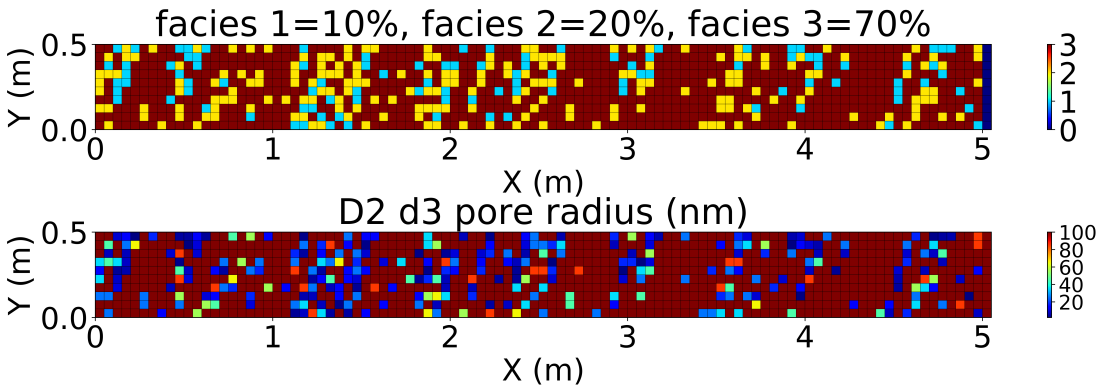

Figure C.16: Facies and pore radius field inside the matrix for distribution D1 d3 (1D matrix block with considered domain 5x0.5m)

C.2.2 Simulation results

The production results in Figure C.17 are different for each of the ten realizations. As the fracture is only present on the right side of the matrix, the flow is uni-dimensional. Therefore the difference of spacial capillary pressure heterogeneity and PVT behavior due to extremely small pore sizes has an important impact on the flow. In order to compare the different distributions D, the production data of the ten realizations of each D are represented by their average value P50 and their percentiles P10 and P90.

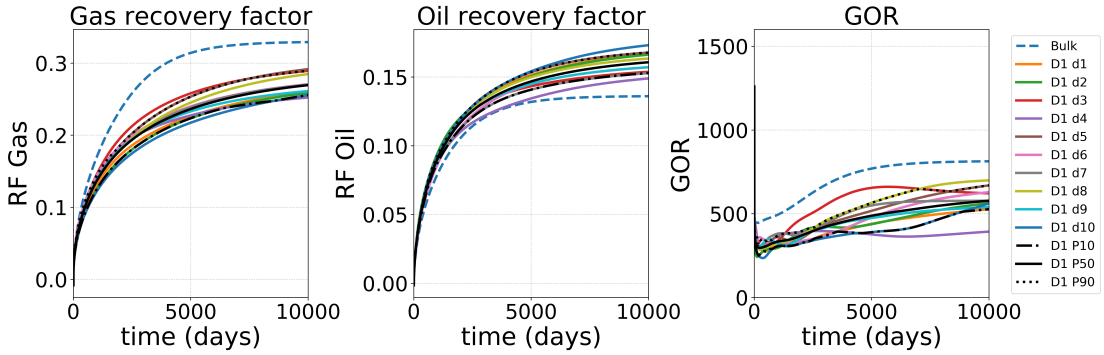

Figure C.17: Production results for the ten samples of distribution D1 compared to bulk for 1D matrix block with considered domain 5x0.5m.

C.3 Block size 10x10m

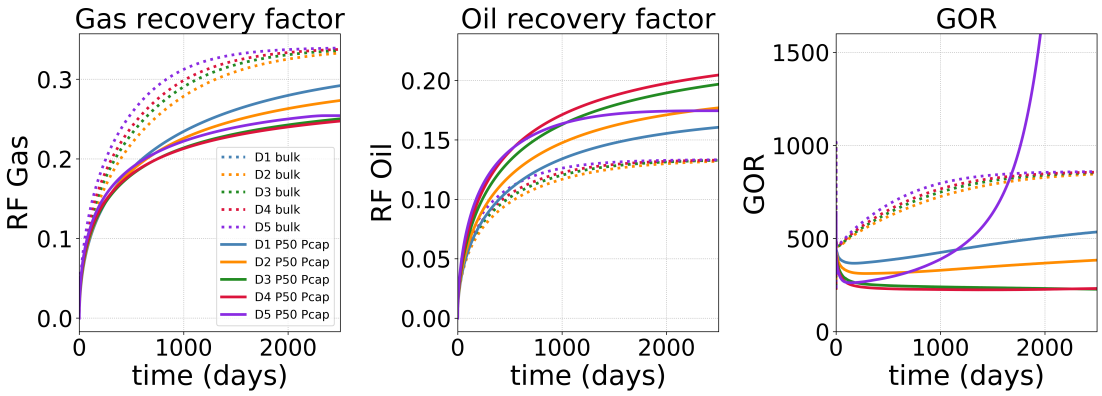

Figure C.18: Comparison of production results for the different distributions for bulk and confined fluid with a flash with capillary pressure for geometry 2 (block size 10x10 m).

C.4 Block size 40x10m

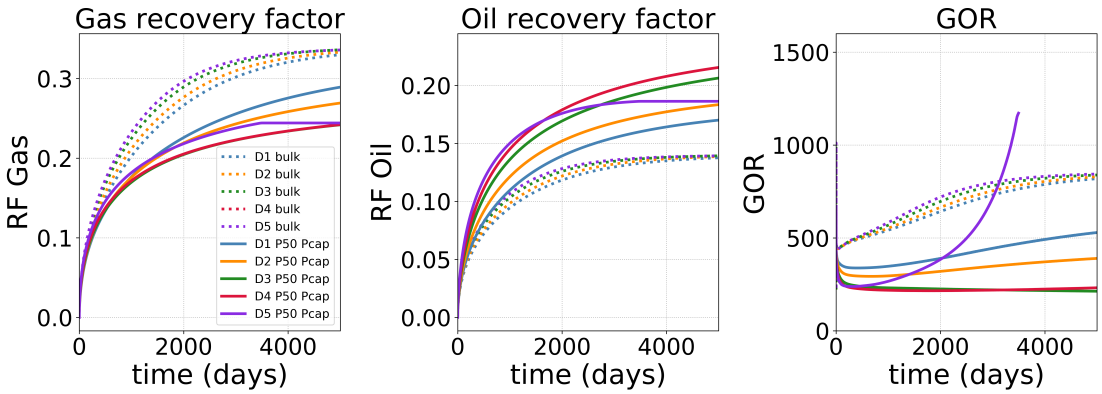

Figure C.19: Comparison of production results for the different distributions for bulk and confined fluid with a flash with capillary pressure for geometry 3 (block size 40x10 m).

Appendix D

Upscaling for large scale reservoir simulation Appendices

D.1 Calibration of simulation case with block size of 20x20m

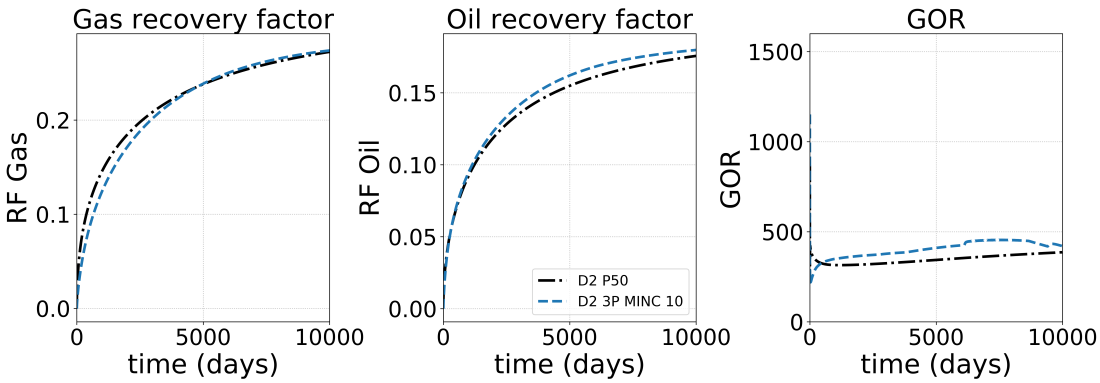

Figure D.1: Calibration of the triple porosity model for D2 (block size 20x20m)

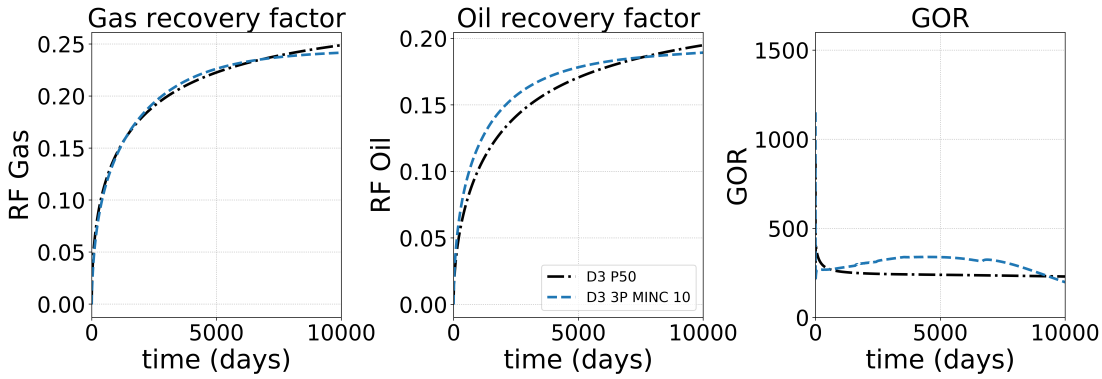

Figure D.2: Calibration of the triple porosity model for D3 (block size 20x20m)

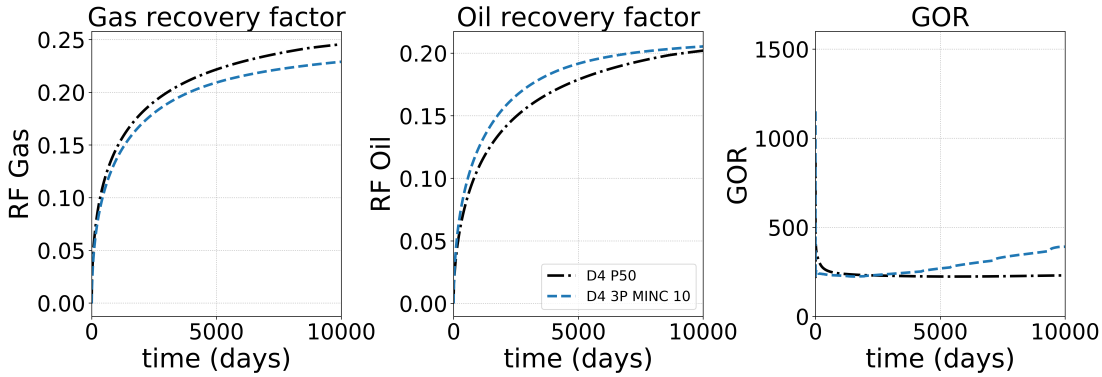

Figure D.3: Calibration of the triple porosity model for D4 (block size 20x20m)

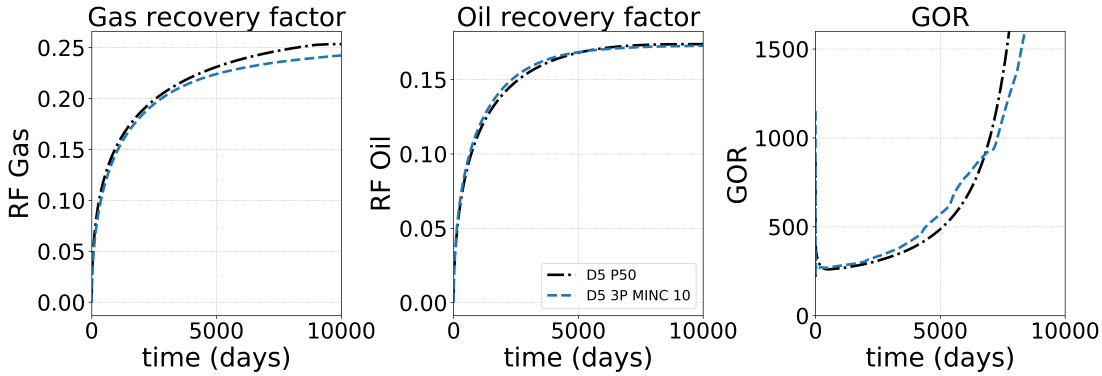

Figure D.4: Calibration of the triple porosity model for D5 (block size 20x20m)

D.2 Calibration of simulation case with block size of 10x10m

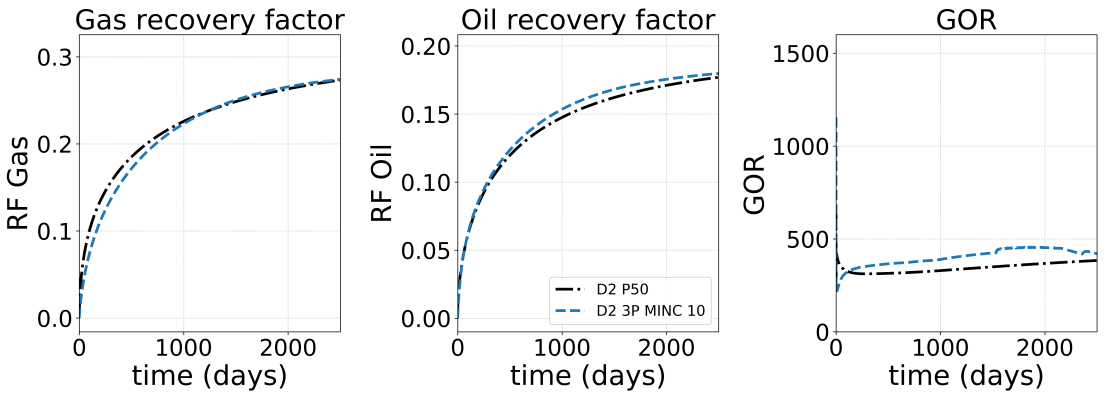

Figure D.5: Calibration of the triple porosity model for D2 (block size 10x10m)

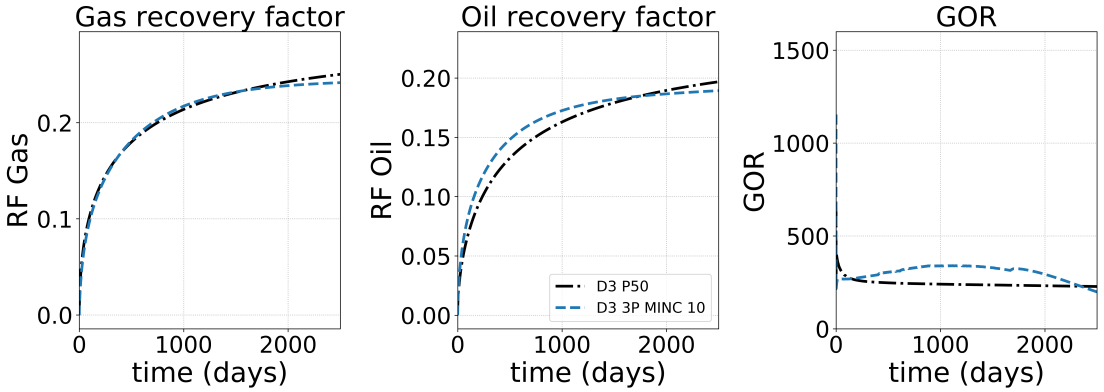

Figure D.6: Calibration of the triple porosity model for D3 (block size 10x10m)

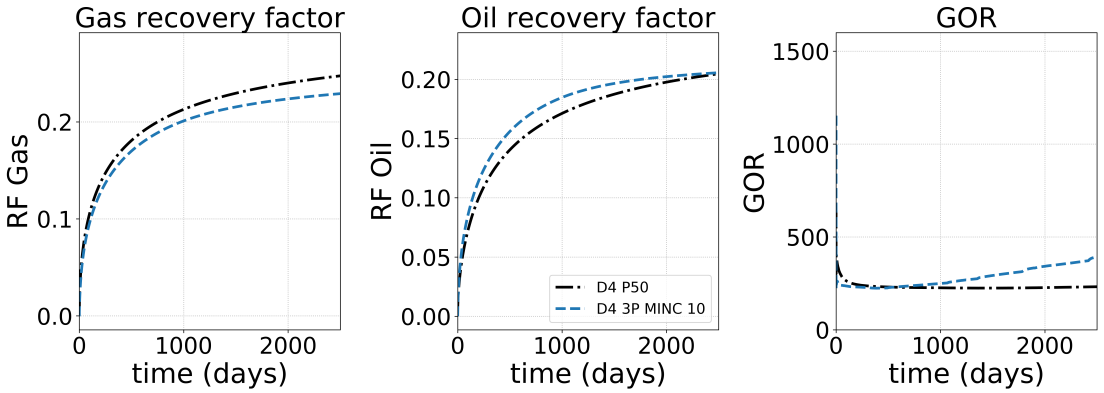

Figure D.7: Calibration of the triple porosity model for D4 (block size 10x10m)

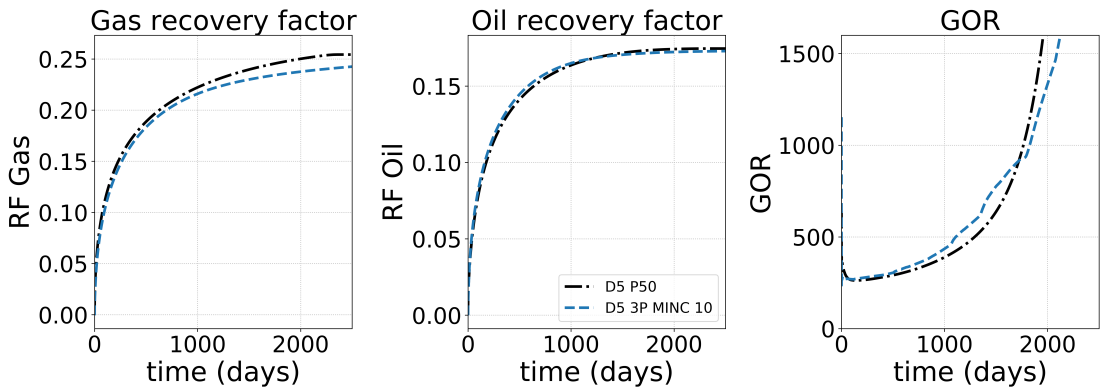

Figure D.8: Calibration of the triple porosity model for D5 (block size 10x10m)

D.3 Calibration of simulation case with block size of 10x40m

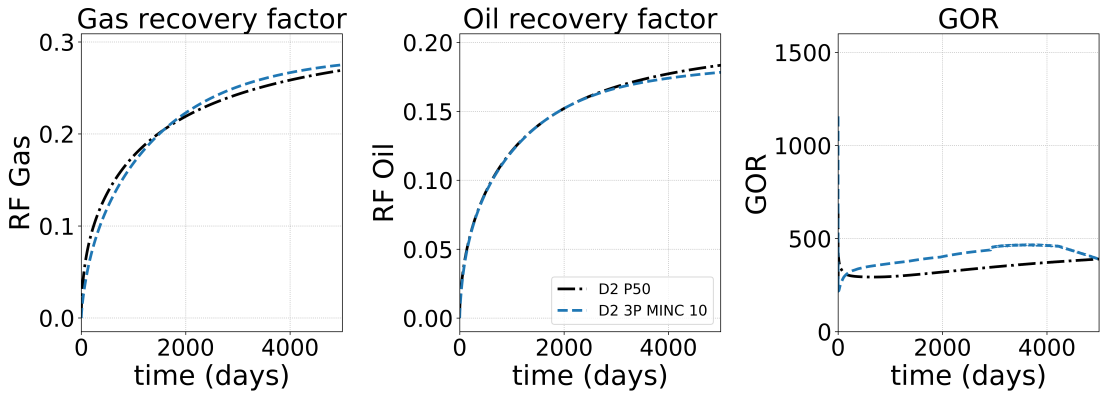

Figure D.9: Calibration of the triple porosity model for D2 (block size 10x40m)

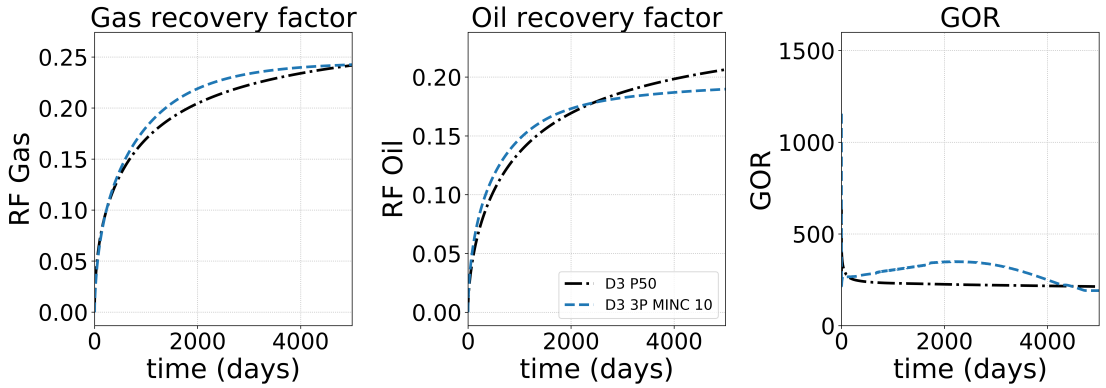

Figure D.10: Calibration of the triple porosity model for D3 (block size 10x40m)

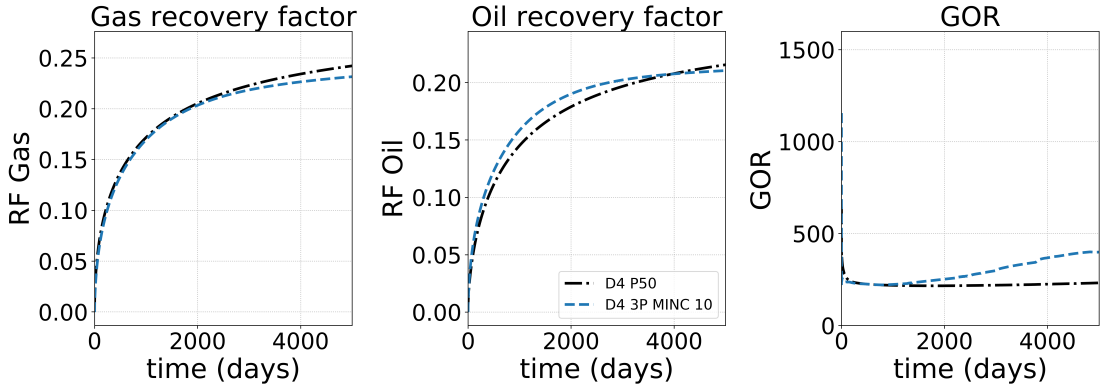

Figure D.11: Calibration of the triple porosity model for D4 (block size 10x40m)

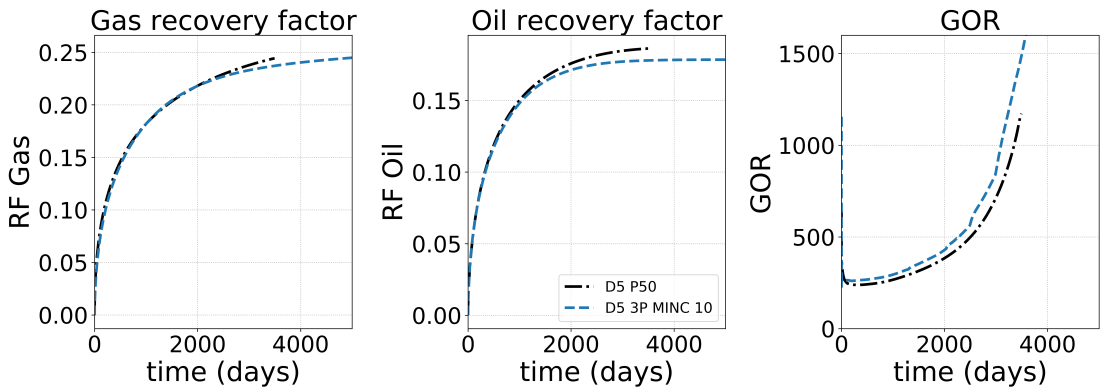

Figure D.12: Calibration of the triple porosity model for D5 (block size 10x40m)

Bibliography

[1] Abdassah, D., Ershaghi, I., 1986. Triple-porosity systems for representing naturally fractured reservoirs. Society of Petroleum Engineers, doi: http://doi.org/10.2118/13409-PA.

[2] Ahmed, T. H., 2007. Equations of state and PVT analysis: Applications for improved reservoir modeling. Gulf Pub, Houston Tex.

[3] Al Ismail, M. I., Horne, R. N., 2014. An investigation of gas-condensate flow in liquid-rich shales. In: SPE Unconventional Resources Conference, 1-3 April. SPE, The Woodlands, Texas, USA, doi: http://doi.org/10.2118/169021-MS.

[4] Alfi, M., An, C., Cao, Y., Yan, B., Barrufet, M. A., Killough, J. E., 2017. Pore size variability and sieving effect in liquid shale-a multiple permeability approach and eagle ford case study. Doi: http://doi.org/10.2118/182643-MS.

[5] Alfi, M., Nasrabadi, H., Banerjee, D., 2016. Experimental investigation of confinement effect on phase behavior of hexane, heptane and octane using lab-on-a-chip technology. Fluid Phase Equilib. 423, 25–33, doi: http://doi.org/10.1016/j.fluid.2016.04.017.

[6] Alharthy, N. S., Nguyen, T., Teklu, T., Kazemi, H., Graves, R., 2013. Multiphase compositional modeling in small-scale pores of unconventional shale reservoirs. In: SPE Annual Technical Conference and Exhibition, 30 September-2 October. SPE, New Orleans, Louisiana, USA, doi: http://doi.org/10.2118/166306-MS.

[7] Alharthy, N. S., Teklu, T. W., Abd El-Gawad, S., Kazemi, H., Graves, R., 2017. Flow dynamics and pore scale physics in unconventional shale reservoirs. In: SPE/AAPG/SEG Unconventional Resources Technology Conference, 24-26 July,. SPE, Austin, Texas, USA, doi: https://doi.org/10.15530/URTEC-2017-2698056.

[8] Ambrose, R. J., Hartman, R. C., Diaz Campos, M., Akkutlu, I. Y., Sondergeld, C., 2010. New pore-scale considerations for shale gas in place calculations. In: Unconventional Gas Conference, 23-25 February. Pittsburgh, Pennsylvania, USA, doi: http://doi.org/10.2118/131772-MS.

[9] Bai, M., Elsworth, D., Roegiers, J.-C., 1993. Multiporosity/multipermeability approach to the simulation of naturally fractured reservoirs. Water Resources Research 29 (6), 1621–1633, doi: http://doi.org/10.1029/92WR02746.

[10] Balbuena, P. B., Gubbins, K. E., 1993. Theoretical interpretation of adsorption behavior of simple fluids in slit pores. Langmuir 9 (7), 1801–1814, doi: http://doi.org/10.1021/la00031a031.

[11] Barbosa, G. D., Travalloni, L., Castier, M., Tavares, F. W., 2016. Extending an equation of state to confined fluids with basis on molecular simulations. Chem. Eng. Sci. 153, 212–220, doi: http://doi.org/10.1016/j.ces.2016.07.033.

[12] Barenblatt, G., Zheltov, I., Kochina, I., 1960. Basic concepts in the theory of seepage of homogeneous liquids in fissured rocks. Journal of Applied Mathematics and Mechanics 24 (5), 1286 – 1303, doi: http://doi.org/10.1016/0021-8928(60)90107-6.

[13] Benet, J., Palanco, J. G., Sanz, E., MacDowell, L. G., 2014. Disjoining pressure, healing distance, and film height dependent surface tension of thin wetting films. J. Phys. Chem. C. 118 (38), 22079–22089, doi: http://doi.org/10.1021/jp506534b.

[14] Bernet, T., Piñeiro, M. M., Plantier, F., Miqueu, C., 2017. Generalization of the fundamental-measure theory beyond hard potentials: The square-well fluid case. The Journal of Physical Chemistry C 121 (11), 6184–6190, doi: http://doi.org/10.1021/acs.jpcc.7b00797.

[15] Bernet, T., Piñeiro, M. M., Plantier, F., Miqueu, C., 2018. Effect of structural considerations on the development of free energy functionals for the square-well fluid. Molecular Physics 116 (15-16), 1977–1989, doi: http://doi.org/10.1080/00268976.2018.1438677.

[16] Bikai, J., Hadi, N., 2016. Phase behavior of multi-component hydrocarbon systems in nano-pores using gauge-gcmc molecular simulation. Fluid Phase Equilib. 425, 324–334, doi: http://doi.org/10.1016/j.fluid.2016.06.018.

[17] Binder, K., Landau, D. P., 1992. Capillary condensation in the lattice gas model: A monte carlo study. J. Chem. Phys. 96 (2), 1444–1454, doi: http://doi.org/10.1063/1.462180.

[18] Bird, R. B., Stewart, W. E., Lightfoot, E. N., 2007. Transport phenomena, revised 2nd edition Edition. Vol. 1. John Wiley & Sons Inc, New York etc.

[19] Bourasseau, E., Ungerer, P., Boutin, A., Fuchs, A. H., 2002. Monte carlo simulation of branched alkanes and long chain n -alkanes with anisotropic united atoms intermolecular potential. Mol. Simul. 28 (4), 317–336, doi: http://doi.org/10.1080/08927020290018723.

[20] Bourbiaux, B., Granet, S., Landereau, P., Noetinger, B., Sarda, S., Sabathier, J. C., 1999. Scaling up matrix-fracture transfers in dual-porosity models: Theory and application. Society of Petroleum Engineers, doi: http://doi.org/10.2118/56557-MS.

[21] BP, 2017 (accessed January 2019). Bp energy outlook.
URL https://www.bp.com/content/dam/bp/pdf/energy-economics/energy-outlook-2017/bp-energy-outlook-2017.pdf

[22] BP, 2017 (accessed January 2019). statistical review of world energy.
URL https://www.bp.com/content/dam/bp-country/de_ch/PDF/bp-statistical-review-of-world-energy-2017-full-report.pdf

[23] Brooks, H., A. T. Corey, R., 01 1964. Hydraulic properties of porous media and their relation to drainage design. Transactions of the ASAE 7, 0026–0028, doi: http://doi.org/10.13031/2013.40684.

[24] Chalmers, G. R., Bustin, R. M., Power, I. M., 2012. Characterization of gas shale pore systems by porosimetry, pycnometry, surface area, and field emission scanning electron microscopy/transmission electron microscopy image analyses: Examples from the barnett, woodford, haynesville, marcellus, and doig units. AAPG Bulletin 96 (6), 1099–1119, doi: http://doi.org/10.1306/10171111052.

[25] Chen, X., Cao, G., Han, A., Punyamurtula, V. K., Liu, L., Culligan, P. J., Kim, T., Qiao, Y., 2008. Nanoscale fluid transport: size and rate effects. Nano letters 8 (9), 2988–2992, doi: http://doi.org/10.1021/nl802046b.

[26] Cho, H., Bartl, M. H., Deo, M., 2017. Bubble point measurements of hydrocarbon mixtures in mesoporous media. Energ Fuel 31 (4), 3436–3444, doi: http://doi.org/10.1021/acs.energyfuels.6b02424.

[27] Churaev, N., Starov, V., Derjaguin, B., 1982. The shape of the transition zone between a thin film and bulk liquid and the line tension. Journal of colloid and interface science 89 (1), 16–24, doi: http://doi.org/10.1016/0021-9797(82)90115-1.

[28] Cipolla, C. L., Lolon, E. P., Erdle, J. C., Rubin, B., 2010. Reservoir modeling in shale-gas reservoirs. SPE Reservoir Evaluation & Engineering 13 (04), 638–653, doi: http://doi.org/10.2118/125530-PA.

[29] Clarkson, C. R., Pedersen, P. K., 2011. Production analysis of western canadian unconventional light oil plays. In: Canadian Unconventional Resources Conference, 15-17 November. SPE International, Calgary, Alberta, Canada, doi: http://doi.org/10.2118/149005-MS.

[30] Coats, K. H., 1989. Implicit compositional simulation of single-porosity and dual-porosity reservoirs. In: SPE Symposium on Reservoir Simulation, 6-8 February. Society of Petroleum Engineers, Houston, Texas, USA, doi: http://doi.org/doi:10.2118/18427-MS.

[31] Curtis H.Whitson and Michael L.Michelsen, 1989. The negative flash. Fluid Phase Equilib. 53, 51–71, doi: http://doi.org/10.1016/0378-3812(89)80072-X.

[32] Daan Frenkel and Berend Smit, 1996. Understanding Molecular Simulation: From Algorithms to Applications. Elsevier, doi: http://doi.org/10.1016/B978-0-12-267351-1.X5000-7.

[33] De Hemptine, J., Mougin, P., Barreau, A., Ruffine, L., Tamouza, S., Inchekel, R., 2006. Application to petroleum engineering of statistical thermodynamics - based equations of state. OGST - Rev. IFP 61 (3), 363–386, doi: http://doi.org/10.2516/ogst:2006039a.

[34] Devegowda, D., Sapmanee, K., Civan, F., Sigal, R. F., 2012. Phase behavior of gas condensates in shales due to pore proximity effects: Implications for transport, reserves and well productivity. In: SPE Annual Technical Conference and Exhibition, 8-10 October. SPE, San Antonio, Texas, USA, doi: http://doi.org/10.2118/160099-MS.

[35] Dong, X., Liu, H., Hou, J., Chen, Z., 2016. Phase behavior of hydrocarbon mixtures in the organic nanopores of unconventional gas condensate reservoirs. In: SPE/AAPG/SEG Unconventional Resources Technology Conference, 1-3 August. URTEC, San Antonio, Texas, USA, doi: http://doi.org/10.15530/URTEC-2016-2460485.

[36] Dong, X., Liu, H., Hou, J., Wu, K., Chen, Z., 2016. Phase equilibria of confined fluids in nanopores of tight and shale rocks considering the effect of capillary pressure and adsorption film. Ind. Eng. Chem. Res. 55 (3), 798–811, doi: http://doi.org/10.1021/acs.iecr.5b04276.

[37] EIA, 2015 (accessed January 2019). World shale resource assessments.
URL https://www.eia.gov/analysis/studies/worldshalegas/

[38] Errington, J. R., Panagiotopoulos, A. Z., 1999. A new intermolecular potential model for the n -alkane homologous series. J. Phys. Chem. B. 103 (30), 6314–6322, doi: http://doi.org/10.1021/jp990988n.

[39] Ferrando, N., 2011 (accessed January 2019). Potentiels intermoléculaires et algorithmes de monte carlo: Application à l'étude des composés oxygénés. Ph.D. thesis, Paris 11.
URL http://www.theses.fr/2011PA112080.pdf

[40] Ferrando, N., Defiolle, D., Lachet V., Boutin, A., 2010. Ethanoled gasoline bubble pressure determination: Experimental and monte carlo modeling. Fluid Phase Equilib. 299 (1), 132–140, doi: http://doi.org/10.1016/j.fluid.2010.09.020.

[41] Firincioglu, T., Ozgen, C., Ozkan, E., 2013. An excess-bubble-point-suppression correlation for black oil simulation of nano-porous unconventional oil reservoirs. In: SPE Annual Technical Conference and Exhibition, 30 September-2 October. SPE, New Orleans, Louisiana, USA, doi: http://doi.org/10.2118/166459-MS.

[42] Firincioglu, T., Ozkan, E., Ozgen, C., 2012. Thermodynamics of multiphase flow in unconventional liquids-rich reservoirs. In: SPE Annual Technical Conference and Exhibition, 8-10 October. SPE, San Antonio, Texas, USA, doi: http://doi.org/10.2118/159869-MS.

[43] Gelb, L. D., Gubbins, K. E., Radhakrishnan, R., Sliwinska-Bartkowiak, M., 1999. Phase separation in confined systems. Rep. Prog. Phys. 62 (12), 1573, doi: http://doi.org/10.1088/0034-4885/62/12/201.

[44] Geren, F., Firincioglu, T., Karacaer, C., Ozkan, E., Ozgen, C., 2014. Modeling flow in nanoporous, membrane reservoirs and interpretation of coupled fluxes. In: SPE Annual Technical Conference and Exhibition, 27-29 October. SPE, Amsterdam, The Netherlands, doi: http://doi.org/10.2118/170976-MS.

[45] Haider, B. A., Aziz, K., 2017. Impact of capillary pressure and critical property shift due to confinement on hydrocarbon production in shale reservoirs. In: SPE Reservoir Simulation Conference, 20-22 February. SPE, Montgomery, Texas, USA, doi: http://doi.org/10.2118/182603-MS.

[46] Iea International Energy Agency, 2017. World energy outlook 2017. Doi: https://doi.org/10.1787/weo-2017-en.

[47] Information Handling Service, 2012 (accessed January 2019. America's new energy future: The unconventional oil and gas revolution and the us economy, volume 1: National economic contributions.
URL https://www.globalenergyinstitute.org/sites/default/files/pdf/americas_new_energy_future-unconventional_oil_and_gas.pdf

[48] Islam, A. W., Sun, A. Y., Dec 2017. A theory-based simple extension of peng–robinson equation of state for nanopore confined fluids. Journal of Petroleum Exploration and Production Technology 7 (4), 1197–1203, doi: http://doi.org/10.1007/s13202-016-0306-y.

[49] Jiang, S., Gubbins, K. E., 1995. Vapour-liquid equilibria in two-dimensional lennard-jones fluids: unperturbed and substrate-mediated films. Mol. Phys. 86 (4), 599–612, doi: http://doi.org/10.1080/00268979500102221.

[50] Jin, B., Bi, R., Nasrabadi, H., 2017. Molecular simulation of the pore size distribution effect on phase behavior of methane confined in nanopores. Fluid Phase Equilib. 452 (Supplement C), 94–102, doi: http://doi.org/10.1016/j.fluid.2017.08.017.

[51] Jin, B., Nasrabadi, H., 2018. Phase behavior in shale organic/inorganic nanopores from molecular simulation. SPE Reservoir Evaluation & Engineering 21 (03), 626–637, doi: http://doi.org/10.2118/187307-PA.

[52] Jin, L., Ma, Y., Jamili, A., 2013. Investigating the effect of pore proximity on phase behavior and fluid properties in shale formations. In: Annual Technical Conference and Exhibition, 30 September-2 October. SPE, New Orleans, Louisiana, USA, doi: http://doi.org/10.2118/166192-MS.

[53] Jin, Z., 2018. Bubble/dew point and hysteresis of hydrocarbons in nanopores from molecular perspective. Fluid Phase Equilib. 458, 177–185, doi: http://doi.org/10.1016/j.fluid.2017.11.022.

[54] Jin, Z., Firoozabadi, A., 2016. Thermodynamic modeling of phase behavior in shale media. SPE Journal 21 (01), 190–207, doi: http://doi.org/10.2118/176015-PA.

[55] Kappa, 2018 (accessed January 2019). Pvtflow.
URL https://www.kappaeng.com/software/pvtflow

[56] Kazemi, H., 1969. Pressure transient analysis of naturally fractured reservoirs with uniform fracture distribution. Society of Petroleum Engineers Journal, doi: http://doi.org/10.2118/2156-A.

[57] Kazemi, H., Gilman, J. R., Elsharkawy, A. M., 1992. Analytical and numerical solution of oil recovery from fractured reservoirs with empirical transfer functions. Society of Petroleum Engineers, doi: http://doi.org/10.2118/19849-PA.

[58] Kazemi, H., Merrill, L. S., Porterfield, K. L., Zeman, P. R., 12 1976. Numerical simulation of water-oil flow in naturally fractured reservoirs. Society of Petroleum Engineers Journal. 16, doi: http://doi.org/doi:10.2118/5719-PA.

[59] Khoshghadam, M., Khanal, A., Yu, C., Rabinejadgangi, N., J. Lee, W., 01 2017. Producing gas-oil ratio behavior of unconventional volatile-oil reservoirs, and its application in production diagnostics and decline curve analysis. In: Unconventional Resources Technology Conference, July 24. Doi: http://doi.org/10.15530/URTEC-2017-2670925.

[60] Kuchin, I., Matar, O., Craster, R., Starov, V., 2014. Influence of the disjoining pressure on the equilibrium interfacial profile in transition zone between a thin film and a capillary meniscus. Colloids and Interface Science Communications 1, 18–22, doi: http://doi.org/10.1016/j.colcom.2014.06.002.

[61] Kuila, U., Prasad, M., 2011. Understanding pore-structure and permeability in shales. In: ATCE Conference, 30 October-2 November. SPE, Denver, Colorado, USA, doi: http://doi.org/10.2118/146869-MS.

[62] Kuila, U., Prasad, M., 2013. Specific surface area and pore–size distribution in clays and shales. Geophysical Prospecting 61 (2), 341–362, doi: http://doi.org/10.1111/1365-2478.12028.

[63] Kumar, S., Hoffman, T., Prasad, M., 2013. Upper and lower bakken shale production contribution to the middle bakken reservoir. In: URTEC Conference, 12-14 August. SPE, Denver, Colorado, doi: http://doi.org/10.1190/urtec2013-001.

[64] Lemmon, E. W., McLinden, M. O., Friend, D. G., 2018. Thermophysical properties of fluid systems: Nist standard reference database number 173. Doi: http://doi.org/10.18434/T4D303.

[65] Lemonnier, P., Bourbiaux, B., 2010. Simulation of naturally fractured reservoirs. state of the art - part 2 - matrix-fracture transfers and typical features of numerical studies. Oil Gas Sci. Technol. - Rev. IFP 65 (2), 263–286, doi: http://doi.org/10.2516/ogst/2009067.

[66] Li, B., Mezzatesta, A., 2017. Evaluation of pore size distribution effects on phase behavior of hydrocarbons produced in shale gas condensate reservoirs. In: SPE Middle East Oil and Gas Show and Conference, 6-9 March. Manama, Kingdom of Bahrain, doi: http://doi.org/10.2118/183833-MS.

[67] Li, B., Mezzatesta, A., Li, Y., Ma, Y., Jamili, A., 2016. A multilevel iterative method to quantify effects of pore-size distribution on phase equilibrium of multicomponent fluids in unconventional plays. Petrophysics 57 (02).

[68] Li, Y., Yu, Y., Zheng, Y., Li, J., Sep 2012. Vapor-liquid equilibrium properties for confined binary mixtures involving co2, ch4, and n2 from gibbs ensemble monte carlo simulations. Sci China Chem 55 (9), 1825–1831, doi: http://doi.org/10.1007/s11426-012-4724-5.

[69] Lim, K., Aziz, K., 1995. Matrix-fracture transfer shape factors for dual-porosity simulators. Journal of Petroleum Science and Engineering 13 (3), 169 – 178, doi: http://doi.org/10.1016/0920-4105(95)00010-F.

[70] Liu, J., Bodvarsson, G. S., Wu, Y.-S., 2003. Analysis of flow behavior in fractured lithophysal reservoirs. Journal of contaminant hydrology 62-63, 189–211, doi: https://doi.org/10.1016/S0169-7722(02)00169-9.

[71] Liu, Y., Li, H. A., Okuno, R., 2016. Phase behavior of fluid mixtures in a partially confined space. In: SPE Annual Technical Conference and Exhibition, 26-28 September. SPE, Dubai, UAE, doi: http://doi.org/10.2118/181716-MS.

[72] Lohrenz, J., Bray, B. G., Clark, C. R., 1964. Calculating viscosities of reservoir fluids from their compositions. SPE, doi: http://doi.org/10.2118/915-PA.

[73] Lopez Jimenez, B. A., Hernandez, G., Czernia, B., Killough, J. E., Barrufet, M. A., 2018. Effects of thermodynamic and rock properties on the performance of liquids-rich nanoporous shale reservoirs. In: SPE Argentina Exploration and Production of Unconventional Resources Symposium, 14-16 August. SPE, Neuquen, Argentina, doi: http://doi.org/10.2118/191813-MS.

[74] Luo, S., Jin, B., Lutkenhaus, J. L., Nasrabadi, H., 2019. A novel pore-size-dependent equation of state for modeling fluid phase behavior in nanopores. Fluid Phase Equilibria 498, 72 – 85, doi: http://doi.org/10.1016/j.fluid.2019.06.009.

[75] Luo, S., Nasrabadi, H., Lutkenhaus, J. L., 2016. Effect of confinement on the bubble points of hydrocarbons in nanoporous media. AIChE Journal 62 (5), 1772–1780, doi: http://doi.org/10.1002/aic.15154.

[76] Malheiro, C., Mendiboure, B., Míguez, J.-M., Piñeiro, M. M., Miqueu, C., 2014. Nonlocal density functional theory and grand canonical monte carlo molecular simulations of water adsorption in confined media. The Journal of Physical Chemistry C 118 (43), 24905–24914, doi: http://doi.org/10.1021/jp505239e.

[77] Meyra, A. G., Zarragoicoechea, G. J., Kuz, V. A., 2005. Thermodynamic equations for a confined fluid at nanometric scale. Fluid Phase Equilib. 230 (1–2), 9–14, doi: http://doi.org/10.1016/j.fluid.2004.10.014.

[78] Michelsen, M. L., 1980. Calculation of phase envelopes and critical points for multicomponent mixtures. Fluid Phase Equilib. 4 (1-2), 1–10, doi: http://doi.org/10.1016/0378-3812(80)80001-X.

[79] Michelsen Michael L. and Mollerup Jorgen M., 2007. Thermodynamic models: fundamentals and computational aspects: second edition.

[80] Miguez, J. M., Gomez-Alvarez, P., Pineiro, M. M., Mendiboure, B., Blas, F. J., 2018. Adsorption and interfacial phenomena of a lennard-jones fluid adsorbed in slit pores: Dft and gcmc simulations. Molecular Physics 116 (21-22), 3417–3424, doi: http://doi.org/10.1080/00268976.2018.1506173.

[81] Mitropoulos, A. C., 2008. The kelvin equation. J. Colloid Interface Sci. 317 (2), 643–648, doi: http://doi.org/10.1016/j.jcis.2007.10.001.

[82] Narasimhan, T. N., Witherspoon, P. A., 02 1976. An integrated finite difference method for analyzing fluid flow in porous media. Water Resources Research - WATER RESOURCES 12, 57–64, doi: http://doi.org/10.1029/WR012i001p00057.

[83] Nelson, P. H., 2009. Pore-throat sizes in sandstones, tight sandstones, and shales. AAPG Bulletin 93 (3), 329–340, doi: http://doi.org/10.1306/10240808059.

[84] Nojabaei, B., Johns, R. T., Chu, L., 2013. Effect of capillary pressure on phase behavior in tight rocks and shales. SPE Reservoir Evaluation & Engineering 16 (03), 281–289, doi: http://doi.org/10.2118/159258-PA.

[85] Page, K. S., Monson, P. A., 1996. Phase equilibrium in a molecular model of a fluid confined in a disordered porous material. Phys. Rev. E: Stat. Phys., Plasmas, Fluids, 54 (1), R29–R32, doi: http://doi.org/10.1103/PhysRevE.54.R29.

[86] Panagiotopoulos, A., Quirke, N., Stapleton, M., Tildesley, D., 1988. Phase equilibria by simulation in the gibbs ensemble. Mol. Phys. 63 (4), 527–545, doi: http://doi.org/10.1080/00268978800100361.

[87] Panagiotopoulos, A. Z., 1987. Adsorption and capillary condensation of fluids in cylindrical pores by monte carlo simulation in the gibbs ensemble. Mol. Phys. 62 (3), 701–719, doi: http://doi.org/10.1080/00268978700102501.

[88] Panagiotopoulos, A. Z., 1987. Direct determination of phase coexistence properties of fluids by monte carlo simulation in a new ensemble. Mol. Phys. 61 (4), 813–826, doi: http://doi.org/10.1080/00268978700101491.

[89] Pathak, M., Cho, H., Deo, M., 02 2017. Experimental and molecular modeling study of bubble points of hydrocarbon mixtures in nanoporous media. Energ Fuel 31, doi: http://doi.org/10.1021/acs.energyfuels.6b02422.

[90] Péneloux, A., Rauzy, E., Fréze, R., 1982. A consistent correction for redlich-kwong-soave volumes. Fluid Phase Equilibria 8 (1), 7 – 23, doi: http://doi.org/10.1016/0378-3812(82)80002-2.

[91] Peng, D.-Y., Robinson, D. B., 1976. A new two-constant equation of state. Industrial & Engineering Chemistry Fundamentals 15 (1), 59–64, doi: http://doi.org/10.1021/i160057a011.

[92] Peterson, B. K., Gubbins, K. E., 1987. Phase transitions in a cylindrical pore. Mol. Phys. 62 (1), 215–226, doi: http://doi.org/10.1080/00268978700102151.

[93] Pitakbunkate, T., Balbuena, P. B., Moridis, G. J., Blasingame, T. A., 2016. Effect of confinement on pressure/volume/temperature properties of hydrocarbons in shale reservoirs. SPE Journal 21 (02), 621–634, doi: http://doi.org/10.2118/170685-PA.

[94] Pitakbunkate, T., Blasingame, T. A., Moridis, G. J., Balbuena, P. B., 2017. Phase behavior of methane–ethane mixtures in nanopores. Ind. Eng. Chem. Res. 56 (40), 11634–11643, doi: http://doi.org/10.1021/acs.iecr.7b01913.

[95] Pommer, M. E., 2014. Quantitative assessment of pore types and pore size distribution across thermal maturity, eagle ford formation, south texas. Ph.D. thesis, The University of Texas at Austin.

[96] Porcheron, F., Rousseau, B., H. Fuchs, A., Schoen, M., 1999. Monte carlo simulations of nanoconfined n-decane films. Phys. Chem. Chem. Phys. 1 (17), 4083–4090, doi: http://doi.org/10.1039/A903431E.

[97] Pruess, K., 1985. A practical method for modeling fluid and heat flow in fractured porous media. Society of Petroleum Engineers, doi: http://doi.org/10.2118/10509-PA.

[98] Pruess, K., 1991. TOUGH2: A general-purpose numerical simulator for multiphase fluid and heat flow. United States.

[99] Pruess, K., Karasaki, K., 10 1982. Proximity functions for modeling fluids and heat flow in reservoirs with stochastic fracture distributions. Lawrence Berkeley Lab., CA (USA) submitted to the geothermal reservoir engineering workshop, Stanford, CA, USA,Doi: http://doi.org/.

[100] Quintard, M., Whitaker, S., 1996. Transport in chemically and mechanically heterogeneous porous media. i: Theoretical development of region-averaged equations for slightly compressible single-phase flow. Advances in Water Resources 19 (1), 29 – 47, doi: http://doi.org/10.1016/0309-1708(95)00023-C.

[101] Radhakrishnan, R., Gubbins, K. E., Sliwinska-Bartkowiak, M., 2000. Effect of the fluid-wall interaction on freezing of confined fluids: Toward the development of a global phase diagram. J. Chem. Phys. 112 (24), 11048–11057, doi: http://doi.org/10.1063/1.481745.

[102] Rahmani Didar, B., Akkutlu, I. Y., 2015. Confinement effects on hydrocarbon mixture phase behavior in organic nanopore. In: Unconventional Resources Technology Conference, 20-22 July. URTEC, San Antonio, Texas, USA, doi: http://doi.org/10.15530/URTEC-2015-2151854.

[103] Rezaveisi, M., Sepehrnoori, K., Pope, G. A., Johns, R. T., 2015. Compositional simulation including effect of capillary pressure on phase behavior. In: Annual Technical Conference and Exhibition, 28-30 September. SPE, Houston, Texas, USA, doi: http://doi.org/10.2118/175135-MS.

[104] Rine, J., Smart, E., Dorsey, W., Hooghan, K., Dixon, M., 10 2013. Comparison of Porosity Distribution within Selected North American Shale Units by SEM Examination of Argon-ion-milled Samples. Doi: http://doi.org/10.1306/13391710M1023588.

[105] Roy, S., Raju, R., Chuang, H. F., Cruden, B. A., Meyyappan, M., 2003. Modeling gas flow through microchannels and nanopores. Journal of Applied Physics 93 (8), 4870–4879, doi: http://doi.org/10.1063/1.1559936.

[106] Sanaei, A., Jamili, A., Callard, J., 2014. Effect of pore size distribution and connectivity on phase behavior and gas condensate production from unconventional resources. In: SPE

Unconventional Resources Conference, 1-3 April. SPE, The Woodlands, Texas, USA, doi: http://doi.org/10.2118/168970-MS.

[107] Sandoval, D. R., Yan, W., Michelsen, M. L., Stenby, E. H., 2016. The phase envelope of multicomponent mixtures in the presence of a capillary pressure difference. Ind. Eng. Chem. Res. 55 (22), 6530–6538, doi: http://doi.org/10.1021/acs.iecr.6b00972.

[108] Schoen, M., Paris, O., Günther, G., Müter, D., Prass, J., Fratzl, P., 2010. Pore-lattice deformations in ordered mesoporous matrices: Experimental studies and theoretical analysis. Phys. Chem. Chem. Phys. 12 (37), 11267–11279, doi: http://doi.org/10.1039/C000782J.

[109] Serra, K., Reynolds, A. C., Raghavan, R., 1983. New pressure transient analysis methods for naturally fractured reservoirs. Society of Petroleum Engineers, doi: http://doi.org/10.2118/10780-PA.

[110] Shabro, V., Torres-Verdin, C., Javadpour, F., 2011. Numerical simulation of shale-gas production: From pore-scale modeling of slip-flow, knudsen diffusion, and langmuir desorption to reservoir modeling of compressible fluid. In: SPE Americas Unconventional Gas Conference, 14-16 June. Society of Petroleum Engineers, The Woodlands, Texas, USA, doi: http://doi.org/10.2118/144355-MS.

[111] Shapiro, A., Stenby, E. H., 1997. Kelvin equation for a non-ideal multicomponent mixture. Fluid Phase Equilib. 134, 87–101, doi: http://doi.org/10.1016/S0378-3812(97)00045-9.

[112] Shapiro, A., Stenby, E. H., 2001. Thermodynamics of the multicomponent vapor-liquid equilibrium under capillary pressure difference. Fluid Phase Equilib. 178 (1-2), 17–32, doi: http://doi.org/10.1016/S0378-3812(00)00403-9.

[113] Siderius, D. W., Gelb, L. D., 2011. Extension of the steele 10-4-3 potential for adsorption calculations in cylindrical, spherical, and other pore geometries. J. Chem. Phys. 135 (8), 084703, doi: http://doi.org/10.1063/1.3626804.

[114] Sigmund, P. M., Dranchuk, P. M., Morrow, N. R., Purvis, R. A., 1973. Retrograde condensation in porous media. Society of Petroleum Engineers Journal 13 (02), 93–104, doi: http://doi.org/10.2118/3476-PA.

[115] Singh, S. K., Singh, J. K., 2011. Effect of pore morphology on vapor–liquid phase transition and crossover behavior of critical properties from 3d to 2d. Fluid Phase Equilib. 300 (1–2), 182–187, doi: http://doi.org/10.1016/j.fluid.2010.10.014.

[116] Singh, S. K., Sinha, A., Deo, G., Singh, J. K., 2009. Vapor−liquid phase coexistence, critical properties, and surface tension of confined alkanes. J. Phys. Chem. C. 113 (17), 7170–7180, doi: http://doi.org/10.1021/jp8073915.

[117] Sobecki, N., Ding, D., Nieto-Draghi, C., Wu, Y.-S., 04 Apr 2019. Procédé pour exploiter un réservoir pétrolier fracturé ayant une taille de pores hétérogène. submitted to l'Institut National de la Propriété Industrielle, numéro 19/03.635.

[118] Sobecki, N., Nieto-Draghi, C., Lella, A. D., Ding, D. Y., 2019. Phase behavior of hydrocarbons in nano-pores. Fluid Phase Equilibria 497, 104 – 121, doi: http://doi.org/10.1016/j.fluid.2019.05.025.

[119] Sobecki, N., Wang, S., Ding, D.-Y., Nieto Draghi, C., Wu, Y.-S., 2019. Tight oil and shale gas pvt modelling for flow simulation with matrix-fracture interaction. In: SPE Reservoir Simulation Conference, 10-11 April. SPE, Galveston, Texas, USA, doi: http://doi.org/10.2118/193867-MS.

[120] Steele, W. A., 1973. The physical interaction of gases with crystalline solids: I. gas-solid energies and properties of isolated adsorbed atoms. Surf. Sci. 36 (1), 317–352, doi: http://doi.org/10.1016/0039-6028(73)90264-1.

[121] Stimpson, B. C., Barrufet, M. A., 2016. Effects of confined space on production from tight reservoirs. In: Annual Technical Conference and Exhibition, 26-28 September. SPE, Dubai, UAE, doi: http://doi.org/10.2118/181686-MS.

[122] Stimpson, B. C., Barrufet, M. A., 2016. Thermodynamic modeling of pure components including the effects of capillarity. Journal of Chemical & Engineering Data 61 (8), 2844–2850, doi: http://doi.org/10.1021/acs.jced.6b00188.

[123] Stone, H. L., 1973. Estimation of three-phase relative permeability and residual oil data. In: Journal of Canadian Petroleum Technology. Petroleum Society of Canada, doi: http://doi.org/10.2118/73-04-06.

[124] Teklu, T. W., Alharthy, N., Kazemi, H., Yin, X., Graves, R. M., AlSumaiti, A. M., 2014. Phase behavior and minimum miscibility pressure in nanopores. SPE Reservoir Evaluation & Engineering 17 (03), 396–403, doi: http://doi.org/10.2118/168865-PA.

[125] Tian, Y., Ayers, W. B., McCain, W. D., 2013. The eagle ford shale play, south texas: Regional variations in fluid types, hydrocarbon production and reservoir properties. In: International Petroleum Technology Conference, 26-28 March. IPTC, Beijing, China, doi: http://doi.org/10.2523/IPTC-16808-MS.

[126] Travalloni, L., Castier, M., Tavares, F. W., 2014. Phase equilibrium of fluids confined in porous media from an extended peng–robinson equation of state. Fluid Phase Equilib. 362, 335–341, doi: http://doi.org/10.1016/j.fluid.2013.10.049.

[127] Travalloni, L., Castier, M., Tavares, F. W., Sandler, S. I., 2010. Critical behavior of pure confined fluids from an extension of the van der waals equation of state. J. Supercrit. Fluids 55 (2), 455–461, doi: http://doi.org/10.1016/j.supflu.2010.09.008.

[128] Ungerer, P., Beauvais, C., Delhommelle, J., Boutin, A., Rousseau, B., Fuchs, A. H., 2000. Optimization of the anisotropic united atoms intermolecular potential for n -alkanes. J. Chem. Phys. 112 (12), 5499–5510, doi: http://doi.org/10.1063/1.481116.

[129] Ungerer, P., Boutin, A., Fuchs, A. H., 1999. Direct calculation of bubble points by monte carlo simulation. Mol. Phys. 97 (4), 523–539, doi: http://doi.org/10.1080/00268979909482852.

[130] Ungerer, P., Tavitian, B., Boutin, A., 2005. Applications of molecular simulation in the oil and gas industry: Monte Carlo methods. Editions Technip, Paris and France.

[131] U.S. Energy Information Administration, 2016 (accessed January 2019). International energy outlook 2016.
URL https://www.eia.gov/outlooks/ieo/pdf/0484(2016).pdf

[132] U.S. Energy Information Administration, 2017 (accessed January 2019). International energy outlook 2017.
URL https://www.eia.gov/outlooks/ieo/pdf/0484(2017).pdf

[133] Van Megen, W., Snook, I., 1985. Physical adsorption of gases at high pressure. Mol. Phys. 54 (3), 741–755, doi: http://doi.org/10.1080/00268978500100591.

[134] Van Poolen, L. J., Holcomb, C. D., Niesen, V. G., 1997. Critical temperature and density from liquid-vapor coexistence data: Application to refrigerants r32, r124, and r152a. Fluid Phase Equilib. 129 (1-2), 105–111, doi: http://doi.org/10.1016/S0378-3812(96)03171-8.

[135] Vega, L., de Miguel, E., Rull, L. F., Jackson, G., McLure, I. A., 1992. Phase equilibria and critical behavior of square–well fluids of variable width by gibbs ensemble monte carlo simulation. J. Chem. Phys. 96 (3), 2296–2305, doi: http://doi.org/10.1063/1.462080.

[136] Vishnyakov, A., Piotrovskaya, E. M., Brodskaya, E. N., Votyakov, E. V., Tovbin, Y. K., 2001. Critical properties of lennard-jones fluids in narrow slit-shaped pores. Langmuir 17 (14), 4451–4458, doi: http://doi.org/10.1021/la001641a.

[137] Wang, C., Xiong, Y., Huang, Z., Winterfeld, P., Ding, D., Wu, Y.-S., 2017. Multi-porosity, multi-physics model to simulate fluid flow in unconventional reservoirs. In: SPE Reservoir Simulation Conference, 20-22 February. Society of Petroleum Engineers, Montgomery, Texas, USA, doi: http://doi.org/10.2118/182698-MS.

[138] Wang, F. P., Reed, R. M., 2009. Pore networks and fluid flow in gas shales. In: ATCE, 4-7 October. Society of Petroleum Engineers, New Orleans, Louisiana, doi: http://doi.org/10.2118/124253-MS.

[139] Wang, L., Parsa, E., Gao, Y., Ok, J. T., Neeves, K., Yin, X., Ozkan, E., 2014. Experimental study and modeling of the effect of nanoconfinement on hydrocarbon phase behavior in unconventional reservoirs. In: SPE Western North American and Rocky Mountain Joint Meeting, 17-18 April. Denver, Colorado, doi: http://doi.org/10.2118/169581-MS.

[140] Wang, S., 2019. Multiphysical simulation of co2 enhanced oil recovery in unconventional reservoirs: from fundamental physics to simulator development. Ph.D. thesis, Colorado School of Mines.

[141] Wang, S., Pomerantz, A. E., Xu, W., Lukyanov, A., Kleinberg, R. L., Wu, Y.-S., 2017. The impact of kerogen properties on shale gas production: A reservoir simulation sensitivity analysis. Journal of Natural Gas Science and Engineering 48, 13 – 23, doi: http://doi.org/10.1016/j.jngse.2017.06.009.

[142] Wang, S., Sobecki, N., Ding, D., Zhu, L., Wu, Y.-S., 2019. Accelerating and stabilizing the vapor-liquid equilibrium (vle) calculation in compositional simulation of unconventional reservoirs using deep learning based flash calculation. Fuel 253, 209 – 219, doi: http://doi.org/10.1016/j.fuel.2019.05.023.

[143] Wang, Y., Yan, B., Killough, J., 2013. Compositional modeling of tight oil using dynamic nanopore properties. In: SPE Annual Technical Conference and Exhibition, 30 September-2 October. New Orleans, Louisiana, USA, doi: http://doi.org/10.2118/166267-MS.

[144] Warren, J. E., Root, P. J., 1963. The behavior of naturally fractured reservoirs. SPE (03), 245–255, doi: http://doi.org/10.2118/426-PA.

[145] World Energy Council, 2016 (accessed January 2019). Unconventional gas, a global phenomenon.
URL https://www.worldenergy.org/wp-content/uploads/2016/02/Unconventional-gas-a-global-phenomenon-World-Energy-Resources_-Full-report-.pdf

[146] Wu, Y., 1998. Msflow: Multiphase subsurface flow model of oil. gas and water in porous and fractured media with water shutoff capability. Documentation and User's Guide. Walnut Creek, California.

[147] Wu, Y.-S., Liu, H., Bodvarsson, G., 2004. A triple-continuum approach for modeling flow and transport processes in fractured rock. Journal of Contaminant Hydrology 73 (1), 145 – 179, doi: http://doi.org/10.1016/j.jconhyd.2004.01.002.

[148] Wu, Y.-S., Pan, L., 2003. Special relative permeability functions with analytical solutions for transient flow into unsaturated rock matrix. Water Resources Research 39 (4), doi: http://doi.org/10.1029/2002WR001495.

[149] Wu, Y.-S., Pruess, K., 1998. A numerical method for simulating non-newtonian fluid flow and displacement in porous media. Advances in Water Resources 21 (5), 351 – 362, doi: http://doi.org/10.1016/S0309-1708(97)00004-3.

[150] Wu, Y.-S., Wang, C., Li, J., Fakcharoenphol, P., 2012. Transient gas flow in unconventional gas reservoir. In: SPE Europec/EAGE Annual Conference, 4-7 June. Society of Petroleum Engineers, Copenhagen, Denmark, doi: http://doi.org/10.2118/154448-MS.

[151] Xiong, Y., 2015. Development of a compositional model fully coupled with geomechanics and its application to tight oil reservoir simulation. Ph.D. thesis, Colorado School of Mines.

[152] Xiong, Y., Winterfeld, P., Wang, C., Huang, Z., Wu, Y.-S., 2015. Effect of large capillary pressure on fluid flow and transport in stress-sensitive tight oil reservoirs. In: Annual Technical Conference and Exhibition, 28-30 September. SPE, Houston, Texas, USA, doi: http://doi.org/10.2118/175074-MS.

[153] Xiong, Y., Winterfield, P. H., Wu, Y.-S., Huang, Z., 2014. Coupled geomechanics and pore confinement effects for modeling unconventional shale reservoirs. Doi: http://doi.org/10.15530/URTEC-2014-1923960.

[154] Zhang, L., Lu, S., Xiao, D., Gu, M., 2016. Characterization of full pore size distribution and its significance to macroscopic physical parameters in tight glutenites. Journal of Natural Gas Science and Engineering 38, 434 – 449, doi: http://doi.org/10.1016/j.jngse.2016.12.026.

[155] Zhang, Y., Lashgari, H. R., Di, Y., Sepehrnoori, K., 2016. Capillary pressure effect on hydrocarbon phase behavior in unconventional reservoirs. In: SPE Low Perm Symposium, 5-6 May. SPE, Denver, Colorado, USA, doi: http://doi.org/10.2118/180235-MS.

[156] Zhu, Z., Yin, X., Ozkan, E., 2015. Theoretical investigation of the effect of membrane properties of nanoporous reservoirs on the phase behavior of confined light oil. In: Annual Technical Conference and Exhibition, 28-30 September. Society of Petroleum Engineers, Houston, Texas, USA, doi: http://doi.org/10.2118/175152-MS.

[157] Ziarani, A. S., Aguilera, R., 2012. Knudsen's permeability correction for tight porous media. Transport in Porous Media 91 (1), 239–260, doi: http://doi.org/10.1007/s11242-011-9842-6.

[158] Zuo, J. Y., Guo, X., Liu, Y., Pan, S., Canas, J., Mullins, O. C., 2018. Impact of capillary pressure and nanopore confinement on phase behaviors of shale gas and oil. Energ Fuel 32 (4), 4705–4714, doi: http://doi.org/10.1021/acs.energyfuels.7b03975.

[159] Zuo, Y.-X., Stenby, E. H., 1998. Prediction of interfacial tensions of reservoir crude oil and gas condensate systems. SPE Journal 3 (02), 134–145, doi: http://doi.org/10.2118/38434-PA.